EPFL

Thèse n° 10022

Multi-scale characterization and modeling of notched strength and translaminar fracture in hybrid thin-ply composites based on different carbon fiber grades

Présentée le 2 juin 2023

Faculté des sciences et techniques de l'ingénieur
Laboratoire de mise en oeuvre de composites à haute performance
Programme doctoral en manufacturing

pour l'obtention du grade de Docteur ès Sciences

par

Guillaume Clément BROGGI

Acceptée sur proposition du jury

Prof. R. Logé, président du jury
Prof. V. Michaud, Prof. J. Cugnoni, directeurs de thèse
Prof. Y. Swolfs, rapporteur
Dr F. Laurin, rapporteur
Prof. A. Vassilopoulos, rapporteur

École polytechnique fédérale de Lausanne

2023

February 20, 2023

To Laurent and Hadrien

The scientist does not study nature because it is useful;
he studies it because he delights in it, and he delights in it because it is beautiful.
If nature were not beautiful, it would not be worth knowing,
and if nature were not worth knowing, life would not be worth living.
Henri Poincaré

Acknowledgements

This thesis has been carried out at the Laboratory for Processing of Advanced Composites (LPAC) in École Polytechnique Fédérale de Lausanne (EPFL), Switzerland. I would like to sincerely acknowledge the European Union's Horizon 2020 research and innovation program under the Marie Sklodowska-Curie grant agreement No 765881 for funding this work.

"*If I have seen further, it is by standing on the shoulders of giants.*" This formulation attributed to Isaac Newton is, arguably, presumptuous. Yet, I like it, not in a vain attempt to compare myself to greater minds, but because I do believe in its message. It is only by standing on my own giants that I could achieve a PhD. I would like to thank them here, although I know the list will not be exhaustive.

I am fortunate to have been born in a time of peace, in a European country, where freedom of expression and thought is guaranteed, and where free access to education for young people is a priority. Especially, I am more than grateful to all my former professors and mentors, who believed in me and fought to transmit their passion for knowledge. Among them, I thank Alain Heckel, Jean-Christophe Wolff, Nicolas Dellinger, Brigitte Juncker, David Prevost, Cyrille Baudouin, Sophie Berveiller, Alain Étienne, Philippe Mayer, and Éric Becker. One way or another, they have had a very positive impact on who I am today, and I would probably never have undertaken a Ph.D. without them.

The last elements of this list are my supervisors, Prof. Véronique Michaud and Prof. Joël Cugnoni, to whom I would like to express my deepest gratitude. They knew how to identify the right subject for me, and they trusted me with it. As many have said before me, they never fail to offer their scientific enthusiasm, their positivism, their support, their involvement, some of their inexhaustible knowledge, and valuable technical advice, including during my late-night writing sessions. Their guidance has truly been the cornerstone of my work.

Additionally, I thank Prof. John Botsis for providing scientific guidance and additional funding for my work. I have been privileged that Prof. Yentl Swolfs, Dr. Frédéric Laurin, and Prof. Anastasios Vassilopoulos agreed to examine and evaluate my thesis. I am grateful for their valuable contributions and for the quality of the discussions we had together.

I want to thank all my colleagues, and friends, from LPAC, who contribute to the amazing spirit of the

group. First, I thank Nathan, who made sure that I would feel at home from the first day. I sincerely acknowledge the most experienced member of the laboratory, Baris, Adrien, Yann, Céline, Robin, Gavin, and Raphaël, for providing extended feedback and pieces of advice, as well as friendly talks around coffee or lunch. More generally, a warm thank to Mayeul, Jeroen, Raymond, Niels, Cecilia, Feyza, Nour, Massimo, Yves, Quentin and all the others who make the conviviality and the support of the group. A special dedication to Aigoul, Joanne, Alexandre and Vincent who perfectly organized many team-building events. Many thanks to Cécile, thanks to whom administrative tasks were always a seamless process. Many warm thanks to my office mates and friends, Jialiang and Helena, for all the discussions, the support, the book and play reviews, and the great (and luxuriant) atmosphere of the room. I acknowledge Dr. Pierre-Etienne Bourban, for providing access to the DLL equipment, and especially to the stereo-digital image correlation setup. I also sincerely thank the ATMX workshop for the frequent use of their equipment, and more specifically Yves Ruschetta for his help and kindness.

I also thank all my friends from the HyFiSyn project: Alex, Salvo, Sina, Camilo, Babak, Olivier, Rajnish, Arya, Paul, Gokul, Jaganath, and Tahreem. Working with all of you on such a project has really been a wonderful experience and led to close friendships. I would like to express my gratitude to Prof. Yentl Swolfs and Prof. Michael Wisnom, from KU Leuven and the University of Bristol, who supported me and welcomed me as a visiting researcher for my secondments.

I would like to acknowledge Prof. Jean-Claude Ameisen for hosting the radio show "*Sur les épaules de Darwin*". He is incredibly gifted at sharing his passion for science and his lectures have accompanied many of my experiences.

I specifically thank my dear friends from Lausanne, Atlanta, Colmar and Metz: Thibault, Mathias, Alexandre, Romain, Clara, Pierrick, Émile, Élise, Hadrien, Chloé, Kenny, Martin, Arnaud, Lucas, and Clément, among others. I thank them for the board-games, movie nights, hiking, skiing and all the other activities that have helped me relaxing when I needed it. They also provided me with the intellectual stimulation that is required for taking on a doctorate.

Finally, I want to thank my last giants, my family. I will always be grateful to my grandparents, who worked their whole life to provide a better future for their children and grandchildren. They taught me the value of work, and thanks to their effort and the ones of my parents, I have never lacked anything. Thus, my success is their success. I also thank my parents and my brother, for their love and their constant moral and material support.

Among them, I am very grateful to Margot for her love. I was fortunate enough to write as poorly as she did in English. While this is hopefully no longer a problem, it allowed me to embark with her brilliant and spontaneous mind on the journey of life, to navigate its storms and uncover its joys.

Morges, the 20th of February 2023

Abstract

Owing to their high specific stiffness and strength, Carbon Fiber Reinforced Composites (CFRP) are ideal candidates for the development of lightweight high-performance structures. Within this family, thin-ply composites allow for wider design freedom and present superior mechanical properties as failure is reached at nearly the ultimate strain of the fiber, in contrast with regular composites, due to the delay or suppression of transverse cracking, micro-cracking, and delamination. However, this results in a very brittle failure, and a low translaminar toughness. As a result, thin-plies are not tolerant to stress intensity concentrators, reducing their advantage, preventing a damage-tolerant design approach, and thus restricting their wider use.

Fiber hybridization is a possible route to reach a trade-off between the translaminar toughness and tensile properties in thin-ply composites. The present thesis work focuses on the combination of two different types of carbon fibers, one with a high strain to failure and lower modulus, and the other with a high modulus, and low strain to failure. Various types of fiber hybridization are explored, from an interlayer configuration to interyarn and intrayarns architectures.

A thorough experimental analysis was conducted to evaluate the Energy Release Rate in Cross-ply laminates, and the tensile properties in unnotched and open-hole tensile mode for Quasi-iso laminates, and identify hybrid effects, as a function of the low-strain fiber volume fraction, ply-block thickness and symmetry. A novel J-integral implementation to derive the experimental mode I translaminar toughness from experimental displacement fields of Compact Tension (CT) specimens measured by Digital Image Correlation (DIC) was proposed and benchmarked for three different formulations.

Results highlighted the large design space opened by hybridization, with a significant change in the damage sequence. The interlayer hybridization yields a substantial positive hybrid effect with respect to the ply-thickness effect. The positive hybrid effect observed for the best-performing arrangements resulted from the presence of secondary damage in asymmetric ply-blocks. In contrast, symmetric ply-blocks were found ineffective as a proper fragmentation of the low-strain plies could not be triggered, due to a lower experimental strain to failure of the high-strain fiber, as compared to the datasheet.

Interyarn and intrayarn configurations were then explored as a means to increase fiber dispersion and mitigate the ply-block thickness increase resulting from layer-by-layer hybridization. A similar exper-

imental test campaign was conducted, highlighting the possibility of obtaining a positive hybrid effect through alternative mechanisms as compared to pull-out, such as crack bridging by low-strain tows.

A phenomenological study was then conducted to account for the change in translaminar toughness, by quantification of the pull-out length in fracture surfaces, completed by a shear-lag model implemented in a finite element model to propose a method for prediction of these changes as a function of microstructure. Results showed that the pull-out bundle height and width distributions are strongly impacted by the ply thickness in agreement with previous studies. More importantly, quantitative data was gathered about the influence of fiber hybridization and its architecture on the pull-out bundle distribution, leading to identify two distinct dissipative mechanisms.

Keywords:
Carbon fiber reinforced polymers, Thin-ply composites, Fiber-hybrids, Translaminar toughness, J-integral, X-ray computed tomography, Multiscale FEmodelling, Cohesive elements.

Résumé

Grâce à leur rigidité et à leur résistance spécifique élevées, les composites renforcés de fibres de carbone sont des matériaux idéaux pour la conception de structures légères et performantes. Parmi eux, les composites à plis fins offrent une plus grande liberté de conception et présentent des propriétés mécaniques supérieures aux composites ordinaires, car la rupture du laminé est atteinte pratiquement à l'allongement ultime de la fibre. Cela s'explique par le décalage ou la suppression de la fissuration transverse, de la microfissuration et de la délamination. Néanmoins, l'absence de ces mécanismes s'accompagne d'un mode de rupture très fragile et d'une faible ténacité translaminaire. Par conséquent, les composites à plis fins ne sont pas tolérants aux concentrateurs de contrainte. Cela impacte significativement leur avantage, interdit l'utilisation d'une approche de conception par tolérance aux défauts et limite donc leur utilisation à grande échelle.

L'hybridation des fibres est une technique prometteuse pour optimiser la ténacité translaminaire et les propriétés en traction des composites à plis fins. Le présent travail de thèse se concentre sur la combinaison de deux types différents de fibres de carbone, l'une avec une forte déformation à la rupture et un faible module, et l'autre avec un module élevé et une faible déformation à la rupture. Différentes approches d'hybridation sont explorées, incluant des hybrides inter-plis, inter-mèches et intra-mèches.

Une analyse expérimentale approfondie a été menée pour évaluer l'énergie critique de propagation des fissures dans des laminés à plis croisés, ainsi que les propriétés en traction, avec ou sans défaut circulaire, de laminés quasi-isotropique, afin d'identifier les effets hybrides, en fonction de la fraction volumique des fibres à faible déformation, de l'épaisseur et de la symétrie des couches du laminé. Une nouvelle implémentation de l'intégrale curviligne J est proposée pour dériver la ténacité translaminaire en mode I à partir des champs de déplacement expérimentaux d'éprouvettes entaillées et mesurés par corrélation d'image.

Les résultats mettent en évidence les nouveaux horizons de conception ouverts par l'hybridation, avec un changement significatif dans la séquence d'endommagement. L'hybridation inter-plis produit un effet positif significatif par rapport à l'effet de l'épaisseur du pli. L'effet positif observé pour les arrangements les plus performants résulte de la présence d'endommagements secondaires dans les couches asymétriques. En revanche, les couches symétriques se sont avérées inefficaces car une fragmentation appropriée des plis à faible contrainte n'a pas pu être obtenue, en raison d'une contrainte

à la rupture expérimentale de la fibre à forte déformation significativement plus faible que la valeur théorique atteignable, d'après la fiche technique.

Les configurations inter- et intra-mèches ont ensuite été explorées comme moyen d'augmenter la dispersion des fibres et de réduire l'épaisseur des couches hybrides. Une campagne d'essais expérimentaux similaire a été menée, mettant en évidence la possibilité d'obtenir un effet hybride positif par des mécanismes alternatifs à l'arrachement, tels que le pontage de fissures par les fibres à faible élongation.

Une étude phénoménologique a ensuite été menée pour rendre compte de la modification de la ténacité translaminaire, par la quantification de la longueur d'arrachement dans le sillage de la fissure, complétée par un modèle de cisaillement implémenté par éléments finis pour proposer une méthode de prédiction de ces changements en fonction de la microstructure. Les résultats ont montré que les distributions de la hauteur et de la largeur des fibres arrachées sont fortement influencées par l'épaisseur de la couche, en accord avec les études précédentes, mais aussi par l'hybridation. Plus important encore, des données quantitatives ont été recueillies sur l'influence de l'hybridation des fibres et de leur architecture sur la distribution des fibres arrachées, ce qui a permis d'identifier deux mécanismes dissipatifs distincts.

Mots clefs: Mécanique de la rupture, Ténacité translaminaire, Composites à plis fins, Intégrale J, Hybridation

Contents

Acknowledgment **ii**

Abstract **iv**

Résumé **vi**

List of Figures **xii**

List of Tables **xvii**

List of acronyms **xix**

List of symbols **xxii**

1 Introduction **1**

1.1 Context and motivation 1

1.2 Objectives 5

1.3 Structure and approach 6

2 State of the art **9**

2.1 Composites: general considerations 9

2.2 Thin-ply composites 10

2.2.1 Thin-ply development and manufacturing 10

2.2.2 Benefits and drawbacks of thin-ply laminates 11

2.2.3 The toughness issue 17

2.3 Fiber-hybrid composites 20

2.4 Translaminar fracture testing 23

3 Experimental materials and methods **27**

3.1 Material selection for carbon-carbon fiber hybridization 27

3.1.1 Maximizing the tensile properties 28

3.1.2 Tensile strength 30

3.1.3 Conclusion 30

3.1.4 Maximizing translaminar toughness 31

3.1.5 Hybrid ply-block configuration . . . 35
3.2 Experimental methods . . . 40
3.2.1 Manufacturing . . . 40
3.2.2 Translaminar toughness testing . . . 44
3.2.3 Unnotched and open-hole tensile tests . . . 47
3.2.4 Fracture surface analysis . . . 48
3.2.5 In-situ computed tomography . . . 49

4 J-integral data reduction methods 51
4.1 J-integral implementation . . . 52
4.1.1 J-integral as a line integral formulation . . . 52
4.1.2 J-integral as a simplified line integral formulation . . . 54
4.1.3 J-integral as a surface integral formulation . . . 54
4.1.4 Displacement derivatives calculation . . . 55
4.1.5 Crack tip identification . . . 56
4.2 Numerical validation . . . 57
4.2.1 Data generation . . . 57
4.2.2 Results . . . 58
4.2.3 Discussion . . . 65
4.3 Experimental validation . . . 66
4.3.1 Experimental methods . . . 66
4.3.2 Results . . . 66
4.3.3 Discussion . . . 71

5 Interlayer thin-ply fiber-hybrids 77
5.1 Translaminar toughness . . . 79
5.1.1 Result overview . . . 79
5.1.2 Hybridization effect . . . 82
5.1.3 Influence of the initial crack length . . . 87
5.2 Unnotched Tensile (UNT) properties . . . 92
5.2.1 Strength . . . 93
5.2.2 Modulus . . . 101
5.3 Open Hole Tensile (OHT) properties . . . 101
5.4 Conclusion . . . 106

6 Interyarn and intrayarn hybrids 109
6.1 Translaminar toughness . . . 112
6.1.1 Result overview . . . 112
6.1.2 Hybridization effect . . . 114
6.2 Unnotched Tensile (UNT) properties . . . 118
6.2.1 Strength . . . 119

6.2.2 Modulus . . . 123
6.3 Open Hole Tensile (OHT) properties . . . 123
6.4 Conclusion . . . 125

7 Phenomenological study **127**
7.1 Optical microscopy observations . . . 128
7.2 Profile analysis . . . 128
7.3 Translaminar toughness modeling . . . 137
7.3.1 Mechanistic assumptions . . . 137
7.3.2 Modeling choices . . . 139
7.3.3 Microscale model . . . 140
7.3.4 Macroscale model . . . 145
7.4 Scanning electron microscope phenomenological observations . . . 149
7.5 In-situ phenomenological observations . . . 154
7.6 Conclusion . . . 157

8 Conclusion and outlook **159**
8.1 Summary and Conclusion . . . 159
8.2 Future outlook . . . 162

Bibliography **163**

A Supporting information for chapter 4 **179**

B Supporting information for chapter 5 and chapter 6 **189**

C Supporting information for chapter 7 **193**

List of Figures

1.1 Final energy consumption in Europe per sector. . . . 2
1.2 Ashby charts for different types of materials, including carbon-epoxy thin-ply and thick-ply composites. . . . 4
1.3 The Dahu foiling over lake Geneva in 2022. . . . 4
1.4 Thesis graphical abstract. . . . 6

2.1 Typical autoclave processing system. . . . 10
2.2 SEM and micrograph of thin-ply material. . . . 12
2.3 Onset of damage and ultimate strength in UNT and QI specimens as a function of ply thickness. 13
2.4 Ply-thickness effect on transverse strength. . . . 14
2.5 Free edge and bulk cracks as a function of ply thickness. . . . 15
2.6 Interlaminar, intralaminar, and translaminar fracture toughness as a function of ply thickness and corresponding pull-out lengths. . . . 17
2.7 SEM fracture surfaces of CP thin-ply laminates exhibiting bundles of fibers pulled out. . . . 18
2.8 SEM fracture surfaces of specimens with engineered micro-cuts. . . . 19
2.9 Fiber hybridization architectures. . . . 20
2.10 Typical multi-scale damage modes in thick-ply or hierarchical thin-ply composites. . . . 24

3.1 Shear-lag model for interlayer hybrids. . . . 33
3.2 characterized with 4ENF samples for the 34-700-TP415 system. . . . 33
3.3 Failure stresses in UD interlayer hybrids. . . . 36
3.4 Tensile properties of UD interlayer hybrids. . . . 37
3.5 Hybrid system selection tools. . . . 38
3.6 Failure map for the HR40-34-700 TP415 system. . . . 39
3.7 General nomenclature. . . . 40
3.8 Autoclave curing procedure. . . . 41
3.9 Autoclave curing cycle. . . . 42
3.10 $^{33}\mathrm{L1A}_{60}^{30}$ micrograph. . . . 43
3.11 CT sample geometry. . . . 45
3.12 Details of a CT specimen pre-crack. . . . 46
3.13 UNT and OHT sample geometries. . . . 47
3.14 Post-mortem fracture surface observations. . . . 48
3.15 Typical fracture profile and simplified profile used to characterize pull-out bundles. . . . 49

4.1 CT sample geometry and parametrization of the J-integral, and DIC data grid. . . . 54

4.2 FEM data generation. . . . 58
4.3 Detailed results of crack identification methods on artificial data. . . . 59
4.4 Overview of the J-integral error committed on artificial and moderately noisy data. . . . 61
4.5 Detailed J-integral error committed on artificial and noiseless data. . . . 63
4.6 Detailed J-integral error committed on artificial and moderately noisy data. . . . 64
4.7 Detailed J-integral error committed on artificial and highly noisy data. . . . 64
4.8 J-integral results obtained for different crack lengths with artificial, moderately noisy and highly noisy data. . . . 66
4.9 Typical CT specimen and fitted experimental displacement field. . . . 67
4.10 Typical load-displacement curve and compliance curve. . . . 68
4.11 Crack lengths measurements with experimental data. . . . 69
4.12 Out-of-plane and in-plane experimental displacement fields. . . . 70
4.13 Detailed J-integral results obtained with experimental data. . . . 70
4.14 Experimental ERR. . . . 72
4.15 Detailed view of fiber pull-out in the wake of the crack. . . . 73
4.16 J-integral validation with a FEM capturing the crack propagation. . . . 74

5.1 Interlayer hybrid nomenclature. . . . 77
5.2 Typical CT loading curves. . . . 81
5.3 Typical R-curves obtained with baseline configuration ${}^{0}\mathrm{B3}^{0}_{120}$. . . . 82
5.4 Baseline and interlayer hybrid ERR. . . . 83
5.5 Baseline hybrid laminate ERR box plots. . . . 84
5.6 Baseline and interlayer hybrid laminate ERR box plots as a function of ply-block FAW. . . . 84
5.7 Linear RoM applied to interlayer hybrids ${}^{33}\mathrm{L3A}^{60}_{120}$, ${}^{33}\mathrm{L4S}^{60}_{120}$ and ${}^{14}\mathrm{L5A}^{30}_{180}$ to predict steady-state ERR values. . . . 87
5.8 Initiation ERR normalized by RoM for interlayer hybrids. . . . 88
5.9 Steady-state ERR normalized by RoM for interlayer hybrids. . . . 88
5.10 Secondary damage introduced by hybridization and corresponding R-curves. . . . 90
5.11 Maximal ERR corresponding to secondary damage normalized by RoM for interlayer hybrids. . . . 91
5.12 Strain fields predicted by FEM for a short and a large initial crack length. . . . 92
5.13 Typical QI UNT stress-strain curves. . . . 93
5.14 Baseline and interlayer hybrid onset of damage and strength. . . . 93
5.15 Baseline strength scaling. . . . 95
5.16 Baseline and interlayer hybrid QI onset of damage and strength boxplots as a function of ply-block FAW. . . . 95
5.17 Bilinear RoM applied to sample ${}^{33}\mathrm{L3A}^{60}_{120}$ and ${}^{33}\mathrm{L4S}^{60}_{120}$ to predict steady-state ERR values. . . . 96
5.18 Strength normalized by RoM for interlayer hybrids. . . . 97
5.19 Baseline and interlayer hybrid strain as a function of ply-block FAW. . . . 98
5.20 Normalized interlayer hybrid strain at the onset of damage as a function of low-strain volume fraction . . . 98
5.21 In-situ monitoring of free-edge delamination. . . . 99
5.22 Updated failure maps. . . . 100
5.23 Baseline and interlayer hybrid ERR boxplots as a function of ply-block FAW. . . . 101

5.24 Typical QI oht load-displacement curves. . . . 102
5.25 Baseline and interlayer hybrid OHT far-field strength and notch sensitivity as a function of ply-block FAW. . . . 103
5.26 Post-mortem failure of OHT specimens. . . . 104
5.27 CT-scan of OHT samples after loading to 95 % of the OHT strength. . . . 105
5.28 Interlayer hybrids Ashby plot. . . . 106
5.29 Overview of experimental hybrid effects observed in this work. . . . 108

6.1 Interlayer hybrid nomenclature. . . . 109
6.2 Interyarn overlayed and offset stacking sequence. . . . 111
6.3 $^{33}C2^{45}$ micrograph 112
6.4 Typical interyarn and intrayarn CT loading curves. . . . 113
6.5 Baseline, interyarn, and intrayarn hybrid ERR. . . . 114
6.6 Compared R-curves between line J-integral and CC for $^{25}Y1^{90}$ and $^{25}Y2O^{90}$. . . . 115
6.7 Baseline, interyarn, and intrayarn hybrid ERR box plots. . . . 116
6.8 Linear RoM applied to the interyarn hybrid $^{25}Y1^{90}$ to predict steady-state ERR values. . . . 116
6.9 Interyarn brifging. . . . 117
6.10 Initiation ERR normalized by RoM for interyarn and intrayarn hybrids. . . . 118
6.11 Steady-state ERR normalized by RoM for interlayer hybrids. . . . 118
6.12 Typical interyarn and intrayarn QI UNT stress-strain curves. . . . 119
6.13 Baseline, interyarn, and intrayarn hybrid onset of damage and strength. . . . 120
6.14 In-situ monitoring of free-edge delamination in an intrayarn $^{20}C1^{75}$ specimen. . . . 120
6.15 Baseline, interyarn, and intrayarn hybrid QI onset of damage and strength box plots as a function of ply-block FAW. . . . 121
6.16 Strength normalized by RoM for interyarn and intrayarn hybrids. . . . 121
6.17 Baseline, interyarn and intrayarn hybrid strain as a function of ply-block FAW. . . . 122
6.18 Baseline and interlayer hybrid strain boxplots as a function of ply-block FAW. . . . 122
6.19 Baseline and interlayer hybrid ERR boxplots as a function of ply-block FAW. . . . 123
6.20 Typical QI oht load-displacement curves. . . . 124
6.21 Baseline and interlayer hybrid OHT far-field strength and notch sensitivity as a function of ply-block FAW. . . . 124
6.22 Post-mortem failure of intrayarn OHT specimens. . . . 124
6.23 CT-scan of OHT samples after loading to 95 % of the OHT strength. . . . 125
6.24 Interyarn and intrayarn hybrids Ashby plot. . . . 126

7.1 Post-mortem observation of CT fracture surfaces. . . . 128
7.2 Typical post-mortem pull-out profile. . . . 129
7.3 Post-mortem observation of CT fracture surfaces. . . . 130
7.4 ull-out length distribution forCT fracture surfaces. . . . 131
7.5 Fiber pull-out distribution. . . . 132
7.6 Maximal pull-out length as a function of ply-block FAW for interlayer hybrids. . . . 133
7.7 Mean pull-out length and width as a function of ply-block FAW for interlayer hybrids. . . . 134
7.8 Maximal pull-out length as a function of low strain volume fraction for interlayer hybrids. . . . 134
7.9 Count of pull-out bundles as a function of ply-block FAW for interlayer hybrids. . . . 135

7.10 Post-mortem observation of $^{33}C2^{45}$ CT fracture surface. . . . 135
7.11 Correlation between maximal pull-out length and shear-lag model predictions. . . . 136
7.12 ERR as a function of maximal pull-out length for baselines and interlayer hybrids. . . . 137
7.13 ERR as a function of maximal pull-out length for specimens reported in the literature. . . . 137
7.14 Modeled failure steps. . . . 138
7.15 Schematic representation of the considered macroscopic cohesive law. . . . 138
7.16 Schematic representation of the considered RVE. . . . 141
7.17 Abaqus FEM illustrations. . . . 141
7.18 Total frictional and debonding energy for a pull-out bundle as a function of its length. . . . 143
7.19 Total frictional and debonding energy as a function of model parameters. . . . 143
7.20 Debonding energy saturation. . . . 144
7.21 Frictional and debonding energy as a function of COD. . . . 145
7.22 Frictional energy parameters identification. . . . 146
7.23 Illustration of a damage law for $^{20}L2S^{30}_{120}$. . . . 147
7.24 Model optimization loop. . . . 147
7.25 CT experimental and numerical load-displacement curves for $^{0}B4^{0}_{180}$ interlayer hybrid specimens. 148
7.26 Correlation between experimental and simulation contribution of debonding and friction to the translaminar toughness. . . . 149
7.27 Comparison of bundle distribution with corresponding predicted energy contributions. . . . 149
7.28 SEM fracture surface observations. . . . 151
7.29 SEM fracture surface detailed observations. . . . 152
7.30 SEM observations of toughening particle clusters. . . . 153
7.31 Comparison of NTPT epoxy system performances. . . . 153
7.32 SRCT of a 34-700 $60\,g \cdot m^{-2}$ FAW specimen showing a pull-out bundle. . . . 155
7.33 Minimum intensity projection for the SRCT of a 34-700 $60\,g \cdot m^{-2}$ FAW specimen showing a pull-out bundle. . . . 156
7.34 Bundle parametrization. . . . 157

8.1 Interyarn and intrayarn hybrids Ashby plot . . . 161

List of Tables

2.1 Overview of the tow-spreading technologies. 11
2.2 Partial summary of the thin-ply effects reported in the literature. 16

3.1 Laminate stress for each damage mode. 33
3.2 Commercial carbon fibers properties. 34
3.3 Parameters used for the HR40-34-700 failure map. 35
3.4 Failure map constitutive equations 38
3.5 Residual stress predictions for $^{33}\mathrm{L3A}_{120}^{60}$ layup. 43
3.6 Residual stress predictions for $^{33}\mathrm{L4S}_{120}^{60}$ layup. 44

5.1 Elastic constants for hybrids CT specimen laminates. 78
5.2 Interlayer hybrids CT specimens properties. 80
5.3 Interlayer hybrid ERR results. 85

6.1 Elastic constants for interyarn and intrayarn hybrids CT specimen laminates. 110
6.2 Interyarn and intrayarn hybrids CT specimens properties. 113
6.3 Interyarn and intrayarn hybrid ERR results. 117

7.1 Pull-out length analysis results. 133
7.2 Pull-out lengths and translaminar toughness reported in the literature for CP laminates. 136
7.3 Homogenized engineering constants for a 34-700-HR40 interlayer hybrid UD laminate. 140
7.4 Cohesive and frictional properties. 142
7.5 Identified analytical parameters. 145

List of acronyms

4ENF Four-point End-Notched Flexion

AE Accoustic Emission
ATL Automated Tape Laying

CAI Compression After Impact
CC Compliance Calibration
CFRP Carbon Fiber Reinforced Polymers
CLT Classical Laminate Theory
COD Crack Opening Displacement
CP Cross-Ply
CT Compact Tension
CT-scan Computed Tomography scan

DENT Double Edge Notched Tensile
DIC Digital Image Correlation

ERR Energy Release Rate

FAW Fiber Areal Weight
FEM Finite Element Model
FPZ Fracture Process Zone
FRP Fiber Reinforced Polymers

LCM Liquid Composite Molding
LEFM Linear Elastic Fracture Mechanics
LVDT Linear Variable Differential Transformer

MCC Modified Compliance Calibration

NTPT North thin Ply Technology

OCT Over-height Compact Tension
OHC Open Hole Compressive
OHT Open-Hole Tensile
OoA Out of Autoclave

QI Quasi-Isotropic

RoM Rule-of-Mixtures
RTM Resin Transfer Molding
RVE Representative Volume Element

SEM Scanning Electron Microscope
SRCT Synchrotron Radiation Computed Tomography

UD unidirectional
UNT Un-Notched Tensile

List of symbols

a The crack length
a_0 The initial crack length
α The low-to-high strain modulus ratio, $\alpha = E_L/E_H$

b The sample thickness
β The low-to-high strain thickness ratio, $\beta = t_L/t_H$

D The damage parameter of a traction-separation law
δ The Crack Opening Displacement (COD)
Δ_{AB} The J-integral path offset AB
Δ_{BC} The J-integral path offset BC
Δ_{CD} The J-integral path offset CD
Δa The crack increment

E_l The laminate longitudinal tensile modulus
E_L The low-strain laminate longitudinal tensile modulus
E_f The fiber longitudinal tensile modulus
E_H The high-strain laminate longitudinal tensile modulus
E_h The hybrid laminate longitudinal tensile modulus
ε_H The high-strain laminate longitudinal ultimate tensile strain
ε_l The laminate longitudinal ultimate tensile strain
ε_L The low-strain laminate longitudinal ultimate tensile strain

γ The low-strain relative fiber volume fraction, $\gamma = \frac{t_L}{t_L+t_H}$
G_{Ic} The mode I linear critical Energy Release Rate (ERR)

J The J-integral
J_H The high-strain material ERR
$J_{Ic,i}$ The mode I critical ERR at initiation
$J_{Ic,ss}$ The mode I critical ERR at propagation
J_L The low-strain material ERR

K_t The stress concentrator factor caused by fragmentation

l_c The critical length in a shear-lag model

λ The pull-out length
l_{FPZ} The fracture process zone length

m The Weibull modulus

σ_0 The Weibull scale parameter
σ_{del} The delamination stress
σ_f The fiber longitudinal tensile strength
σ_{LF} The low-strain fragmentation stress
σ_{HF} The high-strain failure stress
σ_H The high-strain laminate longitudinal tensile strength
σ_h The hybrid laminate longitudinal tensile strength
$\acute{\sigma}_L$ The low-strain laminate longitudinal tensile strength distribution mean
σ_l The laminate longitudinal tensile strength
σ_L The low-strain laminate longitudinal tensile strength
σ^Y The laminate onset of damage (yield) stress
σ_h^Y The hybrid laminate onset of damage (yield) stress

t_L The low-strain ply thickness
τ_{max} The frictional shear stress maximum
τ_y The shear strength

V The specimen volume
V_f The fiber volume fraction

Chapter 1

Introduction

1.1 Context and motivation

Passenger and freight transport is one of the most energy-intensive sectors of the post-industrial economies. For instance, in the European Union (excluding the United Kingdom), domestic transport accounts for roughly 30% of the energy consumption, totaling $12.1e^3$ PJ in 2019, according to the European Statistical Office (see Figure 1.1). To put this figure in perspective, it amounts to approximately 14 times the energy liberated by the 1883 eruption of Krakatoa[1], an explosion so powerful that the resulting pressure wave was recorded several times by barographs around the world and up to 121 hours after the eruption [2, 3]. Or, at a time when space travel is attracting much interest again, it represents enough energy to deliver the Space Shuttle to low Earth orbit around one million times[2].

From a greenhouse gas emission perspective, it represented 835 $MtCO_2eq$, i.e., almost 1.9 tCO_2eq per capita[3]. This amount is above the global per capita yearly limit of 1.7 tCO_2eq proposed in a 2015 report published by the Swiss Federal Office for the Environment [6], which has been calculated not to exceed 2 °C of global warming by 2100 (and which is even lower when considering anterior greenhouse emissions of European countries, for instance, 0.6 tCO_2eq per capita and year in Switzerland). Finally, the economic impact of this energy consumption is not negligible either, as it equates to the combustion of at least 2.15 billion barrels of Brent. Its value is roughly US$ 2.2 billion in 2022[4]. To conclude, the impact of transportation on European energy consumption is significant, and both sustainability and costs are fundamental incentives for its reduction.

Transport vehicles mainly use energy to overcome motion resistance. For instance, power is required for a vehicle to accelerate and acquire momentum or to overcome gravity and elevate itself. Most of these resistive mechanisms, with the notable exception of drag, are directly or indirectly proportional to vehicle mass [10]. Consequently, reducing vehicle mass is considered one of the most effective ways

[1] Estimated as 840 PJ [1].

[2] Assuming 1.16 TJ per launch as calculated in [4] and based on values from the third Space Shuttle mission of 1982.

[3] In 2019, the European population was 446.56 million people[5].

[4] Assuming a Brent density of 835 $kg \cdot m^{-3}$, a crude oil energy density of 41.868 $MJ \cdot kg^{-1}$ and an average price of $105 per barrel of Brent over Jan-Sep 2022[7].

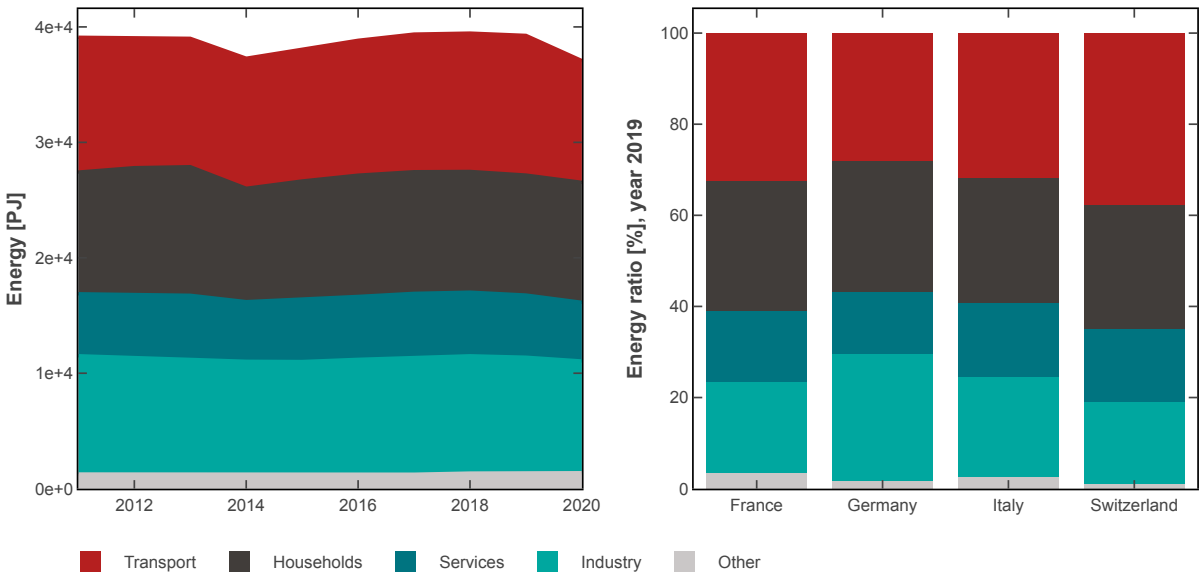

Figure 1.1: Final energy (covers all energies supplied to consumers) consumption in Europe per sector. Data aggregated from [8, 9].

to increase energy efficiency. In a 2009 study, Tolouei and Titheridge [11] reported that a 100 kg increase in the mass of automatic diesel cars on the British market at that time typically increased urban and extra-urban fuel consumption by 4.8% and 6.2%, respectively. In 2020, Weiss et al. [12] noted that each 100 kg saved on electric car mass may reduce energy consumption by approximately 0.4 to 1.3 $\mathrm{kW \cdot h \cdot 100\,km^{-1}}$. In a 2017 technical report from the Zurich University of Applied Sciences, R. Steinegger [13] estimated from empirical data that a 100 kg increase in mass of planes increases fuel consumption by $\mathrm{20\,kg \cdot 1000\,km^{-1}}$, to which is added a marginal fuel burn rate of 0.02 to $\mathrm{0.03\,kg \cdot 1000\,km^{-1}}$ for every added kg. However, these individual outcomes are intended as illustrative examples as varying results were reported over the years, depending on the assumptions or methodologies used. Moreover, lower energy consumption during the vehicle's functional operation does not guarantee a lower energy footprint over the whole life cycle of the vehicle. Nevertheless, it is estimated that about 85% of the total life-cycle energy consumption occurs in the use phase [14] and several publications, including harmonized reviews, reported that over an entire life-cycle, using lightweight components may achieve significant energy savings [15–18].

Structural mass saving is also essential to ensure the functional properties of high-performance vehicles such as spacecraft. For instance, the Tsiolkovsky rocket equation shows that a vehicle launcher mass is limited as the ratio between the propellant mass and the dry launcher mass increases exponentially with the energy required to reach a given destination. Furthermore, with the currently available chemical propulsion technology, about 90% of a launch vehicle mass is propellant [19]. Optimizing aerospace structural parts has, consequently, a significant effect on the allowable payload. Aerospace is, therefore, one of the leading industries in developing high-performance materials such as fiber-reinforced polymers, which constitute up to 80% of modern launch vehicles [14].

Indeed, structural mass saving may be achieved through two complementary approaches: optimizing the part geometry, for instance, by topology optimization, or using a material with an increased desired property-to-mass ratio. As such, composites, especially Carbon Fiber Reinforced Polymers (CFRP), have been extensively used in the aerospace industry since the mid-twentieth century, including commercial aviation, for their high specific strength (see Figure 1.2a), high specific stiffness, and good environmental resistance [20–22]. For instance, the specific strength of a Ti-6Al-4V alpha-beta titanium alloy is around $200\,\mathrm{kN \cdot m \cdot kg^{-1}}$[23], depending on the heat treatment. In contrast, a standard thick-ply quasi-isotropic laminate of T800 carbon fibers reaches approximately $350\,\mathrm{kN \cdot m \cdot kg^{-1}}$[24]. These figures represent a theoretical mass reduction of 43% and explain why CFRP use in aerospace is likely to increase in the future, as shown by the ongoing development of PHOEBUS, a carbon composite upper-stage demonstrator for Ariane 6 [25] or the growing need for lenticular deployable composites [26, 27].

Composite materials also represent a valuable asset to achieve a sustainable transition in the automotive industry [28], with a theoretical mass saving of 50% to 60% when replacing conventional stamped steel [29]. However, further manufacturing developments are ongoing to achieve automotive production costs and cycle times standards [30, 31]. Moreover, a positive environmental impact of CFRP parts is not granted in automotive applications [18]. Indeed, automotive vehicles are not as energy-intensive as aircraft. Thus, the energy savings obtained in the use phase thanks to mass optimization are lower and may not compensate for the extra energy required to produce carbon fibers and laminates [29], especially when efficient recyclability solutions are lacking, although significant progress has been made to address this issue over the recent years, see for instance [32–35]).

Among CFRP, thin-ply composites have been thoroughly studied over the past decade and shown to exhibit superior mechanical properties [24, 38, 42–45]. For instance, a thin-ply T800 quasi-isotropic laminate fails in tension at a strain as close as 95% of the fiber ultimate strain, whereas a thick-ply equivalent fails in the range of 41 to 66 % [24, 38]. Moreover, using thin-ply composites leads to a specific strength around $630\,\mathrm{kN \cdot m \cdot kg^{-1}}$ and a theoretical mass reduction of 68% compared to Ti-6Al-4V. As such, thin-ply composites have been a key material for developing innovative vehicle concepts such as the Solar Impulse plane or the Swiss Solar Boat, depicted in Figure 1.3. Similarly, the Aurora concept study reported that using thin-ply in space launchers would lead to mass savings of approximately 20% compared to regular CFRP [46]. These outstanding properties are explained by the in-situ effect [47, 48], which delays or even suppresses micro-cracking, transverse cracking, and delamination in thin-ply laminates. Nevertheless, these mechanisms are dissipative and are required for the initiation of secondary damage, such as crack splitting. Consequently, thin-ply composites exhibit a translaminar toughness even lower than regular CFRP. As a result, thin-plies are not tolerant to stress intensity concentrators, and prone to quasi-brittle failure [38, 39, 49–51]. This lack of translaminar toughness reduces the advantages or even prevent the use of thin-ply composites in a damage tolerant design approach, and this restricts a wider use of thin-ply composites.

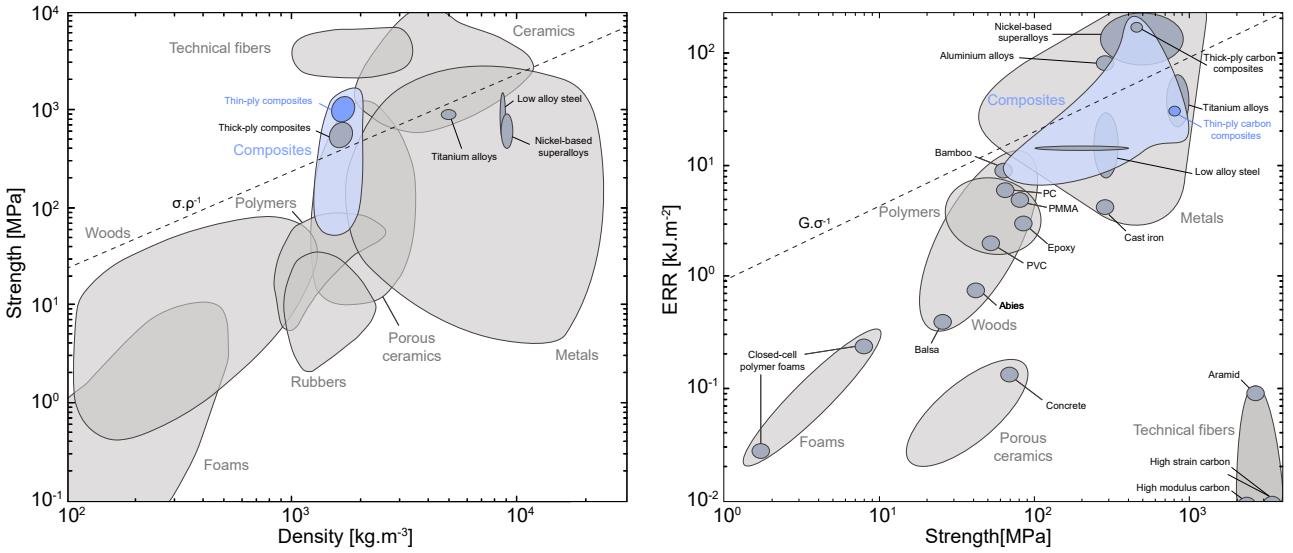

(a) **(b)**

Figure 1.2: Ashby charts for different type of materials, including carbon-epoxy thin-ply and thick-ply composites: (a) strength versus density and (b) toughness (mode I translaminar toughness for composites) versus strength. Adapted from [36] and [37], see these articles for the data sources. Additional data sources: thin-ply and thick-ply in [24, 38, 39], flax-epoxy composites in [40, 41].

Figure 1.3: The Dahu foiling over lake Geneva in 2022, picture by Swiss Solar Boat.

Consequently, significant efforts have been made to restore crack-shielding mechanisms or pseudo-ductility in thin-ply laminates by engineering hierarchical microstructures, often following bio-inspired approaches [52–57]. Among these solutions, carbon-carbon hybridization is seen as a promising technique[52] to increase damage tolerance in high-performance thin-ply composites with a minimal modification of the existing industrial processes, and without introducing detrimental defects in the laminate.

1.2 Objectives

As highlighted in Figure 1.4, this study takes place within a broader framework, HyFiSyn, funded by the European Union's Horizon 2020 research and innovation program under the Marie Sklodowska-Curie grant agreement No 765881. The HyFiSyn framework aims to address challenges faced by composites through fiber-hybridization. More specifically, it proposes to improve (i) the toughness of composites, (ii) their cost competitiveness, (iii) their recyclability, and (iv) their functionality. Overall, the HyfiSyn framework seeks to understand the synergistic microstructural effects obtained by fiber hybridization in composite laminates and assess their impact on macroscale properties. Achieving these objectives through simulation and experimental validation brings state-of-the-art composites to industrial applications.

Based on these requirements, the present research work focuses on (i) designing tough and high-performance thin-ply fiber-hybrid composites, (ii) establishing a methodology to assess the properties of these materials and especially their translaminar toughness, (iii) providing an understanding of the failure mechanisms in relation to the fiber-hybrid microstructure, and (iv) documenting guidelines to reach a trade-off between these materials' toughness and tensile properties.

Given the above objectives, the main research questions are therefore defined as follows:

- How does fiber hybridization affect the translaminar fracture toughness of and the ERR of thin-ply composites?
- Which methodology can be applied to reliably measure translaminar toughness of Cross-Ply (CP) fiber-hybrid composites?
- Which phenomenological mechanisms explain the fiber hybridization effect on the translaminar toughness and how to model them?
- How much are the tensile properties of Quasi-Isotropic (QI) thin-ply composites affected by fiber hybridization?
- What is the trade-off between toughness and tensile properties, and what are the prospective solutions to improve it?

These questions are answered through these research activities:

1. Extend the thin-ply design space by investigating different carbon-carbon hybridization in terms of material and fiber dispersion. In addition, industrial viability must be considered, especially regarding fiber choice and processability.
2. Assess the mode I translaminar toughness of these hybrids, implementing and validating a J-integral data reduction method.

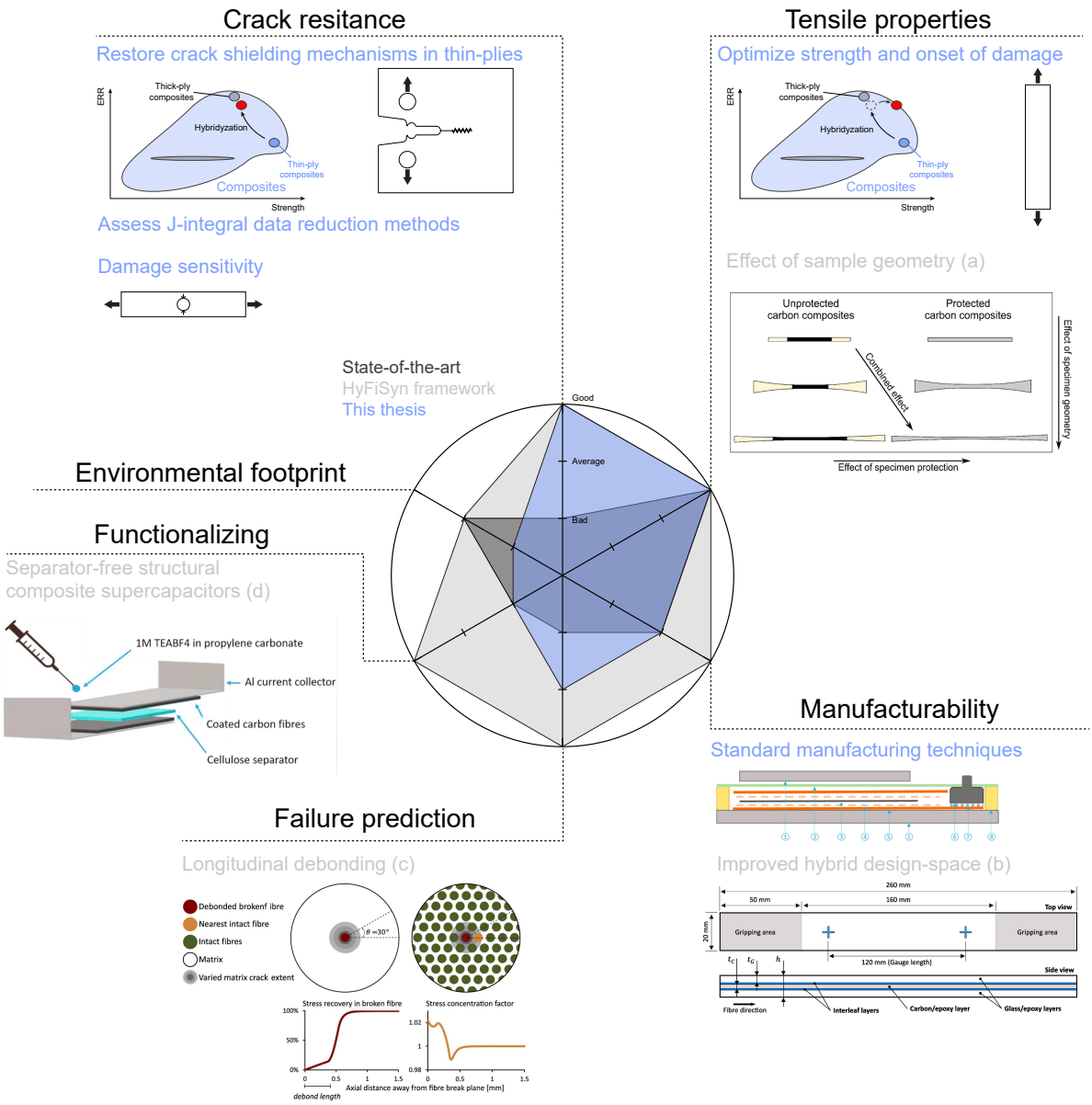

Figure 1.4: Graphical abstract illustrating the scope of this thesis and how it fits the HyFiSyn framework. Published results: a [58], b [59], c [60], d [61].

3. Perform a load-bearing characterization of these hybrids through Un-Notched Tensile (UNT) tests and Open-Hole Tensile (OHT) tests.

4. Carry out mechanistic investigations to identify the toughening mechanisms at play in carbon-carbon hybrids based on an assessment of fiber pull-out and in-situ synchrotron experiments.

1.3 Structure and approach

Following this introduction, chapter 2 provides a comprehensive literature review clarifying the thin-ply technology, its advantages but also its current limitations. The concepts behind fiber-hybridization

are also introduced, explaining how it can address the toughness issue of thin-ply laminates. Finally, it reviews the fundamental concepts of fracture mechanics and discusses the state-of-the-art methodologies for the translaminar toughness characterization of composites.

The detailed manufacturing and experimental testing methods are then presented in chapter 3, together with the methodology to select the materials used in this work.
A large part of this work is dedicated to developing and validating a novel J-integral implementation to derive the experimental mode I translaminar toughness from experimental displacement fields of Compact Tension (CT) specimens measured by Digital Image Correlation (DIC), which is exposed in chapter 4. In particular, three different formulations are benchmarked over both synthetic data, obtained from a Finite Element Model (FEM), and experimental data. Finally, the resulting implementation is proposed as a Python package.

Then, chapter 5 is dedicated to characterizing the mode I translaminar toughness and tensile properties of interlayer hybrids, which are discussed with respect to the ply-thickness effect and the observed failure modes. Finally, the system potential for pseudo-ductility is discussed based on the experimental results.

The following chapter 6 follows the same approach but is applied to innovative hybrid microstructures, namely interyarn and intrayarn hybrids.

The experimental findings are then discussed with respect to phenomenological observation, especially the pull-out length and formation, in chapter 7. Moreover, a multi-scale FEM is proposed to account for the translaminar toughness based on the pull-out length distribution.

Finally, the chapter 8 summarizes the findings and exposes future perspectives.

Chapter 2

State of the art

2.1 Composites: general considerations

A composite material typically contains two or more constituents sufficiently well distributed to form a continuous medium whose properties can be homogenized at the appropriate scale [62]. Following this definition, composite refers to a wide range of materials from concrete to filled polymers[1]. This thesis focuses on a sub-category of filled polymers, Fiber Reinforced Polymers (FRP), which contain technical fibers, such as carbon fibers, or natural fibers, such as hemp [64], embedded in a polymer matrix, such as epoxy [22]. The fibers are generally long enough to be considered continuous.

FRPs' mechanical performances are related not only to the individual fiber and matrix properties but also to the interaction between these two constituents at the microstructural scale. Microstructural features include properties such as fiber volume fraction, packing, or voids distribution, which generally depend on the manufacturing process [65]. A broad range of FRP manufacturing technologies are available, including but not limited to, Resin Transfer Molding (RTM) [66], stamping of composite sheets [67] or massive parts [68, 69], infusion [70], Liquid Composite Molding (LCM) [71], or autoclave and Out of Autoclave (OoA) [72] prepreg processing.

Among them, autoclave processing, depicted in Figure 2.1, is considered the state-of-the-art method to produce high-performance composite parts [73]. On the one hand, typical autoclave processing uses woven fabrics or unidirectional (UD) plies of fibers impregnated with a catalyzed but uncured thermoset resin (prepregs). The prepreg production and layup are highly suitable for automation [74], which provides accuracy, uniformity, and consistency to the resulting microstructure in terms of fiber arrangement or resin content. On the other hand, the heat and pressure applied in autoclave curing promote voids dissolution or migration [65, 73, 75]. As a result, autoclaved parts typically exhibit high volume fraction, low void contents, improved mechanical properties, and better reproducibility compared to parts obtained by other means.

[1] Or even chocolate with nut inclusions [63].

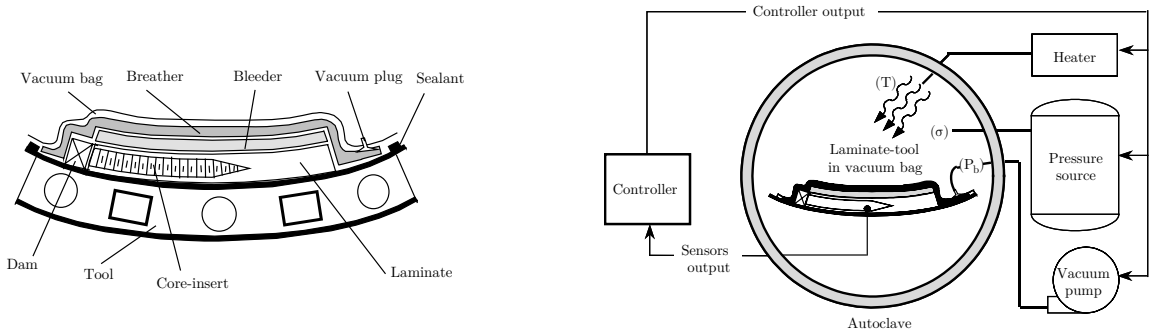

Figure 2.1: Typical autoclave processing system, reproduced with permission from [73].

2.2 Thin-ply composites

2.2.1 Thin-ply development and manufacturing

In the 1980s, Bailey et al. [76], and Crossman and Wang [77], were among the first researchers to report a positive ply-thickness effect on transverse cracking and delamination in both CP and QI laminates. Two decades later, Sihn et al. [42] proposed a comprehensive experimental study where improved mechanical properties were reported for thin-ply (40 µm) compared to thick-ply (200 µm) composites. Since then, thin-ply composites have continued to attract growing interest, as evidenced by two extensive reviews published independently in 2020 by Arteiro et al. [44] and Galos [45][2].

The nomenclature "thin-ply" refers to laminates whose ply thickness has been reduced below a limit usually set between 100 µm and 150 µm [45, 78]. These high-performance laminates are typically obtained by curing thin-ply prepregs, usually in an autoclave, although thermoplastic thin-plies have also been proposed [79–83]. Depending on the tape resin content, the thin-to-thick limit corresponds approximately to a Fiber Areal Weight (FAW) ranging from $100\,\mathrm{g}\cdot\mathrm{m}^{-2}$ to $150\,\mathrm{g}\cdot\mathrm{m}^{-2}$. Commercial thin-ply prepregs are available with FAW down to $15\,\mathrm{g}\cdot\mathrm{m}^{-2}$ [84].

Several composites manufacturers have developed thin-ply technologies, namely, North thin Ply Technology (NTPT) UD (Thin Ply Prepregs, Switzerland), Oxeon (TeXtreme, Sweden), Chomarat (C-ply, France), Hexcel (PrimeTex, United States), Sakai Ovex (Japan), Mitsuya (Japan) and Mitsubishi Rayon (Japan), TPCM (Germany), or SK Chemicals (South-Korea), among others. Overall, a typical thin-ply manufacturing line comprises a tow-spreading unit, a weaving unit (optional), and an impregnation unit. However, spreading units were often developed under trade secrets, and few publications are available about the state-of-the-art tow-spreading processes. Irfan et al. [85] reviewed the patent literature. They identified mechanical, electrostatic, pneumatic-vacuum, and vibration-acoustic tow-spreading technologies, which can be distinguished in passive and active methods [86]. As reported in Table 2.1, the former take advantage of tension and movement to spread the fibers passively over teeth, grooves, or special surface morphologies. The latter achieves tow-spreading by acting directly on the fibers through airflow, ultrasonic waves, or mechanical vibrations. NTPT produced the thin-ply

[2]The reader is referred to these high-quality publications for a further review of thin-ply composites.

prepregs used in this thesis.

Technology	Method	Description	Patents	References
Mechanical	Passive	Fibers are typically spread over 3 to 5 spreading bars or any other apparatus favoring spreading, heated up to 150 °C and a pre-tension is applied up to 20 N. Limited spreading capability and tend to damage the fibers.	[87–95]	[79, 85, 96]
Pneumatic-vacuum	Active	An airflow is used to separate and spread the tows. Increased spreading capability, but performances depend on fiber sizing. Fibers are less likely to be damaged [42].	[97–101]	[42, 80, 102–105]
Electrostatic	Active	Fibers are electrostatically charged to achieve spreading.	[106–108]	
Vibrations and acoustic	Hybrid	Similar to the mechanical methods with the addition of acoustic or mechanical vibrations improve the spreading.	[109, 110]	

Table 2.1: Overview of the tow-spreading technologies, adapted from [85, 86, 111]. The patent list is restricted to the last 30 years.

2.2.2 Benefits and drawbacks of thin-ply laminates

The most evident benefits of thin-ply composites are improved microstructural quality and enlarged design space. Due to tow-spreading, the fiber packing in thin-ply laminates is usually more homogeneous than in conventional (thick) composites, as highlighted by the Scanning Electron Microscope (SEM) observation reported in Figure 2.2a. As a result, the fiber tortuosity decreases, the fibers are better aligned, and the local V_f increases, as documented by Amacher et al. [38]. Moreover, analyzing the microstructure of in-house produced thin-plies, Wu et al. [105] found that the proportion of large resin-rich area was more substantial in thick-ply laminate, even though the V_f was 54 % in thick plies and only 45 % in thin plies. This improved microstructure brings stability to the laminate, which is especially noticeable in UD compression, where thin-ply laminates are less prone to fiber kinking and instabilities than thick-ply laminates [38]. As shown in Figure 2.2b, the microstructure is also significantly improved in thin-ply woven laminates, which exhibit a much more favorable crimp angle, much smaller resin-rich areas, and no noticeable voids compared to a conventional woven composite. Furthermore, tow-spreading brings more design freedom to the composite industry. Indeed, working with smaller FAW allows for further stacking sequence optimization and is particularly useful for non-critical monolithic and sandwich structures. For instance, these structures are often oversized in the aerospace industry when using conventional plies [46], due to guidelines specifying a minimal number of plies in the different loading directions [113]. Moreover, for a given target FAW, prepreg tapes

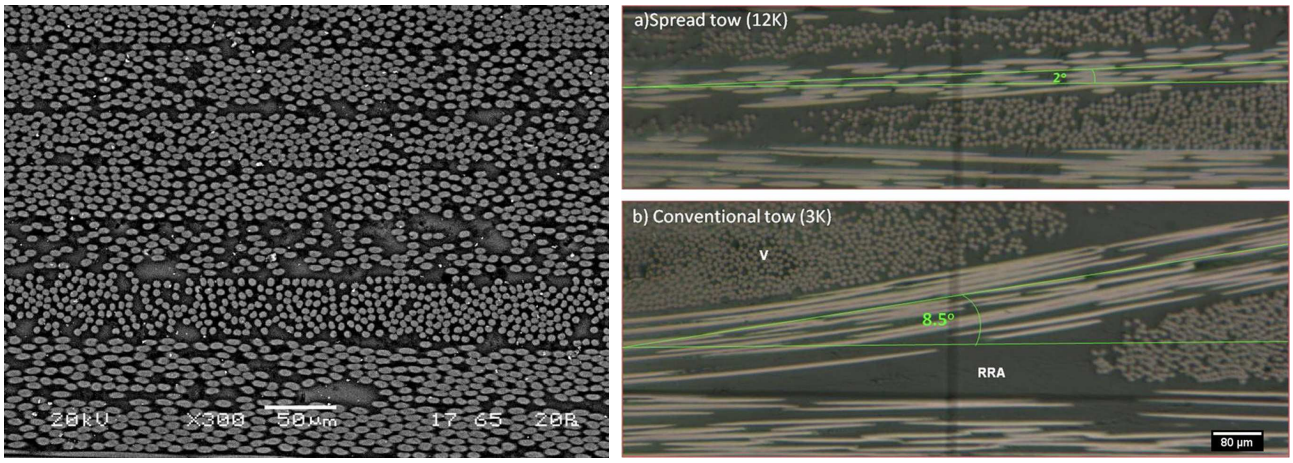

(a) **(b)**

Figure 2.2: (a) SEM image of a multidirectional thin-ply laminate (reproduced with permission from [112]), and (b) comparison of micrographs of a thin-ply woven laminate and a conventional woven laminate comparing the crimp angle, voids content (V) and resin rich area (RRA) (reproduced with permission from [80]).

can be produced from wider and cheaper tows using tow-spreading, allowing for cost optimizations compared to using low Tex tows. Finally, at constant laminate thickness, the use of thin-plies allows for a more progressive angle mismatch which reduces damage at the interface, improving impact resistance (Bouligand structures) [55, 114] and more generally providing at the same time a higher onset of damage and a more progressive failure [115–117].

Besides these geometrical improvements, outstanding mechanical properties of composites made from thin-ply UD prepregs have been reported throughout the literature. In particular, composites frequently used in real-life applications such as QI laminates benefit significantly from the ply-thickness effect, as documented independently by several researchers [24, 38, 42, 43, 118–123] and summarized in Table 2.2. Overall, thin-ply laminates exhibit a positive effect on UNT strength, UNT onset of damage stress, fatigue, Open Hole Compressive (OHC) strength, and Compression After Impact (CAI) strength. Both the material system and the thin-to-thick thickness contrast govern the extent to which the properties increase. Some authors reported substantial gains, as Amacher et al. [38], with +42 % UNT strength and +231 % UNT onset of damage stress when going from a thick-ply ($300\,\mathrm{g}\cdot\mathrm{m}^{-2}$) made of high modulus M40JB fibers and NTPT TP80EP epoxy to a thin-ply ($30\,\mathrm{g}\cdot\mathrm{m}^{-2}$) (see Figure 2.3).

In their study, Cugnoni et al. [24] highlight the remarkable failure strength of thin-ply QI laminates. Given a matrix that is ductile and tough enough (above 2 % ultimate strain), the strength approaches or corresponds to the theoretical value calculated by laminate theory, based on the fiber ultimate strain, as defined in the supplier certificates, although these values should be considered with care as they are usually obtained with the impregnated fiber bundle test [124] and do not consider size effects [125, 126]. Furthermore, the fiber strength σ_f is probabilistic and, for instance, values ranging from approximately 2 to 6.5 GPa have been reported for 34-700 carbon fibers using single fiber testing [127],

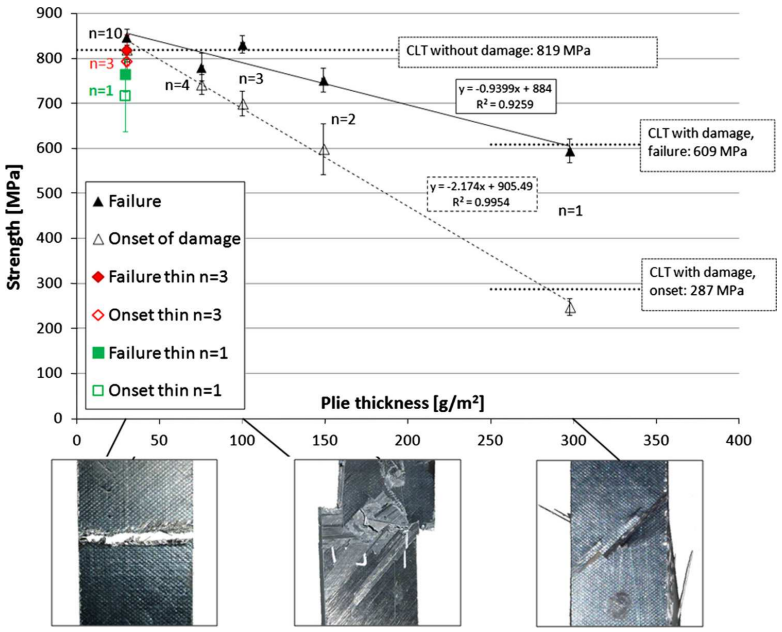

Figure 2.3: Onset of damage and ultimate strength in UNT and QI specimens as a function of ply thickness. Reproduced with permission from [38].

while the datasheet indicates a value of 4.8 GPa. In any case, this result indicates that the laminate failure is dominated by fiber breakage and not by transverse cracking nor edge delamination, as usually observed in conventional laminates [119]. Thus, thin-plies, unlike thick-plies, take advantage of more, if not all, of the fiber strength potential.

As reported in Table 2.2, there is a slight decrease in UNT strength between UD thick-ply laminates and UD thin-ply laminates, although the difference is within the reported standard deviation. The apparent decrease was attributed to fibers broken by the tow-spreading process at the ply interface, according to in-situ X-Ray computed tomography observations by Mesquita et al. [128]. Nevertheless, the absence of significant difference demonstrates that the observed ply-thickness effect is not a material property due to the improved microstructure quality but rather an in-situ effect. Indeed, in a laminate, the adjacent plies exert a constraining effect on the embedded ply. In thin-plies, this constraint reduces the available elastic energy to a point where transverse cracks are delayed or even suppressed [47, 48, 122, 129–134]. This in-situ effect, highlighted in Figure 2.4a, was conceptualized as an analytical model by Camanho et al. [47].

Based on early works from Dvorak and Laws [136], Camanho et al. [47] derived a Linear Elastic Fracture Mechanics (LEFM) scaling law in $1/\sqrt{t}$ for the in-situ transverse tensile strength as a function of the ply thickness t. As the transverse crack formation drives the CP and QI laminate failure, it is expected that the laminate strength should follow approximately a $1/\sqrt{t}$ relation. However, this is not always the case. For instance, Figure 2.3 shows that the M40JB-TP80ep system does not follow a $1/\sqrt{t}$ trend. To reach this conclusion, Amacher et al. [38] monitored the onset of damage by Accoustic Emission (AE). They found that the onset of damage and ultimate strength increase linearly with the

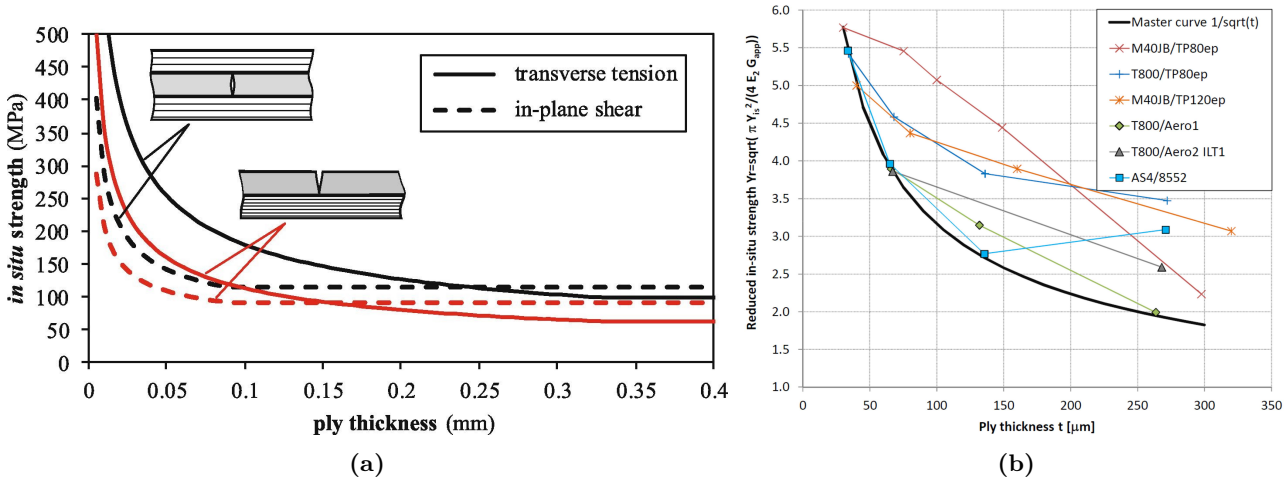

Figure 2.4: (a) Transverse tensile and in-plane shear strengths of an embedded inner or outer ply as a function of ply thickness illustrating the in-situ effect proposed by Camanho et al. [47]. Reproduced with permission from [44]; (b) In-situ transverse strength normalized by the apparent ply toughness. Reproduced from [135].

ply thickness decrease.

As shown in Figure 2.5b, Kohler et al. [48] subsequently reported a good correlation between the free-edge crack nucleation and the in-situ scaling law proposed by [47] in M40JB-TP80ep samples. However, they also demonstrated that these free-edge damage events are only precursors that do not extend far into the laminate and thus are not representative of bulk material damage (see Figure 2.5a). Thus, free-edge cracking and bulk transverse cracking are two different mechanisms. The latter is induced by the former at a stress well correlated with the onset of damage identified by AE. The observed discrepancy with the LEFM-based in-situ model was attributed to a decrease in apparent transverse toughness for the thinnest plies. Indeed, thin-plies may reach such thinness that, when embedded in a laminate, the COD is too small to develop a complete Fracture Process Zone (FPZ), especially when the matrix is toughened. Following the works of Saito et al. [137] and [138], Kohler et al. [48] identified a ply-thickness dependence of the transverse cracking ERR and proposed a numerical framework to capture it. Simultaneously, Catalanotti [132] formulated an extended version of the analytical in-situ effect to include this dependence. Therefore, the ply-thickness effect should be seen as a dual one. On the one hand, it increases the transverse strength of embedded plies. On the other hand, it decreases the transverse ply fracture toughness. This duality explains that not all systems follow a $1/\sqrt{t}$ relation as outlined in Figure 2.4b.

All in all, the ply-thickness effect drives the failure mechanisms in laminates [123, 135]. In thick-plies, approximately above $150\,\mathrm{g}\cdot\mathrm{m}^{-2}$, free-edge damage and transverse cracking induce severe delamination (see Figure 2.5a), which is the preponderant failure mechanism. In intermediate plies, from about $150\,\mathrm{g}\cdot\mathrm{m}^{-2}$ to $100\,\mathrm{g}\cdot\mathrm{m}^{-2}$, free-edge induced delamination is not present, while transverse cracking-induced delamination is delayed and scaled down. Finally, in thin-plies below $100\,\mathrm{g}\cdot\mathrm{m}^{-2}$, minor or no transverse cracking and delamination are observed before the sample failure.

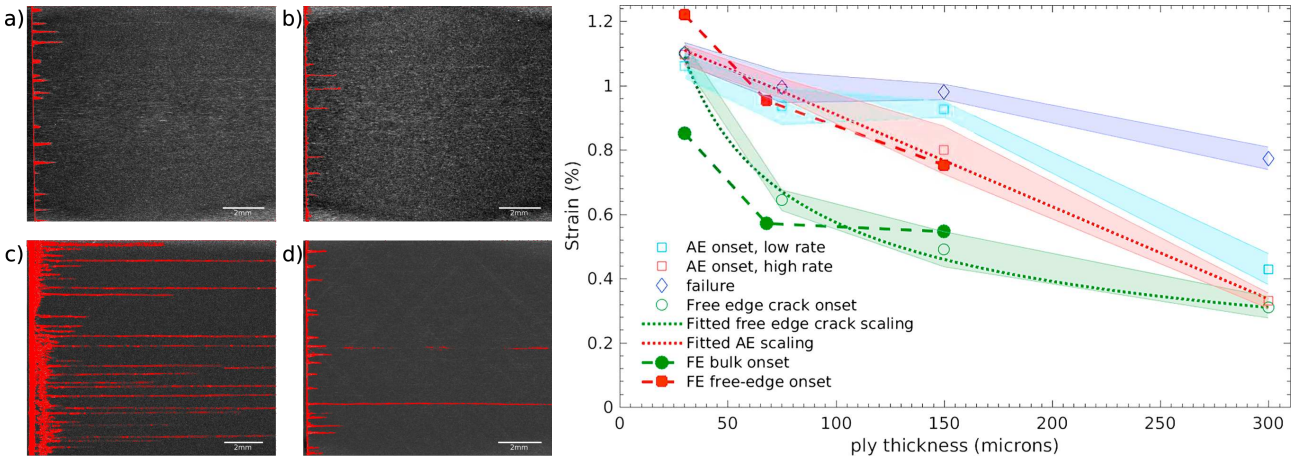

(a) **(b)**

Figure 2.5: (a) X-ray tomography of typical 90° plies of M40JB-TP80ep samples of: a) t=150 µm tested at 500 MPa, b) t=100 µm tested at 650 MPa, c) t=150 µm tested at 700 MPa, d) t=100 µm tested at 700 MPa. Reproduced from [135]; (b) Macro-scale results, showing the good agreement of the free edge cracks to a 1/ t scaling, whereas the onset of damage defined by an acoustic emission threshold is in better agreement with a linear scaling, and lightly loading-rate dependent. The corresponding numerical results are shown in dashed line, showing good agreement with experimental results. Reproduced with permission from [48].

This change in failure sequence fundamentally explains why thin-ply composites exhibit outstanding load-bearing properties. It also clarifies why thin-ply composites are particularly tolerant to use-induced damage. For instance, Sihn et al. [42] and Amacher et al. [38] reported that thin-ply laminates do not suffer from fatigue under significant cyclic stress. Likewise, thin-plies retain superior load-carrying capacity after a low-velocity impact [24, 43]. The absence of micro-cracking propagation into the bulk material has further practical applications, such as the reliable gas barrier layer for cryogenic propellant tank reported by Hamori et al. [139].

Nevertheless, the thin-ply effect also comes with significant drawbacks. First, thin-ply laminates require significantly more consumables (carrier paper or film), more stacking operations, and, therefore, more lead time, although manufacturing optimization is possible using preforms stacked by Automated Tape Laying (ATL). Second, the thin-ply effect can be described as a change from a damage-tolerant failure to a quasi-brittle failure. Indeed, micro-cracking, transverse-cracking, and delamination are dissipative mechanisms required to diffuse damage in the material. Therefore, thin-ply composites are not tolerant to stress concentrators such as open-hole and are prone to brittle catastrophic failure, as reported by Wisnom et al. [49], Arteiro et al. [140], or Amacher et al. [38].

						FAW		Value			
Property	**Unit**	**Fiber**	**Resin**	**Layup**	V_f	**Thick**	**Thin**	**Thick**	**Thin**	**Change**	**Ref.**
UNT strength	MPa	M40JB	TP80EP	QI	55 %	30	300	595 ± 27	847 ± 18	+42 %	Amacher et al. [38]
UNT strength	MPa	T800	Aero2 - ILT1	QI	55 %	67	270	760	1087 ± 19	+43 %	Cugnoni et al. [24]
UNT strength	MPa	T800SC	BT250E-1	QI	60 %	40	200	850 ± 41	940 ± 48	+11 %	Sihn et al. [42]
UNT strength	MPa	MR50K	1063EX	QI	60 %	75	145	812 ± 5	974 ± 3	+20 %	Yokozeki et al. [120]
UNT strength	MPa	M40JB	TP80EP	UD	55 %	30	300	2360 ± 150	2250 ± 139	−5 %	Amacher et al. [38]
UNT onset	MPa	M40JB	TP80EP	QI	55 %	30	300	248 ± 18	821 ± 23	+231 %	Amacher et al. [38]
UNT onset	MPa	T800	Aero2 - ILT1	QI	55 %	67	270	400	678 ± 240	+70 %	Cugnoni et al. [24]
OHT far field strength	MPa	M40JB	TP80EP	QI	55 %	30	300	545	380	−30 %	Amacher et al. [38]
OHT far field strength	MPa	T800SC	BT250E-1	QI	60 %	40	200	547	492	−10 %	Sihn et al. [42]
OHT fatigue	# cycles to ruin	M40JB	TP80EP	QI	55 %	30	300	$<2e^4$	$>1e^6$		Amacher et al. [38]
OHC strength	MPa	M40JB	TP80EP	QI	55 %	30	300	216 ± 9	255 ± 10	+18 %	Amacher et al. [38]
OHC strength	MPa	MR50K	1063EX	QI	60 %	75	145	296 ± 4	323 ± 5	+9 %	Yokozeki et al. [120]

Table 2.2: Partial summary of the thin-ply effects reported in the literature. Change is indicated with respect to the thick-ply laminate.

2.2.3 The toughness issue

The absence of damage before the laminate failure in thin-ply composite indicates that there are no mechanisms to redistribute stresses and mitigate stress concentrations. It results in a severe lack of toughness, as reported by Frossard [39] and outlined in Figure 2.6a. They found that neither the interlaminar nor the intralaminar mode I initiation values were ply-thickness dependent [141]. However, the steady-state ERR decreases significantly in M40JB-TP80ep thin-ply laminates, by respectively about 50 % and 23 % when using $30\,\mathrm{g}\cdot\mathrm{m}^{-2}$ plies instead of $150\,\mathrm{g}\cdot\mathrm{m}^{-2}$ plies. The steady-state ERR remained higher than the initiation value, indicating an R-curve effect. These observations were explained by the better microstructure of thin-ply laminates, introduced in subsection 2.2.2. Indeed, a uniform microstructure reduces the extent of fiber bridging, which is known to drive the development of a FPZ in the wake of the crack. On the other hand, the interlaminar mode II was found independent of the ply thickness.

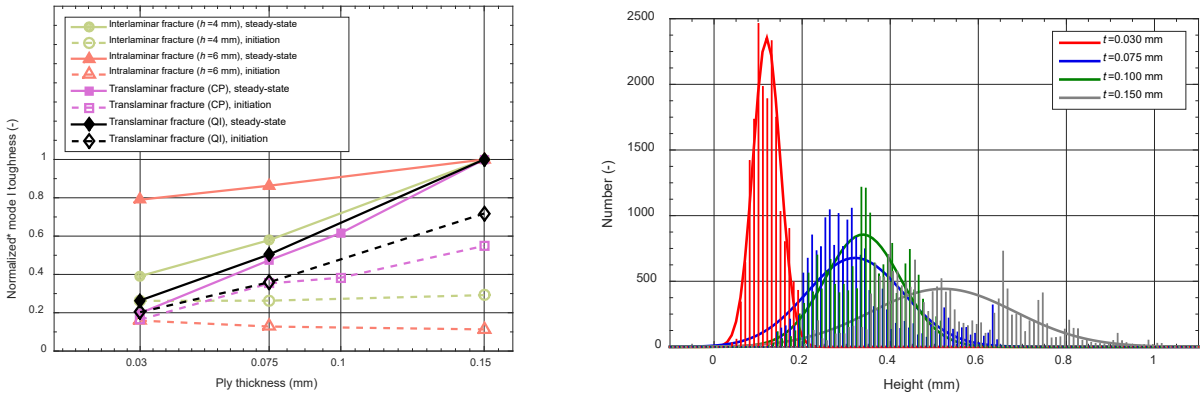

(a) **(b)**

Figure 2.6: (a) Normalized interlaminar, intralaminar, and translaminar fracture toughness as a function of ply thickness. (* Values normalized by the steady-state ERR at t=0.150 mm of the corresponding fracture orientation). Reproduced from [39]. (b) Histogram of the height of the top envelope profile as a function of ply thickness and corresponding fitted normal distributions. Reproduced from [39].

Furthermore, the translaminar mode I ERR of CP and QI laminates decreased linearly with the ply thickness at initiation and steady state. Frossard et al. [142] reported a substantial loss of translaminar toughness, respectively about 70 % and 80 percent, when replacing $150\,\mathrm{g}\cdot\mathrm{m}^{-2}$ plies with $30\,\mathrm{g}\cdot\mathrm{m}^{-2}$ plies. These results corroborate those reported by Teixeira et al. [51] for thin-plies and by Laffan et al. [50] for intermediate ply thicknesses. These results were correlated with a decrease in pull-out length for thin-ply laminates, as shown in Figure 2.6b and Figure 2.7. This confirms the key function of debonding and pull-out to dissipate energy in brittle composites [143]. Moreover, Pimenta and Pinho [144] have proposed a hierarchical analytical model that captures the translaminar toughness of laminates by considering only the contribution of fiber-matrix debonding, matrix fracture, and the friction during the pull-out. Thus, it indicates that pull-out length drives the thin-ply translaminar toughness in the absence of secondary damage.

Figure 2.7: SEM fracture surfaces of CP thin-ply laminates exhibiting bundles of fibers pulled out. The pull-out height increases when blocking 0° plies together. Crack propagates from the bottom left corner to the right top corner. Reproduced with permission from [51].

The loss of translaminar toughness is, arguably, the most critical one. On the one hand, the reported interlaminar and intralaminar values remain acceptable. Moreover, strategies to improve composite interlaminar and intralaminar toughness have been extensively studied. They range from optimizing the fiber-epoxy system [24], introducing toughening interlayer [24, 59], tailored defects [145] or bridging pins [146]. On the other hand, translaminar toughness is a key property to ensure that structural parts retain strength while sustaining damage. The values reported for $30\,\mathrm{g}\cdot\mathrm{m}^{-2}$ thin-ply laminates, about $20\,\mathrm{kJ}\cdot\mathrm{m}^{-2}$ [39, 51], are in the low range of aerospace grade material (see the Ashby chart reproduced in Figure 1.2b). Furthermore, and as noted by Frossard [39], the toughness reduction in thin-ply composites is proportionally more important than the increase in strength. Therefore, the gain of strength brought by thin-plies is canceled by the loss of translaminar toughness. This forces a compromise on the ply thickness, virtually making ultra-thin-ply laminates nonpractical in applications where damage tolerance is the dominant requirement.

Consequently, significant efforts have been made to improve thin-ply translaminar toughness by restoring crack-shielding mechanisms, often following bio-inspired approaches [57]. Among them, Rodríguez-García et al. [147] proposed "brick-and-mortar" specimens manufactured with an ATL process to duplicate nacre-like weak interfaces. This approach has been reported to increase, for instance, the energy dissipated in very brittle material like glass by a factor 700, at the cost of a substantial strength loss [148]. A "brick-and-mortar" architecture achieves this result by promoting debonding and pull-out, and introducing geometrical hardening. However, the brick-like pattern obtained by ATL can not

leverage geometrical hardening and "only" 29 % improvement of translaminar toughness was reported by Rodríguez-García et al. [147], thanks to extensive ply pull-out. Moreover, the tensile properties of the specimen were not reported.

Bullegas et al. [53] proposed a second approach inspired by biological composites. This approach effectively brings the hierarchical fracture accounted for by Pimenta and Pinho [144] to the ply scale by introducing laser micro-cuts in the 0° plies of CP and QI laminates. These micro-cuts set a preferential crack propagation path which is designed to maximize crack deflection according to a fracture mechanics framework. Thanks to this approach, an impressive 460 % increase of translaminar toughness was reported in CP laminates (TR50s-K51), reaching about $70\,\mathrm{kJ \cdot m^{-2}}$ with $20\,\mathrm{g \cdot m^{-2}}$ plies (evaluated by the area method). Furthermore, Bullegas et al. [149] demonstrated that considering only the energy dissipated by debonding and friction during the pull-out process accurately captures the translaminar toughness, in the absence of secondary damage. Bullegas et al. [53] obtained significantly larger pull-out, but they accounted only for about half of the fracture energy, which indicates that secondary damage was triggered in the 90° ply, as highlighted by the SEM images reproduced in Figure 2.8.

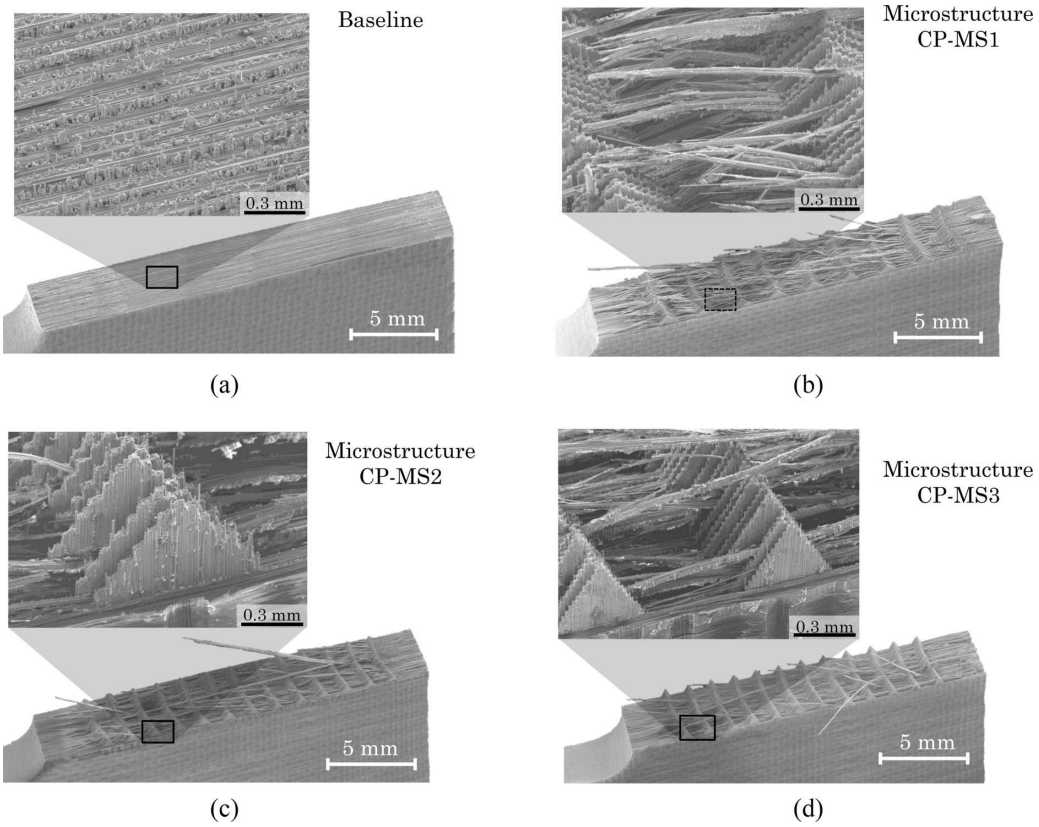

Figure 2.8: SEM fracture surfaces of four specimens: (a) baseline material without any micro-cut; (b), (c), (d) laminates with a hierarchical microstructure promoting an increasing crack deflection. Reproduced with permission from [53].

Despite the outstanding results reported by Bullegas et al. [53], the proposed approach comes with a few drawbacks. First, the micro-cuts reduce the UNT strength by at least 12 % [149], canceling the thin-ply positive effect on strength. Second, the micro-cut processing and necessary alignment

induce a significant manufacturing overhead which is probably not compatible with industrial lead time. Third, the reported results were obtained with a perfect alignment of the crack with respect to the micro-cut pattern. The misalignment effect was not evaluated and is likely to reduce the maximal achievable deflection, reducing the translaminar toughness improvement. Lastly, in real-life applications, the micro-cut density should cover adequately the whole laminate surface, leading to a further reduction in UNT strength.

Therefore, there is a need for a "built-in" toughening method that will provide a good balance between manufacturing complexity, translaminar toughness, and strength. In this regard, Cugnoni et al. [52] proposed fiber hybridization as a third promising approach that does not require the introduction of defects in the laminate.

2.3 Fiber-hybrid composites

Adopting the terminology proposed by Swolfs et al. [150] in their comprehensive review, fiber-hybridization refers to the use of at least two different fiber grades in the same laminate. These fibers generally exhibit contrasting properties and the resulting composite is expected to retain to some extent the advantages of each. Figure 2.9 highlights three different fiber-hybrid microstructures that can be processed with minimal impact on the existing manufacturing methods, ordered in increasing degree of dispersion: interlayer, interyarn, and intrayarn. These configurations are also often referred to as ply-by-ply, tow-by-tow, and fiber-by-fiber hybrids. Interlayer fiber-hybrids are the easiest to produce, by interlaying a different grade of prepreg when stacking the laminate. Interyarn and intrayarn fiber hybridization are achievable during prepreg production, for instance by spreading two different fiber types at the same time, comingling, by calendering (as currently investigated within the HyFiSyn project), or even by recycling discontinuous fibers [151].

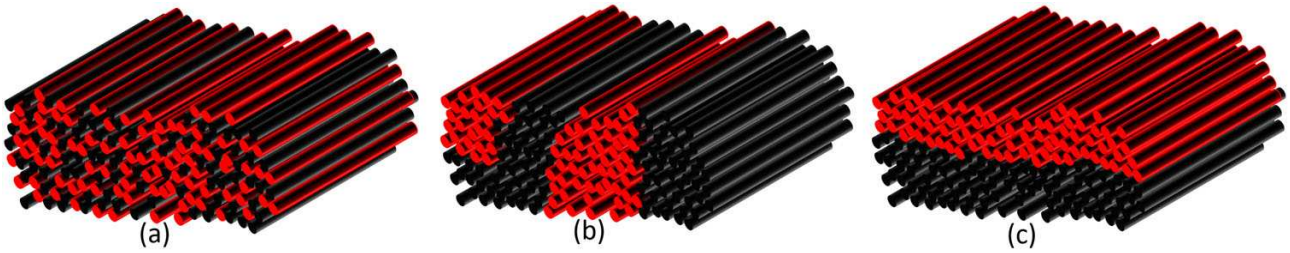

Figure 2.9: Fiber hybridization architectures: (a) intrayarn, (b) intralayer, and (c) interlayer. Reproduced with permission from [150].

Phillips [152] reported that the concept of fiber-hybridization was already debated in the first International Conference on Composite Materials, organized in 1975 in Geneva, Switzerland. This discussion followed a paper from Bunsell and Harris [153], where they reported the UNT behavior of carbon-glass interlayer hybrids. They found that both modulus and strength followed a rule-of-mixtures up to the failure of the carbon layer, then the carbon layer failed gradually as evidenced by AE, almost achieving a pseudo-ductile behavior (which was demonstrated four decades later at the University of Bristol). Therefore, Bunsell and Harris [153] concluded that there was no hybrid effect since a rule-of-mixtures

could reasonably predict the material properties. In a 1978 review, Summerscales and Short [154] reached a different conclusion. They highlighted that some carbon-glass hybrids exhibited mechanical properties above the rule-of-mixture prediction, evidencing a synergistic effect. This discussion outlines a common pitfall when analyzing the mechanical properties of fiber-hybrids: a synergetic effect is found when results are not aligned with expectations, thus the presence of a synergistic effect and its magnitude both depend entirely on the definition of the expectations. The rule-of-mixtures defined with respect to the volume fraction of each fiber is the most common one [150], but the baseline properties should be measured to achieve a meaningful comparison.

Since the 1970s, the increasing state-of-the-art on fiber and matrix properties, and manufacturing processes capabilities create new opportunities for fiber hybridization. Synergetic effects have therefore been reported for a broad range of properties by hybridizing low-modulus, high-strain fibers, e.g., glass fibers, with high-modulus, low-strain fibers, e.g., carbon fibers. For instance, Swolfs et al. [150] reviewed studies on UNT strength [155, 156], OHT strength [157, 158], fatigue [159, 160], bending [161], impact resistance [162] or translaminar fracture toughness, although this latter topic has received comparatively little attention in the literature.

Two research groups, Swolfs et al. [162] and Ortega et al. [163], reported simultaneously a positive synergetic effect on translaminar toughness in carbon-glass woven hybrids. However, Swolfs et al. [162] attributed the synergetic effect to a greater pull-out length while Ortega et al. [163] attributed it to more extensive secondary damage such as delamination and matrix cracking. These two different conclusions are in fact not incompatible. As highlighted by Bullegas et al. [53], an increased pull-out length indeed leads to improved translaminar fracture toughness. However, as previously mentioned, pull-out accounts only for a portion of the translaminar toughness for the longest pull-outs, and Bullegas et al. [53] reported a substantial contribution of secondary failure mechanisms in 90° plies. Therefore, it is possible that increased pull-out length causes delamination initiating from the debonding interface, as well as multiple transverse cracks in the 90° plies, promoting intralayer bridging as evidenced by the SEM observations of post-mortem fracture surfaces. Furthermore, both studies used thick-plies and reported the best synergetic effect when blocking together the plies. This effectively increases the ply thickness and promotes delamination as well as transverse cracking (see subsection 2.2.2). These studies outline a second pitfall: when characterizing the synergetic effect, it should be compared to the concurrent ply-thickness effect.

None of these studies considered the use of thin-plies even though they could substantially improve the potential of fiber hybridization. On the one hand, they can achieve better fiber dispersion which has been proven to be beneficial to synergistic effects. Indeed, a better dispersion features smaller clusters of low-strain fibers [151]. Furthermore, the low-strain fibers are more likely to fail close to the low-strain-to-high-strain interface, as reported by Mesquita et al. [128] based on computed tomography observations of UD carbon-glass hybrids. As the failure occurs close to high-strain fibers, the low-strain broken fibers are less likely to reach a critical cluster size which causes an unstable

ply failure [155, 164, 165]. The material is therefore more tolerant to fiber breaks. The implication of these observations is that given a better dispersion, the likelihood of obtaining a high density of noncritical cluster of broken fibers before failure increases. As the carbon fiber strength follows a Weibull distribution, the position of the fiber breaks along the fiber axis is partially randomized and not coplanar with the crack [144], especially since strength variability increases by using two fiber types. Therefore, the clusters of broken fibers could act at the microscale similarly to the micro-cuts proposed by Bullegas et al. [53] and toughen thin-ply laminates.

On the other hand, the failure of thin-plies (or of fiber clusters) releases little energy, especially with very brittle fibers. If the interface is tough enough [59, 166], delamination will not occur and the ply will continue to carry the load through shear-lag, allowing for ply fragmentation. This effect has been successfully used to develop pseudo-ductile fiber-hybrid thin-ply laminates [166–172] and could be used to induce a "brick-and-mortar" architecture in thin-ply fiber-hybrids just before the failure, leading to a local accumulation of stable damage. For instance, Furtado et al. [173] obtained a pseudo-ductile-like behavior by hybridizing carbon thin-plies with carbon thick-plies. They observed a notch sensitivity reduction. Czél et al. [54] observed the same result by hybridizing low-strain and high-strain carbon fibers, reporting an accumulation of damage around the notch. Wu et al. [158] also obtained notch sensitivity reduction with thin-ply angle-ply carbon-carbon fiber-hybrids. They observed ply fragmentation and dispersed delamination, noting that the ratio of geometrical pseudo-ductile strain (see [115] for the definition) to yield strain drives the damage redistribution around the hole. However, the first two reported studies used rather thick ply-blocks, raising the question of a concurrent ply-thickness effect. The last result is very encouraging as a ply thickness of about $30\,\mathrm{g}\cdot\mathrm{m}^{-2}$ was used. However, no baselines were included in the study and non-hybrid angle-ply laminates have already been reported to induce pseudo-ductility [116] or even to reduce notch sensitivity [174] Furthermore, open-hole does not formally account for a crack tip singularity and the load is shared across the net section, which may promote the obtention of fragmentation.

Reaching the same conclusion that fiber-hybrids are promising to improve the translaminar toughness in thin-ply laminates, Danzi et al. [56] proposed in 2021 carbon-carbon interlayer fiber-hybrids designed to achieve pseudo-ductility. They characterized UNT strength and translaminar fracture toughness (although a different terminology of intralaminar longitudinal toughness is used in their paper) by means of Double Edge Notched Tensile (DENT) tests, following a procedure proposed by Catalanotti et al. [175]. Overall, they reported a significant increase in fracture toughness but attributed it to the ply-thickness effect. However, they observed distinctive failure modes, indicating that fiber hybridization has an influence on damage diffusion.

In light of this review, it appears that the effect of fiber-hybridization in thin-plies is insufficiently understood. Thus, clarifying its intrinsic mechanisms requires additional experimental and modeling efforts. Cugnoni et al. [52] proposed two different fiber-hybridization strategies. The first one relies on large-scale fiber bridging enabled by high strain and high toughness fibers such as Aramid. The

second consists in promoting longer pull-out lengths by adding low-strain carbon fibers to high-strain carbon fibers. Given the industrial interest in carbon-carbon hybrids, the latter is investigated in this thesis.

2.4 Translaminar fracture testing

The fracture mechanics taxonomy usually considers three categories of cracks in a UD composite. First, an interlaminar crack may propagate between the plies, as delamination. Second, a crack can propagate inside a ply, in a direction parallel to the fibers. This is an intralaminar crack. Finally, a crack can propagate inside the ply, through the fibers. This configuration is referred to as translaminar cracking, although some authors refer to it as longitudinal intralaminar crack propagation [175]. These three cracks may appear under three different loading conditions: mode I (opening), mode II (shearing), and mode III (tearing). Each typology of crack comes with its own challenge, in terms of effects on structural parts and testing. Among them, mode I translaminar crack propagation is of primary importance as it leads to unstable failure in brittle composites such as thin-plies.

Overall, the translaminar crack growth in materials involves extrinsic and intrinsic dissipative mechanisms [176]. These mechanisms act over a FPZ and are usually accounted for through a critical ERR that may depend on COD (R-curve effect). In thick-plies composites, these mechanisms typically include delamination, extensive fiber pull-out, or fiber bridging (see Figure 2.10) and affect a large FPZ, but these are precisely reduced or even suppressed in thin-ply laminates. As aforementioned, significant efforts have been made to restore these crack-shielding mechanisms in thin-ply laminates by engineering hierarchical microstructures. Consequently, these hierarchical thin-ply composites exhibit non-linear and large-scale FPZ.

CT is the prevailing test to grow stable cracks in composites and characterize their translaminar toughness [178], although different geometries have been recently proposed to overcome its limitations [56, 175]. However, there is no standard data reduction methodology associated with CT samples to obtain the ERR. The most established ones rely on the LEFM theoretical framework to yield the mode I critical ERR G_{Ic} as a function of the crack increment Δa, commonly referred to as R-curve [179]. Most of these methods are challenging to apply to hierarchical thin-plies. Methods based on the stress intensity factor were found to be inaccurate for orthotropic materials [179, 180]. The compliance calibration methods were shown to be more adapted to composites but raise specific issues whether the compliance is derived from a closed-form formulated for orthotropic materials [181], an experimental fitting, or a FEM [180, 182]. The first requires a negligible FPZ. The second offers the benefit of accounting for the FPZ but is unreliable since thin-ply composites tend to follow a saw-tooth behavior [39], meaning that too few propagation points are available for a robust fitting. Alternatively, the compliance may be fitted from specimens with an increasing machined crack length [179, 183], but this consumes too much material and does not allow for capturing the effect of the

1. Ply pull-out and delamination (not shown)
2. Secondary crack, ply fragmentation
3. Crack branching
4. Bundle pull-out (not shown)
5. Fiber pull-out
6. Fiber bridging
7. Fiber/matrix debonding
8. Fiber failure
9. Matrix cracking
10. Local delamination (not shown)

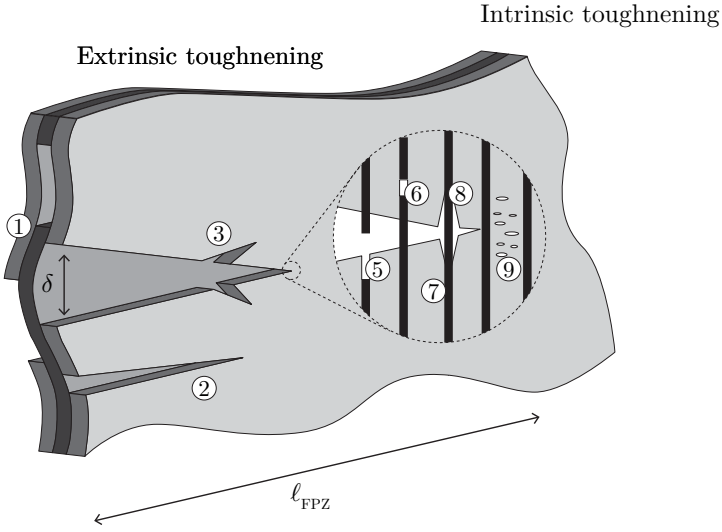

Figure 2.10: Typical multi-scale damage modes in thick-ply or hierarchical thin-ply composites. The FPZ usually extends over several millimeters. Adapted from [176, 177].

FPZ in the wake of the crack, for instance, when extensive fiber pull-out occurs. Additionally, the experimental compliance fitting requires the crack length measurement. With a large FPZ the crack tip position is clearly ambiguous and subjective. Moreover, the crack tends to propagate differently in the bulk [184] and optical observation of the sample surface is usually not representative of the crack front. In-situ x-ray Computed Tomography scan (CT-scan) has been successfully used to characterize the translaminar toughness [185] but this approach is cumbersome. The last approach, the Modified Compliance Calibration (MCC), is based on FEM and does not require measuring the crack length. The MCC has recently been extensively used [50, 51, 53, 186] but adds the overhead of a numerical model. It involves the a priori knowledge of material properties, damage mechanisms, and constitutive laws. Moreover, such a model does not account for the FPZ in the wake of the crack unless a cohesive law is specifically developed.

Furthermore, all these methods were derived under LEFM assumptions, even if not explicitly, see, for instance, the derivation of the Irwin-Kies equation [177]. Their validity is thus questionable in CT specimens exhibiting a large FPZ length l_{FPZ}. Ortega et al. [187] and Maimí et al. [188] have shown analytically and experimentally that R-curves obtained from LEFM-based methods are not independent of the sample size. When the length l_{FPZ} increases, such as in the presence of extensive pull-out, LEFM-based methods tend to overpredict the translaminar toughness. The later publication also reported that Over-height Compact Tension (OCT) specimens [189, 190] improve the ratio of l_{FPZ} to specimen size and thus better approximate LEFM conditions. However, this geometry requires large quantities of material and is not guaranteed to be large enough to develop a self-similar FPZ as reported by Xu et al. [191, 192].

When the material response is non-linear, it is commonly admitted that the non-linear J-curve is an appropriate descriptor of the fracture process where crack stability is defined as $J_I < J_{Ic}$. The J-curve

is more general than LEFM-based methods, accounts for material non-linearities such as plasticity as well as large FPZ, and has been shown to better account for the translaminar fracture toughness of composites [188]. When LEFM conditions are fulfilled, J_c is, therefore, equal to G_c as experimentally verified by several authors [186, 193]. The J-curve has been derived by indirect and direct methods [194]. The former, also known as inverse methods, rely on the identification of the suitable parameters through an optimization procedure to match a FEM response with respect to experimental data, as used, for instance, by Frossard to identify bridging traction [142]. Regarding the translaminar toughness in CT specimens, Ortega et al. [163, 195] proposed a cohesive law identification based on a generalized Dugdale-Barenblatt model. Based on J-integral approaches [196, 197], the latter can be simplified to straightforward equations for selected geometries [198]. For the remaining geometries, including the CT specimen, the J-integral requires a numerical evaluation along a contour using full-field displacement data acquired, for instance, by DIC [39, 186, 199, 200]. This experimental step is often criticized as cumbersome and subjected to scattering, leading to the preference for different methods. Nevertheless, J-integral methods are of great interest as they rely on conservative assumptions, i.e., material homogeneity and the knowledge of stress and strain over the evaluated contour, regardless of the constitutive equations used to derive them. They are, therefore, suitable for a wide range of geometries and materials, including hierarchical thin-ply or thick-ply laminates, as long the FPZ is included inside the J-integral contour.

One of the reasons behind the prevalence of the MCC compared to the J-integral to derive the translaminar toughness of composite CT specimens is probably the lack of published practical guidelines, reinforcing the notion that this approach is complex and challenging to master. Several publications reported using J-integral methods [186, 193, 201, 202] but the details of the numerical derivation and its sensitivity to noise or parameter variations are rarely discussed. One of the best efforts in this regard is the JMAN routine proposed by Becker et al. [201] and reported as an efficient implementation of the surface J-integral. However, too few details are given about its implementation, i.e, the code was not distributed to the best of the authors' knowledge. Indeed, many solutions with different pitfalls may be implemented to derive the J-integral, which leads to costly development. Publication of the code is therefore deemed necessary to further diffuse the J-integral method. More recently, Barhli et al. [202] made available the Oxford University Reinjection-Optimized Meshing Add-on (OUR-OMA). It is based on a FEM approach for solving the displacement field at the crack tip based on the displacement field acquired by DIC, effectively dealing with noisy or partial data. However, this approach is believed to not be adequate for hierarchical thin-ply laminates as it requires an accurate FEM of the FPZ.

Finally, simultaneously with the final writing stage of this thesis, the German Aerospace Center (DLR) released a Python toolbox to perform fracture mechanics analysis from DIC and simulation results [203]. It contains, among other tools, a line J-integral implementation.

Chapter 3

Experimental materials and methods

This chapter first introduces the material selection approach which was followed in this work to design the fiber hybrids. Then, the material properties and the sample preparation methods are presented. Finally, the experimental techniques used in this work are detailed.

The list of available data, codes, and publications generated for this work is available on Zenodo [204].

3.1 Material selection for carbon-carbon fiber hybridization

The choice of a suitable material system for a given application is a complex process that must satisfy several objectives such as the expected toughness improvement, preservation of tensile properties (onset of damage and strength) of the thin-ply composites (onset of damage and strength), manufacturing, as well as industrial relevance. Consideration of industrial interest and material availability eventually drove the material selection in this work, as an industrial partner is involved in the Hyfisyn project. In particular, the fiber cost and ease of spreading, as well as the loss of strength when hybridized were considered.

Furthermore, thin-ply is a cost-intensive material and a significant part of the cost comes from the prepreg line setup. Therefore, the material requirement should be rationalized as much as possible and it is not possible to test a wide range of prepreg grades in a pre-design step.

The stiffness and strength properties of carbon fibers are of great importance for industrial applications, but despite a favorable influence on fracture properties, hybridization with tough fibers such as glass [54] or aramid [52, 205, 206] tends to decrease the overall stiffness and strength performances of the laminate.

Thus, the following sections discuss the parameters driving the composite properties when hybridizing a low-strain material exhibiting a modulus E_L, a strength σ_L, and an ultimate strain ε_L, with a high-strain material exhibiting a modulus E_H, a strength σ_H and an ultimate strain ε_H. Note that these values refer to the longitudinal properties of a non-hybrid UD laminate, i.e., E_l, σ_l, and ε_l. For the sake

of conciseness, the lowercase subscript $_l$ is dropped in this document when referring to the properties of the low-strain material, denoted by a uppercase subscript $_L$, or to the ones of the high-strain material, denoted by uppercase $_H$. In practice, the longitudinal modulus E_l and strength σ_l of a non-hybrid UD laminate are, as a first order approximation, proportional to the fiber longitudinal values, E_f and σ_f, and the fiber volume fraction V_f, given that the matrix properties are significantly lower than the ones of the fiber in this direction (see for instance Equation 3.1) [22]. Moreover, the hybrid properties, denoted by the lowercase subscript $_l$, will often be reported as a function of the low-strain material volume fraction γ. For instance, in an interlayer hybrid, $\gamma = \frac{t_L}{t_H + t_L}$ where t_L is the total thickness of the low-strain material contained in one ply-block and t_L the high-strain counterpart.

$$E_l \approx E_f V_f \quad \text{and} \quad \sigma_l \approx \sigma_f V_f \tag{3.1}$$

3.1.1 Maximizing the tensile properties

Tensile modulus

The UD tensile modulus of a hybrid laminate made of two linearly elastic fibers has been reported to follow a linear rule-of-mixtures as in Equation 3.2 throughout the literature [152, 153, 207–211], presuming that the relative fiber volume fraction V_f is accurately determined for each fiber. Consequently, higher fiber-hybrid modulus can be achieved by increasing the moduli of high-strain and low-strain materials, respectively E_H and E_L, which is the same as selecting higher modulus fibers considering Equation 3.1. Alternatively, the relative volume fraction of low-strain fiber γ may also be increased, assuming that the low-strain fiber is stiffer than the high-strain fiber. The ply thickness is not expected to have an effect on the tensile modulus, as observed by Amacher et al. [38].

$$E_h = E_L \gamma + (1 - \gamma) E_H \tag{3.2}$$

Any deviation from a linear rule-of-mixtures will be interpreted as a hybrid effect, although they are not expected. As reported by Swolfs et al. [212], the few ones that were accounted for in the literature could be explained by extrinsic factors, such as fiber misalignment or errors in the relative V_f estimations.

Tensile onset of damage

The broken fiber clustering and propagation are considered the main mechanism governing the failure of UD laminates. In an idealized laminate, the onset of damage σ^Y is expected to take place when the fiber reaches its ultimate strain. However, the strength of fibers is probabilistic (and usually accounted for by a Weibull distribution of modulus m and scale parameter σ_0). This causes early fiber breaks in the laminate, which induce stress concentrators on the neighboring fibers [213–215]. As a consequence, fiber breaks tend to develop unstably into clusters [216] leading to laminate failure before reaching the fiber's ultimate strain in the average sense.

In a hybrid laminate, the low-strain material strength thus follows a distribution of mean $\acute{\sigma}_L$. The onset of damage σ_h^Y is therefore expected to occur before the low-strain strength $\acute{\sigma}_L$. However, using in-situ synchrotron computed tomography observations, Mesquita et al. [128] established that fiber-hybrids are more tolerant to fiber breaks compared to a non-hybrid baseline. The presence of high-strain fibers hinders the development of critical broken-fiber clusters, delays the onset of damage, and leads to a positive hybrid effect on the failure strain of the low-strain fiber. Thus, with an appropriate hybridization, the stress at the onset of damage is expected to follow Equation 3.3.

$$\sigma_h^Y = E_{hybrid}\varepsilon_L \tag{3.3}$$

The experimental works reviewed by Swolfs et al. [212] show that the hybrid effect increases with a decrease in the low-strain relative volume fraction γ, highlighting that a negative hybrid effect can be obtained if this fraction is too important. Swolfs et al. [217] proposed a parametric study based on an analytical stress redistribution model coupled to a FEM of a hybrid fiber microstructure. The model parameters were chosen to correspond to a typical glass-carbon hybrid with a volume fraction of 50 %. By varying some of the parameters, they found that the strain at the onset of damage can be maximized by:

- Decreasing the low-strain fiber Weibull modulus m. It means that the fiber exhibit a greater strength variability, thus the fiber breaks are more gradual and less likely to reach a critical cluster size. However, as pointed out by Swolfs et al. [212], researchers that used state-of-the-art carbon fibers with a higher Weibull modulus did not report a decrease in the hybrid effect [218]. Furthermore, little reliable data are available in the literature about the Weibull parameters of carbon fibers, and it is noteworthy that a low Weibull modulus fiber may be challenging to spread at an industrial scale.
- Increasing the high-strain fiber stiffness E_H to relax stress concentrators on low-strain fibers.
- Aiming for a sufficiently large high-to-low strain ratio $\varepsilon_H/\varepsilon_L$ to avoid high-strain fibers failure following low-strain fiber breaks. A value of 2 was reported as suitable for the considered glass-carbon hybrid and a higher one did not lead to further improvements as the failure propagation was governed by the low-strain fiber break clustering.

The ply thickness can have a concurrent effect on the strain at the onset of damage observed in QI laminates. Indeed, if the ply thickness is increased due to hybridization, the longitudinal failure of the 0° ply may occur after transverse cracking and delamination (see chapter 2).

The hybrid effect on the onset of damage is therefore defined as the relative change in the failure strain of the low-strain fibers within the hybrid composite, with respect to the failure strain of a pure low-strain laminate. Furthermore, in a QI laminate, where transverse cracking or free edge delamination are usually the first damages to occur, the strain at the onset of damage should be scaled according to the ply-block thickness. More details are given about this approach in section 5.2.

3.1.2 Tensile strength

The tensile strength of fiber-hybrids UD laminates is expected to follow a bilinear Rule-of-Mixtures (RoM) as in Equation 3.4 [212, 219]. The tensile strength is therefore either dominated by the high-strain fiber tensile strength σ_H or by the low-strain fiber tensile strength σ_L, depending on their relative volume fraction. Thus, the tensile strength can be maximized by either reducing the volume fraction of low-strain fibers γ and increasing σ_H or by increasing the volume fraction of low-strain fibers γ along with σ_L. When the tensile strength is dominated by the low-strain fibers, it may be improved by a positive hybrid effect for the same reasons exposed for the onset of damage.

$$\begin{cases} \sigma_h = \sigma_H (1-\gamma) & \text{for } \gamma \leqslant \zeta \\ \sigma_h = \sigma_L \gamma + \varepsilon_L E_H (1-\gamma) & \text{for } \gamma \geqslant \zeta \\ \zeta = \frac{\sigma_H - \varepsilon_L E_H}{\sigma_H + \sigma_L - \varepsilon_L E_H} \end{cases} \tag{3.4}$$

The hybrid effect is defined as the relative change of tensile strength with respect to the bilinear RoM. As previously, the ply thickness has a concomitant effect on the ultimate strength of QI laminates and should be evaluated accordingly.

3.1.3 Conclusion

For a given fiber dispersion, the tensile properties of a fiber-hybrid laminate can be optimized by using constituents exhibiting improved properties or by leveraging a hybrid effect. The hybrid laminate modulus E_h increases with E_H, E_L or γ following a rule-of-mixtures. The onset of damage strain may be increased by promoting the hybrid effect. Positive hybrid effects up to 50 % have been reported in the literature when γ is below approximately 40 % [212]. Above this value, a substantial negative hybrid effect may be observed. However, as pointed out by Swolfs et al. [212], many of those measurements where performed before the recent developments regarding the influence of sample geometry, tabs, and hybridization on the stress concentration in tensile specimens [220–222]. Thus, the baseline values are likely to be underestimated, potentially leading to an overestimated positive hybrid effect.

Furthermore, it has been shown by modeling that decreasing the low-strain fiber Weibull modulus, increasing E_H, or ensuring a sufficient strain contrast between the fibers may improve the hybrid effect, although these indications should be considered with care as the model was found by Mesquita et al. [128] to underestimate significantly the hybrid effect. Indeed, it does not take into account the local or dynamic stress intensities. Moreover, positive hybrid effects were reported even with high Weibull modulus fibers and the industrial spreading of a low Weibull modulus fiber may be problematic. Positive hybrid effects may also improve the tensile strength when it is dominated by the low-strain fiber failure, for the same reasons as for the onset of damage.

To conclude, there is a clear interest in using intermediate-modulus carbon fibers as high-strain fibers instead of the glass fibers usually reported in the literature as this would improve the hybrid effect while preserving high specific properties of thin-plies. However, ensuring a sufficient strain ratio will require using high-modulus carbon fibers with a low ultimate strain. For instance, the HR40-34-700 system exhibits a strain ratio of 1.82 (see Table 3.2). While this will bring further improvement to the expected tensile properties, it may decrease the hybridization effect through a high Weibull modulus [127].

3.1.4 Maximizing translaminar toughness

As aforementioned in chapter 2, the translaminar toughness of thin-ply composites is driven by the pull-out lengths in the 0° plies, mainly dissipating energy through debonding and pull-out. Pimenta and Pinho [144] proposed an analytical model to predict the translaminar toughness in UD laminates exhibiting pull-out bundles of fibers. Even though the model was formulated for pure laminates, it relies on sufficiently generic parameters to provide insight into possible toughening mechanisms of fiber-hybrid laminates, if the assumed damage sequence remains unchanged. For instance, they assumed two sequences of events:

- Stress concentrations lead to the translaminar failure of fiber bundles. The bundles are then debonded. This sequence seems to mostly concern small-scale bundles.
- The bundles first debond and then break. This sequence seems to prevail for large-scale bundles.

The authors proposed a parametric study for their model, which suggests that:

- Increasing the fiber strength can improve significantly the translaminar toughness, both in debonding and pull-out contributions, as it drives the debonding length. The debonding length is an upper limit for the pull-out length.
- Fibers with a higher strength variability, hence with a lower Weibull modulus, are more likely to break away from the crack tip and dissipate more energy during pull-out.
- The toughening is maximized for intermediate interfacial in-situ mode II toughness and pull-out frictional stress. As an illustration, the model indicates that a macroscopic mode II interlaminar toughness G_{IIc} value of approximately $0.7\,\mathrm{kJ \cdot m^{-2}}$ would lead to a good compromise between debonding and pull-out dissipation for small bundles.

Thus, the hybridization of a high-strain fiber with a low-strain fiber may produce a very positive hybrid effect on the translaminar toughness by increasing both the mean fiber strength and the fiber strength variability. The results reported for instance by Swolfs et al. [162] could be interpreted in this sense, as they reported a positive hybrid effect associated with a greater pull-out length.

However, the model also indicates that thin-ply layers are inherently too thin to develop large-scale hierarchical pull-out bundles. Indeed, Teixeira et al. [51] and Frossard [39] have observed that thin-ply

composites are characterized by an almost "flat" fracture surface. For instance, Frossard reported that the pull-out length in a 0° plies of a $30\,\mathrm{g}\cdot\mathrm{m}^{-2}$ FAW CP M40JB-80ep laminate follows a distribution centered on 0.12 mm, against 0.52 mm for an intermediate laminate of $150\,\mathrm{g}\cdot\mathrm{m}^{-2}$ FAW. At the same time, the aforesaid mechanisms' magnitude grows geometrically with the pull-out length. Thus, fully leveraging these mechanisms by fiber-hybridization would require to increase substantially the pull-out length, which seems unrealistic when relying only on the fiber variability.

Finally, it is worth noting that the model relies on assumptions that are not always supported by experimental evidence. For instance, as shown in their Appendix C, Pimenta and Pinho [144] assume a geometrical scaling of the experimental interlaminar fracture toughness that is challenging to validate empirically. Thus, the model validity should be considered with caution.

Another approach consists in selecting the carbon fibers in such a way that their strength distributions are sufficiently contrasted to fail at two completely distinct strains. This approach, similar to the one recently investigated by Danzi et al. [56], enables fragmentation and pseudo-ductility. Once fragmented, the low-strain material may be pulled-out as large scale-bundles. Pseudo-ductility has been well documented in the past years for glass-carbon hybrids [59, 156, 166, 167, 170, 171, 223] and extrapolated to carbon-carbon hybrids [171, 224, 225]. Note that pseudo-ductile composites often make use of thin-ply composites to achieve favorable low-strain material volume fraction γ.

The analytical failure map approach proposed by Jalalvand et al. [166] was used in the present work as a guideline to design fiber-hybrids. This approach relies on the shear-lag model reported by Jalalvand et al. [169] and designed for interlayer hybrids, assuming that the low-strain ply is embedded within the high-strain material in the same ply-block (see Figure 3.1). It relates the stresses at which hybrid failure modes occur, i.e., the low-strain fragmentation stress σ_{LF}, the delamination stress σ_{del}, and the high-strain failure stress σ_{HF}; to the low-strain material proportion γ (for the record, $\gamma = \frac{t_L}{t_L+t_H}$) and laminate properties. Note that in the original paper, the thicknesses refer to half the effective thicknesses as the analysis is carried out on a symmetric half-representative element. In this work, it is preferred to use effective thicknesses for clarity. The relevant constitutive equations are reproduced in Table 3.1 and scaled accordingly.

Most of the parameters required in Table 3.1 are available in the literature and are listed in Table 3.2 or Table 3.3. Similarly to Jalalvand et al. [169], the low-strain strength distribution average $\acute{\sigma}_L$ was considered equal to the strength σ_L. For NTPT materials, an approximate 1:1 relation can usually be assumed between the ply thickness in µm and the prepreg FAW in $\mathrm{g}\cdot\mathrm{m}^{-2}$. As shown in Table 3.1, the use of a tough resin is beneficial to delay delamination. Thus, the toughened TP415 from NTPT was selected. Its mode II interlaminar toughness G_{IIc} was characterized through Four-point End-Notched Flexion (4ENF) tests [24, 198] carried out on 4 mm thick, 25 mm wide, and 200 mm long UD samples made of $60\,\mathrm{g}\cdot\mathrm{m}^{-2}$ 34-700-TP415 plies. The results are reported in Figure 3.2. The nominal width and gauge length of a UNT sample, respectively 25 mm and 150 mm, were used to determine the high

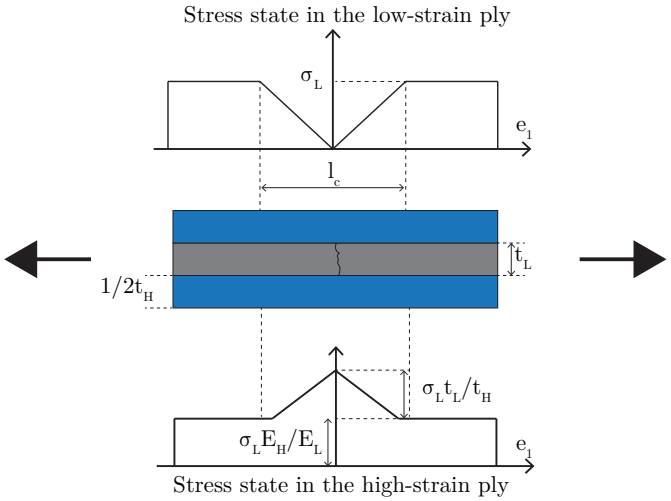

Figure 3.1: Shear-lag model for interlayer hybrids. Reproduced with permission from [169].

Failure mode	**Stress**
Fragmentation	$\sigma_{LF} = \acute{\sigma}_L \dfrac{\alpha\beta + 1}{\alpha\,(\beta + 1)}$
Delamination	$\sigma_{del} = \dfrac{1}{1+\beta}\left(\dfrac{1+\alpha\beta}{\alpha\beta}\dfrac{4G_{IIc}E_H}{t_H}\right)^{\frac{1}{2}}$
High strain failure	$\sigma_{HF} = \dfrac{1}{1+\beta}\dfrac{\sigma_H}{K_t V^{\frac{1}{m}}}$

Table 3.1: Laminate stress for each damage mode. α is the low-to-high strain modulus ratio $\alpha = E_L/E_H$, β is the low-to-high strain thickness ratio $\beta = t_L/t_H$, G_{IIc} is the interlaminar mode II toughness, K_t is the stress concentration factor caused in the high-strain material by the low-strain fragmentation, V is the volume of high-strain material implied in the fragmentation process and m is the Weibull modulus of the high-strain material strength distribution.

strain material volume. The remaining values were assumed from the literature.

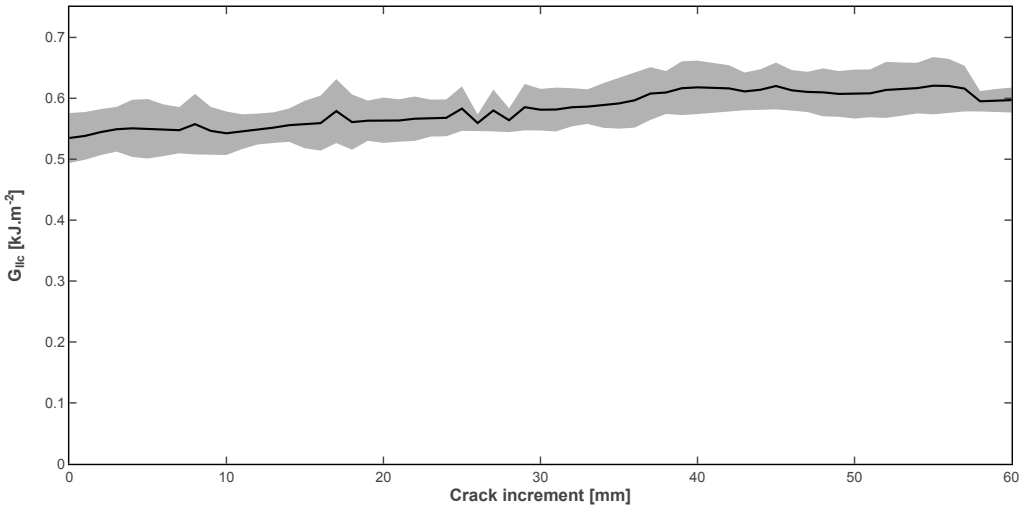

Figure 3.2: G_{IIc} characterized with 4ENF samples for the 34-700-TP415 system.

Name	**Manufacturer**	$\boldsymbol{E}$ **[GPa]**	σ **[MPa]**	ε [%]	ρ $[\mathbf{g \cdot cm^{-3}}]$	σ_0 **[MPa]**	m
HR40	Mitsubishi	375	4410	1.1	1.82		
HS40	Mitsubishi	425	4610	1.1	1.85	6.54 ± 0.25	5.40 ± 0.78
M35J	Toray	343	4700	1.4	1.75		
T300	Toray	230	3530	1.5	1.76	3.79 ± 0.16	4.75 ± 0.63
34-600	Mitsubishi	234	4500	1.9	1.80		
34-700	Mitsubishi	234	4830	2.0	1.80	4.66 ± 0.14	5.24 ± 0.57
T800S	Toray	294	5880	2	1.80		
T1100S	Toray	324	7000	2	1.79		

Table 3.2: Commercial carbon fibers properties: longitudinal modulus E, strength σ, ultimate strain ε^{ult}, and density ρ according to the published datasheets; Weibull parameters σ_0 and m according to [127]. Note that the fiber properties differ from the laminate properties used is Table 3.1.

To achieve fragmentation, the material system must be chosen such that the fragmentation stress is inferior to the delamination or failure stresses. At the same time, it is desirable to delay the fragmentation as much as possible to not jeopardize the ply-thickness advantage with a low-strain onset of damage. Furthermore, the pull-out length must be maximized to leverage the dissipation of energy through pull-out. The pull-out length upper bound is defined by the maximal distance between two successive fragmentation cracks. The aforementioned shear-lag model, which assumes an elastic-perfectly plastic shear response for the matrix, associates this distance to the critical length l_c over which a broken layer recovers stress (see Figure 3.1). l_c is related to the mean strength distribution in the low-strain material, $\acute{S}_L$, and to the interface shear strength, τ_y, through Equation 3.5.

$$l_c = \frac{\acute{\sigma}_L t_L}{\tau_y} \tag{3.5}$$

Introducing $\beta = \frac{\gamma}{1-\gamma}$, the failure mode stresses, the predicted maximal pull-out length, and the tensile properties were plotted as a function of γ in Figure 3.3 and Figure 3.4 for different combinations of carbon fibers available on the market. The predictions were done for a representative hybrid UD ply-block that will serve as the building block for a multi-axis laminate, with a high-strain ply-thickness of 100 µm. This choice allows for up to 50 µm of low-strain material before reaching the thin-to-thick ply limit. In this case, γ reaches 0.33.

For most of the considered materials, the high-strain material fails before fragmentation beyond these a γ value of 0.2. All the considered configurations fail before delamination between the two UD plies. The pull-out length, which is directly linked to translaminar toughness [39], is mostly influenced by the low-strain volume content. Indeed, the selected fibers must exhibit an adequate modulus ratio to enable fragmentation. For instance, notice that the system 34-600-T800S reported Figure 3.3b will

Parameter	Description	Value	Ref.
m	Laminate Weibull modulus	41	[126]
G_{IIc}	Mode II critical ERR	$550\,\mathrm{kJ \cdot m^{-2}}$	NA[a]
τ_y	Shear strength	73.6 MPa	[84]
K_t	Stress intensity factor	1.08	[169]
L	Sample length	150 mm	NA[a]
W	Sample width	25 mm	NA[a]

[a] Measured

Table 3.3: Parameters used for the HR40-34-700 failure map.

fail before fragmentation. As a consequence, all the suitable low-strain fibers on the market exhibit a similar strength. Thus, the most effective way of increasing the pull-out length to promote translaminar toughness is to increase the low-strain volume fraction γ (see Equation 3.5). Thus, the most favorable hybrid configuration appears to be the HR40/T1100S system. However, the T1100S is a high-performance, expensive carbon fiber, and is not suitable for every application. Moreover, it is noticed that hybridization leads to an important loss of predicted strength for the T1100S. Thus, it is not necessarily the most optimal one in terms of toughness improvement and strength loss.

To select the optimal material system with respect to the maximizing of pull-out (and thus translaminar toughness) and tensile properties, it is proposed to use a figure of merit by normalizing the pull-out length by the loss of strength in the hybrid material with respect to the strength of the pure high-strain material (Figure 3.5a). In addition, the stress at the onset of damage, i.e., the stress at the fragmentation, is normalized by the predicted laminate strength (Figure 3.5b).

Figure 3.5a and Figure 3.5b show that the HR40-34-700 system is the most optimal among those considered based on those criteria. Indeed, compared to the HR40-T1100S system, it provides substantially more pull-out length for the same loss of strength and the onset of damage is closer to the failure of the laminate. In this regard, the T300-T800S and M35J-T800S are also very promising, but the delayed onset of damage comes at the cost of restricted design space to promote pull-out (as shown by the highlighted "stable fragmentation" zones in Figure 3.3). Considering these elements, the HR40-34-700 hybrid system was selected and has been characterized in this work.

3.1.5 Hybrid ply-block configuration

Equating any two equations from Table 3.1 for a given hybrid system defines boundary conditions corresponding to the transition between the different failure modes (see Table 3.4). These equations

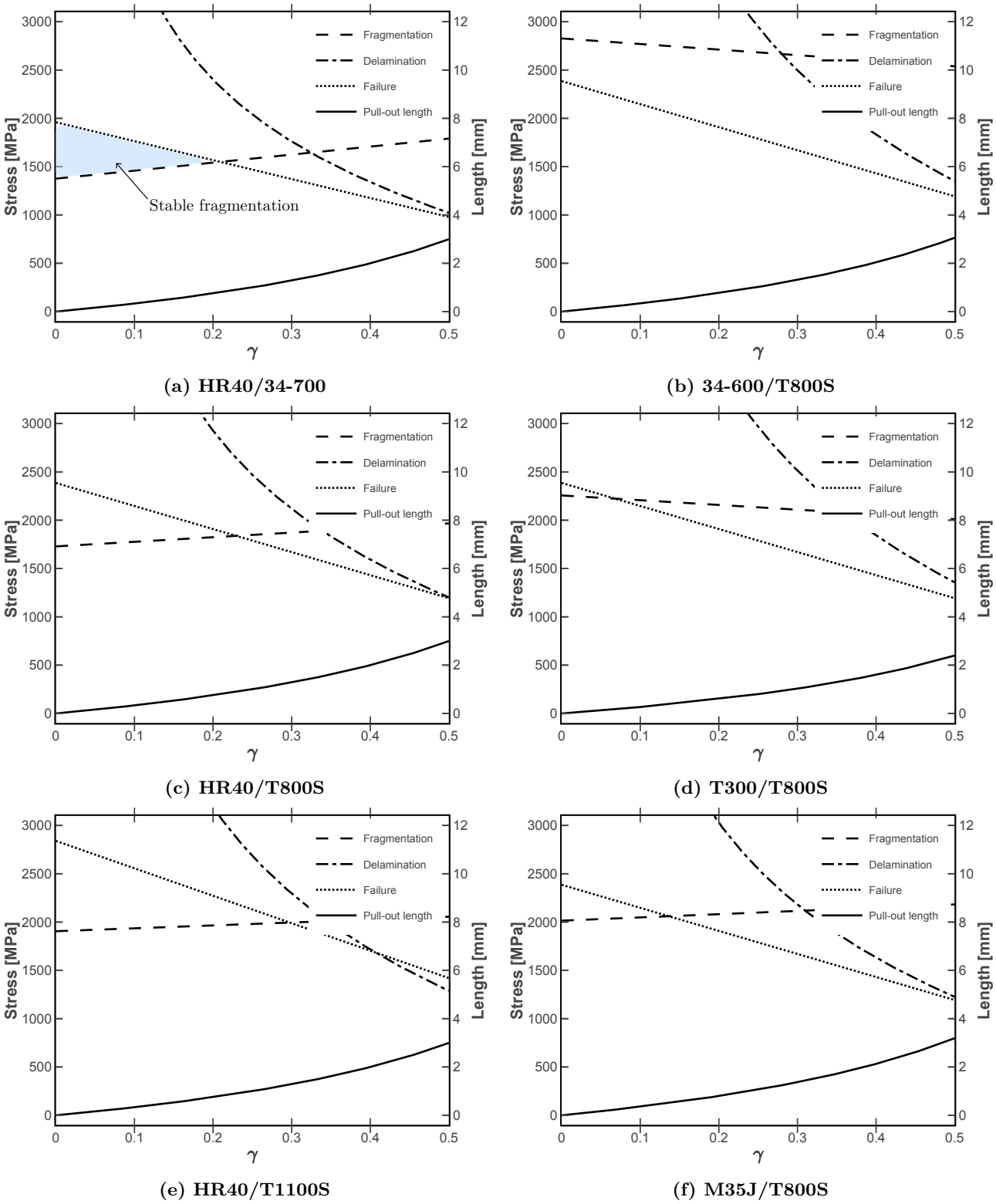

(a) HR40/34-700 **(b) 34-600/T800S**

(c) HR40/T800S **(d) T300/T800S**

(e) HR40/T1100S **(f) M35J/T800S**

Figure 3.3: Failure stresses in UD interlayer hybrids for different combinations of carbon fibers available on the market (see Table 3.2), as a function of the low-strain volume fraction γ and for a high-strain thickness t_H of 100 µm, predicted according to the equations reported in Table 3.1. For $\gamma = 0.33$, the low-strain thickness t_L is 50 µm and the total ply-block thickness is 150 µm, the thin-ply upper bound. The first fibers are reported as low/high strain fibers. Normalized for 50 % V_f.

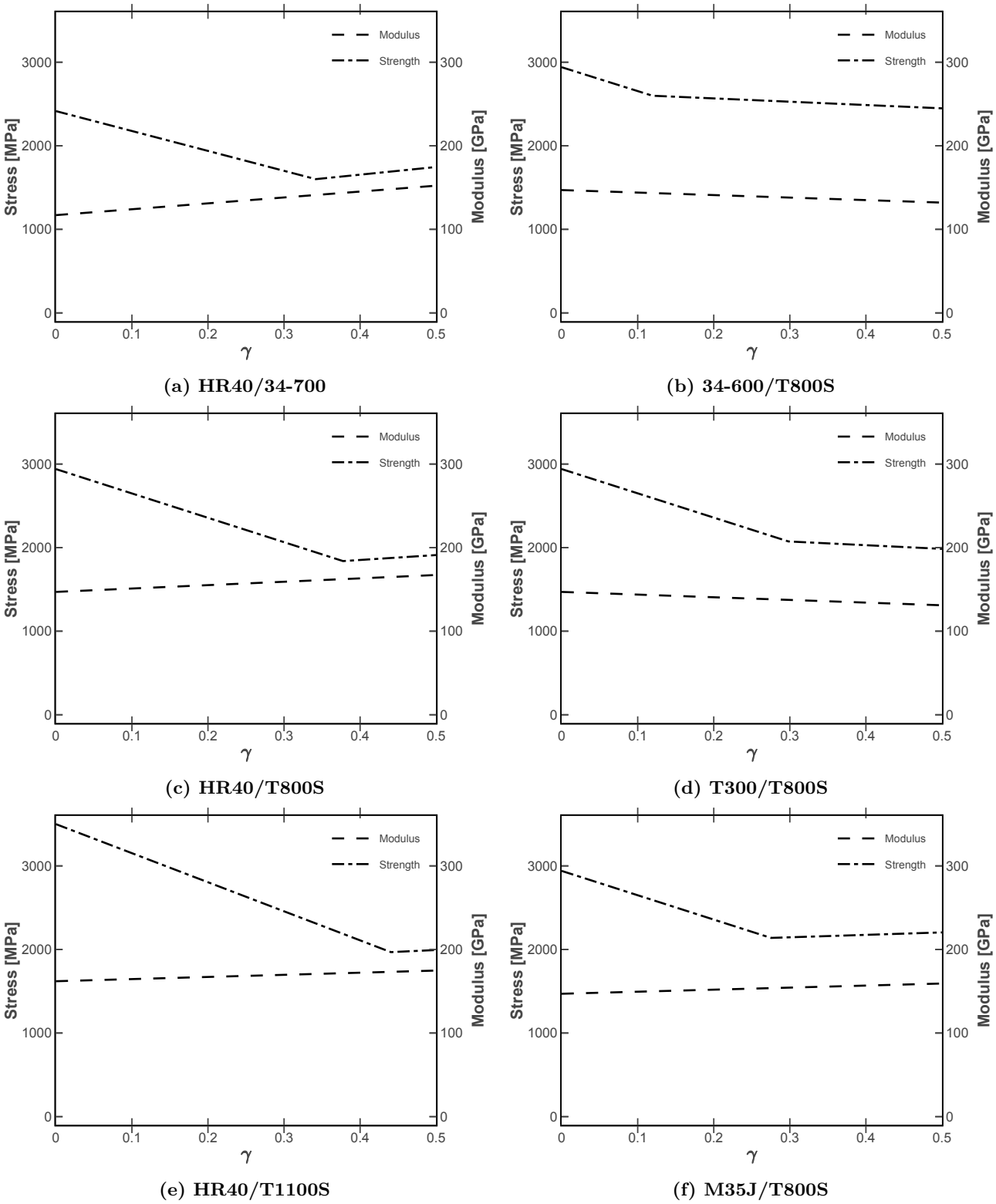

(a) HR40/34-700 **(b) 34-600/T800S**

(c) HR40/T800S **(d) T300/T800S**

(e) HR40/T1100S **(f) M35J/T800S**

Figure 3.4: Tensile properties of UD interlayer hybrids for different combinations of carbon fibers available on the market (see Table 3.2), as a function of the low-strain volume fraction γ and for a high-strain thickness t_H of 100 µm, predicted by RoM without accounting for the ply-thickness effect or the stress concentrator considered by the fragmentation model. For $\gamma = 0.33$, the low-strain thickness t_L is 50 µm and the total ply-block thickness is 150 µm, the thin-ply upper bound. The first fibers are reported as low/high strain fibers. Normalized for 50 % V_f.

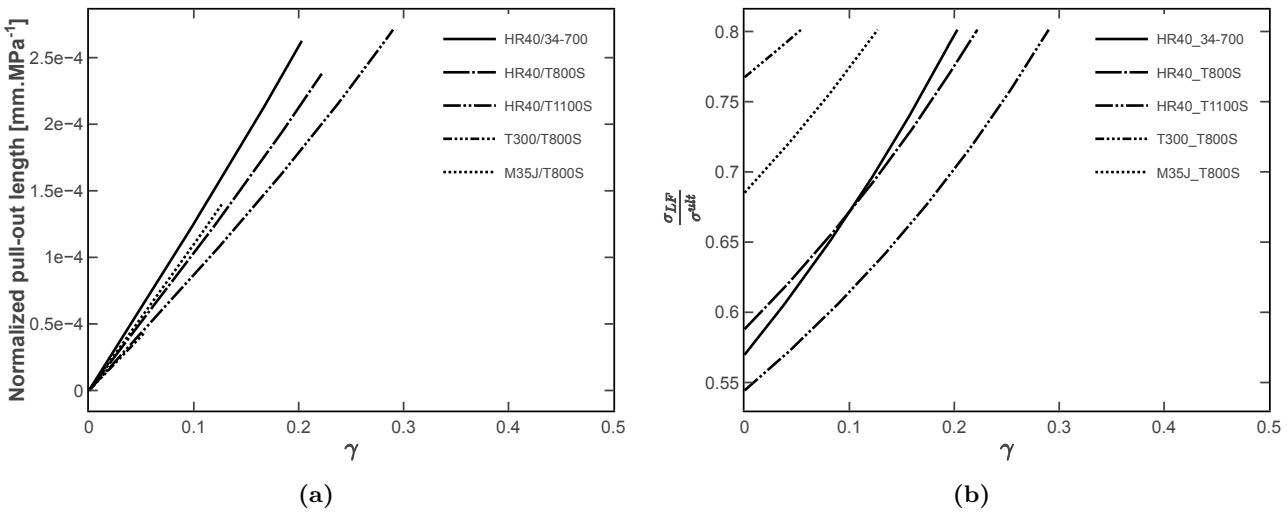

Figure 3.5: Hybrid system selection tools: (a) pull-out length achievable by fragmentation normalized by the loss of strength compared to a pure high-strain laminate, and (a) stress at the onset of damage to strength ratio. Incomplete lines indicate that the hybrid can not be fragmented beyond this low-strain volume fraction γ.

were implemented with a Python script to draw the failure map proposed by Jalalvand et al. [169]. The failure map for the HR40-34-700 system is reported in Figure 3.6.

Boundary	**Equation**
Fragmentation / Delamination	$\frac{t_L}{2} = \frac{2G_{IIc}E_H}{S_L^2}\frac{\alpha(1-\gamma)}{\alpha\gamma+1-\gamma}$
Fragmentation / High strain failure	$\frac{t_L}{2} = \frac{\gamma}{2WL}\left(\frac{S_H}{KtS_L}\frac{\alpha}{\gamma(\alpha-1)+1}\right)^m$
Delamination / High strain failure	$\left(\frac{t_L}{2}\right)^{\left(\frac{1}{2}-\frac{1}{m}\right)} = \left(\frac{\gamma}{1-\gamma}\right)^{\left(-\frac{1}{m}\right)}\frac{K_t}{S_H}(2LW)^{\frac{1}{m}}(2G_{IIc}E_H)^{\frac{1}{2}}\left(\frac{\gamma(\alpha-1)+1}{\alpha(1-\gamma)}\right)^{\frac{1}{2}}$

Table 3.4: Failure map constitutive equations

Six different interlayer fiber-hybrid laminates were selected according to the failure map and are indicated by symbols in Figure 3.6. The effect of fiber hybridization was assessed by varying the low-strain volume fraction γ from 14 to 33 %. To characterize the concurrent effect of ply-thickness, the same γ is employed for different ply-block thicknesses. Finally, symmetric and asymmetric interlayer architectures are considered. Figure 3.7 outlines the differences between a symmetric ply-block where the low-strain layer is embedded inside two layers of high-strain material and an asymmetric ply-block where the low-strain layer is not embedded. Symmetric ply-blocks were used to promote fragmentation. However, pseudo-ductility was not sought explicitly in this work as the difference between the stress at fragmentation and the strength was kept as small as possible to maximize the onset of damage. The asymmetric layup may promote secondary damage, such as delamination, thanks to the increased modulus mismatch at the ply-block interfaces. It was therefore included in the test matrix. Some hybrids are thick or unstable according to the failure map. They were included to identify contrasting mechanisms. Additionally, to these interlayers hybrids, novel interyarn and intrayarn ar-

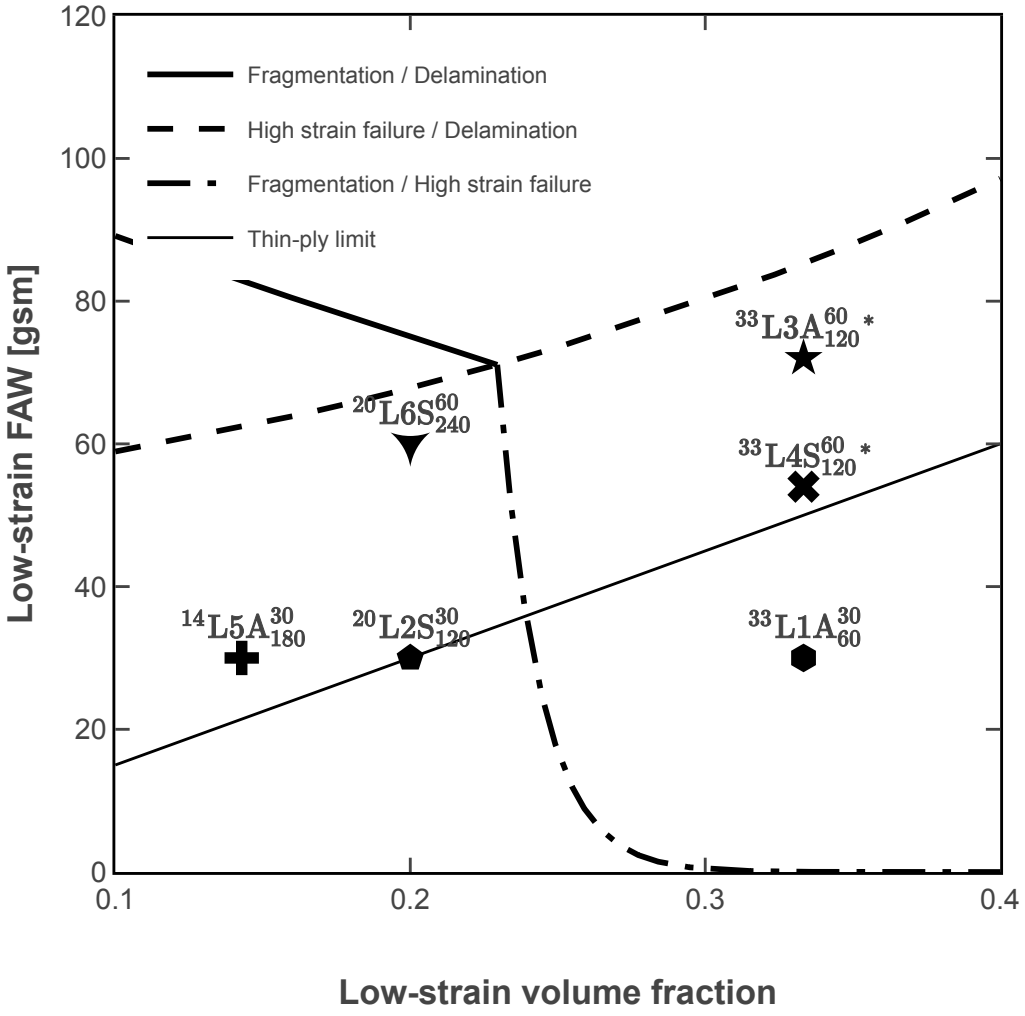

Figure 3.6: Failure map for the HR40-34-700 TP415 system assuming a 1:1 relation between the FAW and the ply thickness. The symbols depicted the interlayer hybrid configurations characterized in this work. The pull-out length increases with the low-strain FAW and the stress at fragmentation increases with the low-strain volume fraction γ.

chitectures developed within the HyFiSyn project are characterized in chapter 6. They were designed following the same principle.

To facilitate the interpretation of the results, a single nomenclature is adopted throughout this document to identify the hybrid configurations. The latter is detailed in Figure 3.7. Its first letter denotes the type of sample: "B" refers to baseline samples, "L" to interlayer hybrids, "Y" to interyarn hybrids, and "C" to intrayarn hybrids. The following number indicates the configuration number. The combination of these two characters forms a unique identifier. The last letter tells whether the ply-block is symmetric or asymmetric (optional, for interlayer hybrids only). The following superscript is the low-strain FAW, and the subscript is the high-strain FAW. Finally, the preceding superscript corresponds to the low-strain volume fraction γ. Additionally to this terminology, the same color code and symbols are used for each figure.

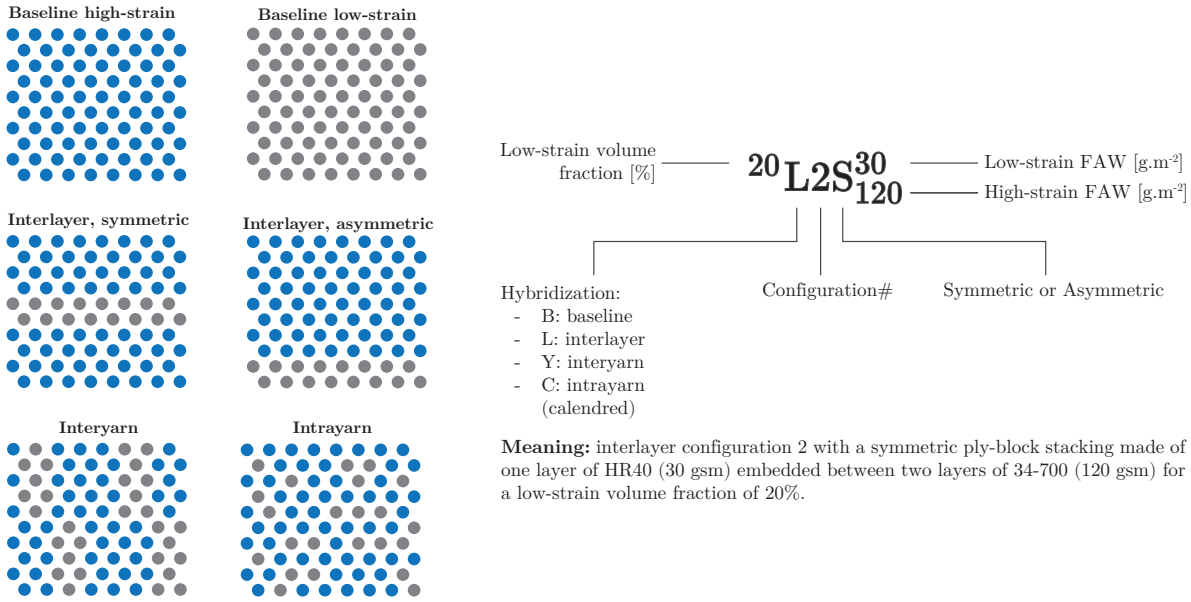

Figure 3.7: General nomenclature.

3.2 Experimental methods

This section introduces the experimental methods used in this thesis. First, the sample manufacturing is presented. Then the testing methods and material characterization techniques are discussed.

3.2.1 Manufacturing

Following the material selection exposed in section 3.1, UD Grafil HR40 and 34-700 thin-ply prepregs were used. The fibers were spread and pre-impregnated with TP415 rubber toughened epoxy resin by NTPT. The exact nominal FAW was $29\,\mathrm{g}\cdot\mathrm{m}^{-2}$ and $60\,\mathrm{g}\cdot\mathrm{m}^{-2}$, respectively. Note that in the case of the HR40 fiber, it corresponds to the lightest commercially available tape. The prepreg resin content by weight was 37 %.

In addition to these standard thin-ply tapes, interyarn and intrayarn prepreg developed in collaboration with Alexios Argyropoulos (other PhD student funded by Hyfisyn, working at NTPT) were received. The interyarns were produced by tow-by-tow spreading, aiming for a FAW of $90\,\mathrm{g}\cdot\mathrm{m}^{-2}$. Interyarns improve the fiber dispersion and the hybrid design space in terms of low-strain material ratio γ with respect to the ply FAW. The yarn dimensions are directly related to the FAW and tex of the tows. Here, the yarn width ranges from approximately 5 to 20 mm. It was not possible to reduce further this width. The intrayarns were obtained by calendering two very thin-ply of HR40 ($15\,\mathrm{g}\cdot\mathrm{m}^{-2}$) and 34-700 ($30\,\mathrm{g}\cdot\mathrm{m}^{-2}$ or $60\,\mathrm{g}\cdot\mathrm{m}^{-2}$). One key aspect of calendered thin-plies is that the tow-spreading does not have to be uniform as the tape uniformity is achieved when combining the two tapes (non-uniformity is actually even favorable to fiber dispersion). Therefore, the hybrid design space can be further optimized with very-thin plies. All the prepregs were supplied as 300 mm width rolls.

A QI stacking sequence was selected to characterize the laminate tensile properties as it is representative of practical applications and is sensitive to the in-situ strength effect. However, the $+45°$ and $-45°$ plies often trigger secondary dissipative damage in the laminate and are not suitable to study the dissipative mechanisms involved in the translaminar fracture process. CP laminates were therefore preferred for the CT tests. The $90°$ plies bring stability to the $0°$ plies[1], ensure a ply-confinement to enable the in-situ effect and have little influence on the translaminar fracture toughness as reported by Frossard [39]. Moreover, they avoid splitting when laid at the surface, which is beneficial for DIC.

Thus, QI laminates were produced with a $[45/0/-45/90]_{ns}$ stacking sequence and the CP laminates with a $[90/0]_{ns}$ stacking sequence. In QI, n was varied in such a way as to reduce as much as possible thickness variations between the samples. However, due to the different ply-block configurations, these variations are unavoidable. In the QI laminates, the $90°$ symmetry ply-block was not doubled to not introduce transverse dominated damage. In the case of an asymmetric ply-block architecture, the low-strain plies were removed at the symmetry plane to not induce residual stresses in the laminate. As the failure of a QI laminate is not dominated by $90°$ in the absence of transverse cracking, this should not influence the failure behavior. In CP plies, the symmetry was performed on the $90°$ ply as the translaminar toughness is dominated by the $0°$ ply.

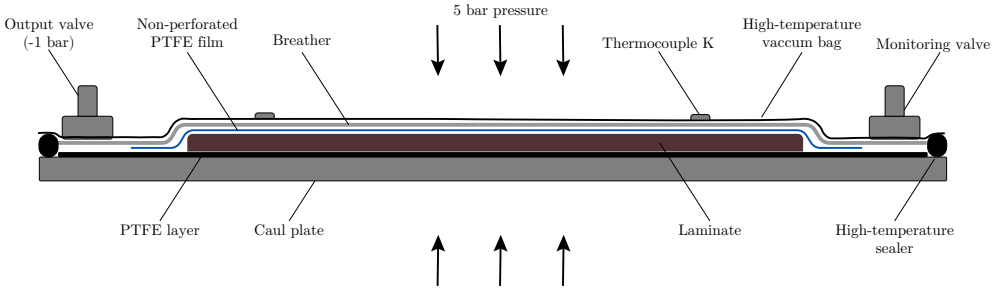

Figure 3.8: Autoclave curing procedure.

The laminates (300×300 mm) were stacked by hand-layup on an aluminum plate covered by a PTFE tape. Every two plies, a debulking of at least 10 min was achieved to remove entrapped air and ensure a flat stacking. For the thinner plies, the debulking was even performed for every ply as the compaction helped with the paper removal. Once stacked, a non-perforated PTFE film was applied to avoid resin leaking during the curing. A breather was then added with a high-temperature vacuum bag and sealer. The laminate was then debulked for at least 10 h. A 10 min drop test was systematically performed

[1] $0°$ plies are always aligned with the load in this work.

to check the vacuum bag sealing. Two thermocouples K were applied at the vacuum bag surface to monitor the temperature during the curing. The complete setup is described in Figure 3.8. The laminate was then cured in an autoclave adhering to NTPT recommendations as shown in Figure 3.9.

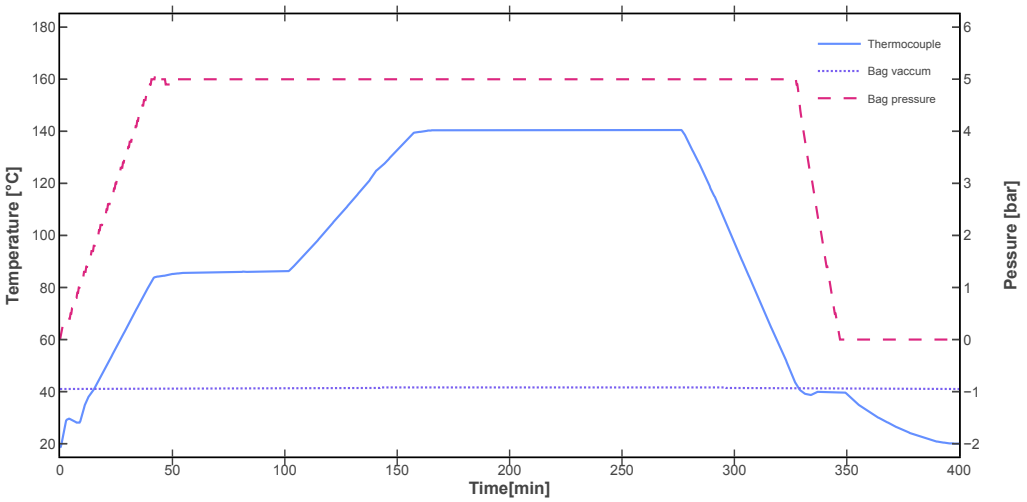

Figure 3.9: Autoclave curing cycle.

As highlighted by the micrograph reported in Figure 3.10, the aforementioned procedure achieved good quality laminates, without visible porosities at this scale. A fiber volume fraction V_f of 50 % was targeted. The effective volume fraction of each laminate was calculated according to its total FAW, as in Equation 3.6 [38]. The different samples characterized throughout this study were milled from the laminates by water-jet cutting. No significant cutting damage resulted from this procedure, as evidenced by optical observations and the CT-scan observations reported for instance in Figure 5.27.

$$V_f = \frac{\sum_n FAW}{\rho_f t_l} \tag{3.6}$$

ρ_l : fiber density

t_l : laminate thickness

Composite laminates are subjected to residual stresses [226], especially when cured at high temperature in an autoclave. They were estimated using eLamX^2 software [227] for a gradient of temperature of 125 °C, from the post-cure temperature to room temperature. In the absence of data for the thermal coefficient of expansion regarding the materials used in this work, the default values proposed by the software were assumed. Namely, it was set to $-5e^{-7}\,°C^{-1}$ for the fibers in the longitudinal direction, $1e^{-5}\,°C^{-1}$ in the transverse direction, and $6e^{-5}\,°C^{-1}$ for the TP415 epoxy. The elastic properties were obtained by Classical Laminate Theory (CLT). Thus, the values reported in Table 3.5 and Table 3.6 are approximations and should only be analyzed qualitatively.

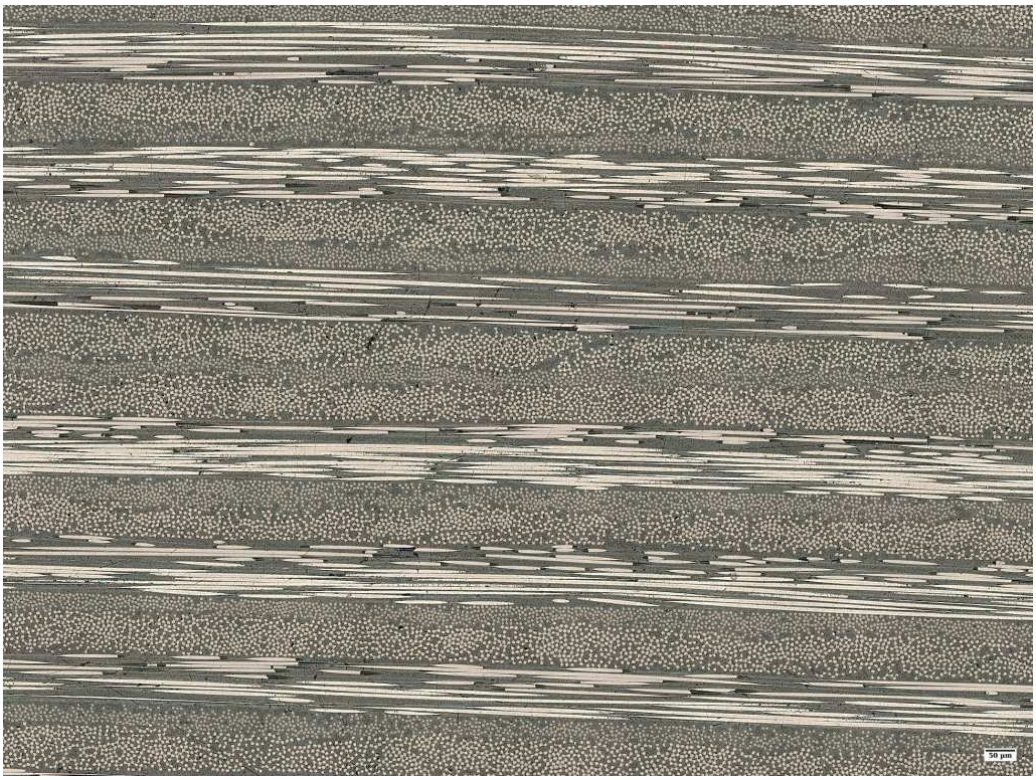

Figure 3.10: $^{33}\mathrm{L1A}_{60}^{30}$ micrograph centered onto the symmetric central ply-block. The two different shades of grey indicate the HR40 and the 34-700 fibers.

Overall, the residual stresses are predicted to be in the range of 20 to 50 MPa, which is similar to the values reported for other composites [226]. They represent 5 to 10 % of the expected laminate strength. The 0° plies are loaded in tension in the longitudinal direction, thus the effect on laminate strength is negative. Furthermore, it is worth noting that the mismatch of residual stress between the 0° ply-blocks and the 90° ply-blocks is much more important in asymmetric ply-block layups. Thus, it may further promote delamination and secondary damage in these laminates, but also reduce the onset of damage. Note that the results reported in the following chapters do not account for the residual stresses.

			Ply [MPa]		**Laminate [MPa]**	
Material	**Orientation**	**FAW**	**Longitudinal**	**Transverse**	**0° direction**	**90° direction**
34-700	0°	$120\,\mathrm{g}\cdot\mathrm{m}^{-2}$	25.3	−23.2	25.3	−23.2
HR40	0°	$60\,\mathrm{g}\cdot\mathrm{m}^{-2}$	46.4	−23.2	46.4	−23.2
34-700	90°	$120\,\mathrm{g}\cdot\mathrm{m}^{-2}$	16.9	−22.9	−22.9	16.9
HR40	90°	$60\,\mathrm{g}\cdot\mathrm{m}^{-2}$	32.3	−22.9	−22.9	32.3

Table 3.5: Residual stress predictions for $^{33}\mathrm{L3A}_{120}^{60}$ layup.

			Ply [MPa]		Laminate [MPa]	
Material	**Orientation**	**FAW**	**Longitudinal**	**Transverse**	**0° direction**	**90° direction**
34-700	0°	$60\,\mathrm{g}\cdot\mathrm{m}^{-2}$	21.4	−23.2	21.4	−23.2
HR40	0°	$60\,\mathrm{g}\cdot\mathrm{m}^{-2}$	39.9	−23.2	39.9	−23.2
34-700	0°	$60\,\mathrm{g}\cdot\mathrm{m}^{-2}$	21.4	−23.2	21.4	−23.2
34-700	90°	$60\,\mathrm{g}\cdot\mathrm{m}^{-2}$	18.2	−23.1	−23.1	18.2
HR40	90°	$60\,\mathrm{g}\cdot\mathrm{m}^{-2}$	34.6	−23.0	−23.0	34.6
34-700	90°	$60\,\mathrm{g}\cdot\mathrm{m}^{-2}$	18.2	−23.1	−23.1	18.2

Table 3.6: Residual stress predictions for $^{33}\mathrm{L4S}^{60}_{120}$ layup.

3.2.2 Translaminar toughness testing

The mode I translaminar toughness of the 0° plies G^0_{Ic} was characterized using the CT test described by Frossard [39] on CP laminates. G^0_{Ic} was then calculated from the CP laminate translaminar toughness using Equation 3.7 [51, 179, 228] where t^{lam}, t^0 and t^{90} are the laminate thickness, the total thickness of 0° and 90° plies, respectively. G^{90}_{Ic} corresponds to the mode I intralaminar toughness and was not characterized in this study and was neglected due to its limited influence. Indeed, the intrinsic mode I intralaminar toughness of 90° plies was shown to be at least one order of magnitude lower than the mode I translaminar toughness of 0° plies in M40JB-TP80ep samples [39]. Neglecting it in Equation 3.7 led to less than 2 % error. The same behavior is assumed in this work and the reported toughness values are the ones of the CP laminate.

$$G^0_{Ic} = \frac{t^{lam}G^{lam}_{Ic} - t^{90}G^{90}_{Ic}}{t^0} \tag{3.7}$$

As previously mentioned, the CT specimens ($60 \times 65\,\mathrm{mm}$) were produced by water-jet cutting according to the geometry reported in Figure 3.11 from a CP laminates with a 4 mm nominal thickness. As reported in section 2.4, alternative geometries may be more advantageous, but the possibility of direct comparison with the previous work of Frossard [39] was privileged. The specific circular cut at the beginning of the notch is used to mount a clip gauge. Initial cracks were machined in the specimens using a diamond wire with a diameter of 0.125 mm to achieve an initial length a_0 ranging from approximately 18 to 25 mm. This resulted in a ratio $\frac{a_0}{W}$ (see Figure 4.1a) ranging from 3.5 to 4.9, which is similar to the one adopted by many authors [39, 50, 51, 178, 186, 191]. The initial crack geometry was verified after milling by optical geometry, as depicted in Figure 3.12, and the exact dimensions of each sample are reported with the results.

Due to the laminate thinness (compared for instance to the 10 mm thick samples used by Frossard [39]), a numerical buckling study was performed to verify that the crack could propagate without

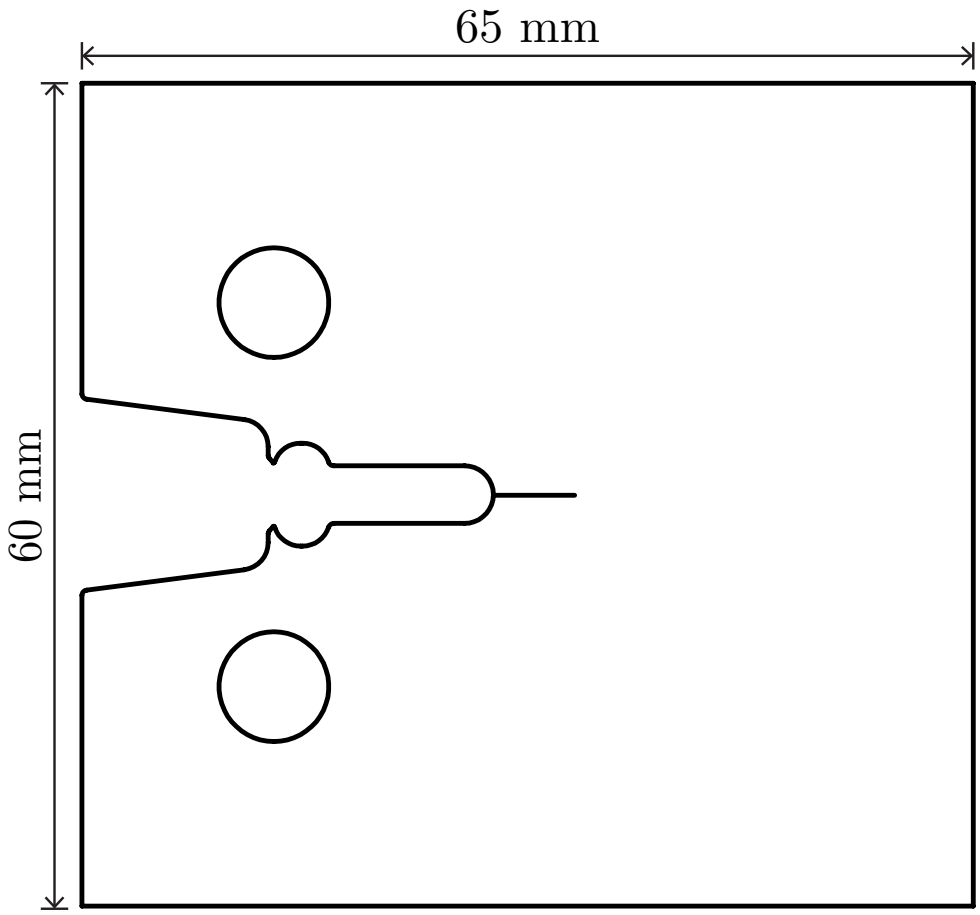

Figure 3.11: CT sample geometry.

risking buckling. In details, an eigenvalue buckling analysis was implemented in Abaqus to identify the critical load as a function of the crack length. The obtained values were compared to experimental ones measured during a preliminary testing. A safety margin of at least 50 % was achieved. This avoided the need for an anti-buckling device proposed by several authors [186, 191]. Using such a device would have complicated the full-field acquisition.

The displacement fields were monitored using a commercial stereo-DIC setup provided by Correlated Solutions. Image correlation was performed with Vic-3D [229] version 8.6.3 software. Good practices recommended by Correlated Solutions and in the literature [230] were adopted, but no further DIC optimization was performed. Pictures were acquired by two 5Mpx Grasshopper3 GS3-U3-51S5M cameras equipped with Schneider Tele-Xenar 2.2 70 mm focal lenses, placed at approximately 800 mm from the specimen and with approximately 60 mm between the two cameras, defining a stereo-correlation angle of 4°. The system calibration was achieved with the maximal aperture, and the aperture was then reduced to increase the depth of field. The exposure time was set to 10 ms and the acquisition rate to 2 Hz. The former allows for a loading rate up to $2\text{mm}\cdot\text{min}^{-1}$ without pixel blurring. While the latter may seem slow compared to the crack propagation dynamics, the critical ERR is evaluated just before the crack propagation. Therefore, no more than 500 ms elapses between the crack propagation

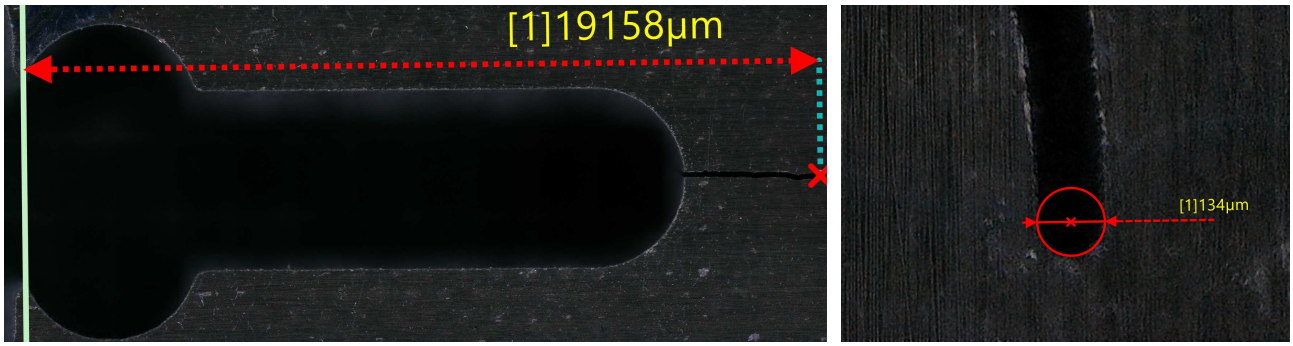

(a) **(b)**

Figure 3.12: Details of a CT specimen pre-crack with (a) the initial crack length a_0 and (b) the crack tip diameter.

and the picture acquisition. Considering the loading rate of 0.5 mm·min^{-1}, the error made on the displacement at the pins is, at worst, 4.16e^{-3} mm. It represents 2.1e^{-1} % of the typical displacement at which the crack starts to propagate (see Figure 4.10a).

A speckle was applied at the sample surface by spraying a thin layer of white matt acrylic paint followed by rubber stamping of black ink. An example is shown in Figure 4.9a. The rubber stamp from Correlated Solutions had a dot size of 0.18 mm and was applied several times with random orientations until more than 50% coverage was obtained (hence the obtained dots are roughly two times larger than the rubber stamp dot size). The DIC setup resulted in an average pixel size of about 33 µm. It corresponds to approximately 10 pixels per dot. Uniform lighting was obtained with two Nanlite LumiPad 25 panels.

A hybrid stereo calibration was performed within Vic-3D to reduce the uncertainty which was ultimately reported to be on average less or equal to 2.2e^{-4} mm and 3e^{-3} mm in and out of plane, respectively. An area of interest of approximately 35×60 mm was defined over the visible surface, excluding the loading fixtures but including the DIC. The visible crack path for which correlation is not possible was then discarded based on the correlation error. A subset size of 47 pixels, suggested by Vic-3D, was used with Gaussian weights, optimized 8-tap, normalized squared difference, and exhaustive search. This resulted in a distance of approximately 0.3 mm between each data point, totaling about 20000 points. Finally, displacement fields were post-processed to remove rigid-body motions and project them over the sample coordinate system.

Based on the data reduction challenges reported in chapter 2, a novel J-integral data reduction was implemented based on the J-integral approach. This data reduction method is described in detail in chapter 4.

3.2.3 Unnotched and open-hole tensile tests

QI laminates were used to characterize the UNT and OHT properties of the produced hybrids. The UNT tests were carried out following ASTM D3039 guidelines and especially the parameters used by Amacher et al. [38] and Cugnoni et al. [24] (at the difference of the stacking sequence which was $[45/90/-45/0]_{ns}$ in these works). The OHT tests were performed according to ASTM D5766-11 guidelines, but with a hole diameter to ratio of 5 instead of 6, due to manufacturing constraints.

The specimen dimensions were $250 \times 25 \times 2.5\,\text{mm}$ and are depicted in Figure 3.13. As for the CT specimens, stacking constraints led to an actual thickness ranging from 2.3 to 3 mm. $50 \times 25 \times 2\,\text{mm}$ aluminum tabs (EN AW-5005) were glued under vacuum with Sicomin Isobond SR7100 mixed with SD7105 hardener after a surface preparation by grinding, resulting in a gauge length of $150 \times 25\,\text{mm}$. Aluminum tabs were found to offer excellent performances in transmitting the load between the fixtures and the samples, and are more convenient to manufacture than the more traditional glass-epoxy tabs.

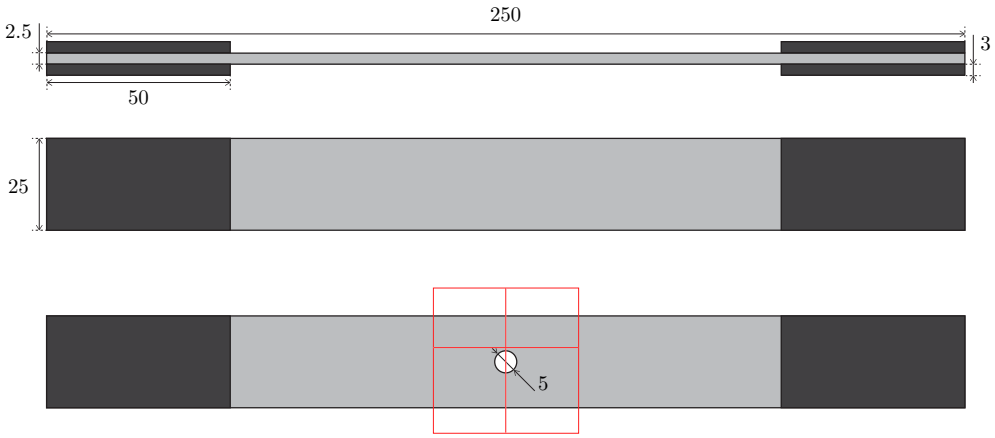

Figure 3.13: UNT and OHT sample geometries, including the aluminium tabs. The red lines depict the cut view analyzed in CT-scan images.

The UNT tests were performed on a MTS 809 hydraulic tensile machine, under monotonic displacement, at a loading rate of $2\,\text{mm} \cdot \text{min}^{-1}$. The strain was monitored with HBM 1-LY-41-6/120 strain gauges glued at the center of the sample with a cyanoacrylate adhesive (SCS Glue X2). The damage development was monitored by AE acquisition performed with an AMSY-5 dual-channel from Vallen Systeme equipped with two NANO-30 S/N749 probes. The probes were fixed at the two ends of the gauge length. Thus, Δt filtering was performed to reject the acoustic events occurring outside of the gauge length.

The OHT tests were carried out at the University of Bristol (United Kingdom) on a Instron 8801 hydraulic tensile machine, at a loading rate of $2\,\text{mm} \cdot \text{min}^{-1}$. The strain was monitored with a Strain

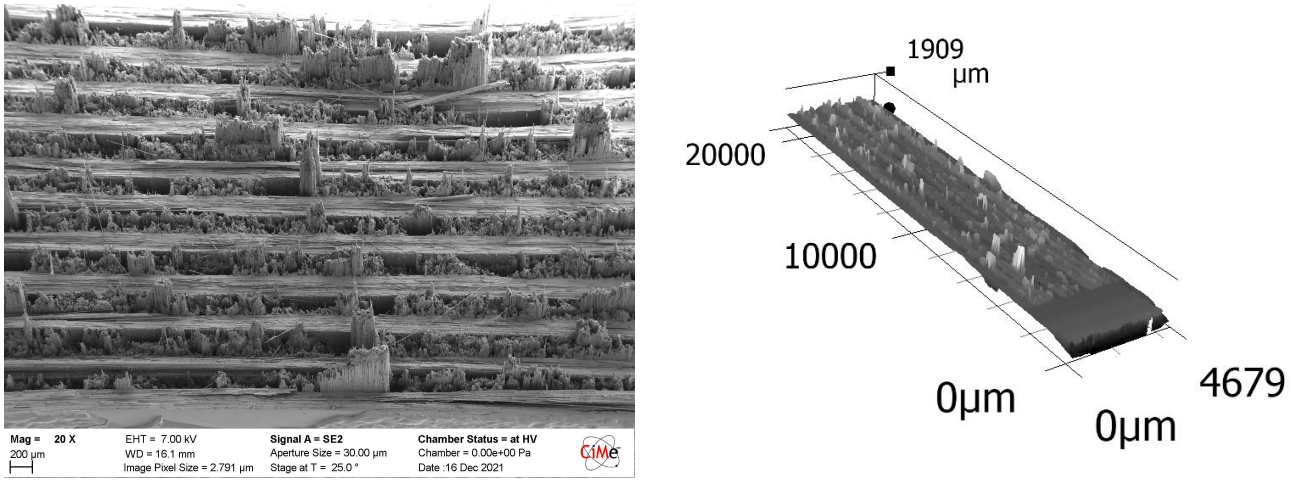

(a) **(b)**

Figure 3.14: Post-mortem fracture surface observations of $^{33}\text{L4S}^{60}_{120}$: (a) SEM observation and (b) optical microscopy observation. See Figure 3.7 for interpretation of the specimen nomenclature.

Master DIC system (LaVision). Interrupted tests were also achieved by loading the samples to 95 % of their strength, then unloaded and analyzed by CT-scan [192].

3.2.4 Fracture surface analysis

The pull-out length in CT specimens was investigated by analyzing the post-mortem fracture surfaces. SEM, confocal laser profilometry, and optical microscopy were explored. As highlighted in Figure 3.14a, SEM provides high-resolution qualitative information about the fracture surface. However, it is not suitable for a systematic quantitative analysis. In this regard, optical microscopy combined with stitching and depth composition features offers a better trade-off between scanning speed, size of the scanned area, and ease to derive quantitative data (see Figure 3.14b).
Figure 3.15 explains the post-mortem analysis strategy implemented in this work. The upper and lower fracture surfaces were observed under 200x magnification with a VHX-5000 Keyence optical microscope. The stitching feature along with the depth-of-field algorithm was used to map in 3D the fracture surfaces, resulting in approximately $20\,000 \times 4000\,\mu\text{m}$ surfaces, with a resolution of $1.055\,\mu\text{m} \cdot \text{px}^{-1}$ in the focus plane.

A typical crack profile is depicted in Figure 3.15 and illustrates the pull-out bundles observed at the crack surface. The profile appears asymmetric with respect to the crack plane. This is due to the failure of the optical microscope to resolve deep and narrow openings, due for instance to a lack of light. To mitigate this issue, both lower and upper crack surfaces were observed. The positive bundles observed at one surface are supplemented by the positive bundles observed at the other surface to form the complete crack profile.

In practice, a crack plane was manually defined using the same 90° plies for both surfaces. Positive

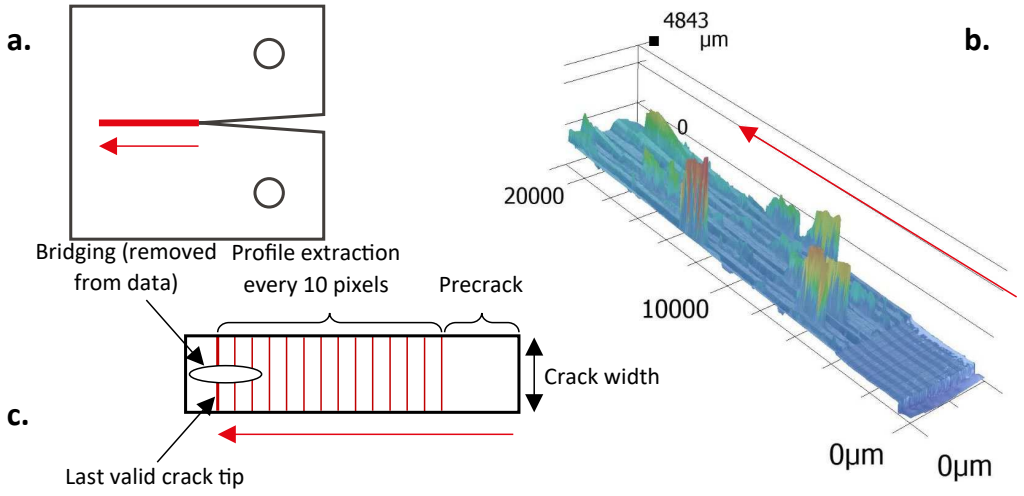

Figure 3.15: Typical fracture profile and simplified profile used to characterize pull-out bundles: (a) situation on the CT sample, (b) optical microscopy observation and (c) top view od the surface.

pull-out bundles were then measured with respect to this crack plane. Due to misalignments and optical artifacts, the profile matching from one surface to another is challenging. Each profile was thus treated as an independent observation. The resulting statistical descriptor is in fact only accounting for 50 % of the information. With this approach, matching the profiles is not required and the whole procedure can be automated but the information may be lost about the small pull-out bundles close to the crack plane, due to the incertitude regarding the crack position, and the distance between two consecutive positive and negative bundles.

A Python algorithm was implemented to match simple steps with the profile as depicted in Figure 3.15. Small features whose dimensions were below 50 µm were considered as noise and discarded. The height, width, and probability of step occurrence were used as statistical descriptors to characterize the pullout distribution for each material configuration. The developed lengths of the profiles were similarly aggregated to characterize the overall crack dimension.

3.2.5 In-situ computed tomography

Time-resolved Synchrotron Radiation Computed Tomography (SRCT) were performed on two baselines, one interlayer, and one intrayarn configuration to clarify the failure mechanisms related to the translaminar fracture of fiber-hybrid composites. The samples were produced based on the mini-protruded CT specimen geometry proposed by Ahmadvashaghbash et al. [184]. The tests were carried out by KU Leuven on their Deben CT500 in-situ rig equipped with a 500 N load-cell at the TOMCAT beamline of the Swiss Light Source (Paul Scherrer Institut, Villigen, Switzerland).

Chapter 4

J-integral data reduction methods

How to reduce the mode I translaminar toughness from Compact Tension (CT) tests?

Publication: this chapter is adapted from the paper "*Implementation and parametric study of J-integral data reduction methods for the translaminar toughness of hierarchical thin-ply composites*" submitted to Engineering Fracture Mechanics.

The list of available data, codes, and publications generated for this work is available on Zenodo [204].

As exposed in chapter 2, the accurate derivation of the mode I translaminar toughness from experimental data is not straightforward. Most of the methods proposed in the literature rely on very restrictive assumptions that are difficult to fulfill in composites or on indirect evaluation through FEM. In both cases, many pitfalls may lead to an erroneous interpretation of the experimental data.

The most robust and reliable approach for quantifying a physical quantity is to measure it directly, with as few assumptions as possible to not miss unexpected behaviors. In this sense, the experimental Compliance Calibration (CC) is ideal. Indeed, it directly uses the load, displacement, and crack length values from the CT test. As such, it captures all the CT failure mechanisms, including the non-linear ones. However, it requires a precise measurement of the crack length. This requirement is very challenging to fulfill in composites, especially in the presence of a large FPZ.

The J-integral is another approach for the direct reduction of the translaminar toughness. It has already been well-documented in the literature and, thanks to its conservative assumptions, it is suitable for a wide range of materials. However, behind the apparent simplicity of the J-integral equation, its implementation is challenging and not well documented. Furthermore, many authors reported experimental issues in measuring the displacement fields required by the J-integral.

In this chapter, it is proposed to investigate three different J-integral formulations for deriving the experimental translaminar toughness of composites from compact tension tests. An emphasis is placed on materials exhibiting large-scale FPZ. The three methods improve the existing approaches by taking advantage of stereo digital correlation to acquire full-field displacement fields. Noise issues reported in previous studies are addressed by a field fitting procedure based on robust and efficient piecewise cubic smooth splines.

Additionally, a novel crack tip extraction procedure is proposed to report the energy release rate as a function of the crack increment, even if knowledge of the crack tip is not required for the proposed J-integral method. The three methods are discussed in light of a parametric study conducted with both synthetic and experimental data, including artificially noisy data. The study reveals that the proposed J-integral methods are suitable for translaminar toughness evaluation of a wide range of materials without the need for restrictive assumptions. However, variations in the propagation values indicate that each formulation does not account for the fracture process zone in the same way. Finally, guidelines are drawn to support the algorithms proposed as a Python package.

4.1 J-integral implementation

This section introduces the theoretical background and the parameters required to derive the J-integral from a CT specimen whose displacement is monitored by DIC, regardless of the specific experimental setup. It also provides a rationale behind some details of the J-integral implementation as a Python script.

4.1.1 J-integral as a line integral formulation

The path-independent J-integral introduced independently by Cherepanov [196] and Rice [197] evaluates the potential energy change seen by an arbitrary enclosed region, assuming a homogeneous solid free of body forces and undergoing a 2D displacement field. When the enclosed region contains a crack, the J-integral may be used to quantify the potential energy accumulated before the crack propagation. It actually evaluates the energy required to propagate the crack, i.e., the material toughness.

The contour J-integral for a crack plane parallel to e_1 and perpendicular to e_2 (see Figure 4.1a) is formulated as in Equation 4.1, using the Einstein summation convention. Note that the crack length a is not required to derive the J-integral.

$$J = \int_\Gamma w de_2 - \int_\Gamma \sigma_{ij} n_j \frac{\partial u_i}{\partial e_1} ds \tag{4.1}$$

where:

i, j : planar cartesian indices

Γ : enclosing contour

w : strain density energy

σ : planar stress tensor
u : displacement field
n : outward unit normal vector along Γ
ds : infinitesimal arc length along Γ

Following Equation 4.1, no other assumption than material homogeneity is made. However, constitutive laws should be assumed to derive the strain energy density and the stress tensor. Here the J-integral is evaluated at the surface of a composite laminate. Therefore orthotropic properties and plane stress conditions are assumed.

$$w = \begin{bmatrix} \varepsilon_{11} & \varepsilon_{22} & 2\varepsilon_{12} \end{bmatrix} C \begin{bmatrix} \varepsilon_{11} \\ \varepsilon_{22} \\ 2\varepsilon_{12} \end{bmatrix} \tag{4.2}$$

$$\begin{bmatrix} \sigma_{11} \\ \sigma_{22} \\ \sigma_{12} \end{bmatrix} = C \begin{bmatrix} \varepsilon_{11} \\ \varepsilon_{22} \\ 2\varepsilon_{12} \end{bmatrix} \tag{4.3}$$

$$C = \frac{1}{1 - \nu_{12}\nu_{21}} \begin{bmatrix} E_1 & \nu_{21}E_1 & 0 \\ \nu_{12}E_2 & E_2 & 0 \\ 0 & 0 & G_{12}\left(1 - \nu_{12}\nu_{21}\right) \end{bmatrix} \tag{4.4}$$

DIC software usually provides the strain field ε. It is, however, the result of calculations made on the grounds of assumptions not always explicit and perhaps not adequate for this peculiar application. Furthermore, should the displacement field not be perfect and subject to noise, proper pre-processing is required before computing the strain. Therefore, in this work, it is preferred to directly derive the strain field from the displacement field, which, under small strain assumption, gives:

$$\varepsilon_{ij} = \frac{1}{2}\left(\frac{\partial u_i}{\partial e_j} + \frac{\partial u_j}{\partial e_i}\right) \tag{4.5}$$

While this formulation requires linearity over the evaluated contour Γ, the enclosed material may exhibit non-linearity, including, for instance, delamination or crack splitting. Since the J-integral is

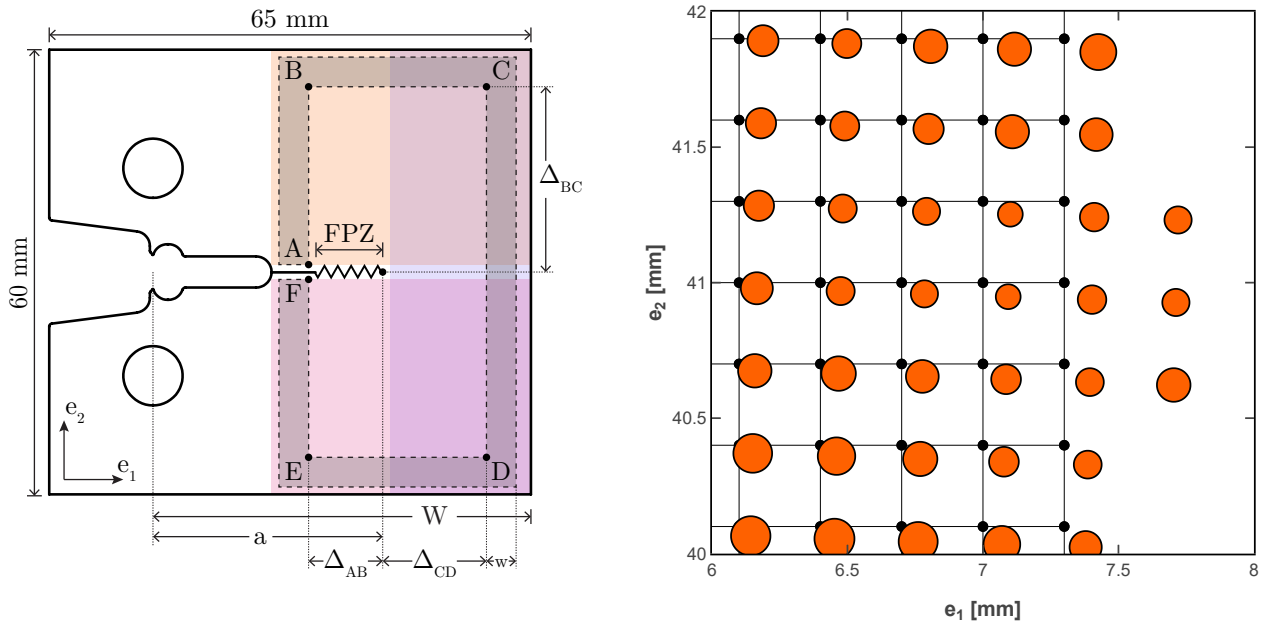

Figure 4.1: (a) CT sample geometry and parametrization of the J-integral contours depicted as the shaded area between dashed lines and the upper, lower, and post crack fitting area shown rectangles filled with different colors; (b) illustration of the misalignment between the data points obtained from DIC and the regular grid in sample's referential over which the data are interpolated. The circle diameter scales with the normalized distance to the first neighbor. The rightmost points are outside of the convex hull defined by the remaining ones and are not interpolated.

path independent, any arbitrary contour may be used. The J-integral is, therefore, convenient to characterize the toughness of composites that exhibit a complex FPZ, such as hierarchical thin-plies or thick-plies with extensive pull-out. In the proposed approach, a rectangular contour is used by convenience as depicted in Figure 4.1a. As the strain is formulated under the small displacement assumption, the contour is evaluated over undeformed coordinates. Thus, the path definition is not affected by the the specimen rotation, and the initial material orientation is used when deriving the stress tensors. Importantly, different constitutive laws may be assumed according to the considered material as, for instance, a quasi-isotropic laminate.

4.1.2 J-integral as a simplified line integral formulation

Frossard [39] proposed a simplified J-integral formulation valid when the contour is defined at the edges of the sample, noticing that normal stresses at free edges are null. In this case, σ_{11} and σ_{22} are null over segment CD and segment BC or DE, respectively, as illustrated in Figure 4.1a.

4.1.3 J-integral as a surface integral formulation

As proposed by Li et al. [231], the divergence theorem can be applied to Equation 4.1 to obtain a surface formulation as in Equation 4.6. This formulation has been successfully implemented by Becker et al. [201]. Here, q is an arbitrary smooth function that translates the inner contour by the unit length along the crack direction (i.e., e_1) and vanishes on the outer contour. It may be interpreted as

a virtual crack extension.

$$J = \int_A \left(\sigma_{ij} \frac{\partial u_i}{\partial e_1} - w\delta_{1j} \right) \frac{\partial q_1}{\partial x_j} dA \tag{4.6}$$

where:

i, j : planar cartesian indices
A : area defined by two enclosing contours
w : strain energy density
σ : planar stress tensor
u : displacement field
δ : Kronecker delta
q : smooth unit translation function
dA : infinitesimal surface

As shown in Equation 4.1 and Equation 4.6, only the elastic constant and the planar displacement field derivatives are required to apply the J-integral data reduction methods. The elastic constants are obtained from usual laminate characterization procedures or assumed from datasheets, while DIC is used to monitor the displacement fields at the sample surface. Implicitly, this approach assumes that the specimen surface displacements represent the homogenized material behavior. This assumption is reasonable as long the J-integral path does not include delaminated or damaged area. In practice, these conditions are met by using 90° outer plies the surface ply when the crack propagates, and defining a path far enough from the FPZ. It is worth noting that for material prone to extensive delamination, such as thick-ply composites, the delaminated area should be carefully monitored. Looking for anomalies in the in-plane and out-of-plane displacement or strain fields may serve this purpose.

4.1.4 Displacement derivatives calculation

Due to the derivative evaluation, the J-integral approach is very sensitive to displacement noise [201]. To overcome this shortcoming, the displacement fields are fitted by a piecewise cubic smoothing spline as proposed by Frossard [39] and Cugnoni et al. [24]. It is achieved with the algorithm proposed by De Boor [232] and implemented in the CSAPS Python package [233]. As cubic, it is twice continuously differentiable and adequate to calculate derivatives. The natural property ensures that the second derivative is null at the endpoint though this feature is not required for this peculiar application. This algorithm was preferred to Scipy [234] spline fitting methods for computational performances and for the ease of controlling the approximation made through the smoothing factor. This latter is a parameter in the range [0,1], where 0 corresponds to the least-squares plane fit and 1 to the natural cubic spline interpolant. Note that the smoothing parameter is normalized to ensure repeatability between different datasets [233]. Finally, the displacement fields above the crack are fitted separately

from those under the crack and those ahead of the crack to exclude the FPZ singularity as shown in Figure 4.1a.

The CSAPS algorithm interpolates and smooths splines over regular gridded data. In practice, the experimental displacement fields are usually not obtained over a suitable grid. For instance, Vic-3D outputs the results in the camera basis defined by the pixel matrix, which differs from the sample frame of reference as highlighted in Figure 4.1b. Moreover, once mapped over the sample frame of reference, the displacement field is not regular anymore. A pre-fitting operation is therefore required to interpolate the data over a regular grid. Here, it is achieved with the griddata method from Scipy package [234]. The grid step size is chosen to minimize the distance between the DIC points and the grid points. This approach effectively deals with missing data points as long they are inside the convex hull defined by the set of input points. Otherwise, the missing points are not extrapolated to avoid edge effects, and the grid size is reduced in order to be enclosed inside the convex hull.

4.1.5 Crack tip identification

As exposed in subsection 4.1.1 and chapter 2, the crack length a is not involved in the J-integral derivation, and its measurement is not critical. The ERR is nonetheless traditionally reported in the literature as a function of the crack increment Δa. Moreover, the crack tip position was used to define the J-integral contour in the context of this study. The crack tip definition is ambiguous in the presence of a large FPZ, especially if based on manual optical observation interpretation. Thus, a bias-free method is required to obtain an objective measure of the crack length. For instance, approaches based on the strain field or local rotational field around the crack tip have been successfully used in the literature [199].

Here, an effective crack length is defined based on the COD profile extracted from the displacement fields. First, it is proposed that the upper and lower COD profile can be linearly fitted far enough from the crack tip and that their intersection is a point that moves with the crack tip but is usually located slightly farther. Thus, the position increment of this intersection can be seen as a good approximation of the crack length increment Δa between two frames. This approximation is later corrected as in Equation 4.7 to account for the non-linearity of the COD near the crack tip. This correction scales the error committed on the crack length by the J_{Ic} value. In practice, the correction term is evaluated for the initial crack length a_0, which is known.

$$a_{intersec}^{corrected} = a_{intersec} - \left(a_{intersec}^{init} - a_0\right) \cdot \frac{\sqrt{J_{Ic,i}}}{\sqrt{J_{Ic}}} \tag{4.7}$$

The COD profile should be extracted as close as possible to the crack plane while avoiding the noise due to DIC edge effects and the zone affected by the crack tip. As a consequence, its extraction implementation is iterative. A more straightforward approach involves identifying the inflexion point introduced by the crack tip in a displacement profile evaluated parallel to the crack plane. The inflexion point position along e_1 is little affected by the position e_2 at which the displacement profile is

evaluated and this method is therefore easier to implement. The displacement profile is extracted at an arbitrary distance e_2 from the crack plane and fitted with a piecewise cubic spline to evaluate its second derivative.

These methods address the crack tip identification in the propagation direction referred to as e_1 in this document. The identification in the e_2 direction is achieved by calculating the midpoint between the CT upper and lower arm center of rotation, which are identified by querying the minimal $||u_1 u_2||$ value. Note that the ERR may be reported more advantageously as a function of the COD δ [186]. In this case, the COD is directly monitored with a clip gauge or by DIC measurement.

4.2 Numerical validation

4.2.1 Data generation

This section investigates the validation and robustness of the line, simplified, and surface J-integral previously formulated. Synthetic DIC data were generated using a compact tension test FEM implemented in Abaqus 6.19 (Dassault-Simulia)[1]. The analysis features a shell-element model of the 60×65 mm specimen used experimentally and whose geometry is reported in Figure 4.1a. A 2 mm symmetric controlled displacement was imposed at the loading holes through kinematic coupling.

The singularity was introduced as quarter-point nodes (collapsed elements with a node parameter of 0.25) with a single crack-tip node, see Figure 4.2a. The model was meshed with CPS8R elements using the free advancing front algorithm and a global size of 0.2 mm, resulting in an average distance to the first neighboring node of approximately 0.1 mm. The material properties were defined as an homogenized orthotropic CP laminate, representative of an experimental specimen (see for instance Table 5.1). The displacement fields were extracted at each node, down-sampled with a 0.3 mm step size to account for the experimental results presented in this work, and fed to the J-integral algorithm, similarly to a DIC result. The 20, 30, and 40 mm crack lengths reported in Figure 4.2b exhibit a FEM J-integral of 145.2, 65.1, and 34.6 $kJ.m^{-2}$, respectively. Note that these values correspond not to actual crack propagation but to the J_I values for a given applied displacement.

The displacement fields were additionally contaminated with additive white Gaussian noise to account for more realistic data. For this purpose, error values were drawn from a zero-mean normal distribution and added to each displacement component at each node. The distribution standard deviation was set to the standard deviation of the correlation errors reported in experimental DIC setups. Namely, $2.2e^{-4}$ mm and $1e^{-2}$ mm standard deviations were used. The former is valid for the experimental setup described in this work for which high-resolution cameras were used to monitor a regular CT specimen, while the latter is an extrapolation to sub-optimal conditions such as an OCT sample with standard

[1]The Python script used to generate the model is available along with the Python package for reproducibility purposes [235]. The figures presented in this thesis were obtained with version v1.0.0-alpha.1.

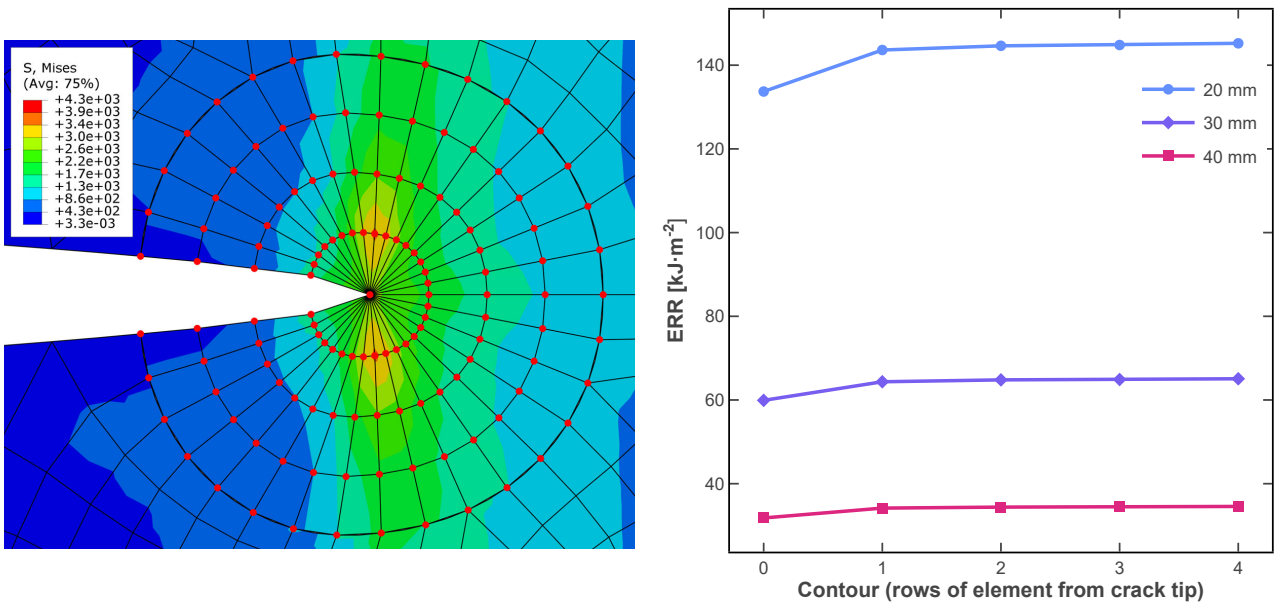

(a) **(b)**

Figure 4.2: (a) Details of the contours used to compute the FEM J-integral and (b) FEM J-integral results that converge quickly when moving away from the crack tip.

resolution cameras.

Note that this noise generation suffers from a few shortcomings. First, the noise is generated for each individual component, whereas the confidence interval is reported as an overall magnitude. Thus, the generated noise is likely to be overestimated. Second, the noise is only applied to the displacement fields. Finally, this procedure does not account for the spatial distribution of the noise, which is likely with a DIC experimental setup, for instance when the lighting conditions are not truly uniform. Nevertheless, it provides valuable insights into the robustness of the J-integral algorithm.

4.2.2 Results

Crack tip identification

The intersection and inflexion procedures were applied to the synthetic data to identify the crack tip position as illustrated for the 30 mm crack length in Figure 4.3a, Figure 4.3b, and Figure 4.3d. Specifically, both u_2 and $||u_1 u_2||$ fields were used for the inflexion method. A Monte-Carlo approach was used with 100 draws to account for the noise variability. The estimations reported in Figure 4.3c were overall well-aligned with the true crack tip position.

Under optimal conditions, i.e, no noise or $2.2e^{-4}$ mm standard deviation noise, the inflexion method error was bounded by the grid data step size. Here, this error was less than 0.3 mm. As expected, the intersection approach overestimated the crack tip position, here by approximately 2 mm. However, the error on the crack length was reduced to less than 0.5 mm after correction according to the initial offset and J_I influence (see Equation 4.7).

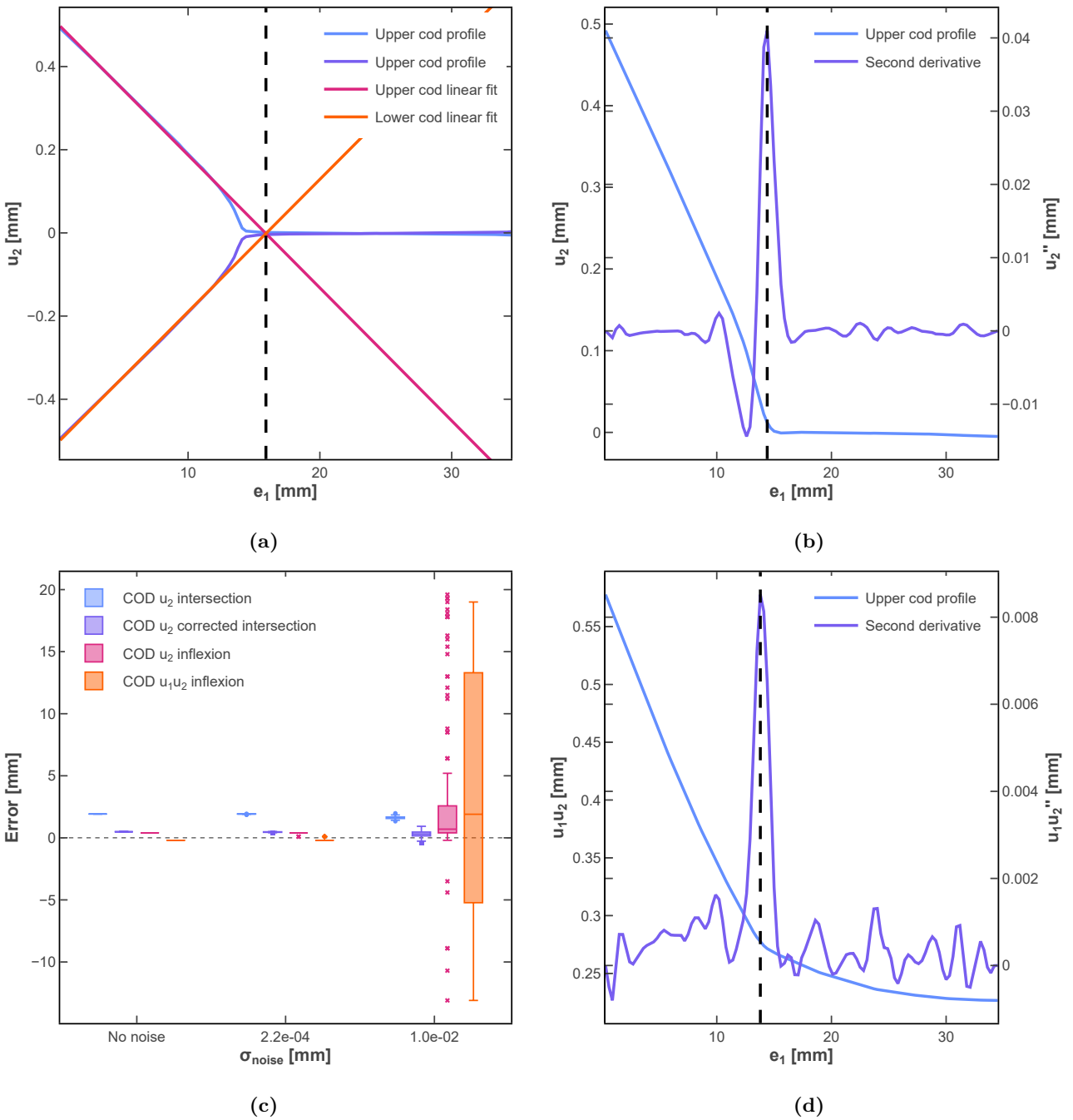

Figure 4.3: (a), (b) and (d) Crack tip identification for the 30 mm crack length case using intersection method over u_2, inflexion method over u_2 and u_1u_2, respectively; (c) Distribution of the error made on the crack tip position for each method obtained with 100 Monte-Carlo draws, as a function of the artificial noise.

Under sub-optimal conditions, i.e, $1e^{-2}$ mm standard deviation noise, the inflexion methods predictions were heavily scattered over the whole range of data along e_1 direction. The high-level noise was the source of sharp local variations in the displacement field which led to the presence of the maximal second derivative at random locations. Thus, these methods still require further refinements, such as noise filtering, to be suitable when working with noisy data. On the other hand, the intersection method was very robust under sub-optimal conditions as the mean error remained below 0.5 mm with

an interquartile range of 0.3 mm.

These findings result in recommending the inflexion methods as the best choice when ideal measurement conditions are feasible. Indeed, they provide a fast and direct estimation of the crack tip position and are convenient to implement. In comparison, the intersection method is implemented as a more complex iterative procedure that identifies the proper COD profiles and converges toward an intersection value. Furthermore, applying Equation 4.7 to calculate the correction term and obtain an accurate crack tip position implies deriving the J-integral at least two times, the first time with a guess value to approximate the crack length and the second time to evaluate J_I with a contour adequately defined. However, the corrected intersection method is more robust and more suitable in practice, as shown in section 4.3.

Data fitting

Data fitting is arguably a crucial step when applying the J-integral reduction methods. The choice of the smoothing value used by the CSAPS algorithm has a significant effect on the result as reported in Figure 4.4. The error made on the J_I value, defined as $error = \frac{J_{I,DIC} - J_{I,FEM}}{J_{I,FEM}}$ (here DIC refers to the synthetic DIC data), was represented as boxplots function of the smoothing value for 2.2e^{-4} mm noise. The remaining noise values produce similar results which are reported in Appendix A (see Figure A.1 and Figure A.2).

Overall, the three J-integral algorithms provided an accurate J estimation with less than 5% error for any smoothing value between 1e^{-2} and 5e^{-1}. In detail, smoothing is beneficial in the presence of noise, even under optimal conditions. Indeed, a smoothing value of 1 corresponds to the natural cubic spline interpolant, which passes through each data point and fully captures both the noise and the rough nature of the discrete displacement field. Thus significant errors are made when evaluating field derivatives. However, the error increases when reducing the smoothing value too much (thus tending towards a linear interpolation).

Qualitatively, a too-important smoothing effect fails to capture the local variations of the displacement fields, especially at the symmetry line of the CT specimens. On the other hand, the local variations are superseded by noise levels and smoothing is beneficial even if small field variations are lost (see Figure A.2). Thus, a trade-off value of 1e^{-1} will be used. This value is only valid for this specific dataset. A convenient method to control that the smoothing value is adequate is to plot the fitting surface, as in Figure 4.9b, to evaluate overfitting or underfitting qualitatively. For a quantitative validation, a convergence study of the J-integral value as a function of the smoothing parameter should be performed as in Figure A.2.

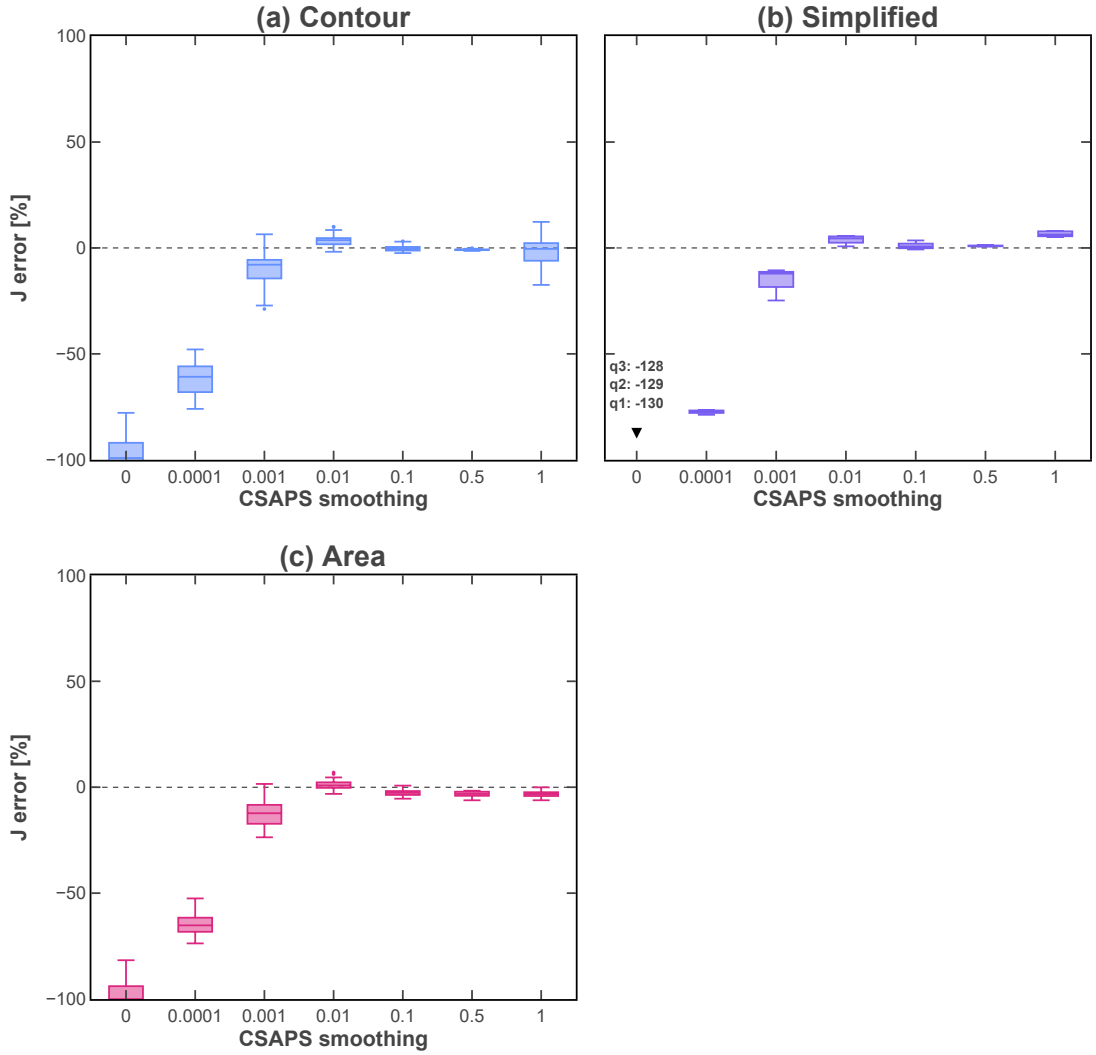

Figure 4.4: Boxplots of the error committed on the J-integral results evaluated at a safe distance from the crack tip, as a function of the csaps smoothing value ranging from 0 to 1. Noise with 2.2e^{-4} mm standard deviation.

J-integral evaluation

A key property of the J-integral approach is path independence. Theoretically, J-integral evaluations over any contour enclosing the FPZ yield the same result. However, in practice, the results are affected for instance by edge effects, numerical singularities, and noise. Thus, a comprehensive numerical study of the path parametrization (see Figure 4.1a) is proposed.

The three J-integral methods were evaluated over all the successive contour from the crack tip to the sample edges by taking discrete values for offsets Δ_{AB}, Δ_{BC}, Δ_{CD}, Δ_{DE}, Δ_{EF} and surface width

(for line and simplified algorithm, the width is always null, see Figure 4.1a). The contours were kept symmetric with respect to the crack, thus Δ_{AB} is equal to Δ_{EF} and Δ_{BC} is equal to Δ_{DE}. This was done for the 30 mm crack length case as the crack tip is approximately at the middle of the crack propagation range.

Violin distributions [236] of the J-integral error as a function of these offsets are provided in Appendix A. Under no noise or 2.2e^{-4} mm noise conditions, the three approaches performed similarly and provided distributions well centered around the true value for the majority of considered offsets (see Figure A.3 to Figure A.8). The only caveat was to avoid contour close to the crack tip, and to a lesser extent close to the sample edges, except for the simplified formulation that predicted correct results only when segments BC and DE are close to the sample edge. Here, 5 mm from the crack tip and 2 mm from the sample edges could be considered appropriate distances.

With high-level noise (see Figure A.9 to Figure A.11), the distributions were more scattered with aggravated edge effects but remained centered within a few percent of the FEM value. The surface algorithm was the most robust one. Increasing the width of the surface integral tended to reduce the scattering at the cost of slightly underestimating the FEM value. The distributions also highlighted that Δ_{CD} had minimal effect on the results and could safely be set to an arbitrary value.

The detailed effect of offsets Δ_{AB} and Δ_{BC} was then investigated while Δ_{CD} and surface width were both fixed to 6 mm. The J-integral error as a function of offset AB and offset BC is reported as contour maps for line, simplified, and surface algorithms under no noise, 2.2e^{-4} mm noise and 1e^{-2} mm noise (Figure 4.5, Figure 4.6 and Figure 4.7, respectively). The maps clearly highlight the crack tip influence when offset Δ_{AB} was too close to the crack tip (close to 0 mm), as shown by the strong gradient of J-integral values.

Interestingly, the offset BC value had almost no significant effect. An investigation of the J-integral terms reveals that the main contribution for segment BC was by far traction forces $-\sigma_{22}\frac{\partial u_2}{\partial e_1}de_1$. In this numerical study, the variation of displacement u_2 along e_1 direction was little impacted by the crack tip. Thus, the position of segment BC was not significant. It also explains why Δ_{BC} value significantly affected the simplified formulation, as σ_{22} is only null at the sample edges. Note that the FEM did not account for the mechanisms such as fiber pull-out. Thus segment BC might require to be evaluated further from the crack tip in an experimental setup.

Overall, the three methods were robust. They provided results within 10% error and path independence when contour offsets were set to appropriate values as depicted in Figure 4.5 to Figure 4.7 by shaded black rectangles. These results are aligned with the ones reported by Becker et al. [201] and Bergan et al. [186] when comparing the surface and the line J-integral with FEM results, respectively.

Under sub-optimal conditions, the noise was found to aggravate the crack tip detrimental influence,

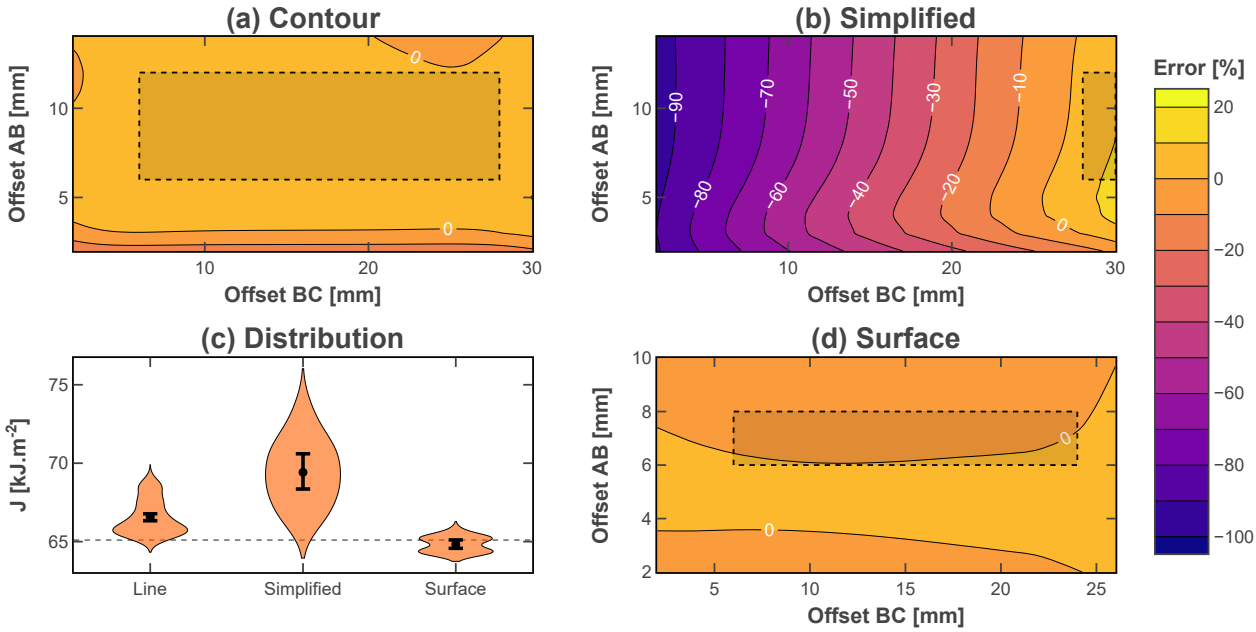

Figure 4.5: Contours of the error incurred by the J-integral algorithm with respect to the FEM J-integral value, as a function of offsets Δ_{AB} and Δ_{BC} using (a) line, (b) simplified, and (d) surface methods, without noise. (c) Corresponding violin distributions obtained after constraining offsets Δ_{AB} and Δ_{BC} to the recommended range represented as a shaded black rectangle. The points stand for mean values and the error bars for the 99% confidence intervals obtained by bootstrapping over $1e^5$ iterations. The violin distributions are not normalized by the number of points for better readability.

and J-integral results need to be evaluated further from it. The maps also reveal that the line J-integral suffered from oscillations when the noise was significant, without clear indications that would help identify the correct value (see Figure 4.7). The oscillations seemed to follow a spatial pattern which may be related to the oscillations of the fitting splines. The surface algorithm was the most robust one. However, the surface width limited the number of possible contours. In contrast, the line method was evaluated over many more contours, leading to artificially thinner confidence intervals.

No correlation was found between the J-integral result and the cumulative nor the mean noise seen along the integration contour. It suggests that noise has an indirect effect on the J-integral, for instance, though derivative errors that would be affected both by the noise values and their spatial distribution.

As the simplified formulation yielded correct results only when segment BC was defined at the specimen edges, the same investigation was conducted with cropped data. Indeed, the displacement fields can not be extracted at the edges with a DIC system and are, in practice, cropped. It is reported that cropping the data by 2 mm had little effect on the simplified value, with at most 2% difference. In this case, the most important source of error was the absence of data itself as the simplified J-integral validity decreased with the distance to the sample edge. Therefore, according to Figure A.4, Figure A.7c and Figure A.10, the DIC data may be cropped up to approximately 5 mm while still

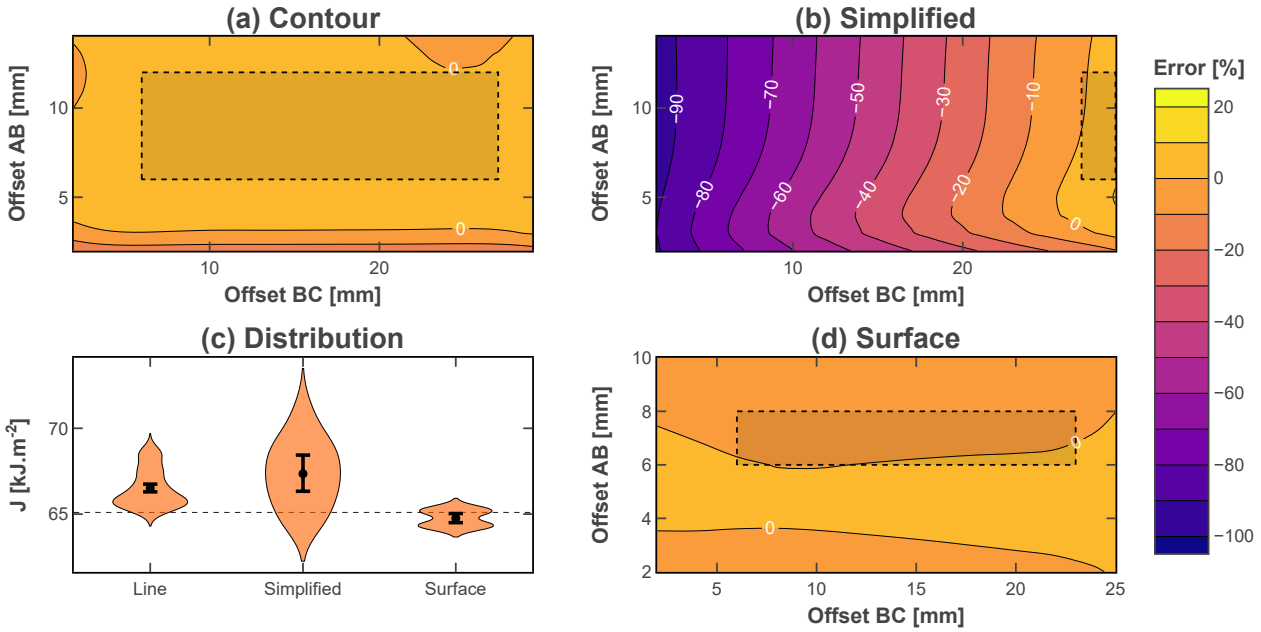

Figure 4.6: Contours of the error incurred by the J-integral algorithm with respect to the FEM J-integral value, as a function of offsets Δ_{AB} and Δ_{BC} using (a) line, (b) simplified, and (d) surface methods, with a 2.2e^{-4} mm standard deviation noise. (c) Corresponding violin distributions obtained after constraining offsets Δ_{AB} and Δ_{BC} to the recommended range represented as a shaded black rectangle. The points stand for mean values and the error bars for the 99% confidence intervals obtained by bootstrapping over 1e^5 iterations. The violin distributions are not normalized by the number of points for better readability.

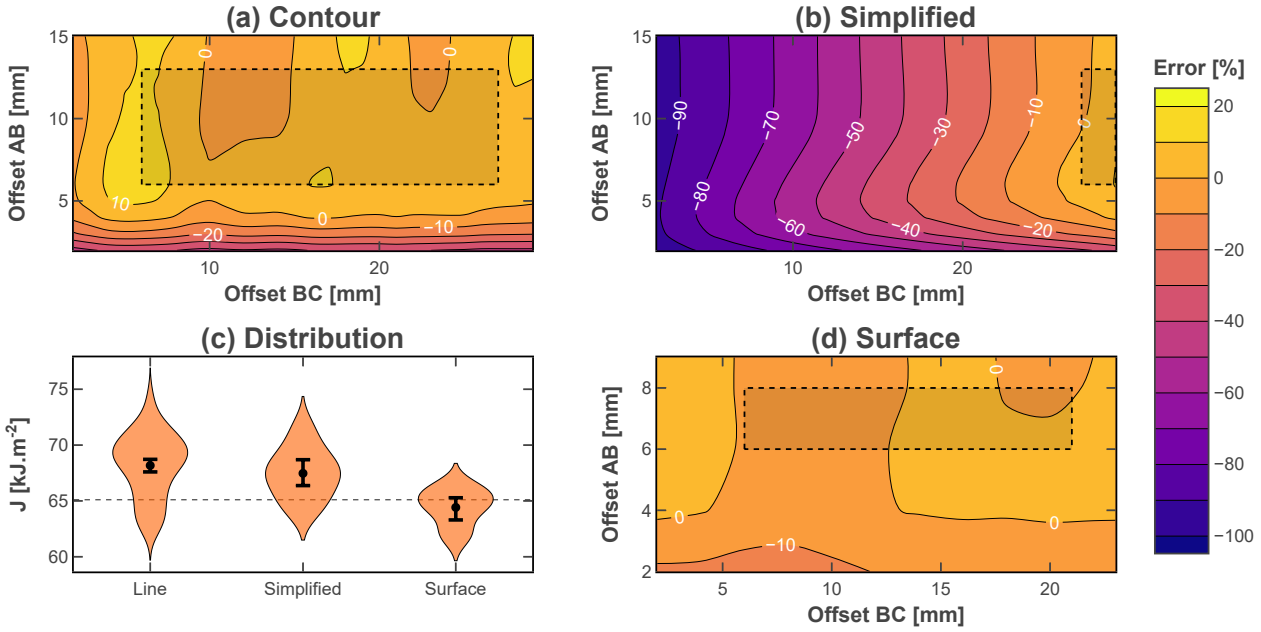

Figure 4.7: Contours of the error incurred by the J-integral algorithm with respect to the FEM J-integral value, as a function of offsets Δ_{AB} and Δ_{BC} using (a) line, (b) simplified, and (d) surface methods, with a 1e^{-2} mm standard deviation noise. (c) Corresponding violin distributions obtained after constraining offsets Δ_{AB} and Δ_{BC} to the recommended range represented as a shaded black rectangle. The points stand for mean values and the error bars for the 99% confidence intervals obtained by bootstrapping over 1e^5 iterations. The violin distributions are not normalized by the number of points for better readability.

providing results within 10% error.

4.2.3 Discussion

Using synthetic displacement fields generated by an Abaqus FEM, all three J-integral methods have been shown to be reliable, even if the data are severely affected by noise. To achieve these results, the J-integral should be evaluated far enough from the crack tip and use a suitable smoothing value. In this numerical study, offsets Δ_{AB} an Δ_{BC} of 5 mm and a smoothing value between $1e^{-2}$ and $5e^{-1}$ were found to be a sound choice. However, these values may be affected by experimental parameters like the FPZ size or the number of DIC points. They should therefore be checked for any given application. To do so, plotting the J-integral results as a surface response function of contour offset values is convenient for detecting steep gradients indicating the displacement field's local perturbations.

The FEM does not account for an FPZ but only for an idealized crack tip. However, the overall path independency of the J-integral indicates that it should remain valid if (i) the FPZ is encompassed by the J-integral path and (ii) the J-integral can be evaluated far enough from the FPZ. This could be verified numerically by further improving the FEM with, for instance, a cohesive law to account for an FPZ.

The simplified J-integral and the surface J-integral perform better than the line J-integral in the sense that they are less sensitive to noise under sub-optimal conditions. However, no physical criterion was identified to identify the correct J-integral values when the algorithms oscillate between multiple outputs. Sampling the results over a range of offsets far enough from the FPZ and the sample edges addresses this issue, as the mean value was shown to be very well correlated with the FEM value. In this way, the line J-integral sensitivity to noise is compensated by the possibility of evaluating it over a great number of contours. On the other hand, the simplified formulation surface response exhibits very steep gradients. This means that the results can only be evaluated on a few points, which increases the risk of undetected errors.

Given these observations, it is proposed as good practice to systematically evaluate the J-integral over all available contour offset combinations and report the mean and the confidence interval. When using the simplified method, the segment BC should be evaluated as close as possible to the data edges (and thus the sample edges). In this study, an offset Δ_{BC} was found suitable from 2 mm before the maximal value to the maximal value. Using these guidelines, results were found to be in good agreement with the FEM values obtained for each crack length as depicted in Figure 4.8. In the event that the three algorithms do not agree, the surface formulation can be considered the most robust. However, surface integration incurs by far the highest computational cost. As it is shown in section 4.3, the line J-integral averaged over several contours provides very similar results and offers the best trade-off between toughness evaluation performances and computational cost.

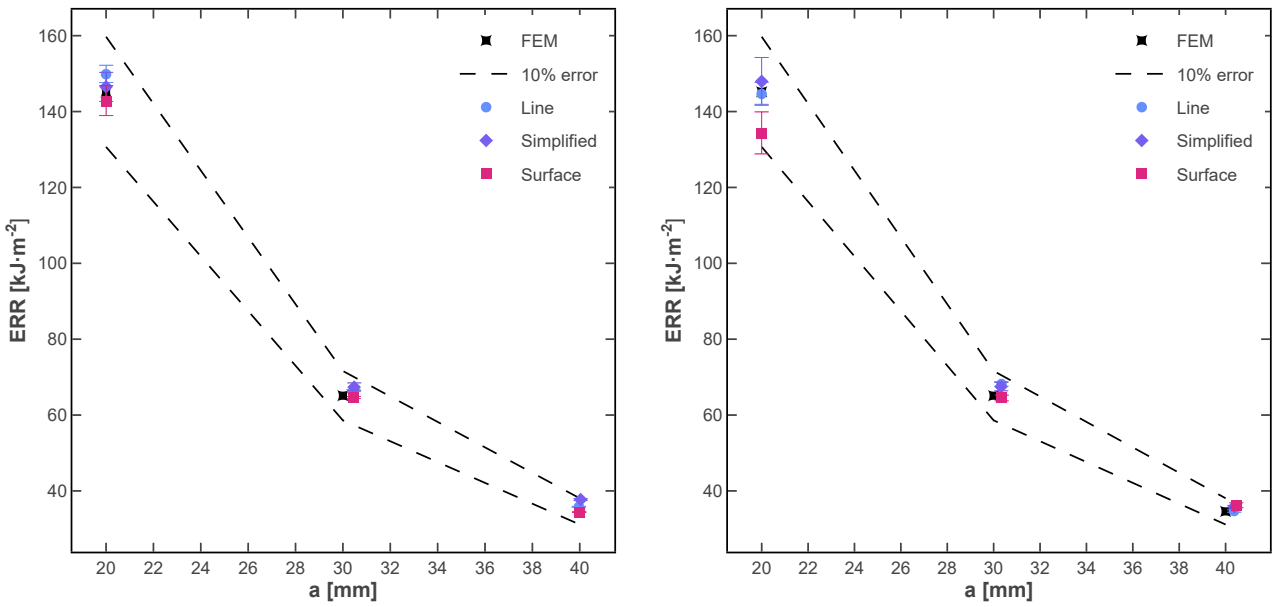

Figure 4.8: J-integral results obtained for the 20, 30, and 40 mm crack-lengths implemented in Abaqus with (a) $2.2e^{-4}$ (b) and $1e^{-2}$ mm standard deviation noise. The crack tip position was estimated with the inflexion method for the former and the corrected interception method for the latter. Notice that with the corrected interception method, errors made on the J value for the initial crack length are propagated when estimating the crack length of the subsequent points.

4.3 Experimental validation

4.3.1 Experimental methods

This section discusses the application of the J-integral data reduction methods described in section 4.1 and validated against synthetic data in section 4.2 to an experimental dataset. The following account is based on the experimental results reported in chapter 5. Baseline ${}^{0}\mathrm{B}4^{0}_{180}$ has been chosen to illustrate the methodology. Indeed, this laminate is in the intermediate to thick-ply range. As such, it exhibits a large FPZ, but without non-linearities or secondary damage that would make the interpretation of the results more controversial. Notwithstanding, every specimen tested in this work could be discussed in the same way. A typical CT sample with its speckle is reported in Figure 4.9, along with an illustration of the fitted displacement field for ${}^{0}\mathrm{B}4^{0}_{180}$. For the record, the sample and laminate properties are listed in Table 5.2 and Table 5.1, respectively.

4.3.2 Results

In the following subsections, the detailed results are reported for sample C ($a_0 = 24.5\,\mathrm{mm}$). Similar findings were observed for the remaining samples. Sample C exhibited a typical CT load-displacement curve reported in Figure 4.10a. The load drops were used to identify the frames just before the crack propagation. Due to the frame acquisition rate, it was often required to rather analyze the previous frame, either because the crack was visually already propagated or the picture was blurred by the

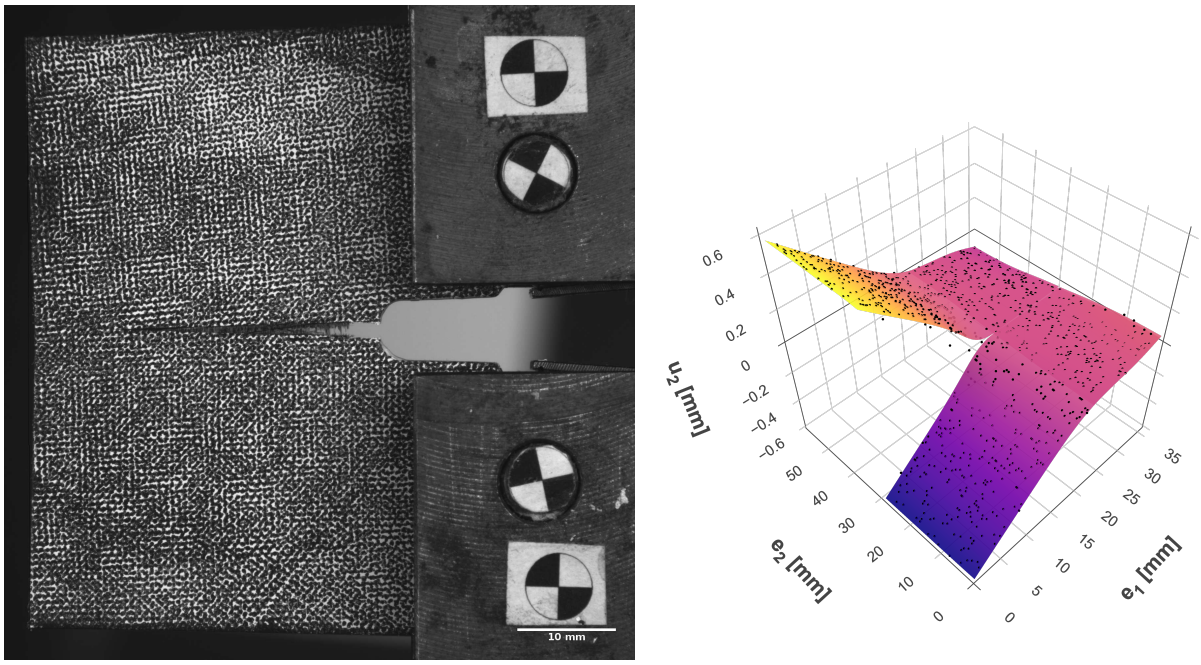

(a) (b)

Figure 4.9: (a) Illustration of a typical CT specimen with its speckle obtained by rubber stamping; (b) Sample C experimental fitting surfaces obtained with a smoothing value of $1e^{-1}$.

crack propagation dynamic. As previously discussed, this has little impact on the result.

Crack tip identification

The crack tip position estimations computed for each critical frame are shown as a function of the applied load in Figure 4.11a. The crack lengths obtained by optical observation of the crack surface are also reported. Overall, the load decreased with both the crack length and sample compliance increase, as expected [51]. On the other hand, the three first propagation points exhibited a different behavior where the load increased with the crack length (see Figure 4.10a). This behavior, which was not observed for every sample, may be caused by an inappropriate initial crack tip radius. However, the crack propagation was reported to be notch independent as long the radius is less than 250 µm for cross-ply IM7/8552 CT specimens [178]. The apparent stiffness increase may thus be related to the development of the FPZ in association with an R-curve effect.

Regardless of this finding, the intersection and inflexion methods are in relatively good agreement with optical observation, as shown in Figure 4.11b, except when using $||u_{2D}||$ field. The latter was found to be more affected by sharp gradients when inspecting the second derivative. Especially, the corrected intersection method values were particularly close to the optical ones with less than 1 mm difference. Thanks to the use of 90° plies at the sample surface, the crack front position at the sample surface could be identified without introducing too much bias. Thus, one may consider the corrected intersection method as a proper indicator of the surface crack position for this material. Furthermore, the COD profile taken far enough from the crack tip is the same at the sample surface and in the bulk

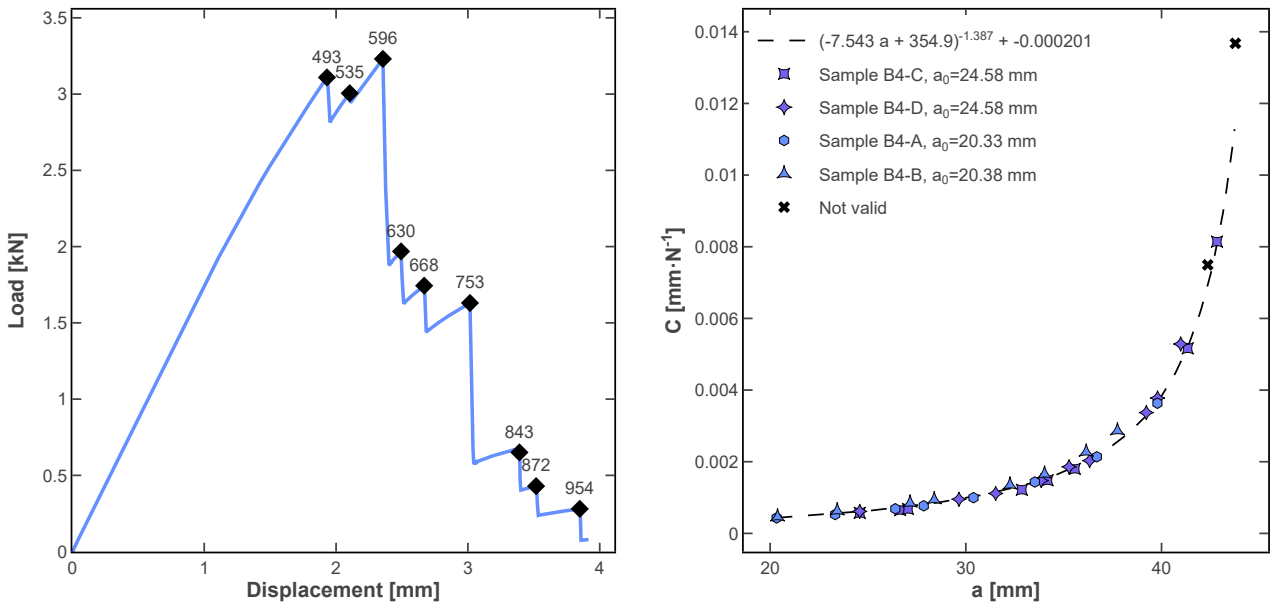

(a) **(b)**

Figure 4.10: (a) Typical load-displacement curve (sample C), a black marker indicates that a given point is used for the J-integral analysis and the corresponding DIC frame number is reported; (b) Compliance calibration.

material. Therefore, this method provides an estimation of the average crack front position, which is a better crack tip descriptor than the surface crack tip. X-ray computed tomography could be used to confirm this assumption as in [192]. Consequently, the corrected intersection method was used to estimate the crack tip position in the following results.

J-integral evaluation

A satisfying fitting of the experimental data was achieved with a smoothing value of $1e^{-1}$ (see Figure 4.9b). As highlighted by Figure 4.12a, experimental samples may undergo a slight out-of-plane displacement. This out-of-plane displacement, which may reach up to 10% of the planar displacement (Figure 4.12b) was not interpreted as buckling but rather as the consequence of slight fixtures misalignment. Indeed, they may induce torsion due to the thinness of the sample. As the out-of-plane displacements remained confined at the free corners of the sample, the test was considered to still be valid.

However, J-integral results were severely affected if the evaluation contour, especially segment AB or EF encompassed an area with out-of-plane displacements. For instance, notice in Figure 4.13a that there was a strong J_{Ic} gradient when Δ_{AB} spanned from 9 to 16 mm with respect to the crack tip. This range corresponded specifically to the sample area undergoing out-of-plane displacements. Therefore, the guidelines expressed in section 4.2 were supplemented to restrain, if possible, the J-integral evaluation to contours with less than 0.1 mm out-of-plane displacement, as represented by the shaded black rectangle in Figure 4.12a and Figure 4.13. Additional ill-behaved cases have been observed and reported in the supplementary information (Figure A.12 and Figure A.13), the same

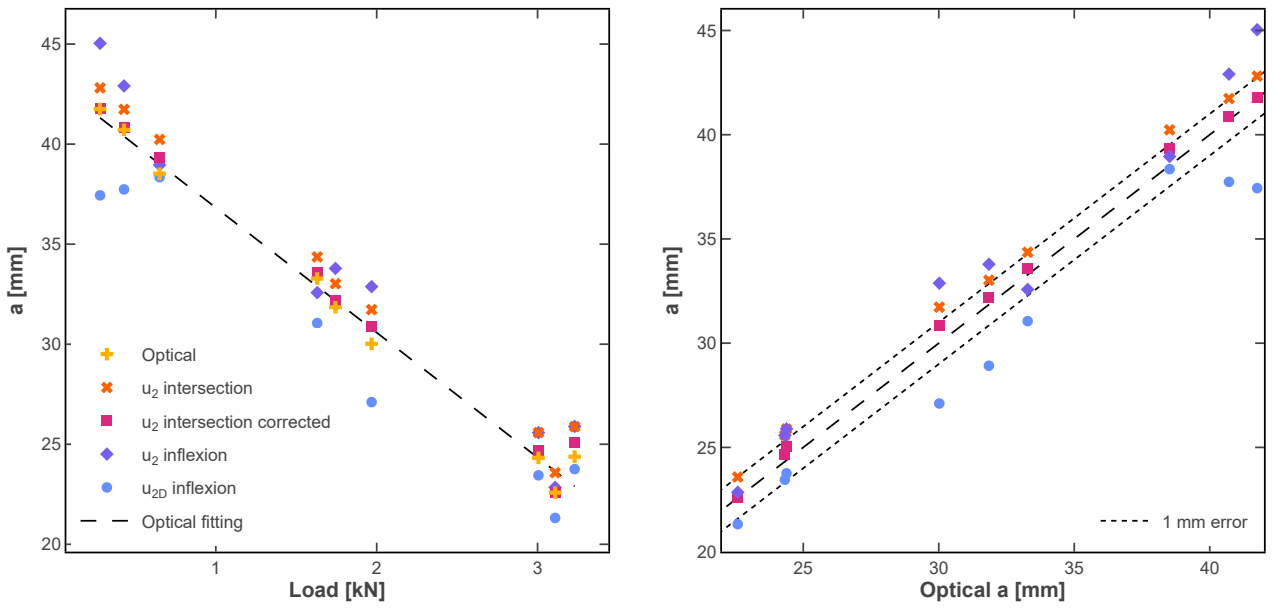

(a) (b)

Figure 4.11: (a) Crack length measured by different methods as a function of the applied load for sample C, and (b) comparison of these methods with respect to optical observations.

approach of defining a contour that did not pass by the problematic area was applied.

Applying these guidelines to frame 630 of sample C, the line and surface J-integral methods yielded results in good agreement, slightly lower for the surface J-integral (see Figure 4.13c). The surface J-integral formulation was the most robust one. The line J-integral produced more scattered results, but this was compensated by the fact that it could be evaluated over a broader range of offsets and averaged. Comparatively to these two methods, the simplified J-integral predicted roughly 5% larger results. These results were in good agreement with the numerical study (see section 4.2). The same procedure was then carried out for each sample.
Additionally, a comparative compliance calibration (CC) was carried out as in [51]. The equation $C = (M_1 \cdot a + M_2)^{M_3} + C_0$ was fitted over the experimental compliance corrected by the setup compliance as reported in Figure 4.10b, as a function of the crack length a obtained by the corrected intersection method. The resulting ERR are presented in Figure 4.14. They confirmed that the line and surface J-integral yield almost identical results for both initiation and steady-state J_{Ic}. As highlighted in the figure, the steady state ERR $J_{Ic,ss}$ seemed to be affected by the initial crack length. For instance, it was observed that according to the line J-integral, $J_{Ic,ss}$ increased by 31.2% from $a_0 = 24.6$ mm to $a_0 = 20.4$ mm. The initiation $J_{Ic,i}$ also increased by 19.7%, but too few experimental points are available to conclude.

It was also observed that both the simplified algorithm and CC accounted for the same behavior, but with an increase of respectively about 10% for the initiation value and about 30% for the steady state value compared to the line or surface J-integral. This contrast was found for all the samples presented

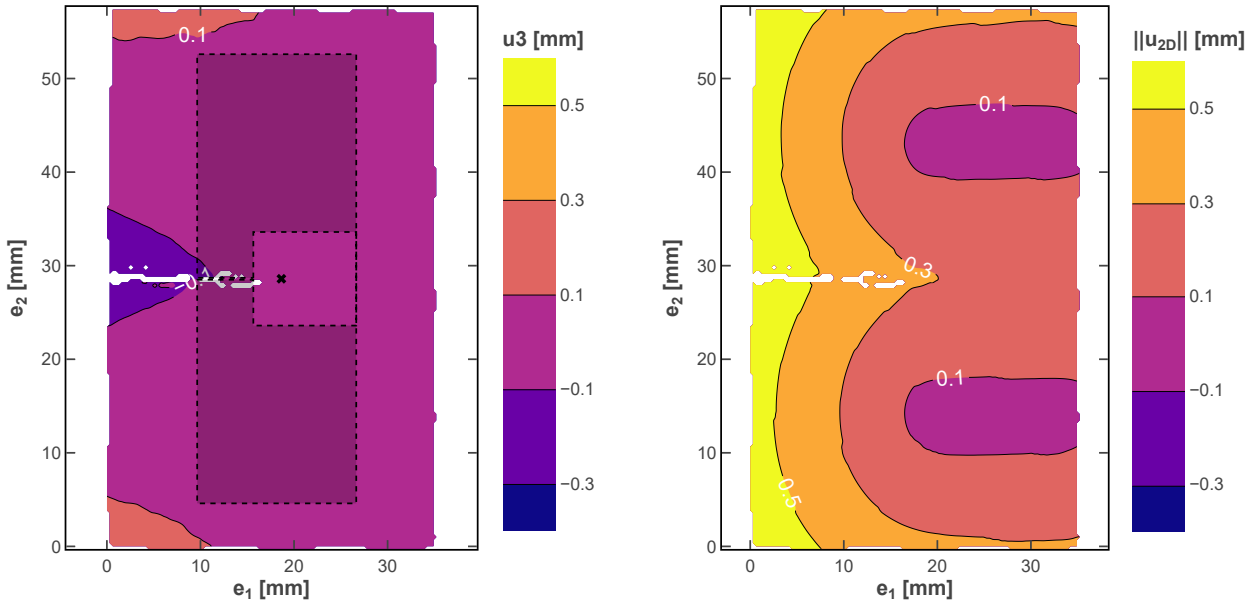

(a) **(b)**

Figure 4.12: (a) Out-of-plane displacement and (b) in-plane displacement norm monitored by DIC for frame 630 of sample C.

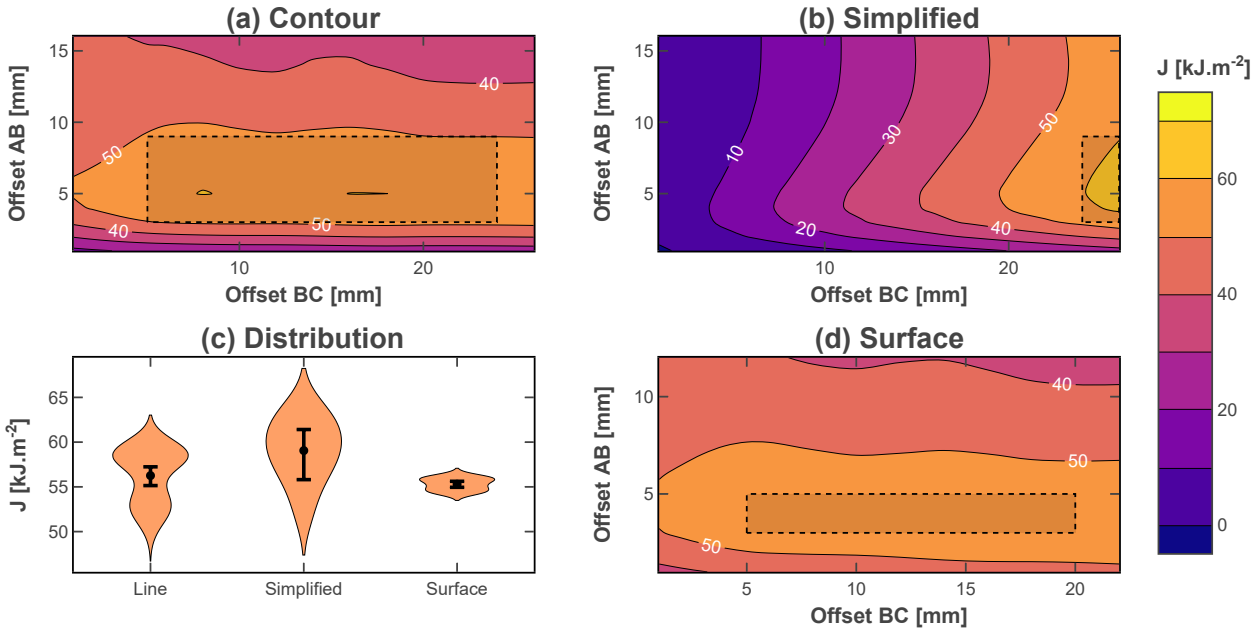

Figure 4.13: Contours of the J-integral values for frame 630 of sample C as a function of offsets Δ_{AB} and Δ_{BC} using (a) line, (b) simplified and (b) surface methods. (c) Corresponding violin distributions obtained after constraining offsets Δ_{AB} and Δ_{BC} to the recommended range represented as a shaded black rectangle. The points stand for mean values and the error bars for the 99% confidence intervals obtained by bootstrapping over $1e^5$ iterations. The violin distributions are not normalized by the number of points for better readability.

in this work.

Assuming that the FPZ is primarily the result of pull-out in the crack wake, an ERR plateau is reached when the FPZ grows to its maximum potential length. As such, plausible l_{FPZ} were reported in Figure 4.14. Due to the limited number of points before the plateau, the true l_{FPZ} might be different, especially for the line and surface J-integral, which are affected by an outlier value at a Δa value of approximately 3 mm. Nevertheless, the FPZ size extrapolated from the J-integral R-curve is of the same order of magnitude as the observed size of the zone affected by pull-out in Figure 4.15.

The toughness values reported in this work are for a CP laminate. For the sake of completeness, it should be mentioned that the translaminar toughness of 0° plies can be calculated a posteriori applying the RoM already defined in section 3.2 and recalled in Equation 4.8 [51, 179, 228], where t^{lam}, t^0 and t^{90} are the laminate thickness, the total thickness of 0°, and 90° plies, respectively. J_{Ic}^{90} corresponds to the intrinsic mode I intralaminar toughness of 90° plies. In M40JB-TP80ep samples, it was shown by Frossard to be one order of magnitude lower than the mode I translaminar toughness of 0° plies [39]. Neglecting it in Equation 4.8 led to less than 2 % error. Following the same logic, the translaminar toughness obtained with the line J-integral is approximately 129 kJ.m^{-2} at initiation and 171 kJ.m^{-2} at propagation.

$$J_{Ic}^{0} = \frac{t^{lam} J_{Ic}^{lam} - t^{90} J_{Ic}^{90}}{t^{0}} \tag{4.8}$$

4.3.3 Discussion

Four CT specimens have been tested to characterize the translaminar toughness of a laminate that exhibits a large FPZ through extensive pull-out. The three J-integral methods have been successfully applied to derive the ERR. Among them, the line and surface yielded very close results and revealed an effect of the initial crack length a_0 on the steady-state ERR $J_{Ic,ss}$. Even if the few replicas call for caution, the contrast is significant and suggests that it is possible to reach a longer FPZ associated with a greater $J_{Ic,ss}$ when a_0 decreases. Therefore, the observed plateau can be interpreted as a virtual upper limit, corresponding to a stop in the development of the FPZ due to the sample size rather than as a true material property.

Interestingly, the simplified J-integral values were overestimated, similar to those obtained by compliance calibration. Maimí et al. [188, 194] previously reported the same contrast between R-curve and J-curve for high toughness samples. Then the same conclusion may be reached, that the compliance calibration tends to overestimate the ERR when the sample is too small compared to the FPZ size, but more data are required to confirm it. The compliance calibration relies on the LEFM theoretical frame, and while its validity is questionable when working with large FPZ, the compliance was obtained experimentally in this work and should capture the FPZ contribution.

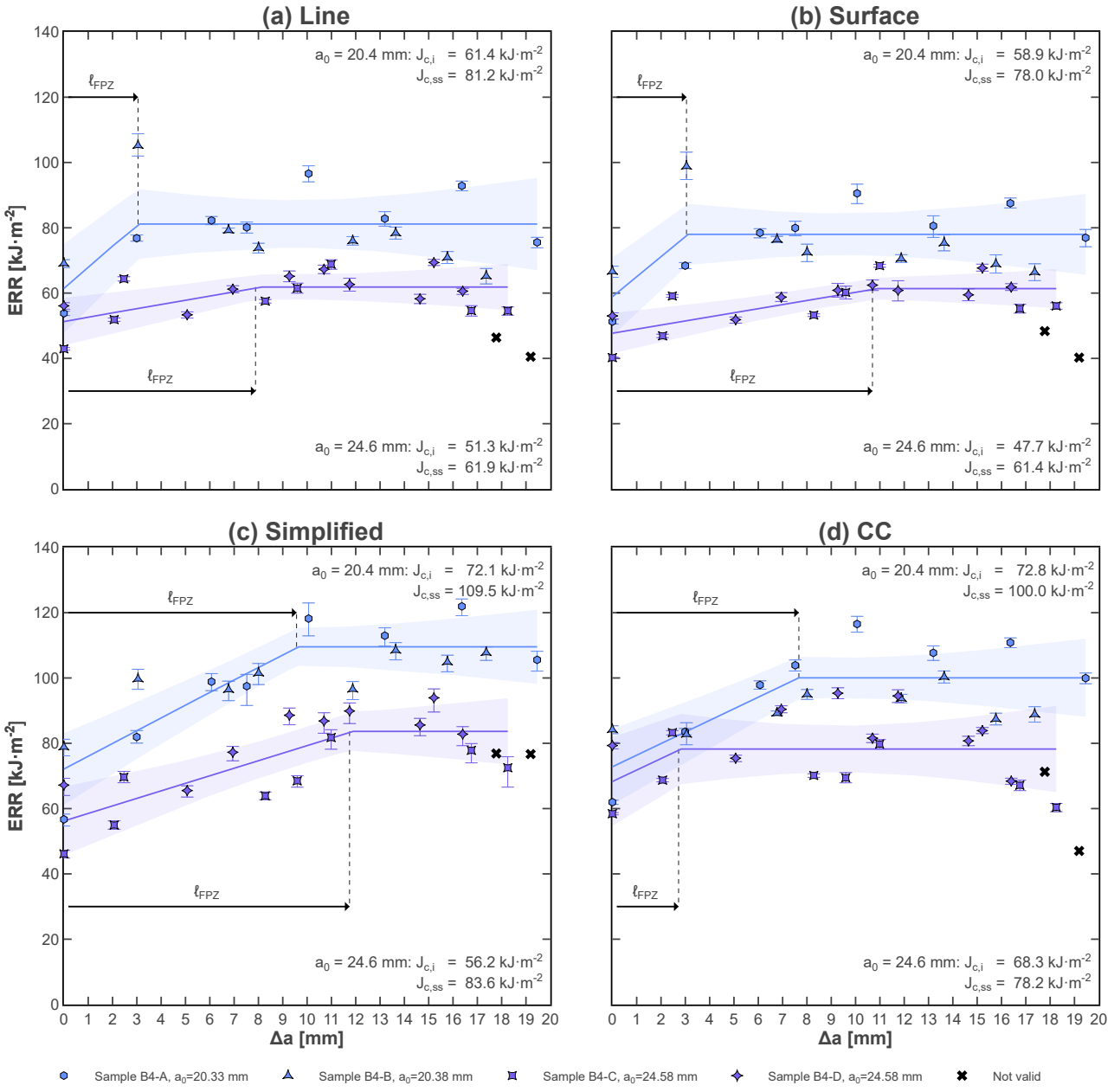

Figure 4.14: Experimental ERR J_{Ic} for which a linear piecewise function has been fitted. The error bars stand for the confidence interval of each individual point while the bands stand for the confidence interval of the fitting, determined assuming a Student law.

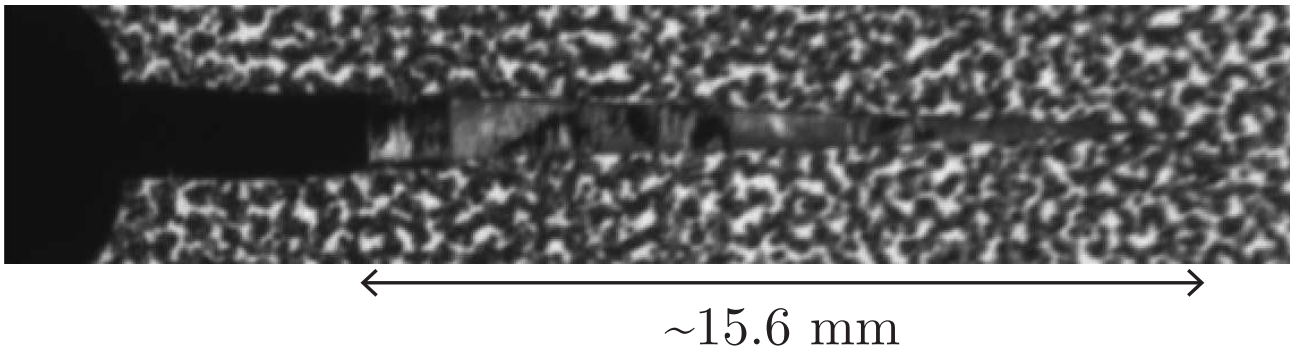

Figure 4.15: Detailed view of fiber pull-out in the wake of the crack.

On the other hand, the J-integral methods have been shown to be reliable in section 4.2, and the displacement fields are of satisfactory quality. Only elastic constant values used in this work could explain the contrast as they were derived by classical laminate theory. However, applying the same calculation to a quasi-isotropic laminate yielded a modulus of 43.9 GPa, in excellent agreement with the experimental value measured as 44.7 ± 1.7 GPa. Following these arguments, the last possible cause is the crack length a measurement required to derive the compliance. The challenge of defining and measuring a, which increases as the FPZ gets larger, may very well explain the observed contrasts. Moreover, inaccurate measurement of a has a more significant impact on smaller samples as the change of compliance is proportionally more important for a given crack increment.

It is worth noting that the simplified J-integral values were found to be close to those calculated by compliance calibration, although no causal link has been established. The experimental results gathered in this investigation do not permit conclusions to be drawn about the most accurate J-integral method. However, the line and surface formulations provide similar results, although their formulation and implementation are significantly different. This observation indicates that they are more suitable than the simplified formulation. The latter adds the traction-free assumption, which overestimates the J-integral results compared to line and surface approaches, possibly due to edge effects, especially in an experimental setup where the sample edges are likely to undergo out-of-plane displacements. These considerations suggest that the displacement field perturbations or fitting errors close to the edge of the specimens are important factors that affect the J-integral calculation methods.

A FEM representative of the experiment, capturing the material toughness through cohesive elements, was implemented as detailed in section 7.3 to provide perspective on these results. Note that the traction-separation laws were formulated to capture a $J_{Ic,i}$ and a $J_{Ic,ss}$ of approximately 60 kJ.m^{-2} and 80 kJ.m^{-2}, respectively. Simulation increments were analyzed with the line and simplified J-integral from the first load drop to simulate the discrete nature of the experimental crack propagation. In addition, the compliance calibration method was applied based on the crack lengths measured with the corrected intersection method. As shown in Figure 4.16a, the line J-integral and the compliance calibration correctly captured the laminate toughness. However, the simplified formulation significantly overestimated the values. Intriguingly, the J-integral did not capture the R-curve

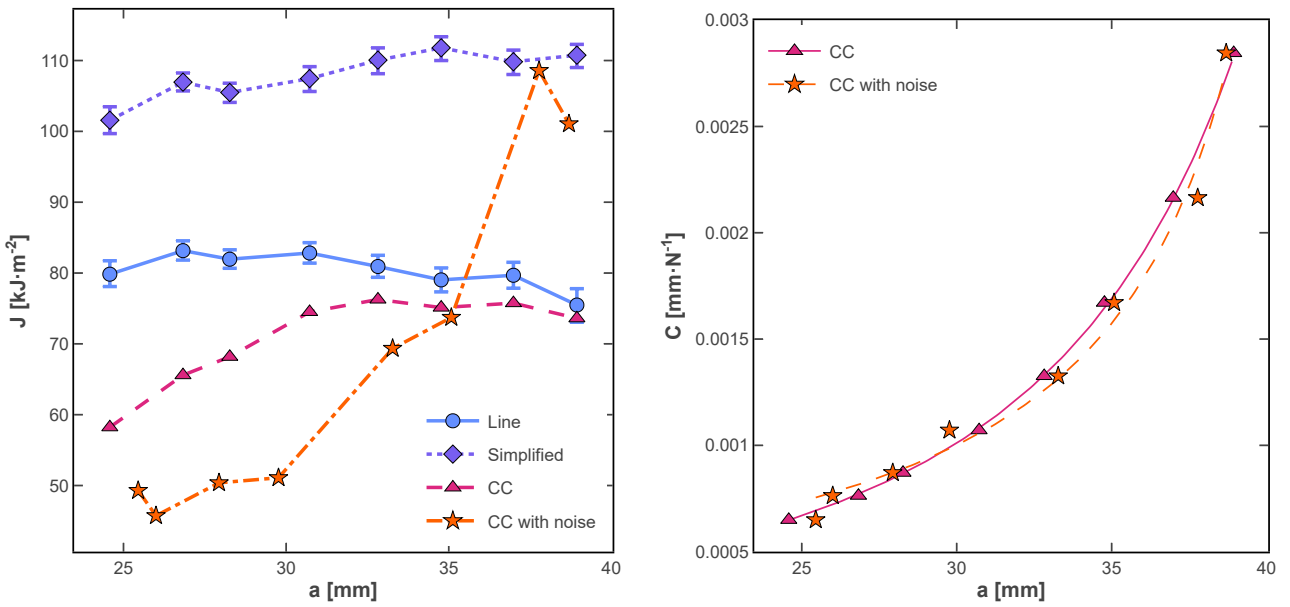

(a) **(b)**

Figure 4.16: (a) ERR J_{Ic} obtained by applying the J-integral and compliance calibration methods with the results of a FEM which captures the crack propagation with cohesive elements; (b) Corresponding compliance calibration. The error bars stand for the confidence interval of each individual point obtained with the J-integral approach.

effect, contrasting with the reported experimental results. Moreover, the choice of the csaps smoothing value and the offset Δ_{BC} values significantly influenced the J-integral result. These three observations are possibly due to the presence of the cohesive elements along the crack path, which disrupt the displacement field, and should be investigated in future studies. Overall, they highlight that the proposed J-integral approach requires a convergence study of its parameters for each new application. Future works should investigate more systematic approaches to identify the adequate parameters. Furthermore, each method should be used within their respective recommended contour parameters, as defined in subsection 4.2.3 and section 4.3.2.

From Figure 4.16a, the compliance calibration may appear as more practical than the J-integral. However, its accuracy is the result of the excellent quality of the FEM data and the use of the corrected intersection method to measure the crack length, as highlighted by the fitting in Figure 4.16b. Lastly, if the crack length is perturbed with a random noise of $\pm$ 1 mm, the compliance calibration fails in capturing the material toughness (see Figure 4.16a), although the compliance fitting is not strongly affected (see Figure 4.16b). This confirms the interest of crack-length agnostic methods, such as the J-integral, over the compliance calibration.

Finally, as mentioned in section 4.2, the computational cost of the surface J-integral is significant, by far the highest one. This cost is negligible when evaluating the J-integral value over one contour. However, the overhead becomes significant when evaluating several hundreds of contours per frame, as in this work. For instance, analyzing the nine frames of sample C on a workstation equipped with

an AMD Ryzen 9 3900X processor required about 160 s for both line and simplified J-integral (which are evaluated simultaneously) while using the surface J-integral required roughly 1300 s. While the Python code could be optimized to address this issue, it demonstrates that the line and simplified formulations are more suitable for live data reduction of the translaminar toughness.

Chapter 5

Interlayer thin-ply fiber-hybrids

What is the impact of interlayer fiber-hybridization on thin-ply laminate properties?

The list of available data, codes, and publications generated for this work is available on Zenodo [204].

This chapter reports the experimental assessment of interlayer fiber-hybridization as a strategy to balance translaminar toughness and tensile properties in high-performance thin-ply laminates. The reader is referred to chapter 3 for a detailed discussion of the material and testing methodology choices. Here, the experimental results are shown first for the translaminar toughness characterization in CP laminates and then for the UNT and OHT properties in QI laminates. The results are discussed by emphasizing the competitive effect between the ply-thickness and the fiber-hybridization.

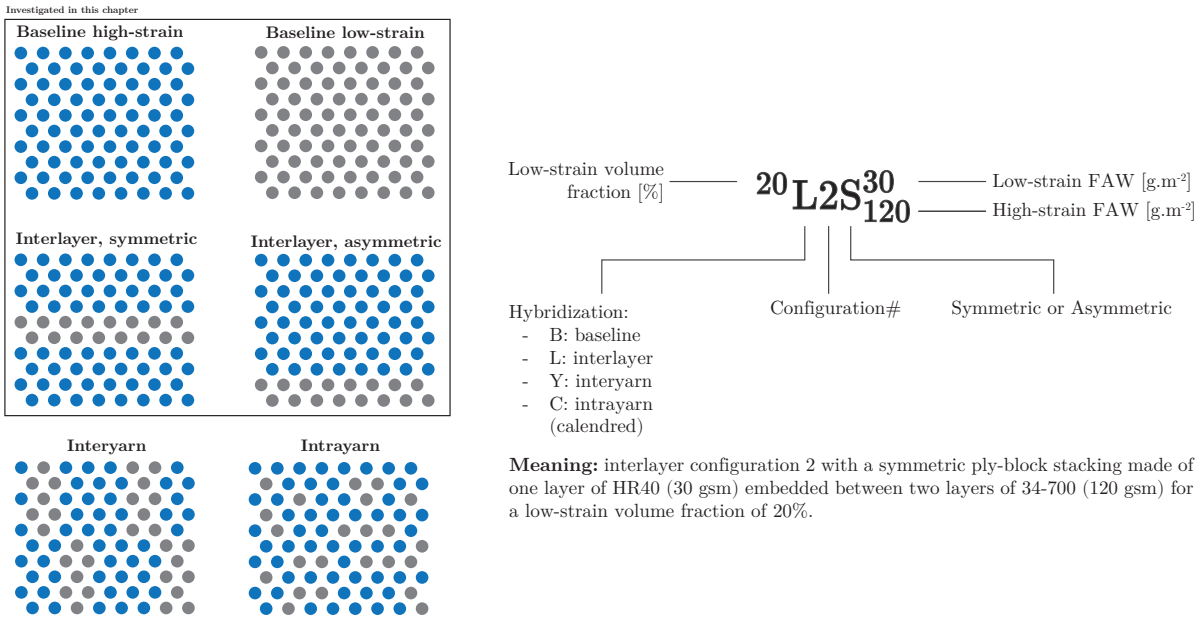

Figure 5.1: Interlayer hybrid nomenclature.

Designation	**Stacking**	E_1 [GPa]	E_2 [GPa]	G_{12} [GPa]	ν_{12}	V_f [%]
$^{100}\mathrm{B1}_{0}^{30}$	$\left[\left(90^L/0^L\right)_{70}/90^L\right]_s$	104.44	103.05	2.88	0.017	51.2
$^{0}\mathrm{B2}_{60}^{0}$	$\left[\left(0^H/90^H\right)_{30}/0^H\right]_s$	64.38	62.49	2.86	0.027	50.9
$^{0}\mathrm{B3}_{120}^{0}$	$\left[\left(90_2^H/0_2^H\right)_{15}/90_2^H\right]_s$	61.46	65.17	2.85	0.026	50.8
$^{0}\mathrm{B4}_{180}^{0}$	$\left[\left(90_3^H/0_3^H\right)_{10}/90_3^H\right]_s$	60.35	65.80	2.84	0.026	50.6
$^{33}\mathrm{L1A}_{60}^{30}$	$\left[\left(90^H/90^L/0^H/0^L\right)_{20}/90^H/90^L\right]_s$	73.70	78.93	2.85	0.021	50.8
$^{20}\mathrm{L2S}_{120}^{30}$	$\left[\left(90^H/90^L/90^H/0^H/0^L/0^H\right)_{12}/90^H/90^L\right]_s$	72.72	77.85	2.80	0.022	50.1
$^{33}\mathrm{L3A}_{120}^{60}$	$\left[\left(90_2^H/90_2^L/0_2^H/0_2^L\right)_5/90_2^H/90_2^L\right]_s$	70.65	77.15	2.74	0.022	49.2
$^{33}\mathrm{L4S}_{120}^{60}$	$\left[\left(90^H/90_2^L/90^H/0^H/0_2^L/0^H\right)_5/90_2^H/90_2^L\right]_s$	66.99	72.09	2.78	0.023	49.7
$^{14}\mathrm{L5A}_{180}^{30}$	$\left[\left(90_3^H/90^L/0_3^H/0^L\right)_4/90_3^H/90_3^L\right]_s$	61.78	74.27	2.82	0.023	50.4
$^{20}\mathrm{L6S}_{240}^{60}$	$\left[\left(90_2^H/90_2^L/90_2^H/0_2^H/0_2^L/0_2^H\right)_2/90_2^H/90_2^L/90_2^H/0_2^H/0_2^L\right]_s$	64.24	75.92	2.80	0.022	50.1

Table 5.1: Elastic constants for hybrids CT specimen laminates obtained by CLT [227] assuming the datasheet properties published by Grafil.

As detailed in chapter 3, laminates were designed to optimize toughness, the onset of damage, and manufacturability. High-strength 34-700 and high modulus HR40 continuous PAN-based carbon fibers from Grafil were selected as high-strain and low-strain materials, respectively. They were spread to $60\,\mathrm{g}\cdot\mathrm{m}^{-2}$ and 30 gsm, and pre-impregnated with TP415 toughened epoxy by NTPT.

For the record, six different interlayer fiber-hybrid laminates were selected according to the failure map and tested. Their properties are summarized in Table 5.1. The effect of fiber hybridization was assessed by varying the low-strain volume fraction γ from 14 to 33 %. To characterize the concurrent effect of ply-thickness, the same γ is employed for different ply-block thicknesses. Finally, symmetric and asymmetric interlayer architectures are considered. Figure 5.1 outlines the differences between a symmetric ply-block where the low-strain layer is embedded inside two layers of high-strain material and an asymmetric ply-block where the low-strain layer is not embedded. Thus, the interface between two ply-blocks of different orientations is also an interface between the low-strain material and the high-strain material.

Symmetric ply-blocks were used previously to achieve a stable pseudo-ductility [169]. However, pseudo-ductility was not sought in this work. The asymmetric layup was used previously by Cugnoni et al. [52] and may promote secondary damage, such as delamination, thanks to the increased modulus mismatch at the ply-block interfaces. The investigation of an asymmetric layup is a key difference from the work of Danzi et al. [56].

5.1 Translaminar toughness

The CT test was retained to characterize the CP laminate mode I translaminar fracture toughness, following the same procedure as Frossard [39] and fully described in chapter 3. The sample properties are listed in Table 5.2. As the objective of this experimental study is to assess the influence of fiber hybridization, the dimensions of the specimen were kept constant as much as possible to avoid size effects. However, the requirement for a symmetric layup, as well as the constraint of batch manufacturing for the prepregs, led to laminate thicknesses ranging from 3.6 to 4.4 mm. Despite this variability, all samples exhibit a fiber volume fraction V_f $\pm 50\,\%$.

CT specimens (60×55 mm) were produced by water-jet cutting according to the geometry reported in Figure 4.1 from 4 mm thick CP laminate made by stacking 34-700 carbon fiber thin-ply prepregs provided by North ThinPly Technology. 90° plies were laid at the sample surface to avoid splitting. Initial cracks were machined in the four samples using a diamond wire with a diameter of 0.125 mm to achieve an initial length a_0 ranging from 18 mm to 25 mm, as reported in Table 5.2.

Cracks were grown under monotonic displacement-controlled tests at a loading rate of $0.5\,\mathrm{mm \cdot min^{-1}}$ on an MTS 809 hydraulic testing machine equipped with a 100 kN cell force. The stiffness of the loading chain was reported to be $20.8\,\mathrm{kN \cdot mm^{-1}}$ [39], approximately seven times greater than the stiffest reported specimen ($3.1\,\mathrm{kN \cdot mm^{-1}}$). This ratio ensures stable crack propagation. The cell force reading was zeroed after installing the fixtures but before mounting the samples (their weight is negligible). The samples were then manually aligned with the fixtures and slightly preloaded to a few tens of N to ensure proper alignment.

5.1.1 Result overview

Figure 5.2 and Figure 5.3 present typical loading curves and typical R-curves, respectively. The reported displacement was measured by the machine Linear Variable Differential Transformer (LVDT). As the samples exhibit different low-strain volume fractions and laminate thicknesses, their apparent compliance differs significantly. The loading curves are not linear before the first significant crack propagation. Frossard [39] attributed this behavior to local in-plane shear plasticity around the crack tip.

The propagation points are shown by a symbol in Figure 5.2. To be considered as crack propagation, a load drop had to be accompanied by a significant change in the displacement fields monitored by DIC, indicating a change in compliance and therefore a significant crack growth. The reported curves for ${}^{33}\mathrm{L3A}_{120}^{60}$ and ${}^{33}\mathrm{L4S}_{120}^{60}$ correspond to the respective sample C in Table 5.2. It is worth noting that both sample exhibit the same low strain fraction γ and a similar initial crack length. Therefore, the significant change in the propagation loads shown in Figure 5.2b highlights qualitatively that an asymmetric ply-block architecture dissipates much more energy than a symmetric architecture.

Designation	Sample	a_0 [mm]	b [mm]	Mass [g]	V_f [%]	S [kN · mm^{-1}]
$^{100}\mathrm{B1}_{0}^{30}$	A	17.93	4.39 ± 0.03	23.0	51.2	3.12
	B	18.99	4.39 ± 0.02	23.0	51.2	3.02
	C	24.22	4.42 ± 0.03	23.0	50.7	2.02
	D	24.36	4.36 ± 0.03	22.9	51.5	2.08
$^{0}\mathrm{B2}_{60}^{0}$	C	24.78	4.02 ± 0.03	NA	50.6	1.92
	D	25.02	3.97 ± 0.02	NA	51.2	1.93
$^{0}\mathrm{B3}_{120}^{0}$	A	18.38	4.02 ± 0.01	21.3	51.4	2.71
	B	18.37	4.07 ± 0.01	21.5	50.8	2.64
	C	24.30	4.07 ± 0.02	21.4	50.8	1.64
	D	24.33	4.02 ± 0.02	21.3	51.4	1.76
$^{0}\mathrm{B4}_{180}^{0}$	A	20.33	4.14 ± 0.02	21.9	50.7	2.32
	B	20.38	4.09 ± 0.01	21.8	51.3	2.16
	C	24.58	4.13 ± 0.02	21.9	50.8	1.75
	D	24.58	4.10 ± 0.02	21.8	51.2	1.63
$^{33}\mathrm{L1A}_{60}^{30}$	C	25.31	4.02 ± 0.03	NA	51.0	1.80
	D	25.46	4.04 ± 0.02	NA	50.9	1.68
$^{20}\mathrm{L2S}_{120}^{30}$	A	18.23	4.15 ± 0.01	21.9	49.8	2.69
	B	18.19	4.16 ± 0.01	22.0	49.7	2.53
	C	24.17	4.10 ± 0.02	21.8	50.3	1.82
	D	24.07	4.10 ± 0.01	21.8	50.3	1.87
$^{33}\mathrm{L3A}_{120}^{60}$	A	17.90	4.26 ± 0.03	22.5	50.2	2.67
	B	17.91	4.25 ± 0.02	22.5	50.3	2.64
	C	23.74	4.29 ± 0.02	22.6	49.8	1.99
	D	23.89	4.20 ± 0.02	22.3	50.1	1.91
$^{33}\mathrm{L4S}_{120}^{60}$	A	18.23	4.20 ± 0.01	22.0	49.3	2.61
	B	18.19	4.17 ± 0.02	21.9	49.6	2.80
	C	23.09	4.13 ± 0.01	21.8	50.0	1.98
	D	23.18	4.28 ± 0.03	22.4	48.3	2.00
$^{14}\mathrm{L5A}_{180}^{30}$	A	19.05	4.02 ± 0.02	21.4	51.5	2.09
	B	19.05	4.09 ± 0.02	21.6	50.7	2.18
	C	22.89	4.10 ± 0.03	21.6	50.6	1.79
	D	23.04	4.04 ± 0.02	21.4	51.3	1.85
$^{20}\mathrm{L6S}_{240}^{60}$	A	19.07	3.68 ± 0.02	19.3	49.4	1.97
	B	18.93	3.61 ± 0.02	19.0	50.4	2.00
	C	25.05	3.58 ± 0.01	19.0	50.7	1.39
	D	24.83	3.62 ± 0.02	19.1	50.2	1.35

Table 5.2: Interlayer hybrids CT specimens properties, measured according to the methods described in chapter 3. S is the sample stiffness at the first crack propagation.

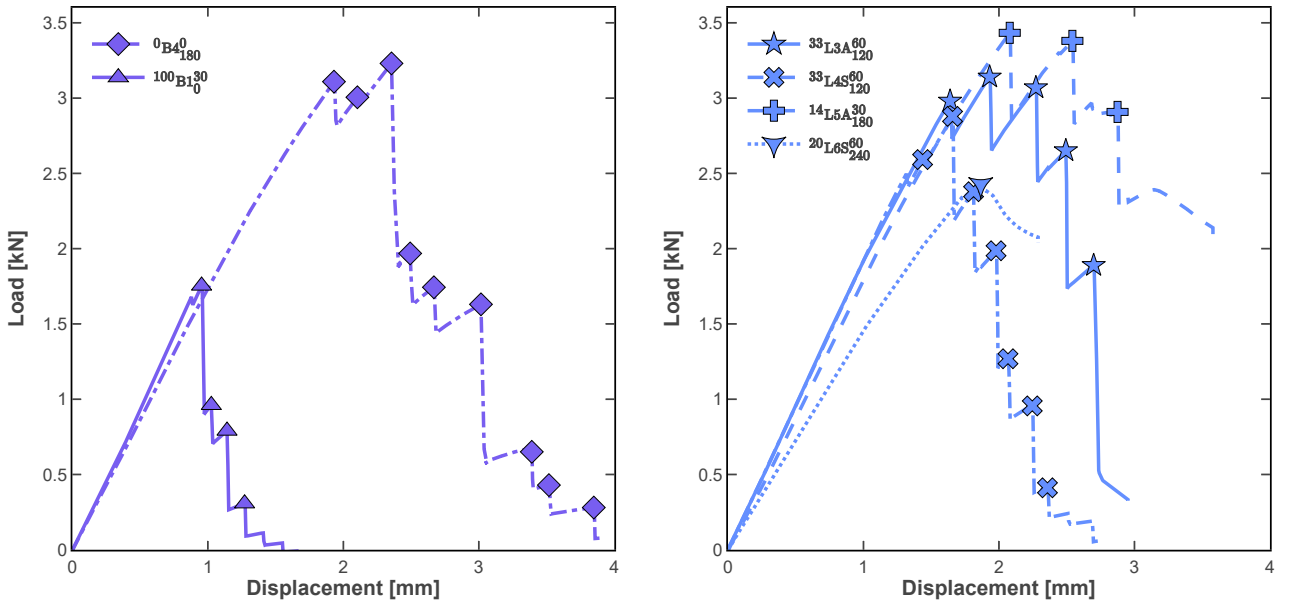

(a) **(b)**

Figure 5.2: Typical loading curves for CT tests: (a) baselines and (b) interlayer hybrids. The compliance variation between samples before the first damage is due to differences in thicknesses (see Table 5.2).

Overall, crack propagation is not smooth and follows a "saw-tooth" behavior. Few propagation points are available and make the result interpretation challenging. However, the samples never fail unstably. Some hybrid samples (see for instance $^{33}\mathrm{L4S}^{60}_{120}$ or $^{20}\mathrm{L6S}^{60}_{240}$) exhibit a strong non-linearity after the first propagation points. This behavior could indicate a failure by backend compression or buckling, which were visually observed for most of the samples affected by this phenomenon.

In the case of backend compression, it was observed that the crack propagated suddenly to more than 20 mm increment. In this case, the crack tip is at less than 10 mm from the backend edge. The same behavior is also observed in samples exhibiting a more stable crack propagation. For instance, Figure 5.3 shows that after approximately 16 mm of crack propagation, the configuration $^{0}\mathrm{B3}^{0}_{120}$ undergoes a severe loss of its apparent toughness. In the case of buckling, the load increases up to the triggering of the non-linearity without proper crack propagation. It is worth noting that buckling concerns essentially $^{20}\mathrm{L6S}^{60}_{240}$. This hybrid ply-block FAW totalizes $300\,\mathrm{g}\cdot\mathrm{m}^{-2}$. It is established that such a ply-block thickness is prone to transverse cracking and delamination in non-hybrid laminates [38]. In both cases, this leads to the belief that the true propagation (or steady-state) ERR was not systematically achieved.

Figure 5.3 confirms the trend already reported in chapter 4. The steady-state ERR increases with the initial crack length a_0, no matter the employed data reduction method, and this contrast increases with the material translaminar toughness. In some cases, this apparent increase was attributed to the clear apparition of secondary damage as analyzed is subsection 5.1.3. However, even configurations

exhibiting a relatively low translaminar toughness and no secondary damage, as the baseline ${}^{0}\mathrm{B3}^{0}_{120}$, show the same trend. A working assumption is that a smaller initial crack allows for developing a larger FPZ. Consequently, the CT specimen may be large enough to generate a more developed FPZ [192, 237].

An overview of the averaged initiation and steady-state ERR values measured in this work is presented in Figure 5.4. Notably, it shows a clear linear and detrimental ply-thickness effect on the mode I translaminar toughness for the 34-700-TP415 system which had never been characterized yet in the literature (baselines ${}^{0}\mathrm{B2}^{0}_{60}$ to ${}^{0}\mathrm{B4}^{0}_{180}$). This scaling is aligned with those reported in chapter 2 and especially the linear scaling law observed by Frossard [39] for M40JB-80ep specimens.

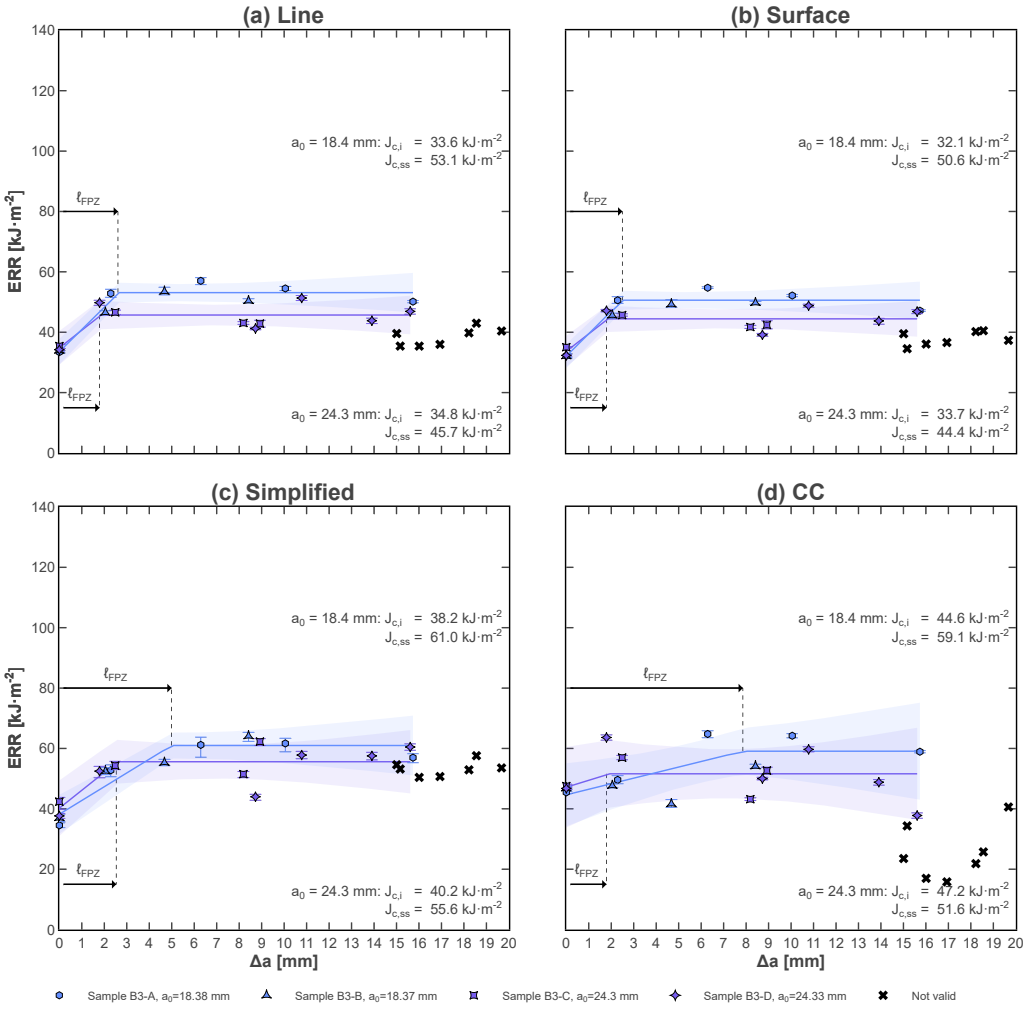

Figure 5.3: Typical R-curves obtained with baseline configuration baseline configuration ${}^{0}\mathrm{B3}^{0}_{120}$ using (a) line J-integral, (b) surface J-integral, (c) simplified J-integral, and (d) compliance calibration. Note that the marker symbols do not correspond to the symbol used elsewhere to represent ${}^{0}\mathrm{B3}^{0}_{120}$.

5.1.2 Hybridization effect

The R-curve graphs such as those presented in Figure 5.3 report initiation, growth, and steady-state values as an approximate bilinear function. This representation gives a clearer picture of the effects

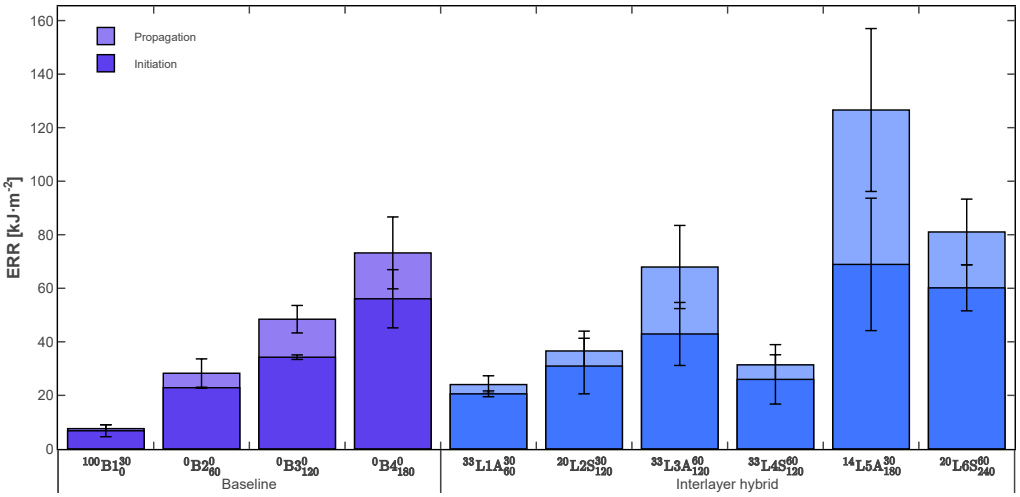

Figure 5.4: Baseline and interlayer hybrid ERR at initiation (dark colors) and steady-sate (light colors), reduced with the line J-integral method.

but assumes a steady-state plateau and tends to hide outliers. A proper steady-state plateau was not always reached in this work, and outliers are significant. It is hypothesized that some of the large outliers correspond to secondary damage. Therefore, apart from the R-curve graphs, the initiation ERR is defined here as the average of the values reported at the first propagation point for the different samples. The steady-sate ERR is defined as the average of the values reported for a crack length greater than the determined l_{FPZ} (see Figure 5.3).

These average values are reported as box plots for the baselines in Figure 5.5 and Table 5.3. First, both initiation and steady-state ERR scale linearly with the ply-thickness as in Equation 5.1. The ${}^{0}\mathrm{B3}^{0}_{120}$ sample is slightly off from the linear scaling but was only tested for large initial cracks with two samples. The low-strain baseline ${}^{100}\mathrm{B1}^{30}_{0}$ exhibits as expected the lowest translaminar toughness as its fibers are more brittle and it is made of the thinnest plies. The initiation values obtained for the 34-700-TP415 baseline were 143 % higher for a ply-block FAW of $180\,\mathrm{g}\cdot\mathrm{m}^{-2}$ compared to a ply-block FAW of $60\,\mathrm{g}\cdot\mathrm{m}^{-2}$ ($56\,\mathrm{kJ}\cdot\mathrm{m}^{-2}$ against $23\,\mathrm{kJ}\cdot\mathrm{m}^{-2}$). The propagation values followed a similar trend with an average increase of 160 % ($73\,\mathrm{kJ}\cdot\mathrm{m}^{-2}$ against $28\,\mathrm{kJ}\cdot\mathrm{m}^{-2}$).

$$J_H = M_H^{ERR} t_H + C_H^{ERR} \tag{5.1}$$

Figure 5.6 summarizes the results obtained for the interlayer hybrids, as a function of the ply-block thickness. It reports the CP laminate translaminar toughness, which is representative of the 0° ply translaminar toughness since G_{Ic}^{90} can be neglected in Equation 3.7. Overall, the interlayer hybrids were found to scale with the ply-block FAW, indicating a predominant ply-thickness effect.

Nevertheless, the hybrid configurations diverge notably from the linear scaling of the baselines, some being tougher while most of them appear weaker. This indicates different types of hybrid effects. Qualitatively, this hybrid effect seems to be positive for two configurations: ${}^{33}\mathrm{L3A}^{60}_{120}$ and ${}^{14}\mathrm{L5A}^{30}_{180}$.

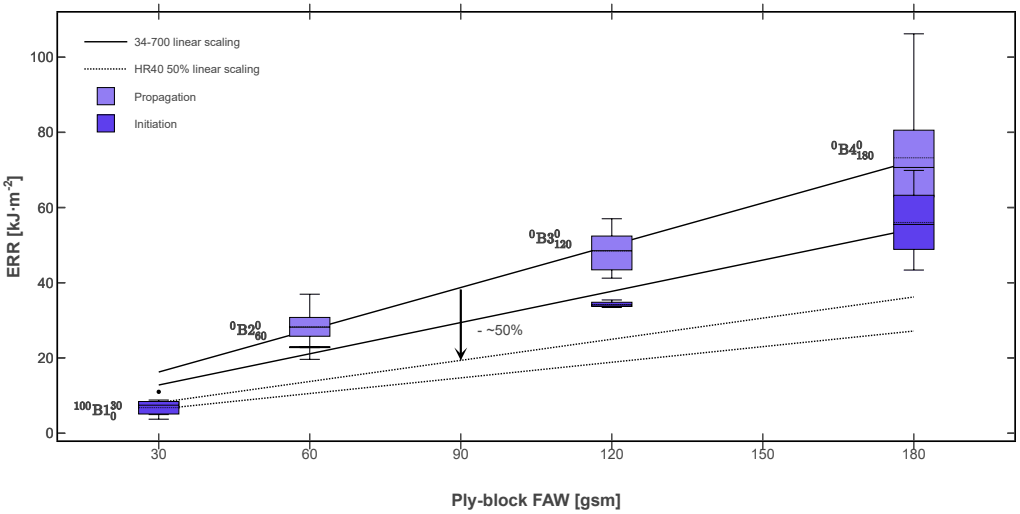

Figure 5.5: Baseline and interlayer hybrid laminate ERR box plots at initiation (dark colors) and steady-sate (light colors), reduced with the line J-integral method.

Interestingly, these two configurations feature an asymmetric ply-block architecture. The figure also highlights the high scattering of the results. This scattering is the consequence of testing two different initial crack lengths which produce different results. This effect will be discussed in detail in subsection 5.1.3.

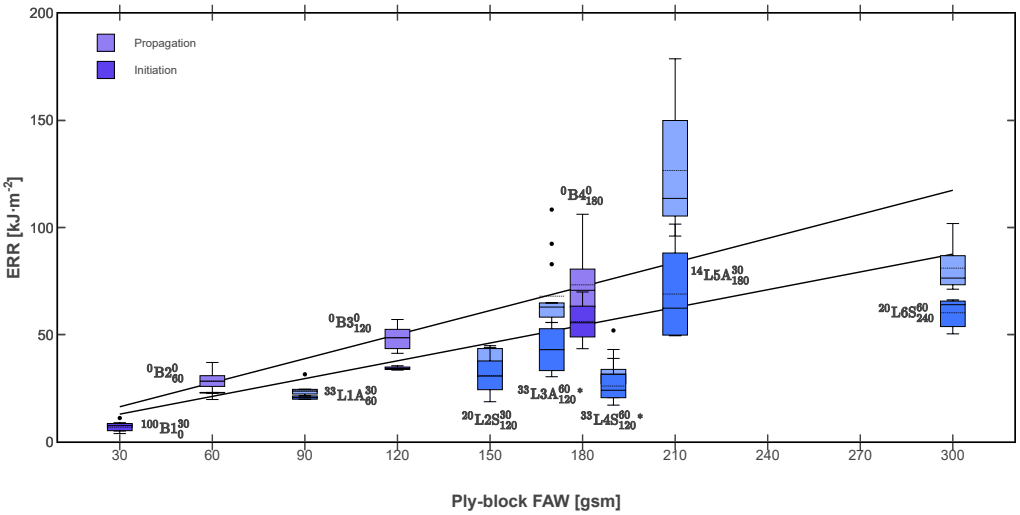

Figure 5.6: Baseline and interlayer hybrid ERR box plots at initiation (dark colors) and steady-state (light colors), reduced with the line J-integral method, as a function of ply-block FAW. * jittered for readability

However, the interpretation of these results is not straightforward as the introduction of low-strain fibers in the high-strain laminate alters the expected properties. As exposed in chapter 3, the hybrid effect is defined with respect to this expectation. For the translaminar toughness, both initiations and propagation ERR are supposed to follow a linear RoM as in Equation 5.2 where each ply contributes additively to the total laminate fracture toughness. This model was proposed by Pinho et al. [180] and validated by Teixeira et al. [238]. However, it assumes that each ply behaves independently from the other. This may be true in a CP laminate where the 90° plies isolate the 0° plies from each other,

	Line J-integral [kJ · m^{-2}]			Compliance calibration [kJ · m^{-2}]		
Designation	$J_{Ic,i}$	$J_{Ic,ss}$	max $(J_{Ic,ss})^*$	$J_{Ic,i}$	$J_{Ic,ss}$	max $(J_{Ic,ss})^*$
$^{100}B1^{30}_{0}$	6.8 ± 2.2	7.6 ± 1.5	8.2 ± 1.5	11.1 ± 1.6	10.6 ± 2.7	9.4 ± 2.6
$^{0}B2^{0}_{60}$	22.9 ± 0.1	28.3 ± 5.3	NA	31.2 ± 0.3	29.0 ± 7.7	NA
$^{0}B3^{0}_{120}$	34.3 ± 0.8	48.4 ± 5.1	53.1 ± 2.9	46.7 ± 0.9	52.6 ± 8.0	59.1 ± 5.0
$^{0}B4^{0}_{180}$	56.1 ± 10.9	73.2 ± 13.4	82.5 ± 11.0	71.9 ± 12.7	89.1 ± 15.6	102.0 ± 10.2
$^{33}L1A^{30}_{60}$	20.6 ± 1.1	24.6 ± 3.5	NA	26.0 ± 1.3	31.4 ± 5.6	NA
$^{20}L2S^{30}_{120}$	30.9 ± 10.4	35.1 ± 7.4	35.6 ± 8.4	38.0 ± 5.4	43.0 ± 9.4	42.5 ± 3.8
$^{33}L3A^{60}_{120}$	42.9 ± 11.8	67.9 ± 15.5	70.8 ± 19.1	51.0 ± 5.2	73.1 ± 6.2	71.1 ± 5.3
$^{33}L4S^{60}_{120}$	26.0 ± 9.2	31.6 ± 7.0	32.6 ± 8.2	35.5 ± 5.5	40.3 ± 9.1	42.2 ± 7.4
$^{14}L5A^{30}_{180}$	68.9 ± 24.7	129.4 ± 29.6	141.9 ± 28.2	85.8 ± 14.7	109.4 ± 19.8	121.5 ± 18.6
$^{20}L6S^{60}_{240}$	60.2 ± 8.6	81.0 ± 12.3	86.5 ± 21.7	56.9 ± 1.8	88.9 ± 3.4	88.5 ± 1.8

Table 5.3: Interlayer hybrid ERR results. Values for a CP laminate. The reported uncertainties correspond to the standard deviation. * maximal value obtained with a small initial crack, see subsection 5.1.3.

but it is not granted when the plies are part of the same ply-block. Therefore, deviations from a linear RoM are expected and will indicate that the plies interact with each other, highlighting a hybrid effect.

$$J_{hybrid} = \gamma J_L + (1 - \gamma) J_H \tag{5.2}$$

To be meaningful, the RoM should incorporate the ply-thickness effect. Therefore, it is proposed to modify the RoM formulated in Equation 5.2 by introducing the linear ply-thickness scaling defined in Equation 5.1. On the one hand, the scaling may be achieved assuming that the whole ply-block behaves as one ply. In this case, the toughness is scaled according to the whole ply-block thickness, as formulated in Equation 5.3. On the other hand, the interface between the low-strain and the high-strain material may be considered as isolating both sub-plies from each other. In this case, the sub-plies behave in parallel and the toughness is scaled according to their individual thickness, as in Equation 5.4.

$$\begin{cases} J_{hybrid} = \gamma J_L + (1 - \gamma) J_H \\ J_L = M_L^{ERR} (t_H + t_L) + C_L^{ERR} \\ J_H = M_H^{ERR} (t_H + t_L) + C_H^{ERR} \end{cases} \tag{5.3}$$

$$\begin{cases} J_{hybrid} = \gamma J_L + (1-\gamma) J_H \\ J_L = M_L^{ERR}(t_L) + C_L^{ERR} \\ J_H = M_H^{ERR}(t_H) + C_H^{ERR} \end{cases} \tag{5.4}$$

The linear scaling law for the HR40-TP415 system was not characterized. The values reported by Frossard [39] for a similar system, the M40JB-80ep, could be used. However, they were found higher than those measured here for the 34-700-TP415 system. Frossard used the simplified J-integral formulation, which tends to overestimate the J value as compared to the line J-integral, and the fiber and matrix system remains sufficiently different to explain the change. Thus, to apply the RoM above and without the experimental scaling for the HR40 translaminar toughness, some assumptions need to be made.

The HR40 is a high-modulus fiber and is unlikely to exhibit a translaminar toughness superior to the 34-700 fibers when used in combination with the same epoxy resin. The 34-700-TP415 scaling law can therefore be used as an upper bound for the HR40-TP415 system. Another possibility would have been to estimate a linear scaling for the HR40 translaminar toughness, for example by considering it as a ratio of the toughness of the HR40 but this could lead to large extrapolation errors for large ply thickness as the only experimental point for HR40 is for the thinnest $30\,\mathrm{g}\cdot\mathrm{m}^{-2}$ plies. By comparing the measured values of HR40 at 30 gsm versus the extrapolated values of 34-700 at the same ply thickness, the HR40 to 34-700 translaminar toughness ratio would correspond to approximately 50 %. However, this option was left aside as it was considered too approximative to support the following discussion. Moreover, using the upper bound calculated by the 34-700-TP415 is a conservative assumption to evaluate the hybrid effect.

As an illustration, the construction of the RoM is proposed for $^{14}\mathrm{L5A}_{180}^{30}$ in Figure 5.7a and for $^{33}\mathrm{L3A}_{120}^{60}$ and $^{33}\mathrm{L4S}_{120}^{60}$ in Figure 5.7b. $^{33}\mathrm{L4S}_{120}^{60}$ features a symmetric ply-block layup, thus the high-strain thickness t_H must be scaled accordingly in Equation 5.4. Indeed, the embedded plies of low-strain fibers isolate the two plies of high-strain fibers and the high-strain material thickness is only half the total high-strain thickness used in the ply-block in the case of a sub-ply scaling.

Figure 5.7a also reports the RoM obtained when assuming a 50 % scaling for the HR40 as aforementioned. The hybrid effect is greater with respect to this scaling, thus the lower bound obtained assuming the 34-700 scaling is reported in this work.
Figure 5.7b shows that the RoM with a sub-ply scaling successfully predicts the propagation ERR of the $^{33}\mathrm{L4S}_{120}^{60}$ hybrid configuration. This suggests that a symmetric ply-block layup does not provide a quantifiable hybrid effect. This result must be nuanced as assuming a less favorable scaling law for the HR40-TP415 system would lead to lower predictions. Moreover, this hybrid contains 33 % of low-strain material. Consequently, the failure map does not predict a stable fragmentation for this configuration (Figure 3.6). Therefore, the symmetric layup is not expected to have a positive effect on

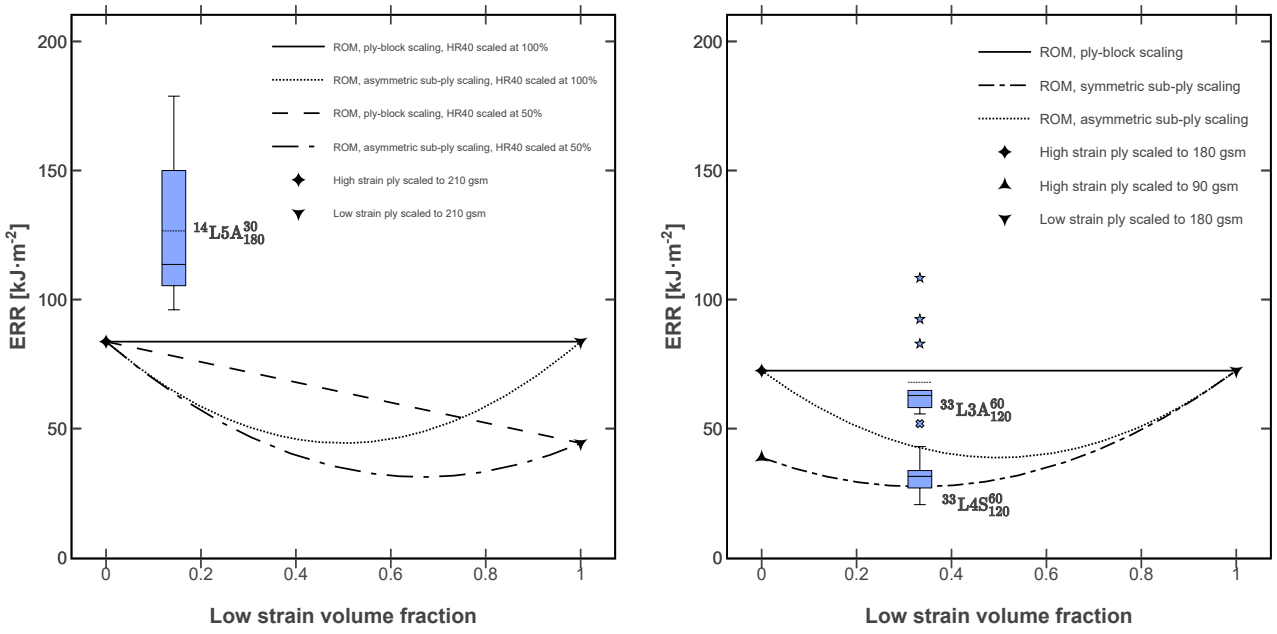

Figure 5.7: Graphical representations of Equation 5.3 and Equation 5.4 evaluated for (a) sample ^{14}L5A$^{30}_{180}$ and (b) samples ^{33}L3A$^{60}_{120}$ and ^{33}L4S$^{60}_{120}$ to predict steady-state ERR values. The individual symbols are outliers.

fragmentation. On the contrary, the asymmetric configuration ^{33}L3A$^{60}_{120}$ shows a significant positive hybrid effect compared to the sub-ply scaling RoM, but a negative effect compared to the ply-block scaling RoM, except for few outliers.

This change is only due to the difference in ply-block architecture. CT-scans performed on OHT samples have shown that the asymmetric scaling can be related to more diffuse damage, as in Figure 5.27. This could be explained by the increased mismatch in modulus caused by the hybridization at the ply-block interface which may promote delamination. More details are discussed section 5.3.

As the RoM proposed in Equation 5.3 and Equation 5.4 depend on ply thicknesses, they output predictions as a function of the low strain volume fraction γ which are different for almost every hybrid configuration. A plot compiling all these results would not be readable. Therefore, Figure 5.8 and Figure 5.9 respectively report the steady-state and the initiation ERR normalized by both types of RoM predictions. They show that sub-ply scaling RoM is a lower bound for the J values while the ply-block scaling RoM is an upper bound. Moreover, the ply-block scaling RoM is a better overall predictor. For instance, it commits an average error of 21 % on the reported propagation values while the sub-ply scaling RoM average error is 49 %. According to these results, only ^{14}L5A$^{30}_{180}$ provides a positive hybrid effect with respect to ply-block scaling RoM for initiation and steady-state ERR.

5.1.3 Influence of the initial crack length

As highlighted for instance in Figure 5.6, the ERR distribution of several hybrid configurations is highly scattered, with outliers exhibiting a significantly improved translaminar toughness. This vari-

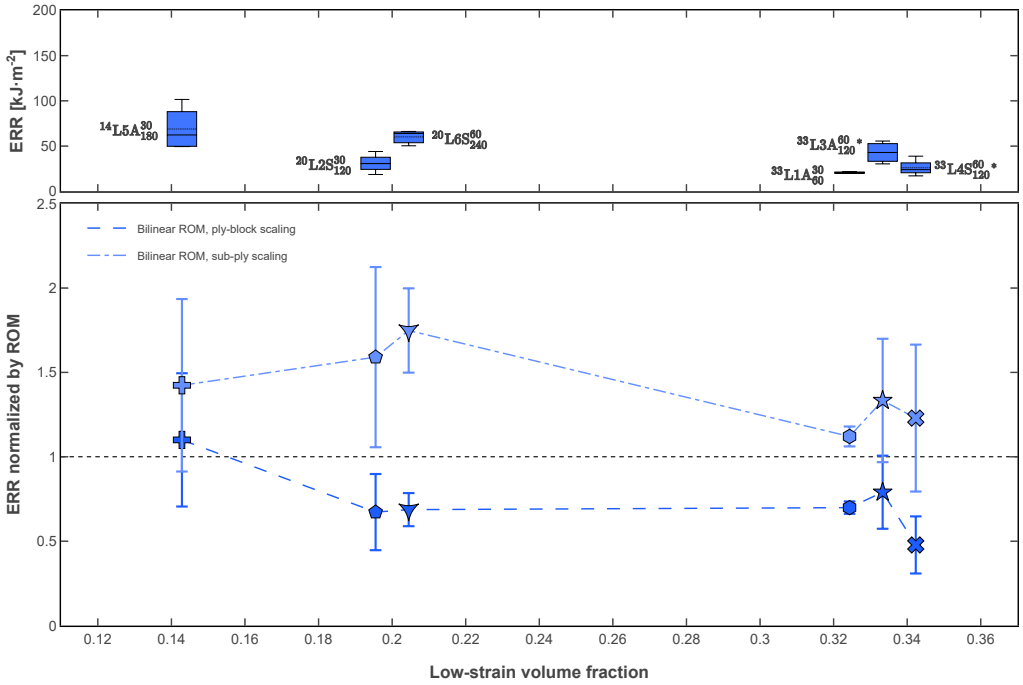

Figure 5.8: Initiation ERR normalized by RoM for interlayer hybrids.* jittered for readability

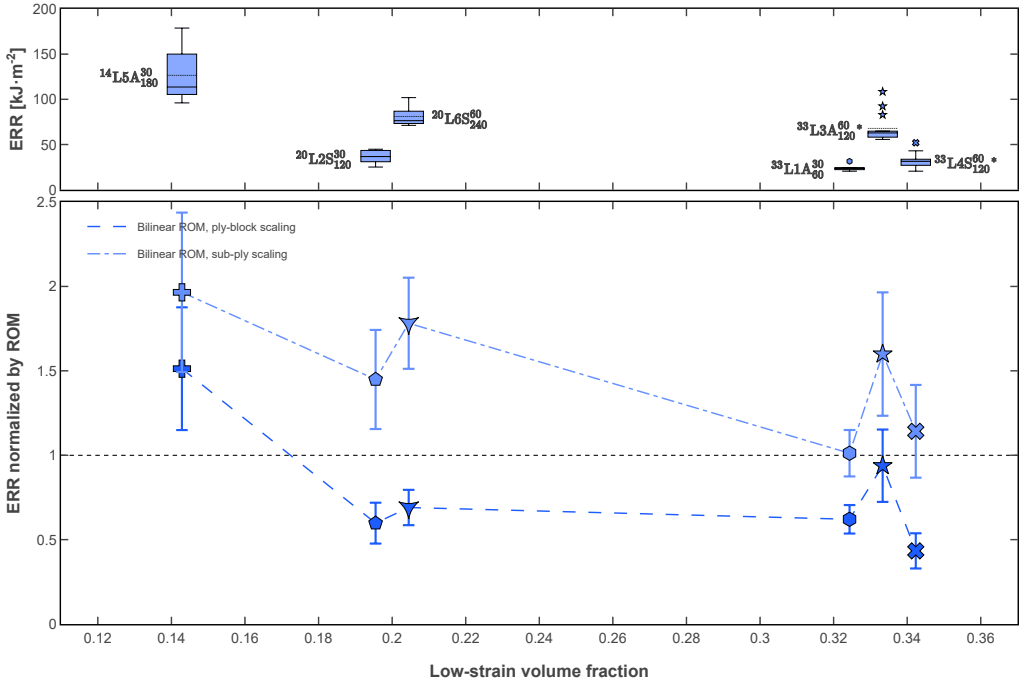

Figure 5.9: Steady-state ERR normalized by RoM for interlayer hybrids.* jittered for readability

ability is explained by the length of the initial crack. As reported in Figure 5.10a and Figure 5.10b, an initial crack length around to 18 mm (in blue) in $^{33}\text{L3A}^{60}_{120}$ and $^{14}\text{L5A}^{30}_{180}$ leads to a substantial ERR increase. This improvement is directly correlated to the apparition of dissipative secondary damage. As shown in Figure 5.10c and Figure 5.10e $^{33}\text{L3A}^{60}_{120}$ exhibits crack branching. As the baseline $^{0}\text{B4}^{0}_{180}$ of equivalent ply-block thickness does not show crack branching, this mechanism could be attributed to the fiber hybridization. Similarly, $^{14}\text{L5A}^{30}_{180}$ exhibits significant crack splitting as in Figure 5.10d

and Figure 5.10f. There is no baseline 34-700 with a ply-block FAW of $210\,\mathrm{g}\cdot\mathrm{m}^{-2}$, but a $30\,\mathrm{g}\cdot\mathrm{m}^{-2}$ increase from the ${}^{0}\mathrm{B4}^{0}_{180}$ baseline is unlikely to cause such a contrast in failure mechanisms. In such case, the crack splitting could therefore also be attributed to an effect of fiber hybridization. It is worth noting that both ${}^{33}\mathrm{L3A}^{60}_{120}$ and ${}^{14}\mathrm{L5A}^{30}_{180}$ exhibit an asymmetric layup.

Furthermore, Figure 5.10a and Figure 5.10b show that the ERR for short initial cracks (in blue) increased to a maximum before dropping catastrophically, corresponding to a failure in backend compression or buckling. It means that the ERR plateau was never reached and further toughness improvements are likely to be achievable. Normalizing the maximal ERR values obtained during the R-curve growth by the RoM predictions leads to positive hybrid effects up to more than 100 % as reported in Figure 5.11.

Three working assumptions may explain the observed contrast between small and large a_0. First, a smaller crack length brings the crack tip closer to the loading axis, leading to a more uniform loading. To investigate this hypothesis, a 3D FEM of the CT ${}^{14}\mathrm{L5A}^{30}_{180}$ samples was performed with Abaqus 6.19. A first model was defined with a short crack length of 18 mm and loaded with the force corresponding to the first crack propagation (4.45 kN). A second model featured a long crack of 23 mm and was loaded to 3.28 kN. The resulting strain fields are reported in Figure 5.12 with an outer contour of 0.6 %. While the low-strain fiber ultimate strain is 1.1 %, the onset of damage was identified by AE to be around 0.6 % in some hybrid QI laminates (see section 5.2).

The reported results show that the loading state is very different between a short initial crack length and a large initial crack length. In the short crack configuration, it could happen that some distributed damage may be generated around the initial crack tip location before the crack propagates. It could lead to secondary intralaminar and translaminar crack nucleation. This difference may explain why secondary damage is triggered in the first case. The distributed stresses around the crack in the short configuration could be due to the 6mm cut-out (used to mount clip gages) that is becoming too close to the crack starter. Thus a modification of the specimen geometry might help mitigate this effect. Nevertheless, none of the baseline samples show evidence of secondary damage in short configuration, highlighting a hybrid effect.

A second hypothesis is the existence of an interaction between the sample free-edges. Indeed, the crack tip is very close to the pre-crack edges when the initial crack is short. As shown by the numerical results (Figure 5.12), these edges interact with the strain field. Furthermore, cracks are known to propagate from free-edge cracking [135]. However, the crack branching does not seem to be caused by free-edge damage propagation and the crack splitting reported in Figure 5.10f appears at almost ten millimeters from the free-edge. Furthermore, the CT specimens were milled by water-jet cutting. The CT-scans performed on OHT samples obtained by the same process show that water-jet cutting induces almost no damage at the sample edges (see Figure 5.27).

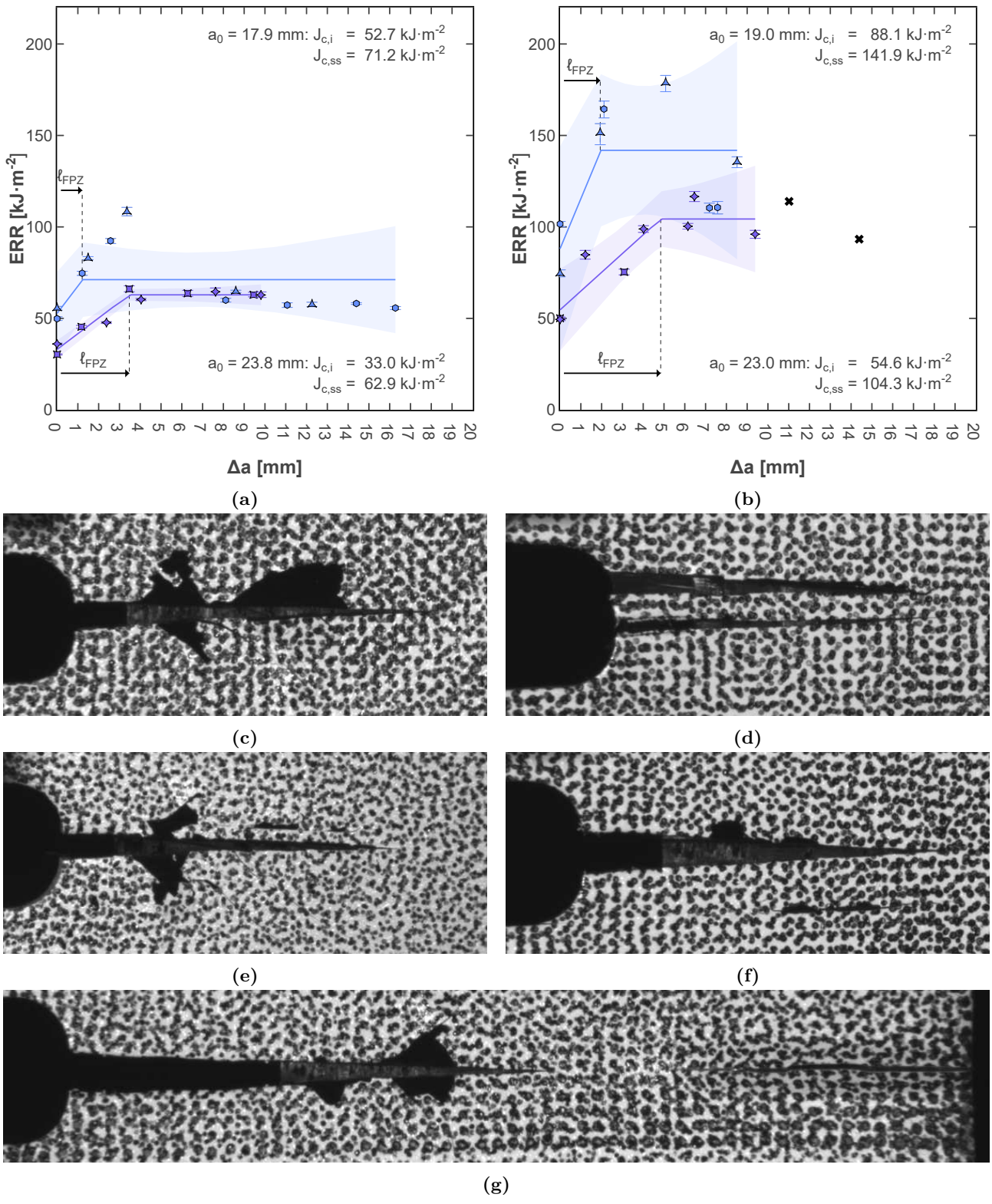

Figure 5.10: R-curves obtained by line J-integral for interlayer hybrid (a) $^{33}\text{L3A}^{60}_{120}$ and (b) $^{14}\text{L5A}^{30}_{180}$; significant crack branching in (c) and (e) short initial crack $^{33}\text{L3A}^{60}_{120}$ specimens (note how the paint layer remains intact otherwise); crack splitting in (d) and (f) short initial crack $^{14}\text{L5A}^{30}_{180}$ specimens; and (g) a crack branching in a large initial crack $^{33}\text{L3A}^{60}_{120}$ specimen leading to immediate backend failure.

Finally, it should be noted that some samples did exhibit secondary damage with large initial cracks as in Figure 5.10. However, the secondary damage apparition was immediately followed by a backend

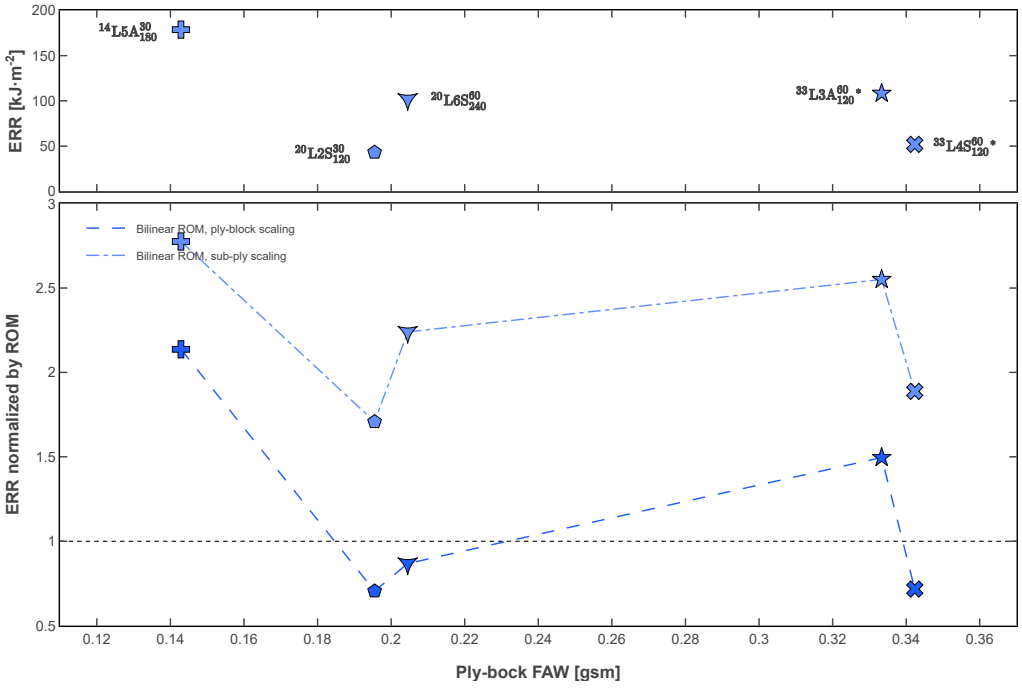

Figure 5.11: Maximal ERR corresponding to secondary damage normalized by RoM for interlayer hybrids.* jittered for readability

or bucking failure and no related ERR increase was reported. The observed contrast may therefore be explained by the sample size. With a large a_0, the sample is not large enough to fully develop the FPZ or fails instantly when secondary damage is triggered.

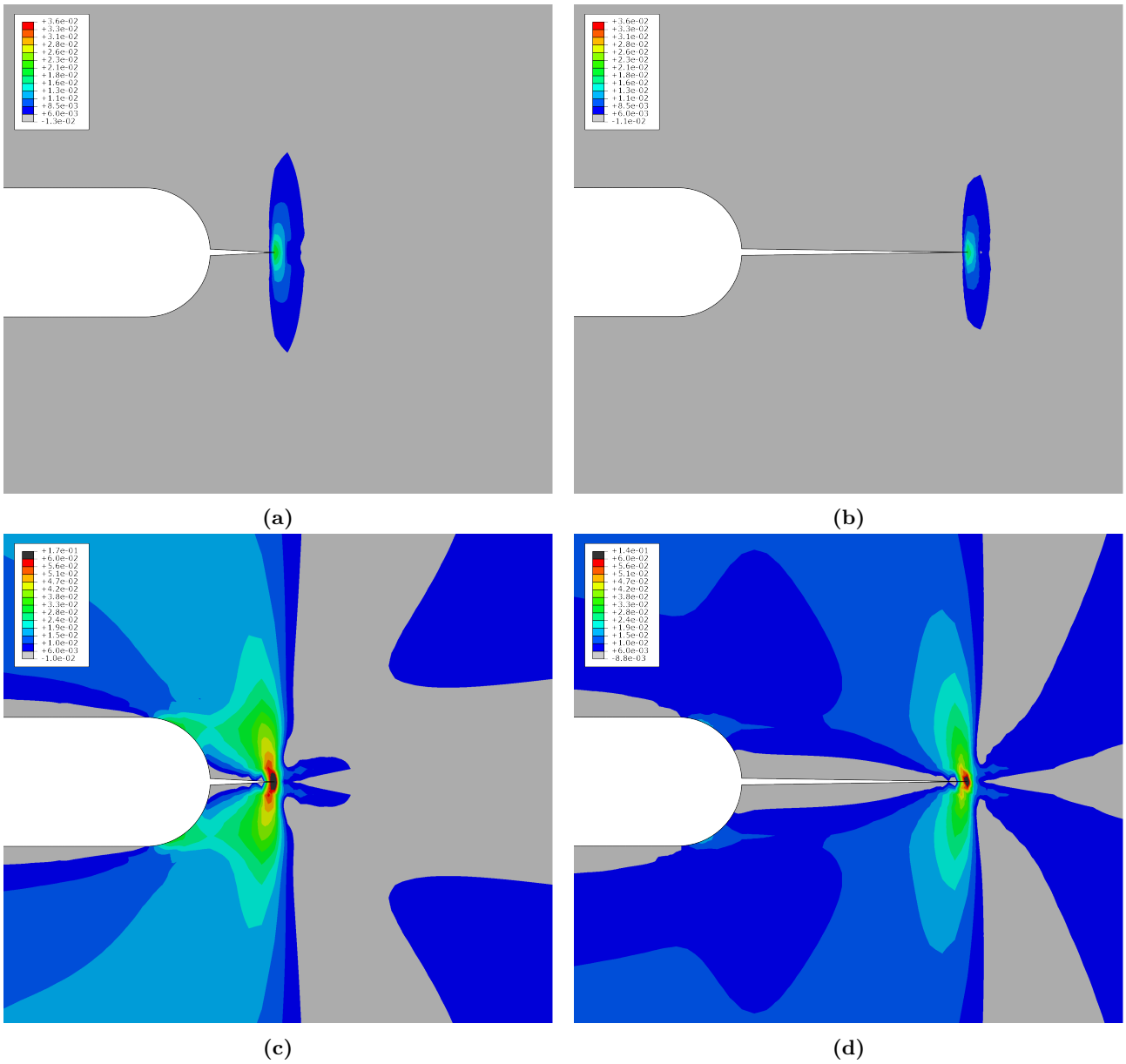

Figure 5.12: Longitudinal strain field predicted by FEM for (a) a short and (b) a large initial crack length; absolute shear strain field for (c) a short and (d) a large initial crack length.

5.2 Unnotched Tensile (UNT) properties

Typical stress-strain curves are shown in Figure 5.13. No hybrids exhibit a stable and noticeable pseudo-ductility. This either means that no fragmentation occurs or that it takes place at a stress level that is very close to the material's ultimate strength such that no load redistribution is possible. The baselines exhibit slightly different moduli from each other. This is due to the symmetric stacking sequence on the 90° ply without doubling it. In the $180\,\mathrm{g}\cdot\mathrm{m}^{-2}$ ply-block baseline ${}^{0}\mathrm{B4}^{0}_{180}$, there is in proportion 25 % more fibers in the 0° direction than in the 90° direction. In the ${}^{100}\mathrm{B1}^{30}_{0}$, this ratio is only 11 %.

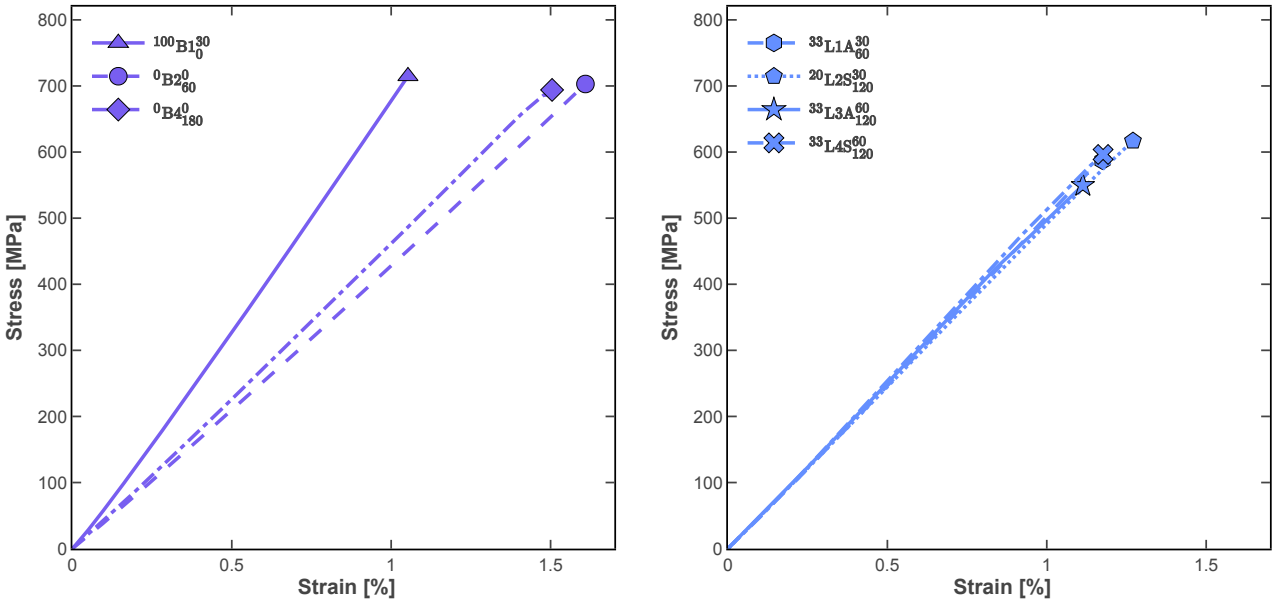

(a) (b)

Figure 5.13: Typical stress-strain curves for QI UNT tests: (a) baselines and (b) interlayer hybrids.

5.2.1 Strength

An overview of the corresponding ultimate strength and stress at the onset of damage normalized to a fiber volume fraction V_f of 50 % is provided in Figure 5.14. The onset of damage was obtained by analyzing AE results as detailed in Appendix B. The 34-700-TP415 system offers a mild ply-thickness effect as compared to the literature. For instance, the strength contrast when going from a FAW of $120\,\mathrm{g \cdot m^{-2}}$ ($^{0}B3^{0}_{120}$) to a FAW of $60\,\mathrm{g \cdot m^{-2}}$ ($^{0}B2^{0}_{60}$) is only 5.8 % while it was reported to be about 14 % for the T800-80ep over a similar range [24]. The toughened TP415 epoxy exhibits 4.89 % of ultimate strain, far more than the 2 % identified as suitable to enable the thin-ply effect by Cugnoni et al. [24]. The observed mild size-effect could therefore be attributed to the fiber type or to the fiber-matrix interface.

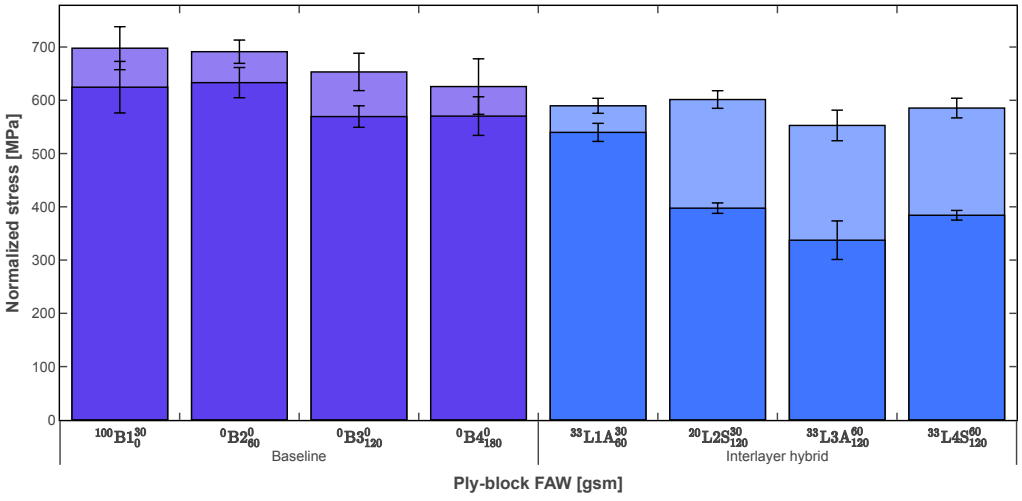

Figure 5.14: Baseline and interlayer hybrid onset of damage (dark colors) and strength (light colors).

Qualitatively, it is noticed that the onset of damage is triggered at lower stresses for the interlayer hybrids. Indeed, the onset of damage corresponds either to low-strain fiber failures, delamination, or transverse cracking which are likely to occur at a much lower strain than the ultimate strain of the high-strain fibers. However, note that the ultimate strength to the onset of damage ratio is much greater for interlayer hybrids. For instance, it is 1.1 for the baseline ${}^{0}\mathrm{B4}^{0}_{180}$ but 1.5 for the interlayer hybrid ${}^{33}\mathrm{L4S}^{60}_{120}$ with the same ply-block FAW. This indicates that while damage appears earlier in interlayer hybrids, it is not critical and does not propagate unstably, allowing the laminate to carry the load up to a stress value slightly inferior to the baseline.

The reduced scatter in strength for the interlayer hybrids are an additional indication that damage occurs in the laminate before reaching its ultimate strength. When it does so, it fails in a more deterministic fashion. This is coherent with the supposed apparition of broken low-strain fiber clusters or fragmented plies acting as stress concentrators.

One noteworthy exception to these observations is the interlayer hybrid ${}^{33}\mathrm{L3A}^{60}_{120}$ whose results are more scattered. Interestingly, this hybrid is one of the configurations reported to exhibit an increased translaminar toughness in section 5.1 (along with ${}^{14}\mathrm{L5A}^{30}_{180}$ which was not tested in tension). This improvement was associated with the triggering of secondary damage, such as crack branching. These mechanisms are likely to be more stochastic than fiber failure and diffuse the damage in the laminate. This interpretation may explain the observed lower and more scattered strength results.

In detail, the 34-700-TP415 strength was found to follow a linear scaling function of the ply-block thickness as depicted in Figure 5.15. This observation agrees with observations reported by Cugnoni et al. [24] for other systems. The stress at the onset of damage was found to be better described by a $1/\sqrt{t}$ scaling law. Again, this is aligned with the results reported in the literature, as the stress evolution at the onset of damage with the ply thickness was shown to be described either by a linear scaling or a $1/\sqrt{t}$ scaling depending on the considered system or the onset of the damage monitoring method. However, linear interpolation could also be suitable considering the scattering and the number of points. These scaling laws are formulated in Equation 5.5 and Equation 5.6.

$$\sigma_H^{ult} = -M_H^{ult} t_H + C_H^{ult} \tag{5.5}$$

$$\sigma_H^{onset} = -\frac{M_H^{onset}}{\sqrt{t_H}} + C_H^{onset} \tag{5.6}$$

Figure 5.16 summarizes the strength results obtained for the interlayer hybrids. Unlike for the translaminar ERR, clear deviations from the ply-thickness scaling are visible for both the onset of damage and ultimate strength. This result indicates that the hybridization effect is the driving mechanism. As detailed in chapter 3, the RoM for strength is expected to follow the bilinear law expressed

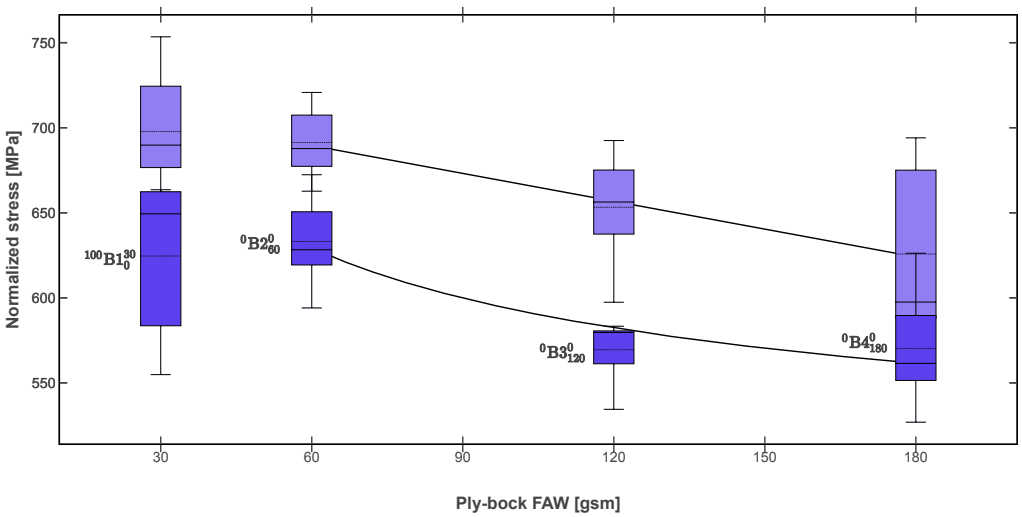

Figure 5.15: Baseline strength scaling.

in Equation 3.4 under displacement-controlled loading. In an idealized hybrid laminate without a hybrid effect, the low-strain fibers are expected to fail first. After their failure, the laminate either fails catastrophically if the low-strain volume fraction γ is too important or the high-strain fibers continue carrying the load up to their ultimate strain.

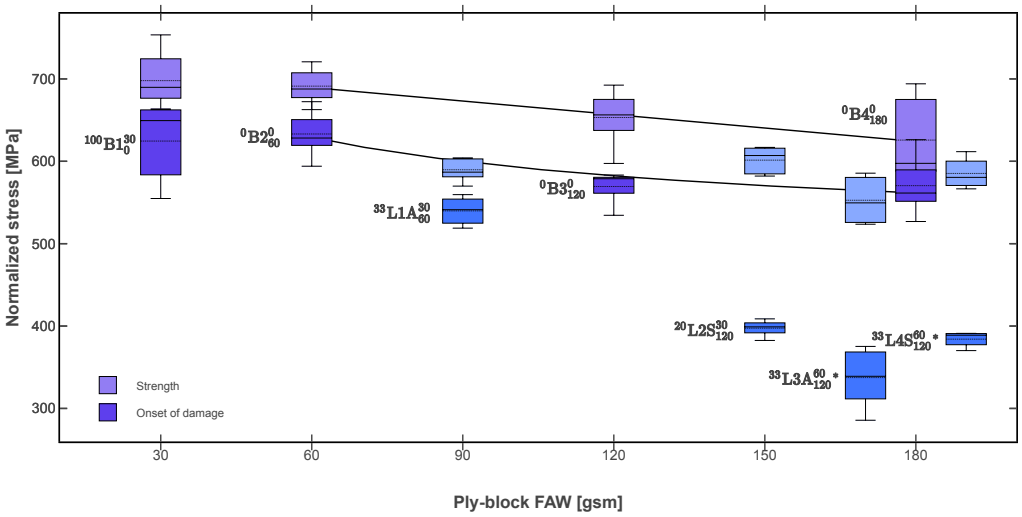

Figure 5.16: Baseline and interlayer hybrid QI onset of damage (dark colors) and ultimate strength (light colors), as a function of ply-block FAW. * jittered for readability

As for the translaminar toughness analysis, an enhanced RoM is proposed to integrate the ply-block thickness scaling (Equation 5.7) or a sub-ply block scaling (Equation 5.8). The construction of these "bilinear" RoM is proposed in Figure 5.17 for interlayer hybrids $^{33}\text{L3A}^{60}_{120}$ and $^{33}\text{L4S}^{60}_{120}$. The HR40-TP415 system was assumed to follow the same scaling law as that reported by [24] for the M40JB high modulus carbon fibers and 120ep toughened epoxy system. Note that even if assuming a constant scaling for the HR40-TP415 (i.e., no strength degradation as the ply thickness increases), the predictions are similar for the low content of low-strain material ($\gamma \leqslant 0.4$) due to the predominant

effect of the high-strain fibers.

$$\begin{cases} \sigma_{hybrid}^{ult} = \sigma_L^{ult}\,(1-\gamma) & \text{for } \gamma \leqslant \alpha \\ \sigma_{hybrid}^{ult} = \sigma_L^{ult}\gamma + \varepsilon_L E_H\,(1-\gamma) & \text{for } \gamma \geqslant \alpha \\ \alpha = \frac{\sigma_H^{ult} - \varepsilon_L E_H}{\sigma_H^{ult} + \sigma_L^{ult} - \varepsilon_L E_H} \\ \sigma_H^{ult} = -M_H^{ult}\,(t_H + t_L) + C_H^{ult} \\ \sigma_L^{ult} = -M_L^{ult}\,(t_H + t_L) + C_L^{ult} \\ \varepsilon_L = -M_L^{\varepsilon}\,(t_H + t_L) + C_L^{\varepsilon} \end{cases} \tag{5.7}$$

$$\begin{cases} \sigma_{hybrid}^{ult} = \sigma_H^{ult}\,(1-\gamma) & \text{for } \gamma \leqslant \alpha \\ \sigma_{hybrid}^{ult} = \sigma_L^{ult}\gamma + \varepsilon_L E_H\,(1-\gamma) & \text{for } \gamma \geqslant \alpha \\ \alpha = \frac{\sigma_H^{ult} - \varepsilon_L E_H}{\sigma_H^{ult} + \sigma_L^{ult} - \varepsilon_L E_H} \\ \sigma_H^{ult} = -M_H^{ult} t_H + C_H^{ult} \\ \sigma_L^{ult} = -M_L^{ult} t_L + C_L^{ult} \\ \varepsilon_L = -M_L^{\varepsilon} t_L + C_L^{\varepsilon} \end{cases} \tag{5.8}$$

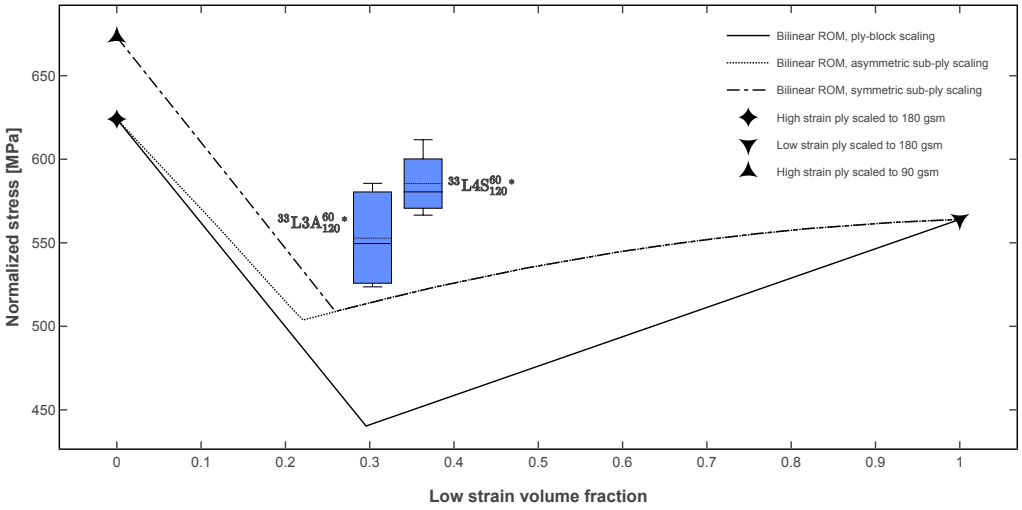

Figure 5.17: Graphical representation of Equation 5.7 and Equation 5.8 evaluated for samples $^{33}\text{L3A}_{120}^{60}$ and $^{33}\text{L4S}_{120}^{60}$ to predict strength values. * jittered for readability

As shown in Figure 5.18, the interlayer hybrid strength was found to be from 10 to 40 % higher than the RoM predictions, highlighting a positive hybrid effect even if it may be overestimated due to the assumption made on the HR40-TP415 scaling law. The hybrid effect is observed to increase with the low-strain volume fraction γ and for the same γ, the hybrid effect is stronger when the ply-block architecture is symmetric rather than asymmetric.

The reported apparent positive hybrid effect is explained by two mechanisms. First, the interaction between the low-strain fibers and the high-strain fibers prevents the former from forming unstable

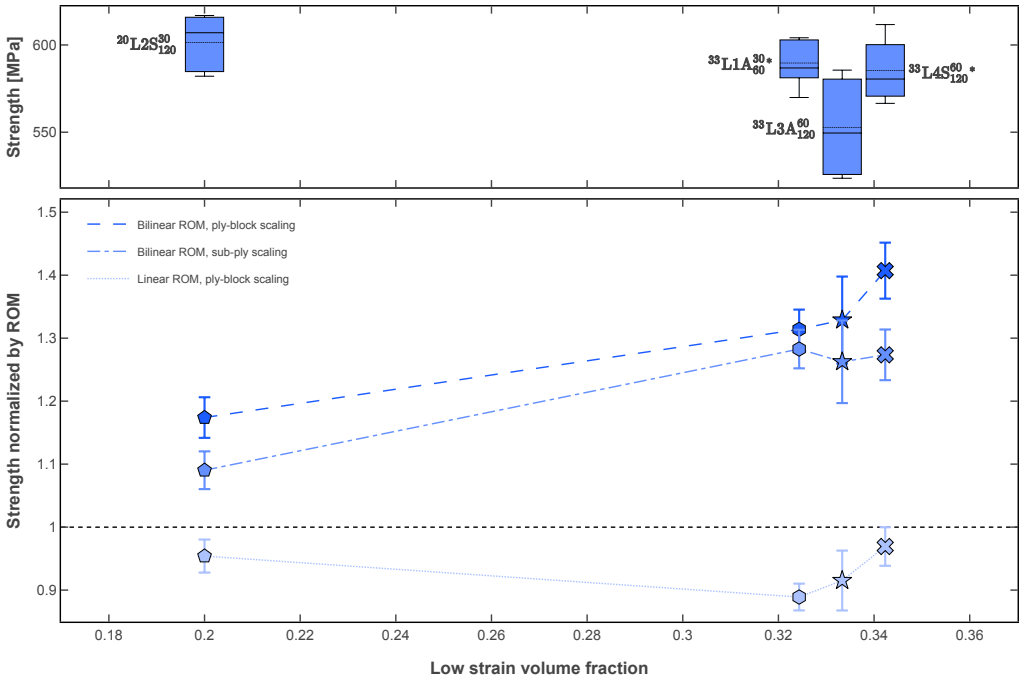

Figure 5.18: Strength normalized by RoM for interlayer hybrids.* jittered for readability

clusters of broken fibers[128]. This delays the low-strain material failure to a strain higher than the one it would have reached alone. Consequently, it improves the laminate strength compared to the RoM predictions.

This effect is clearly visible for hybrid $^{33}L1A^{30}_{60}$ in Figure 5.19 where the onset of damage is delayed to a value higher than the one recorded for the low-strain material alone, and very close to the ultimate failure strain of the HR40. Up to this strain value, there was thus no significant contribution to the cumulative acoustic energy. Therefore, the broken low-strain fibers did not propagate into significant damage. Reaching the same conclusion for $^{20}L2S^{30}_{120}$, $^{33}L3A^{60}_{120}$ and $^{33}L4S^{60}_{120}$ is less straightforward. Indeed, the onset of damage occurs at a strain substantially lower compared to the HR40 alone.

However, these hybrids exhibit extensive delamination. In-situ free-edge observations reported in Figure 5.21 reveal that delamination was triggered at strain values in good agreement with the onset of damage recorded by AE for $^{20}L2S^{30}_{120}$ and $^{33}L3A^{60}_{120}$. In contrast, delamination appears much later in $^{0}B4^{0}_{180}$ and is much less extensive. The delamination is therefore attributed to the presence of HR40 fibers. Indeed, when scaling down the strain at the onset of damage for the HR40 plies, as in Figure 5.20, it is found to be close to the strain at the onset of damage of the hybrid laminate. Note that extensive free-edge delamination was also observed in $^{33}L4S^{60}_{120}$. Some free-edge delamination was also observed in $^{33}L1A^{30}_{60}$, but it remained confined to the outer skin.

Furthermore, Figure 5.19 indicates that $^{33}L3A^{60}_{120}$ fails at the ultimate strain of the HR40 fiber. On the one hand, this is remarkable considering its high content of low-strain material and the extent of delamination reported in Figure 5.21. On the other hand, it suggests that critical damage in the

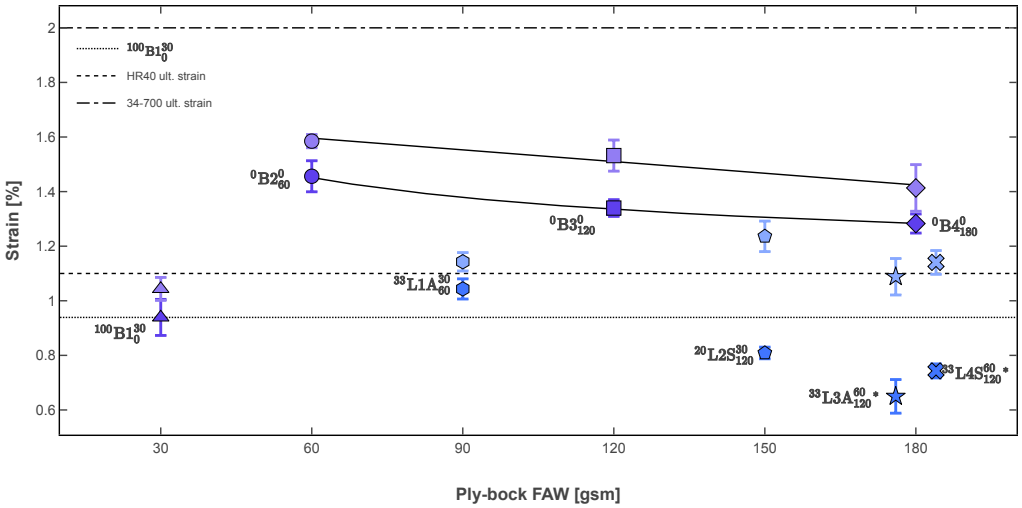

Figure 5.19: Baseline and interlayer hybrid strain at the onset of damage monitored by AE (dark colors) and failure (light colors), acquired with strain gauges, and compared to the HR40 ultimate strain (1.1 %) and 34-700 ultimate strain (2 %).

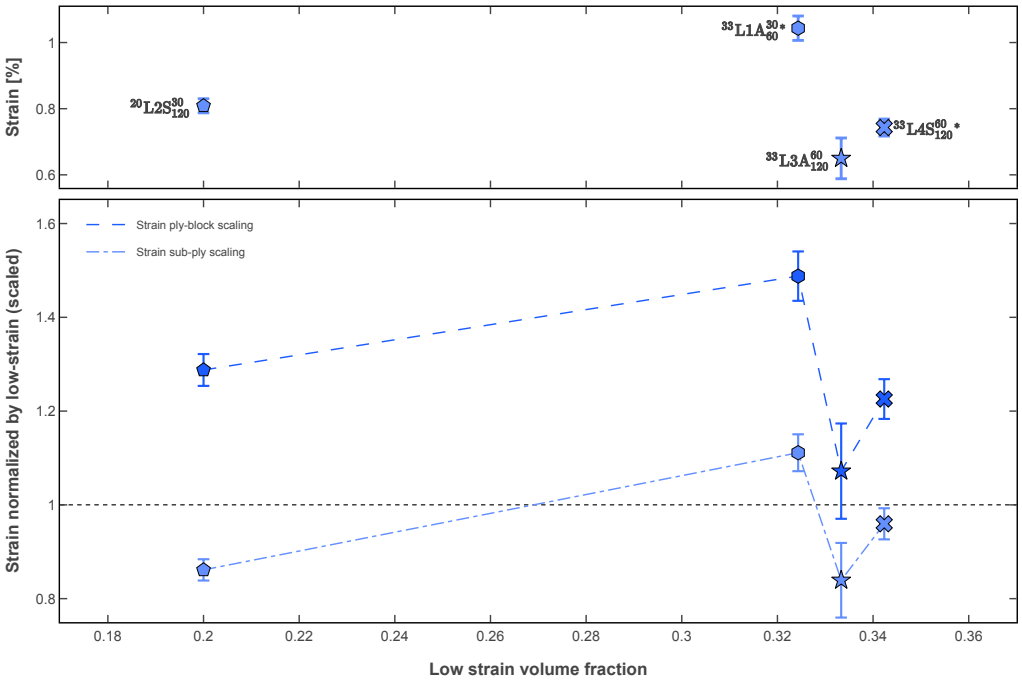

Figure 5.20: Interlayer hybrid strain at the onset of damage monitored by AE, acquired with strain gauges and normalized with respect to the scaled HR40 strain at the onset of damage. * jittered for readability

low-strain material was delayed up to the ultimate failure of the low-strain fibers. Therefore, fiber hybridization can be seen as having the same effect as reducing the ply thickness on the low-strain material strength. As the low-strain volume fraction increases, the laminate modulus increases. For the same failure strain, it leads to higher strength and explains the reported increase of the apparent hybrid effect with V_f. Note that there should exist a low-strain volume fraction limit beyond which a positive hybrid effect is not possible, but it was not reached in this work.

A second mechanism is at play. When the low-strain fraction is such that its failure does not lead to

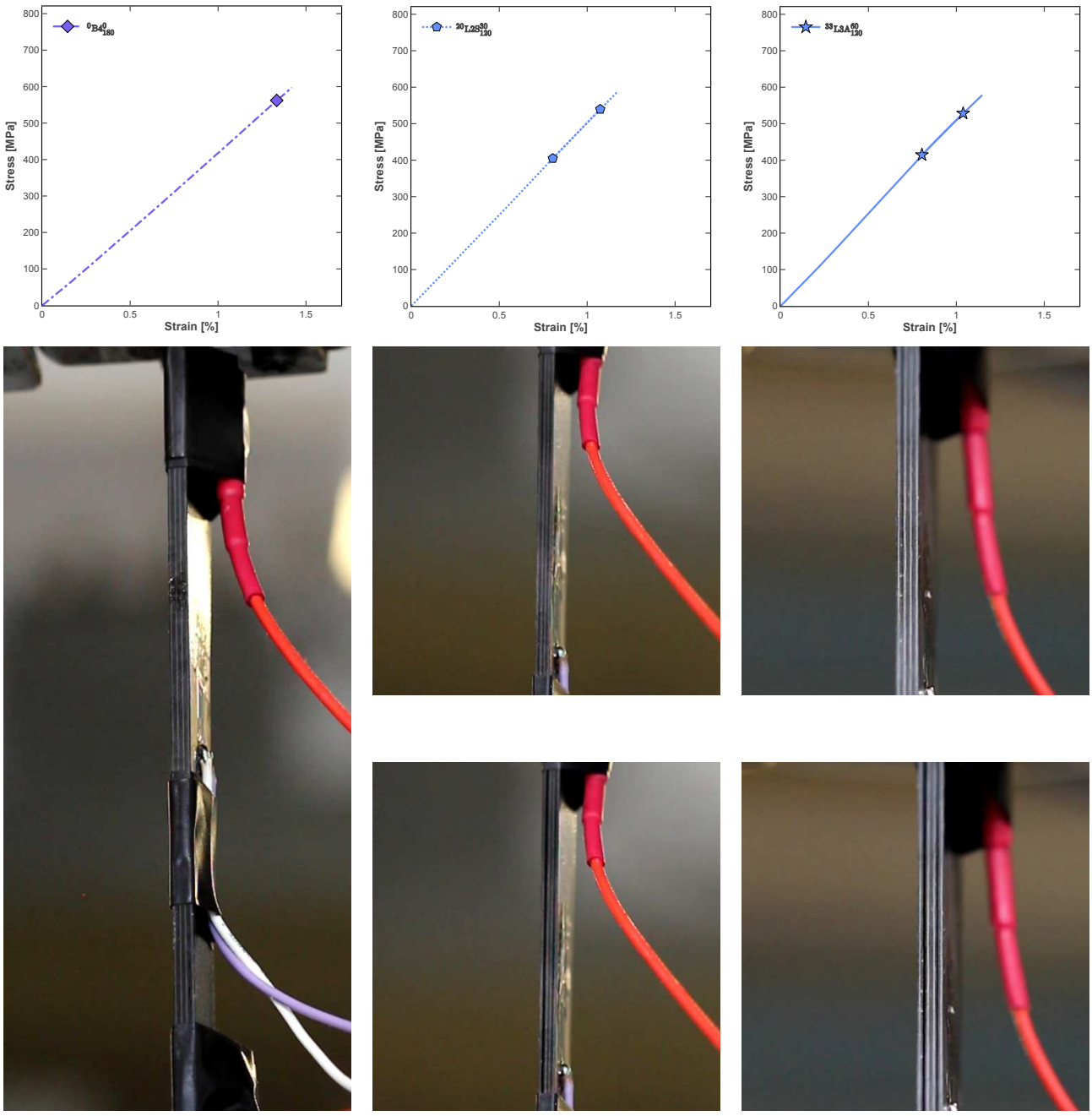

(a) $^{0}\mathrm{B4}^{0}_{180}$ **(b)** $^{20}\mathrm{L2S}^{30}_{120}$ **(c)** $^{33}\mathrm{L3A}^{60}_{120}$

Figure 5.21: In-situ monitoring of free-edge delamination. The symbols on the load curves highlight the load state of the sample when the pictures were acquired. For each sample, the first picture corresponds to the first visible delamination. For $^{20}\mathrm{L2S}^{30}_{120}$ and $^{33}\mathrm{L3A}^{60}_{120}$, the second picture corresponds to the laminate state few moments before failure and highlights extensive but not catastrophic delamination in the outer plies.

the catastrophic failure of the hybrid laminate nor delamination [169], the high-strain fibers continue to carry the load. This effect is reinforced by a higher dispersion that leads to a more gradual failure of the low-strain material [150], as in symmetric ply-block architecture. For instance, $^{20}\mathrm{L2S}^{30}_{120}$ is reported to fail at a strain 10 % higher than that of the HR40 fibers. Similarly, $^{33}\mathrm{L1A}^{30}_{60}$ and $^{33}\mathrm{L4S}^{60}_{120}$ fail at a strain slightly higher than the HR40. As the RoM predicts that their failure is dominated by the low-strain material, it explains the apparent positive hybrid effect.

The absence of load drops or change in modulus in the stress-strain curves (Figure 5.2b) shows that the observed delamination was not catastrophic. Moreover, it indicates that no pseudo-ductility was achieved. Nevertheless, the failure of $^{20}\mathrm{L2S}^{30}_{120}$ well above the HR40 ultimate strain suggests that fragmentation may have happened despite the extensive delamination.

From a practical point of view, a linear RoM on the laminate strength is more informative as it indicates to designers if hybridizing two fibers provides better properties. As indicated by Figure 5.18, this approach leads to a negative hybrid effect of a few percent. More interestingly, the scaled linear RoM provides strength predictions within roughly 10 % of the reported values.

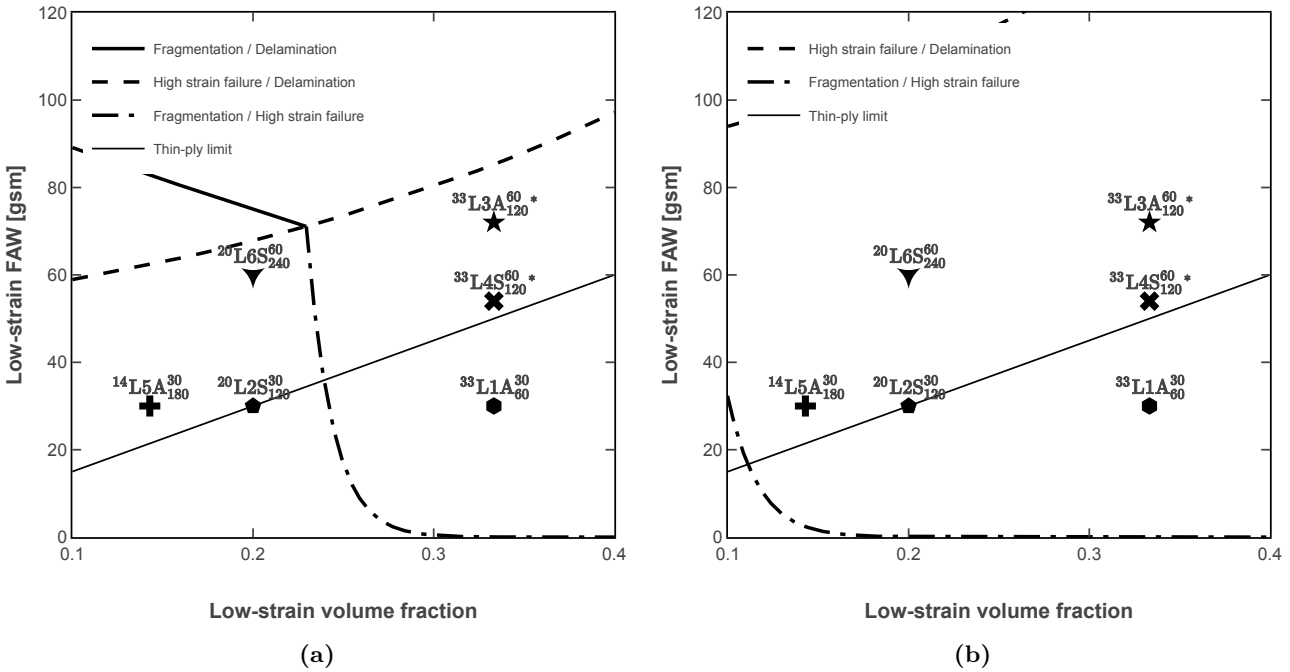

Figure 5.22: Failure maps: (a) original failure map assuming 2 % of ultimate strain for the 34-700 fiber as specified by the datasheet and (b) updated failure map assuming 1.6 % of ultimate strain for the 34-700 fiber as measured in QI UNT samples. * jittered for readability

Finally, Figure 5.19 indicate that the low-strain baselines reach at best 1.6 % of ultimate strain ε_H. This represents a 20 % decrease with the value of 2 % reported by the manufacturer's datasheet, although no extensive damage diffusion was observed for the $60\,\mathrm{g}\cdot\mathrm{m}^{-2}$ baseline, indicating that the failure is close to the one of the 0° ply. In comparison, the M40JB-80ep system reached an ultimate strain only 8 % lower than the fiber strain for a FAW of $75\,\mathrm{g}\cdot\mathrm{m}^{-2}$, and 3 % lower for a FAW of $30\,\mathrm{g}\cdot\mathrm{m}^{-2}$. This is a key observation that implies that the failure map was designed with a significantly overestimated strain value. An updated failure map for a strain of 1.6 % is shown in Figure 5.22. In this case, all the configurations are expected to fail by low-strain failure, in good agreement with the experimental observations.

5.2.2 Modulus

Figure 5.23 shows that the QI interlayer hybrid laminates follow a perfect linear RoM for their moduli, as expected. The absence of deviations highlights the good quality achieved when manufacturing the laminates, especially in terms of FAW uniformity and fiber orientation. It also indicates that calculating the fiber volume fraction as in Equation 3.6 is a valid method. Moreover, the relative volume fraction of low-strain and high-strain fibers can be confidently evaluated according to the prepreg FAW for interlayer hybrids. Finally, it implies that modulus values can be used as an indirect measurement of γ for interyarn and intrayarn microstructures where the FAW value can not be used.

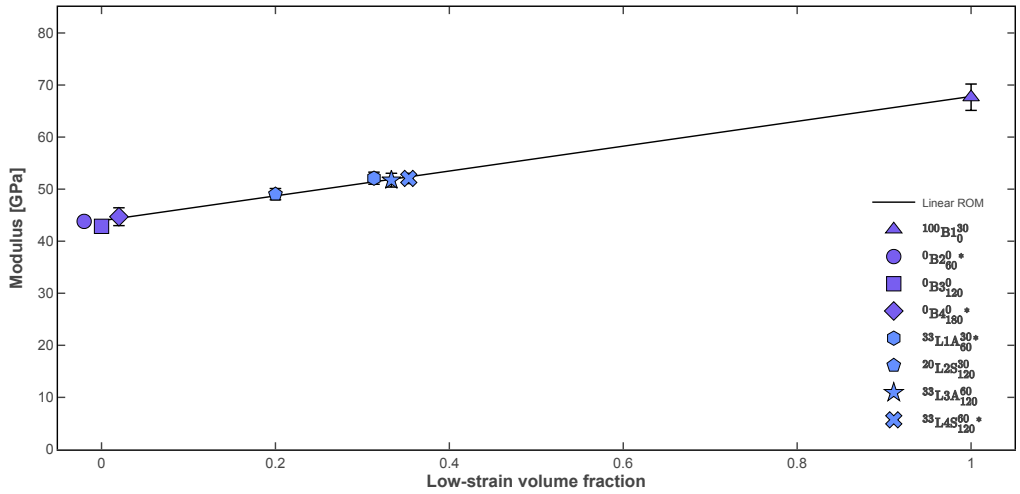

Figure 5.23: Baseline and interlayer hybrid ERR at initiation (dark colors) and steady-state (light colors), reduced with the line J-integral method, as a function of ply-block FAW. * jittered for readability

5.3 Open Hole Tensile (OHT) properties

The tests reported in this section were performed by the author at the University of Bristol (United Kingdom) as part of his secondment here, except for the CT-scan that the University of Bristol performed and reconstructed but were analyzed by the author. The author gratefully acknowledges Prof. Michael Wisnom, Dr. Xiaodong Xu, and Xiaoyang Sun for their assistance with the experimental work and analysis, and for making available their CT-scan resources.

The typical loading curves for the OHT specimens are shown in Figure 5.24. The samples were obtained from the same laminates as for the UNT ones. Qualitatively, the load-displacement curves are very similar for all configurations. This observation is confirmed by the OHT far-field strength and notch sensitivity, which is defined as the ratio of OHT strength over the UNT strength, as reported in Figure 5.25. The notch strength is almost the same for every configuration, including the baselines. This result goes against the expectations and previous observations found in the literature. Indeed, thin-plies are brittle and expected to be more sensitive to notch than thick-plies. For instance, Amacher et al. [38] reported a 22 % decrease in far field strength when reducing the ply-block FAW

from $150\,\mathrm{g}\cdot\mathrm{m}^{-2}$ ($510 \pm 40\,\mathrm{MPa}$) to $75\,\mathrm{g}\cdot\mathrm{m}^{-2}$ ($399 \pm 10\,\mathrm{MPa}$) in M40JB-80ep samples.

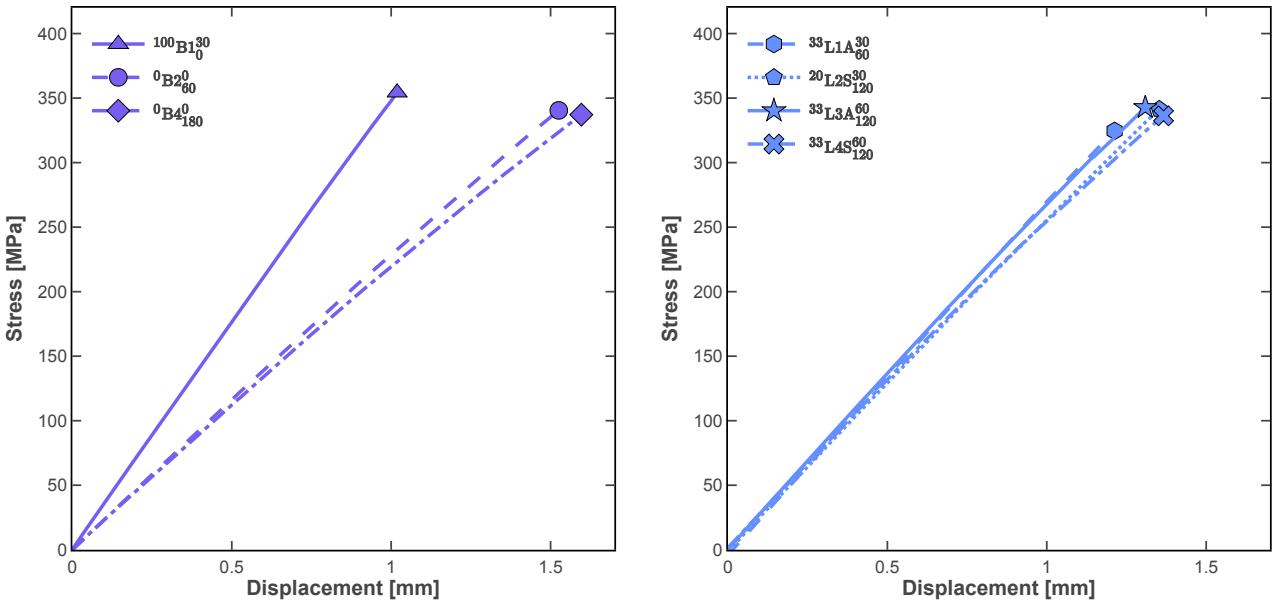

(a) **(b)**

Figure 5.24: Typical load-displacement curves for QI OHT tests: (a) baselines and (b) interlayer hybrids.

Two different possible causes may explain this result. First, a sample width to hole diameter ratio of 5 ($W/D = 5$) was used while ASTM D5766-11 guidelines recommend a ratio of 6 as used by Amacher et al. [38]. However, the rest of the dimensions are in accordance with the standard. Furthermore, if the fracture process was purely driven by the circular hole, the failure would be purely brittle and the notch strength reduction would theoretically reach a value of 3. The maximal value of 1.7 obtained for the baseline $^{0}B2^{0}_{60}$ as shown in Figure 5.25 indicate that this is not the case. Finally, the post-mortem observations of OHT specimens reported in Figure 5.26 clearly show a transition from a brittle-like failure in samples exhibiting a low ply-block FAW and a low γ towards a more diffuse failure in samples exhibiting a larger ply-block FAW or a larger γ.

A second hypothesis is that as exposed in section 5.2, the ply-thickness effect is mild for the 34-700-TP415 system. Thus, the contrast between intermediate ply-block thicknesses and thin-plies is not as sharp as for the M40JB-80ep system, for instance. Indeed, the notch strength reduction of 1.5 reported for $^{0}B4^{0}_{180}$ is slightly inferior to the notch reduction of 1.7 reported for $^{0}B2^{0}_{60}$. In this case, testing thicker ply-block laminates would highlight improved contrasts.

All in all, the fiber hybridization brings an apparent notch strength reduction improvement compared to the baselines. While this outcome may appear as positive, it is only the consequence of two simultaneous effects that may be purely fortuitous. Firstly, the far-field OHT strength remains almost constant, against all expectations. Secondly, the UNT strength of interlayer hybrids is lower than the baseline one. Thus, the notch strength reduction decreases with the hybridization, but this does not

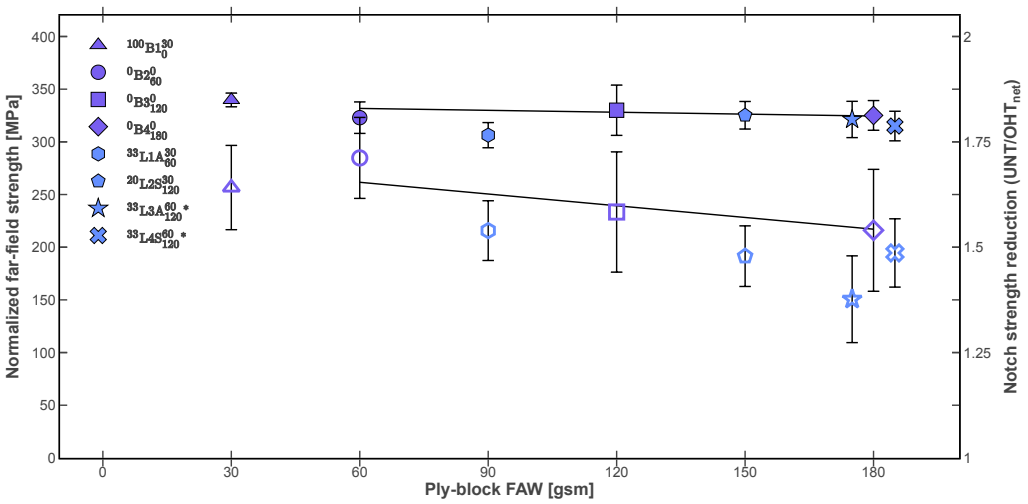

Figure 5.25: Baseline and interlayer hybrid OHT far-field strength (filled symbols) and notch strength reduction (open symbols). Values normalized for 50 % V_f. * jittered for readability

correspond to an absolute increase of the OHT tensile strength.

To investigate the failure mechanisms at play, OHT specimens were loaded to 95 % of the ultimate OHT load, then unloaded and analyzed with CT-scan. The results, reported in Figure 5.27, show a clear suppression of damage in very-thin ply before the failure ($^{100}B1_0^{30}$). As the ply-block thickness increases, transverse cracking appears in the 90° and 45° plies ($^{0}B2_{60}^{0}$ to $^{0}B4_{180}^{0}$), but no delamination or debonding. It is interesting to note that a small longitudinal split of the 0° plies can be observed near the hole, which has been found in the literature to cause a reduction of the stress concentration. On the contrary, the formation of diffuse delamination and significant ply-block debonding and ply pull-out (few mm) is observed in all interlayer hybrids, and to a greater extent in the asymmetric ply-block architecture ($^{33}L3A_{120}^{60}$ and $^{14}L5A_{180}^{30}$) which develop a FPZ up to 3 mm in the 0° direction before failure. This is confirmed by the post-mortem observations (Figure 5.26), where 0° pull-out is visible for $^{33}L3A_{120}^{60}$ and $^{14}L5A_{180}^{30}$.

Nevertheless, these observed changes in failure mechanisms did not lead to a change in OHT strength while it led to a change in propagation ERR in CP laminates (see section 5.1). In contrast to OHT specimens, CT specimens allow for the development of a stable FPZ. The experimental results collected in this work tend to indicate that the development of a large FPZ is required for interlayer hybrids to exhibit damage resistance. Indeed, the initiation ERR values were found not significantly improved by interlayer hybridization. This is aligned with the observations of [56] who reported no positive hybridization effect in T800-HR40 interlayer hybrids. They used DENT specimens to characterize the translaminar toughness. This specimen geometry is also not suitable to grow stable crack propagation, thus a fully developed FPZ can not be established, which limits the R-curve effect.

Finally, the obtained results contrast for instance with those reported by Sapozhnikov et al. [225] for pseudo-ductile carbon-carbon hybrids. It confirms that no significant pseudo-ductility took place, at

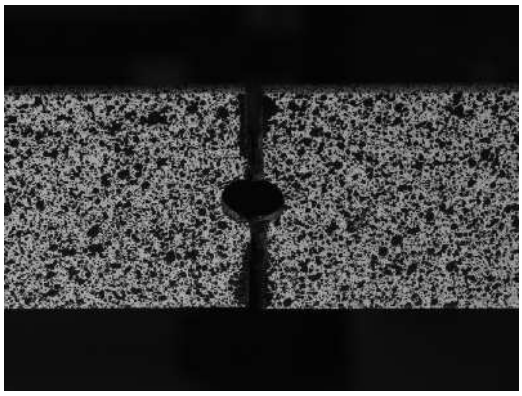

(a) $^{100}\mathrm{B1}_{0}^{30}$

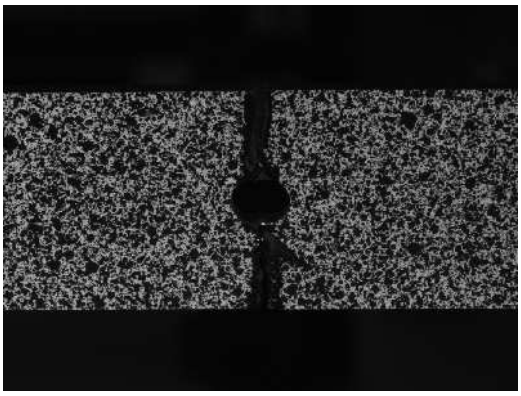

(b) $^{0}\mathrm{B2}_{60}^{0}$

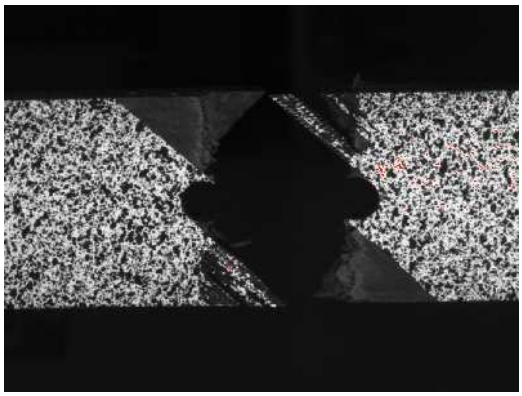

(c) $^{0}\mathrm{B3}_{120}^{0}$

(d) $^{0}\mathrm{B4}_{180}^{0}$

(e) $^{33}\mathrm{L1A}_{60}^{30}$

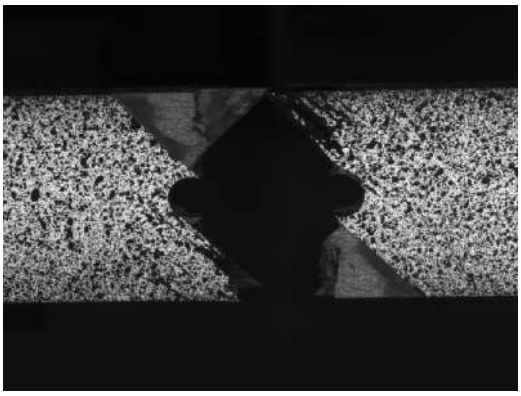

(f) $^{20}\mathrm{L2S}_{120}^{30}$

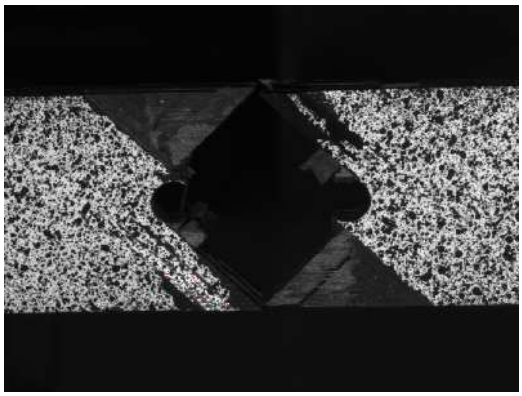

(g) $^{33}\mathrm{L3A}_{120}^{60}$

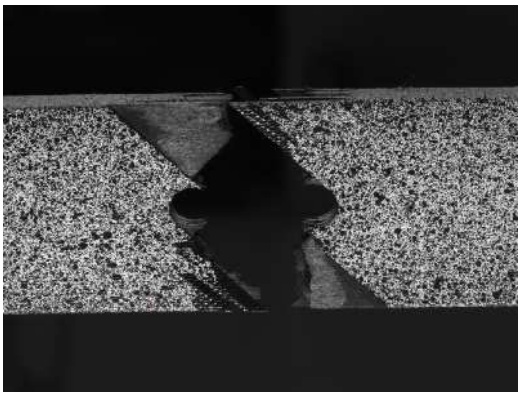

(h) $^{33}\mathrm{L4S}_{120}^{60}$

Figure 5.26: Post-mortem failure of OHT specimens.

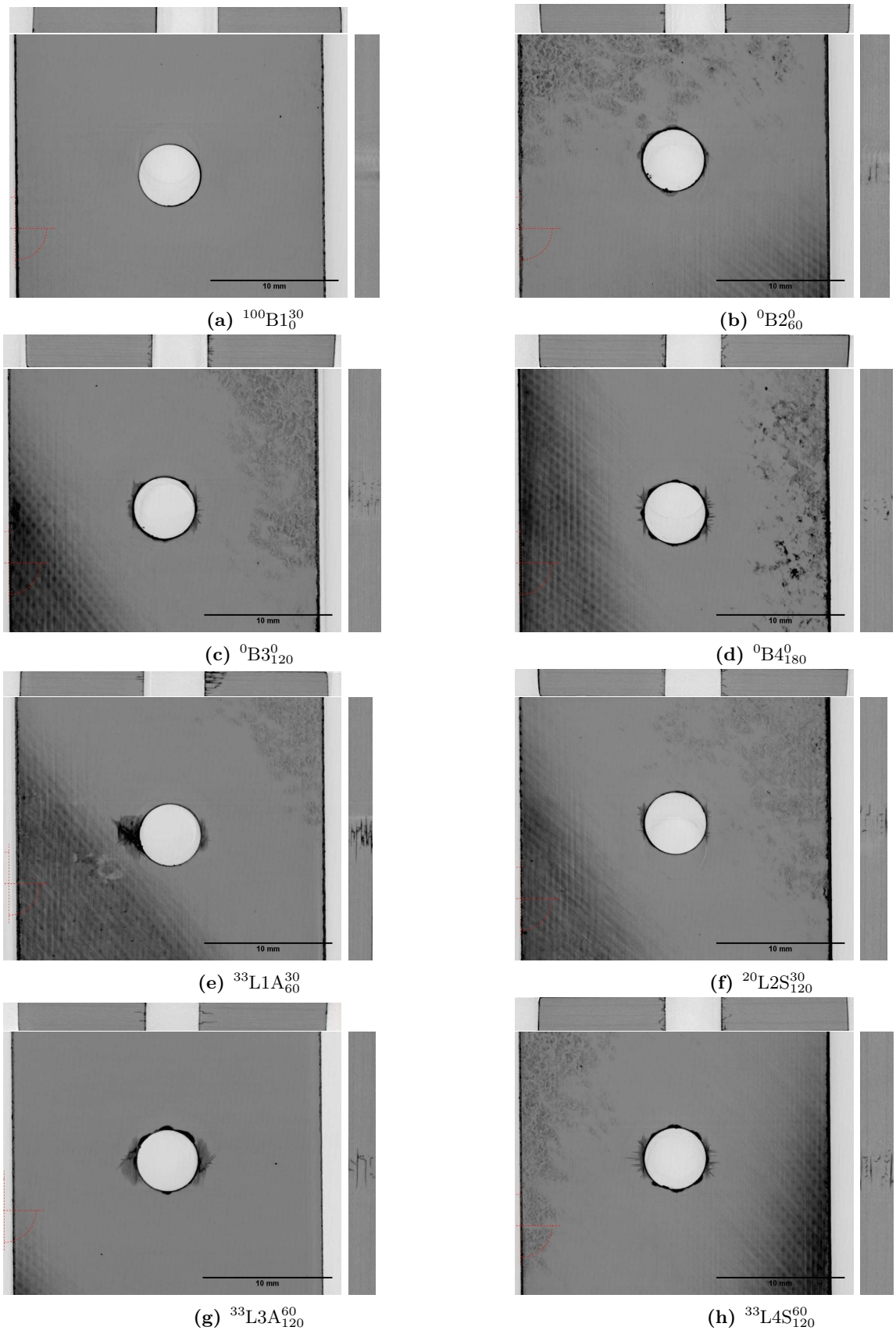

(a) $^{100}\mathrm{B1}_{0}^{30}$ **(b)** $^{0}\mathrm{B2}_{60}^{0}$

(c) $^{0}\mathrm{B3}_{120}^{0}$ **(d)** $^{0}\mathrm{B4}_{180}^{0}$

(e) $^{33}\mathrm{L1A}_{60}^{30}$ **(f)** $^{20}\mathrm{L2S}_{120}^{30}$

(g) $^{33}\mathrm{L3A}_{120}^{60}$ **(h)** $^{33}\mathrm{L4S}_{120}^{60}$

Figure 5.27: CT-scan of OHT samples after loading to 95 % of the OHT strength. The loading direction is aligned with the vertical direction of the document.

least for the baseline and symmetric hybrid specimens. For the asymmetric hybrids, the fact that a large FPZ is observed could be considered as a sign of local pseudo ductility, but as pseudo-ductility was not observed at the macroscale in UNT tests, it may be wiser to consider it as a large FPZ that can develop stably thanks to R-curve effect. It is worth noting that all hybrid and thick-ply laminates exhibit a longitudinal crack split at the apex of the hole (see Figure 5.27). This longitudinal split cancels the stress singularity introduced by the hole. Thus, it makes sense that the OHT strength is similar for hybrids and thick baselines.

5.4 Conclusion

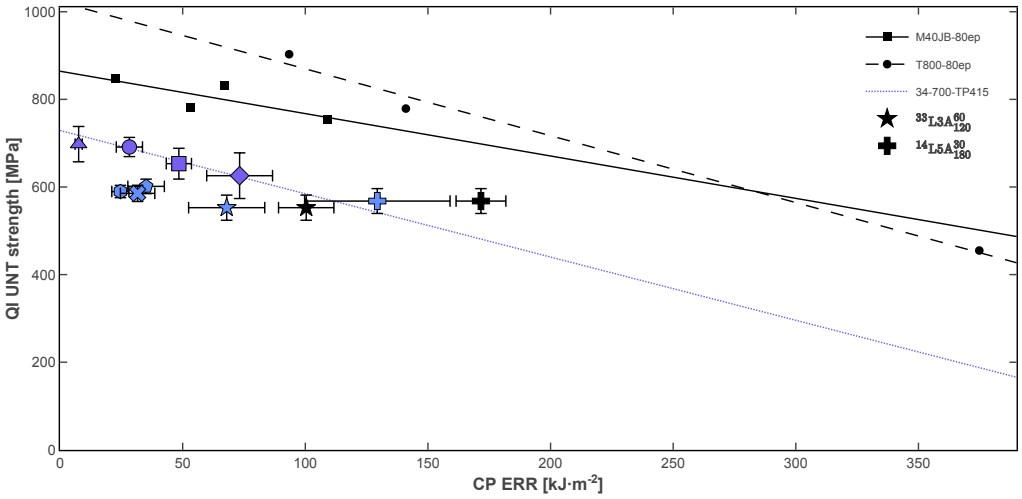

Figure 5.28: Ashby plot of the QI UNT strength with respect to the CP translaminar toughness of the interlayer hybrids. The strength of $^{14}\text{L5A}^{30}_{180}$ was predicted according to the scaled RoM. M40JB-80ep reference values: ERR from [39], strength from [38]. T800-80ep reference values: ERR from DENT tests [56] and [175] assuming a similar behavior for the IM21 system, strength scaled from [24].

This chapter reported the results of the extensive experimental characterization carried out on interlayer hybrids produced with 34-700 and HR40 carbon thin-plies, pre-impregnated with the TP415 epoxy. Overall, interlayer hybridization is an approach highly compatible with the existing manufacturing processes and was used to produce high-quality laminates with an autoclave. The reported results highlight several key points:

- It is noticed that the thin-ply systems reported in the literature, notably by Danzi et al. [56] and [24], follow a linear relationship between the QI UNT strength and the CP steady-state ERR as depicted in Figure 5.28. The 34-700-TP415 system follows the same trend. Then, the performance of fiber hybridization can be evaluated against this linear relationship. Most of the interlayer hybrids are below the 34-700-TP415, indicating that the loss of strength caused by the hybridization is not compensated by the gain of translaminar toughness. Only the specimens exhibiting secondary damage for short initial crack have shown a large enough improvement in ERR to improve this ratio. Note that the propagation plateau was never reached for these specimens and that they may exhibit an even higher steady-state translaminar toughness.

- Interlayer hybrids increase the design space for thin-ply composites, as the QI laminate modulus follows a perfect linear RoM and can be tuned without varying the fiber volume fraction of laminates.

- When the ply-block FAW is below $100\,\mathrm{g}\cdot\mathrm{m}^{-2}$, the onset of damage of the laminate is delayed up to almost the ultimate strain of the low-strain fibers, even for high γ and asymmetric architectures ($^{33}\mathrm{L1A}^{30}_{60}$).

- Interlayer hybridization changes significantly the damage sequence as reported in Figure 5.29. For the same ply-block thickness, the interlayer hybrids $^{33}\mathrm{L3A}^{60}_{120}$ and $^{33}\mathrm{L4S}^{60}_{120}$ are reported to trigger extensive delamination while $^{0}\mathrm{B4}^{0}_{180}$ does not. This effect is reinforced in $^{33}\mathrm{L3A}^{60}_{120}$ that exhibits an asymmetric interlayer. Consequently, these hybrids exhibit a substantial negative hybrid effect on the onset of damage. The promoted delamination is attributed to an increased mismatch of moduli at the ply-block interfaces.

- The reported hybrid configurations all fail for a strain superior or equal to the ultimate strain of the low-strain fiber.

- The interlayer hybridization yields a substantial positive hybrid effect with respect to the scaled bilinear RoM, even in thick ply-blocks and in the presence of extensive delamination. This is attributed to the protective action of the high-strain fibers on the low-strain fibers, allowing them to reach their ultimate stain while they would fail earlier in a non-hybrid laminate. This is possible because, at the considered ply-block FAW, the HR40 ultimate strain remained below the strain of the onset of damage in the high-strain plies.

- However the hybrid laminate ultimate strain always remained below the strain of the onset of damage of the high-strain plies. This indicates that it was not possible to trigger proper fragmentation of the low-strain plies, in contrast to the prediction of the failure map (Figure 5.22a). Note that the ultimate failure strain of the 34-700 laminates reached at best 1.6 % with $60\,\mathrm{g}\cdot\mathrm{m}^{-2}$ ply-block, far from the 2 % value proposed by the datasheet. This indicates that this particular material system can not achieve a full thin-ply effect as discussed in section 7.4. In any case, the high-strain material never reaches the strain for which the failure map was designed.

- Consequently, the positive hybrid effect in the steady-state ERR reported for $^{33}\mathrm{L3A}^{60}_{120}$ is correlated to the presence of delamination in the QI laminate and secondary damage in the CP laminate Figure 5.29, but not to ply fragmentation. This effect is promoted by an asymmetric ply-block architecture.

- The OHT tensile strength was reported almost unaffected by the ply-block FAW or hybridization, although different failure mechanisms where observed by CT-scan. This finding is against the state-of-the-art literature and suggests that another mechanism is at play. Further studies should investigate it.

Finally, interlayer hybridization comes with two major drawbacks. First, the fiber dispersion is limited. Second, the hybridization increases the ply-block thickness and this is all the more true when low γ is required. As a consequence, even in the presence of a positive hybrid effect, the interlayer hybrids do not reach the outstanding properties of thin-ply composites, as highlighted in Figure 5.28. Thus, interyarn and intrayarn fiber-hybridization will be investigated in the following chapter.

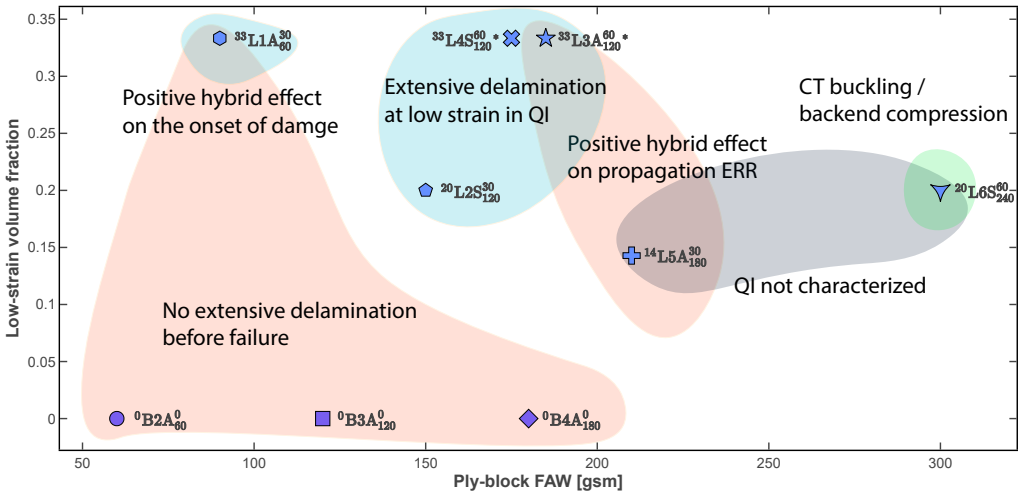

Figure 5.29: Overview of experimental hybrid effects observed in this work. * jittered for readability

Chapter 6

Interyarn and intrayarn hybrids

What is the influence of a more dispersed microstructure on the fiber-hybrid composites?

The list of available data, codes, and publications generated for this work is available on Zenodo [204].

This chapter summarizes the experimental results for the translaminar toughness characterization in CP laminates and for the UNT and OHT properties in QI laminates made of interyarn and intrayarn fiber-hybrid thin-plies. Overall, the same chapter structure, as well as methods, are employed for direct comparison. As such, not all the details are repeated twice and the reader is referred to chapter 5 and chapter 3 for a detailed discussion of the material and testing methodology choices.

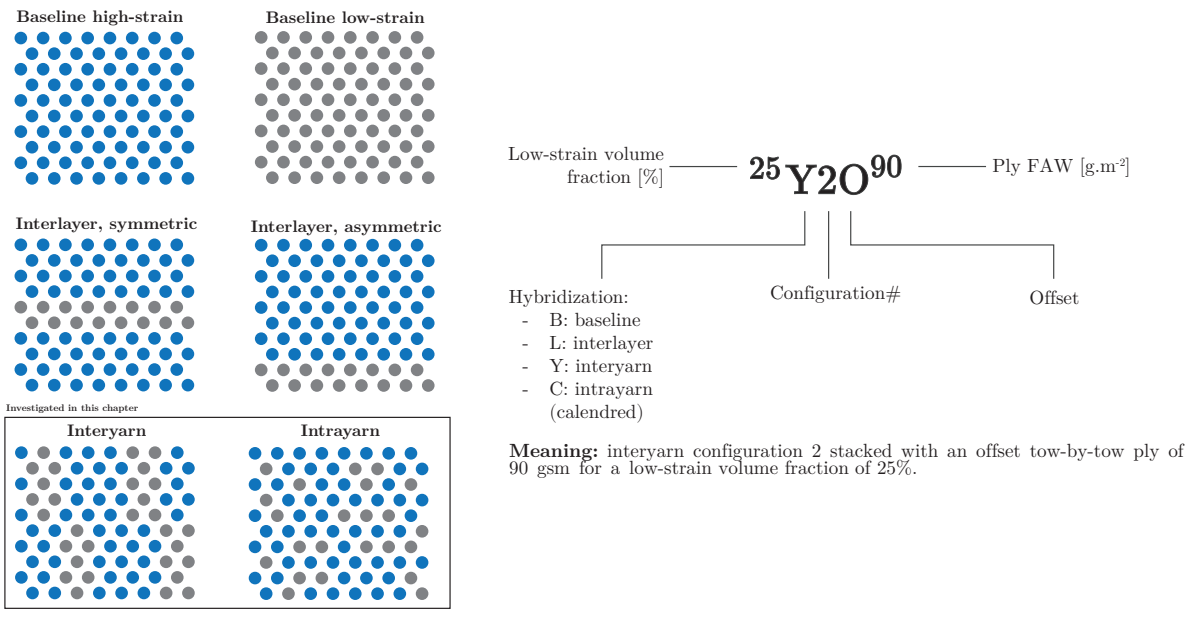

Figure 6.1: Interlayer hybrid nomenclature.

Designation	**Stacking**	E_1 **[GPa]**	E_2 **[GPa]**	G_{12} **[GPa]**	ν_{12}	V_f [%]
$^{100}\mathrm{B1}_{0}^{30}$	$\left[\left(90^L/0^L\right)_{70}/90^L\right]_s$	104.44	103.05	2.88	0.017	51.2
$^{0}\mathrm{B2}_{60}^{0}$	$\left[\left(0^H/90^H\right)_{30}/0^H\right]_s$	64.38	62.49	2.86	0.027	50.9
$^{0}\mathrm{B3}_{120}^{0}$	$\left[\left(90_2^H/0_2^H\right)_{15}/90_2^H\right]_s$	61.46	65.17	2.85	0.026	50.8
$^{0}\mathrm{B4}_{180}^{0}$	$\left[\left(90_3^H/0_3^H\right)_{10}/90_3^H\right]_s$	60.35	65.80	2.84	0.026	50.6
$^{25}\mathrm{Y1}^{90}$	$\left[(90/0)_{20}/90\right]_s$	71.04	74.30	2.82	0.023	50
$^{25}\mathrm{Y2O}^{90}$	$\left[(90/0)_{20}/90\right]_s$	71.04	74.30	2.82	0.023	50
$^{31}\mathrm{Y3}^{45}$	$\left[(90/0)_{42}/90\right]_s$	74.22	75.83	2.82	0.022	50
$^{20}\mathrm{C1}^{75}$	$\left[(90/0)_{24}/90\right]_s$	69.38	72.02	2.82	0.023	50
$^{33}\mathrm{C2}^{45}$	$\left[(90/0)_{42}/90\right]_s$	75.25	76.53	2.82	0.022	50

Table 6.1: Elastic constants for for interyarn and intrayarn hybrids CT specimen laminates obtained by CLT [227] assuming the datasheet properties published by Grafil.

As aforementioned, laminates were designed to optimize toughness, the onset of damage, and manufacturability. High-strength 34-700 and high modulus HR40 continuous PAN-based carbon fibers from Grafil were selected as high-strain and low-strain materials, respectively. In this chapter, they were spread as interyarn and intrayarn tapes (see Figure 6.1) according to a manufacturing technique developed by Argyropoulos (NTPT). The main advantages of interyarn and intrayarn tapes are, besides the improved fiber dispersion that may enable new effects, the possibility to achieve lower low-strain volume fraction γ compared to interlayer hybrids of similar FAW. Moreover, these novel materials bring competitive advantages in terms of manufacturability as they are ready-to-process and do not require complex stacking sequences, as reported in Table 6.1. It is worth noting that the manufacturing parameters and fiber dispersion performances are not discussed in this thesis, instead, the reader is referred to the work of Argyropoulos.

Three different interyarn and two different intrayarn fiber-hybrid laminates were characterized. They are listed in Table 6.1. One current limitation of the interyarn process is the impossibility to divide the tows. As a result, the low-strain volume fraction can not be reduced without spacing too much the low-strain tows. For instance, the distance between two consecutive low-strain tows in $^{25}\mathrm{Y2O}^{90}$ is about 40 mm. This means that there is on average approximately one low-strain tow per ply in the FPZ of a CT specimen.

Two different stacking strategies depicted in Figure 6.2 were investigated for the interyarn hybrids. In $^{25}\mathrm{Y1}^{90}$, all the plies along the same direction were overlayed at the same position. Therefore, all the low-strain tows are aligned and the CT specimens were milled in a way that the overlayed tows are approximately at the center of the crack propagation path. In $^{25}\mathrm{Y2O}^{90}$, the plies were stacked with

an offset of approximately half the low-strain tow width. The latter approach is intended as a crack deflection strategy, assuming that the neighboring 0° plies may interact with each other is the plies are thin enough.

Besides these different stacking approaches, ^{25}Y1^{90} and ^{25}Y2O^{90} are strictly identical (same ply-block FAW, same stacking sequence and same number of plies). Finally, Figure 6.3 shows a micrograph of the intrayarn ^{33}C2^{45}. It shows that the resulting microstructure is not a fiber-by-fiber one. However, the fiber dispersion is better than in interlayer hybrids.

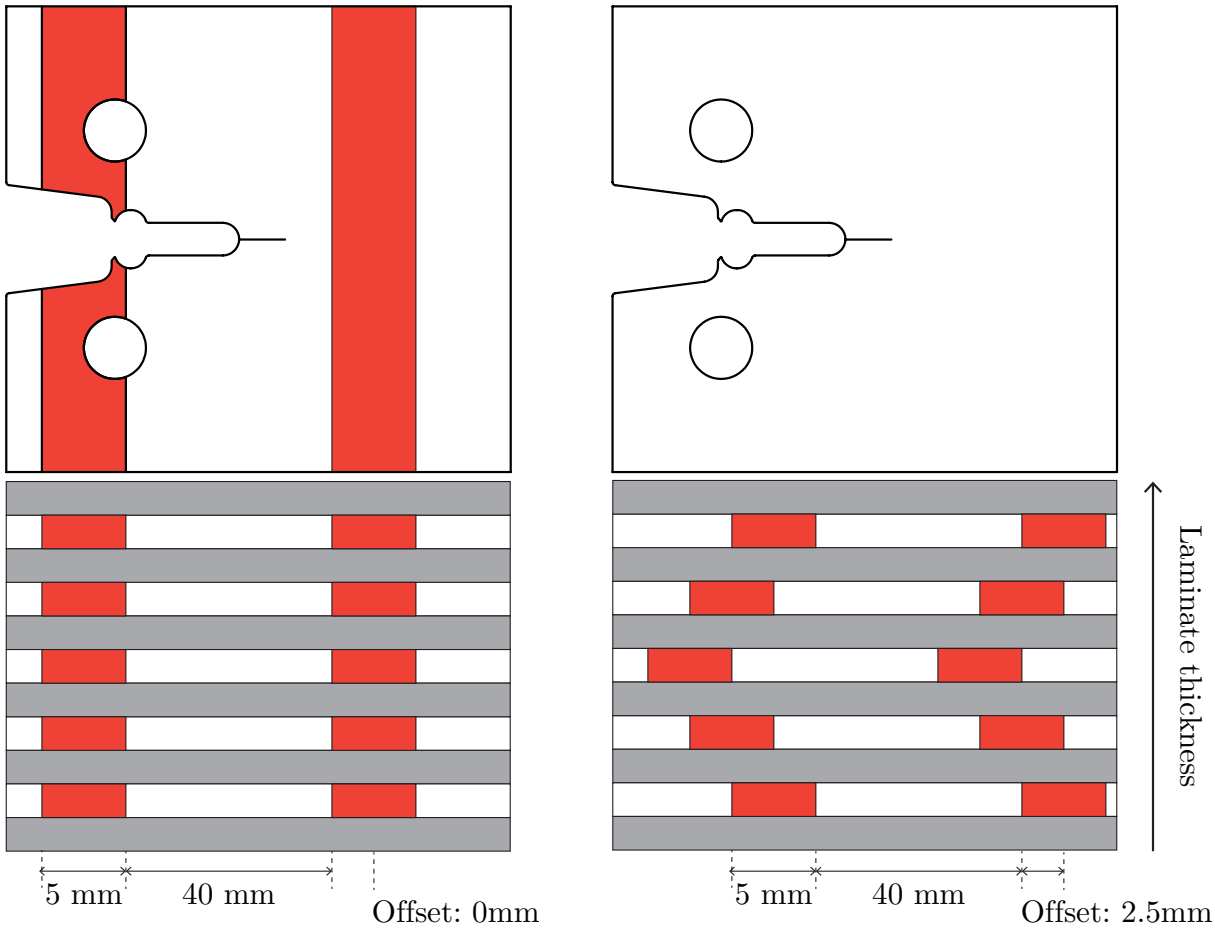

Figure 6.2: (a) Overlayed and(b) offset schematic view of a CP laminate and the approximate position of the yarns with respect to a CT sample. Yarns are not represented in the 90° direction. Note that in the offset case, there is at least one yarn along the thickness of the laminate at any point due to the number of plies. Not at scale.

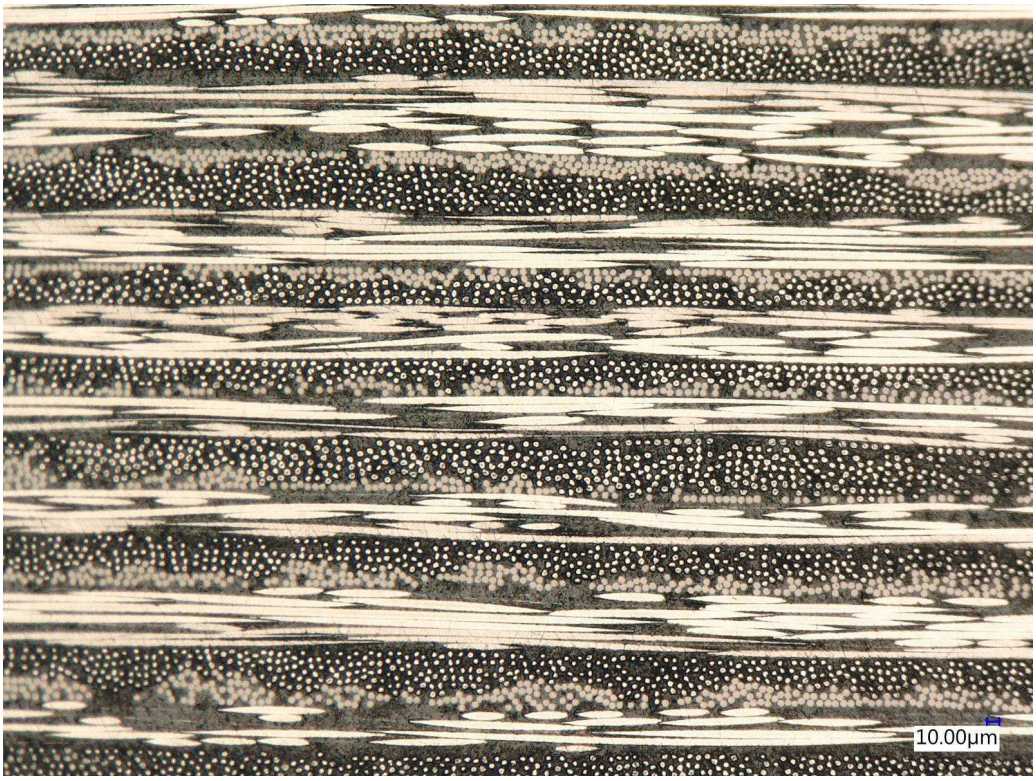

Figure 6.3: $^{33}C2^{45}$ micrograph (by Argyropoulos).

6.1 Translaminar toughness

The CT test method was strictly identical to that employed for the interlayer hybrids (see chapter 5), except that all the initial cracks were machined at a length of 18 to 19 mm, comparable to the smallest lengths achieved in interlayer hybrids. Indeed, the translaminar toughness was shown to depend on the initial crack length for interlayer hybrids and the short initial crack specimens exhibited secondary damage while the long ones did not. Thus, the short geometry was deemed the most interesting to characterize. As for interlayer hybrids, all samples exhibit a fiber volume fraction V_f of $\pm 50\,\%$.

6.1.1 Result overview

Figure 6.4 shows typical loading curves for interyarn and intrayarn hybrids, and the propagation points are indicated by a symbol. The reported displacement was measured by the machine LVDT. The loading curves are not linear before the first significant crack propagation, similar to the CP interlayer hybrids. The samples all exhibit similar apparent compliance and, thus the significant difference in load at the first crack propagation qualitatively indicates a strong contrast in ERR. Compared to the interlayer hybrids and baselines displayed in Figure 4.10a, the crack propagation is smoother, and much more propagation points are available, especially for the interyarn hybrids. All in all, these observations suggest that the hybrids presented in this chapter are more suitable to develop a stable crack resistance.

Designation	a_0 **[mm]**	b **[mm]**
$^{25}\mathrm{Y1}^{90}$	19.12 ± 0.06	4.20 ± 0.05
$^{25}\mathrm{Y2O}^{90}$	19.87 ± 0.27	4.16 ± 0.10
$^{31}\mathrm{Y3}^{45}$	19.23 ± 0.34	3.88 ± 0.04
$^{20}\mathrm{C1}^{75}$	19.29 ± 0.24	3.82 ± 0.04
$^{33}\mathrm{C2}^{45}$	19.34 ± 0.25	4.03 ± 0.04

Table 6.2: Interyarn and intrayarn hybrids CT specimens properties, measured according to the methods described in chapter 3.

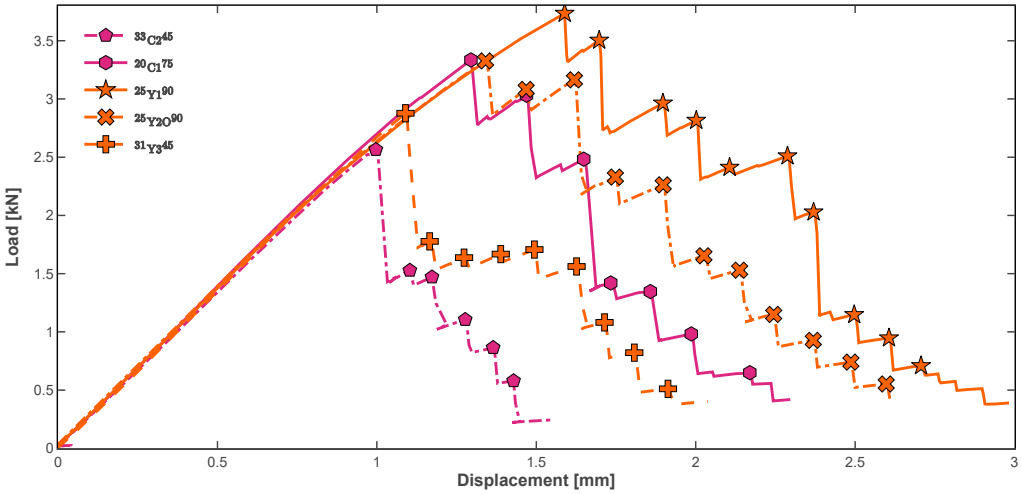

Figure 6.4: Typical loading curves for CT tests on interyarn and intrayarn hybrids.

An overview of the averaged initiation and steady-state ERR values measured for the proposed hybrid configurations is shown in Figure 6.5. Notably, it reveals that the interyarn hybrid results are competitive in terms of translaminar toughness with respect to the baselines. Especially, it is remarkable that the $90\,\mathrm{g \cdot m^{-2}}$ ply-block $^{25}\mathrm{Y1}^{90}$ exhibit a better initiation ERR and a similar propagation ERR than the baseline $^{0}\mathrm{B3}^{0}_{120}$ whose ply-blocks are $30\,\mathrm{g \cdot m^{-2}}$ thicker and do not contain HR40. The only potential issue is the reduced difference between the initiation and propagation ERR.

It must be outlined that the J-integral data reduction methods rely on the material compliance tensor, which is assumed homogeneous in chapter 4. This assumption is disputable for the interyarn laminates that exhibit overlayed low-strain tows, especially for $^{25}\mathrm{Y1}^{90}$ where they are separated by almost 40 mm. Moreover, the elastic properties were homogenized at the laminate level, thus the elastic properties of the samples are not guaranteed to be correct. However, the line J-integral measure is sufficiently repeatable as shown in Figure 6.6a and Figure 6.6c. Furthermore, the CC method reported in Figure 6.6b or in Figure 6.6d is not more repeatable and highlights a similar contrast between $^{25}\mathrm{Y1}^{90}$ and $^{25}\mathrm{Y2O}^{90}$. Therefore, the following analysis conducted with the line J-integral is

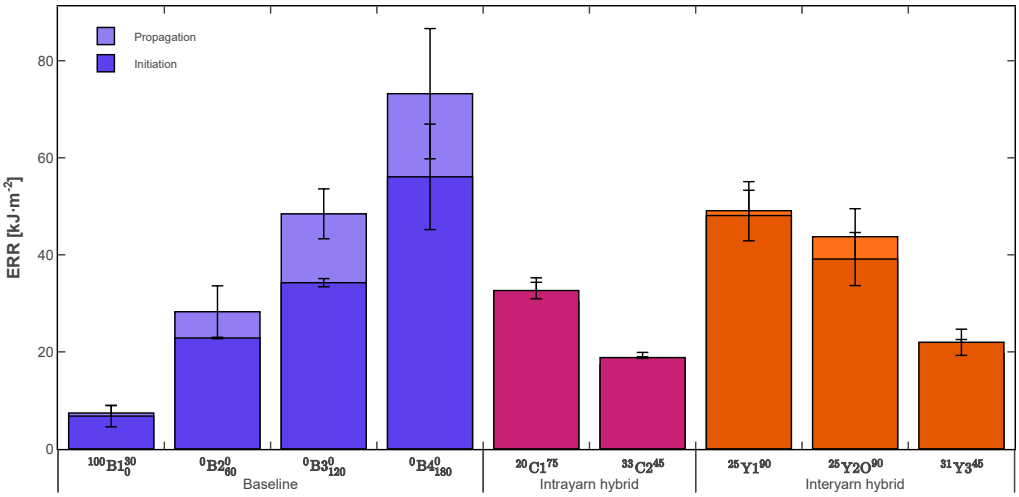

Figure 6.5: Baseline, interyarn, and intrayarn hybrid ERR at initiation (dark colors) and steady-sate (light colors), reduced with the line J-integral method.

considered as valid.

6.1.2 Hybridization effect

The R-curve shown in Figure 6.6 highlights the apparent lack of R-curve growth in interyarn specimens. This is due to the important scattering of the propagation values with respect to the initiation value. It is worth noting that the compliance calibration method seems to show a growing R-curve. But due to the large scatter of the ERR data obtained with CC, this trend is difficult to interpret.

These average values are reported as box plots in Figure 6.7 and Table 6.3. This figure clearly highlights the deviation of ^{25}Y1^{90} from the linear scaling of the 34-700-TP415 system. This indicates a substantial positive hybrid effect. The remaining interyarn hybrids are also found to perform slightly better than the linear scaling while the intrayarn specimens ^{20}C1^{75} and ^{33}C2^{45} are mostly aligned with it.

As for the interlayer hybrids, the ERR results were compared to the modified RoM formulations proposed in Equation 5.3, with the difference that a sub-ply scaling is not appropriate for interyarn in intrayarn hybrids (even if in this case, the intrayarn microstructure is closer to an interlayer hybrid than a fiber-by-fiber hybrid). The construction of the RoM is shown in Figure 6.8 for ^{25}Y1^{90}, following the same procedure as exposed in chapter 5. Then, the ERR values were normalized by the RoM predictions and reported in Figure 6.10 for the initiation ERR and in Figure 6.11 for the propagation ERR.

Overall, a significant positive hybrid effect is observed for all the interyarn and intrayarn configurations with respect to the scaled RoM for the initiation. The reported results do not highlight any trend with respect to the low-strain volume fraction γ. However, it is noticed that the overlayed stacking strategy yields a slightly better hybrid effect than the equivalent offset stacking strategy. This suggests that

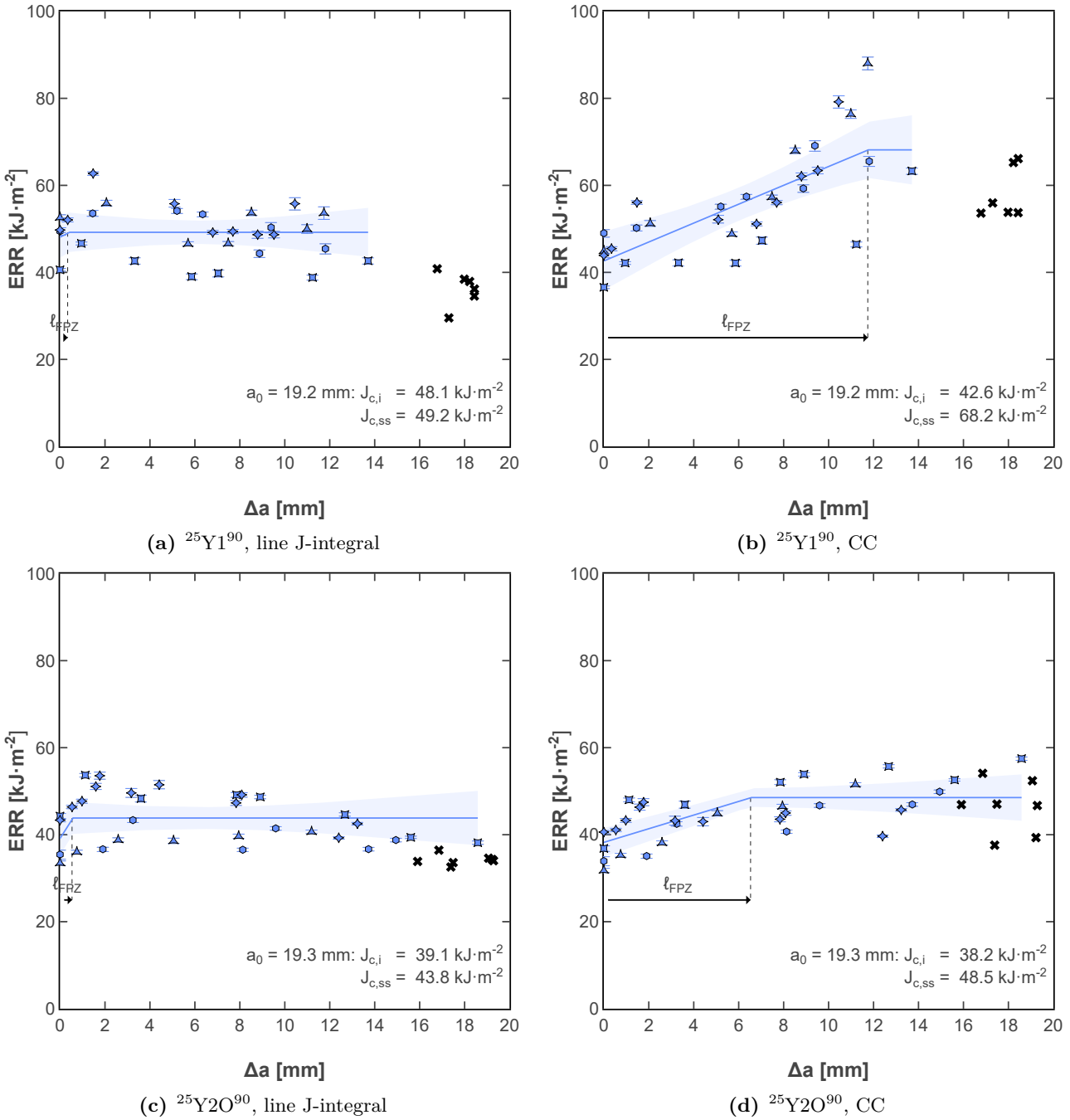

(a) $^{25}Y1^{90}$, line J-integral

(b) $^{25}Y1^{90}$, CC

(c) $^{25}Y2O^{90}$, line J-integral

(d) $^{25}Y2O^{90}$, CC

Figure 6.6: Compared R-curves between line J-integral and CC.

the crack deflection approach produces a less contrasting effect. Nevertheless, it is worth noting that both interyarn $^{25}Y1^{90}$ and $^{25}Y2O^{90}$ exhibit an initiation ERR at least two times higher than $^{33}L1A^{30}_{60}$, the interlayer hybrid with the same ply-block FAW and the same low-strain volume fraction γ. Thus, it can be concluded that the interyarn hybridization strategy is significantly more effective to improve the translaminar toughness. The same conclusion can be reached for the intrayarn configuration as the ERR is relatively well aligned with the 34-700 baseline, contrasting with the interlayer hybrids.

The toughening effect in the overlayed specimens is attributed to a massive bridging of the low-strain

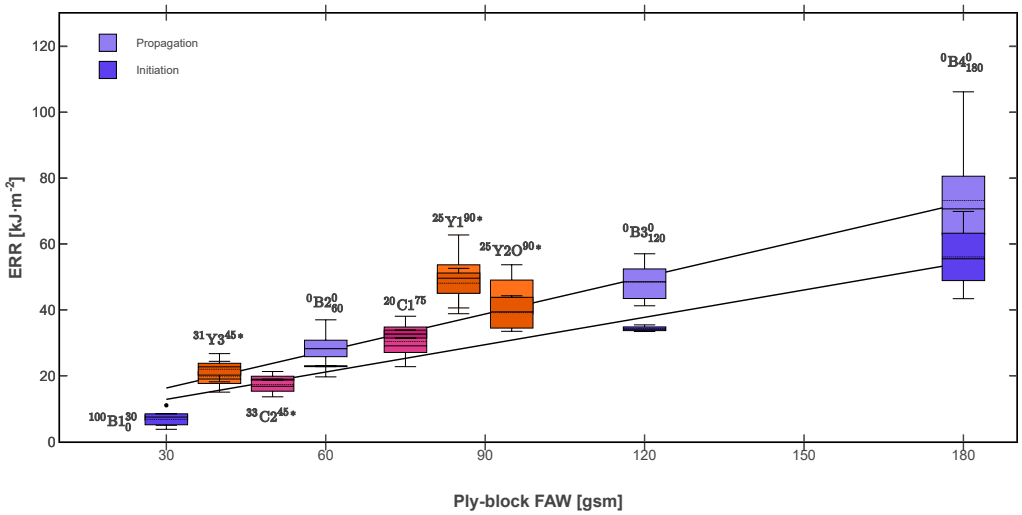

Figure 6.7: Baseline, interyarn, and intrayarn hybrid ERR box plots at initiation (dark colors) and steady-sate (light colors), reduced with the line J-integral method.

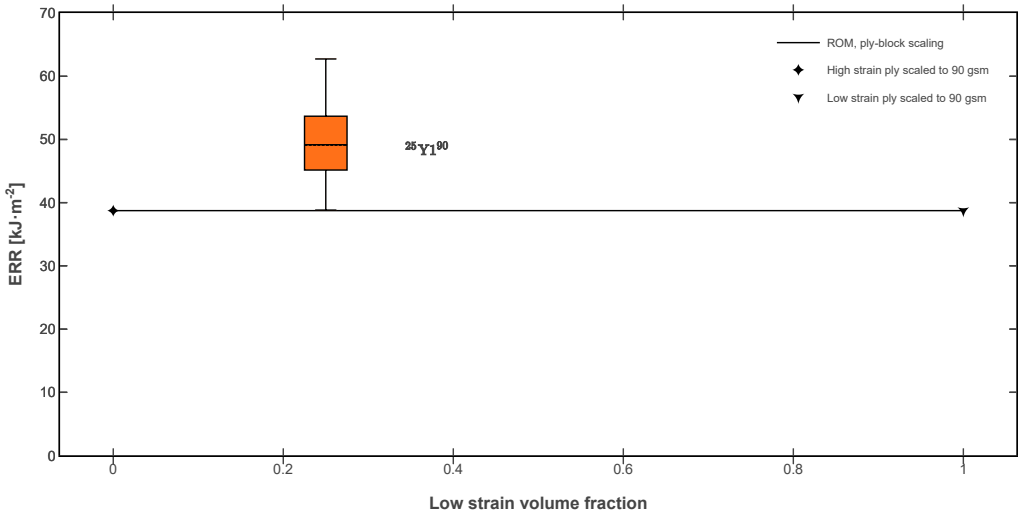

Figure 6.8: Graphical representations of Equation 5.3 evaluated for the interyarn hybrid ^{25}Y1^{90} to predict steady-state ERR values.

tows. This bridging is particularly visible during the crack propagation in ^{31}Y3^{45} specimens. Indeed, the $45\,\mathrm{g}\cdot\mathrm{m}^{-2}$ ply-block exhibit almost no fiber pull-out, thus the bridging low strain tow can be distinguished easily as highlighted in Figure 6.9a. Moreover, the post-mortem observation of the fracture surface of the same sample reported in Figure 6.9b shows no sign of extensive fiber bridging. This indicates that either the HR40 tows were broken in the crack plane during the final opening of the sample or that they were only deformed elastically.
The low-strain tow bridging accounts for the smooth loading curves shown in Figure 6.4 since it bridges the crack up to the end of the propagation. It also explains the scattering of the reported ERR values, depending on its exact location with respect to the initial crack-tip position.

Regarding the steady-state ERR, a negative effect with respect to the scaled RoM is reported for ^{31}Y3^{45}, ^{20}C1^{75}, and ^{33}C2^{45}. However, a positive effect is reported for ^{25}Y1^{90} and ^{25}Y2O^{90}, with

	Line J-integral		Compliance calibration	
Designation	$J_{Ic,i}$ [kJ · m^{-2}]	$J_{Ic,ss}$ [kJ · m^{-2}]	$J_{Ic,i}$ [kJ · m^{-2}]	$J_{Ic,ss}$ [kJ · m^{-2}]
$^{100}\mathrm{B1}_{0}^{30}$	6.8 ± 2.2	7.6 ± 1.5	11.1 ± 1.6	10.6 ± 2.7
$^{0}\mathrm{B2}_{60}^{0}$	22.9 ± 0.1	28.3 ± 5.3	31.2 ± 0.3	29.0 ± 7.7
$^{0}\mathrm{B3}_{120}^{0}$	34.3 ± 0.8	48.4 ± 5.1	46.7 ± 0.9	52.6 ± 8.0
$^{0}\mathrm{B4}_{180}^{0}$	56.1 ± 10.9	73.2 ± 13.4	71.9 ± 12.7	89.1 ± 15.6
$^{25}\mathrm{Y1}^{90}$	48.1 ± 5.2	49.1 ± 6.0	43.6 ± 5.2	90.7 ± 75.4
$^{25}\mathrm{Y2O}^{90}$	39.1 ± 5.5	43.7 ± 5.8	35.8 ± 3.8	48.9 ± 7.8
$^{31}\mathrm{Y3}^{45}$	22.0 ± 2.7	19.7 ± 2.9	18.9 ± 2.0	30.4 ± 7.7
$^{20}\mathrm{C1}^{75}$	32.6 ± 1.7	30.4 ± 4.9	30.0 ± 0.7	42.0 ± 7.9
$^{33}\mathrm{C2}^{45}$	18.8 ± 0.2	17.3 ± 2.6	17.8 ± 0.3	23.2 ± 6.3

Table 6.3: Interyarn and intrayarn hybrid ERR results. Values for a CP laminate. The reported uncertainties correspond to the standard deviation.

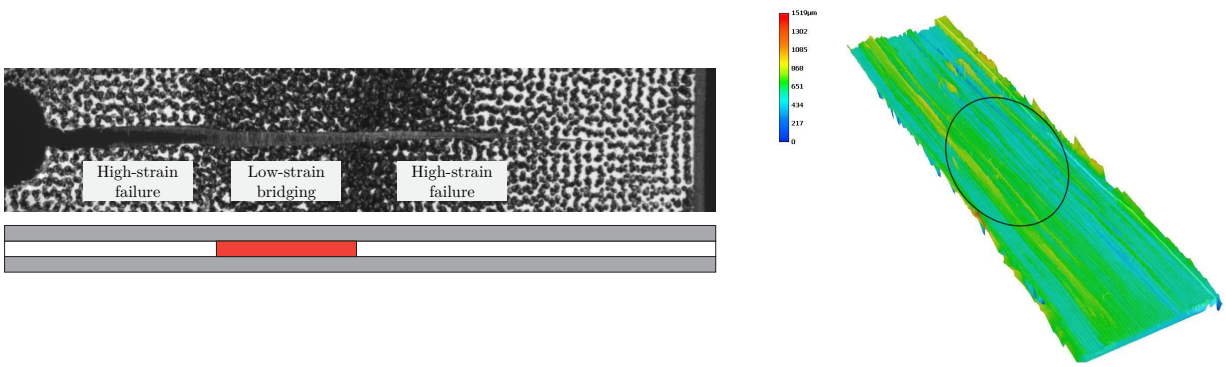

(a) **(b)**

Figure 6.9: (a) bridging and corresponding fracture surface(b) in a $^{31}\mathrm{Y3}^{45}$ specimen.

respectively 27 % and 13 %. The negative effect is aligned with the results obtained for the interlayer hybrids, as the relative low-strain volume fraction γ combined with the ply-block thinness has a detrimental effect on the propagation ERR in the absence of pseudo-ductility.

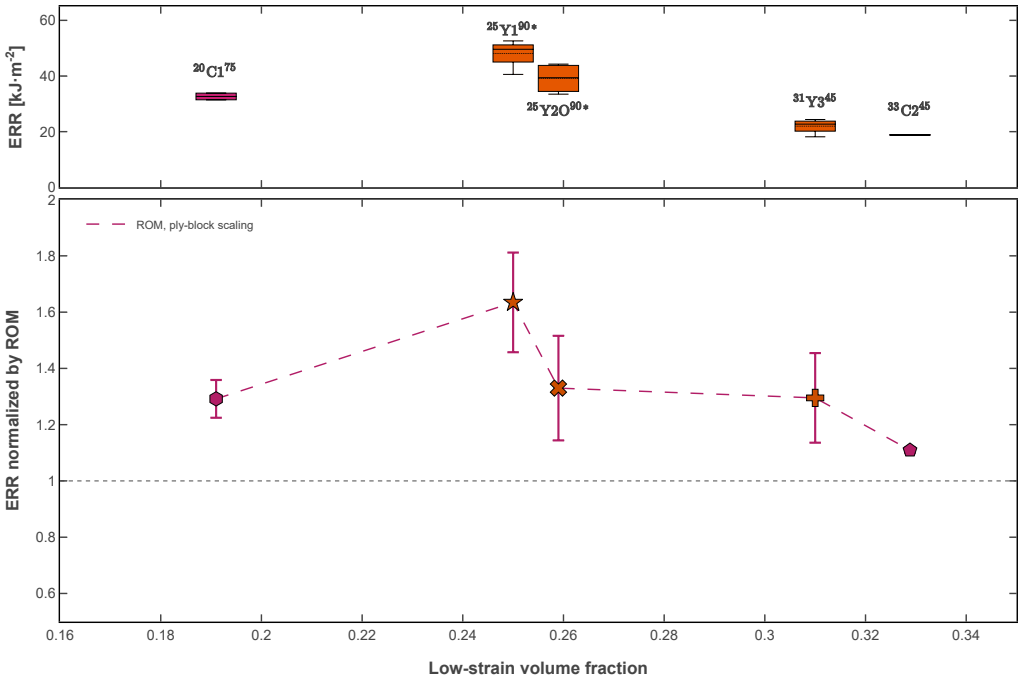

Figure 6.10: Initiation ERR normalized by RoM for interyarn and intrayarn hybrids.* jittered for readability

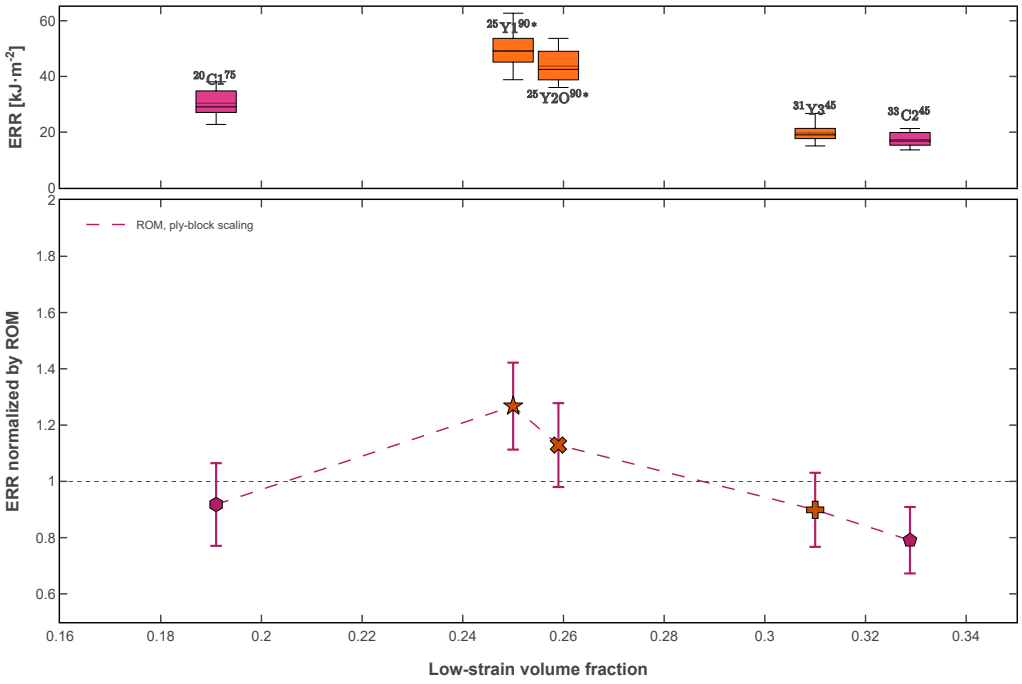

Figure 6.11: Steady-state ERR normalized by RoM for interyarn and intrayarn hybrids.* jittered for readability

6.2 Unnotched Tensile (UNT) properties

The QI specimens reported in this section were manufactured by NTPT and tested in collaboration with Argyropoulos. The manufacturing methods employed by NTPT differed slightly from those exposed in chapter 3. Notably, NTPT used preforms, and the symmetrical 90° ply was doubled. This is unfortunate since it promotes transverse cracking and delamination in the specimens. Thus, the

reported initiation value should be considered with care. Additionally, the tabs were made of carbon composite instead of aluminum. This point had no noticeable consequence on the tests. Finally, the interyarn hybrids were produced with a random position stacking for the tows, and the specimens were milled with a circular saw instead of water-jet cutting. Thus, the reported configuration is closer to the ^{25}Y2O^{90} architecture than the ^{25}Y1^{90}.

Typical stress-strain curves are shown in Figure 6.12. It can be observed that some of the ^{20}C1^{75} specimens exhibit a slight non-linearity before the failure. As this configuration is the closest to the fragmentation zone of the updated failure map, this may be due to fragmentation (Figure 5.22b).

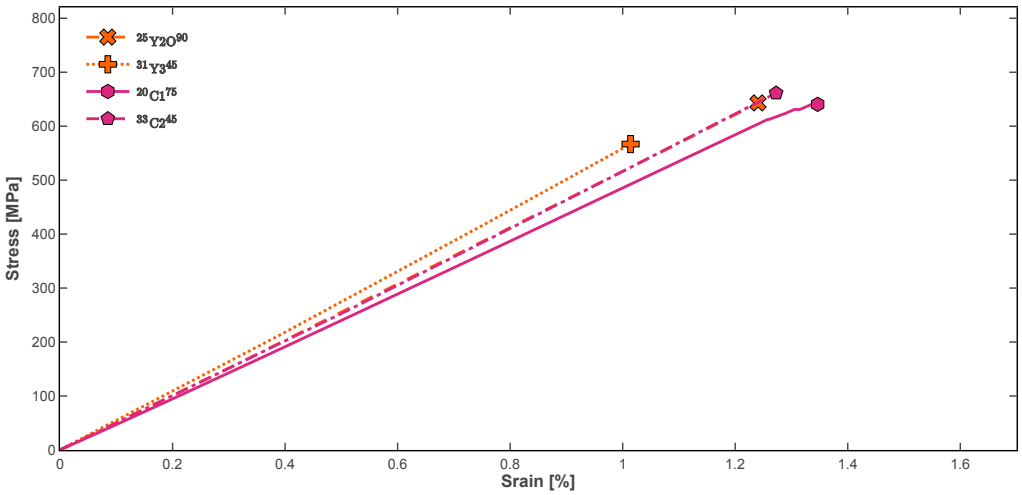

Figure 6.12: Typical stress-strain curves for QI UNT tests on interyarn and intrayarn hybrids.

6.2.1 Strength

An overview of the corresponding ultimate strength and stress at the onset of damage normalized to a fiber volume fraction V_f of 50 % is provided in Figure 6.13. The onset of damage was obtained by analyzing AE results as detailed in Appendix B. Qualitatively, it is noticed that the onset of damage is triggered at lower stresses for the interyarn and intrayarn hybrids. As aforementioned, this result is difficult to interpret due to the doubled 90° ply. For instance, the central ply delamination was observed in a ^{20}C1^{75} specimen as shown in Figure 6.14, however, this visible event took place at a strain much higher that the stress at the onset of damage reported by AE. The AE may have picked up early transverse cracking of the double 90° ply. Furthermore, the apparition of the delamination at the free edge correlates with the aforementioned loss of linearity, indicating that the non-linearity can not be attributed to pseudo-ductility. Overall, the hybrid strength is found comparable to most of the baselines. Especially, ^{25}Y2O^{90} and ^{20}C1^{75} strengths are very similar to ^{0}B3$^{0}_{120}$.

Figure 6.15 summarizes the strength results obtained for the intrayarn and interyarn hybrids. The loss of stress at the onset of damage is clearly highlighted for the interyarn hybrids. For instance,

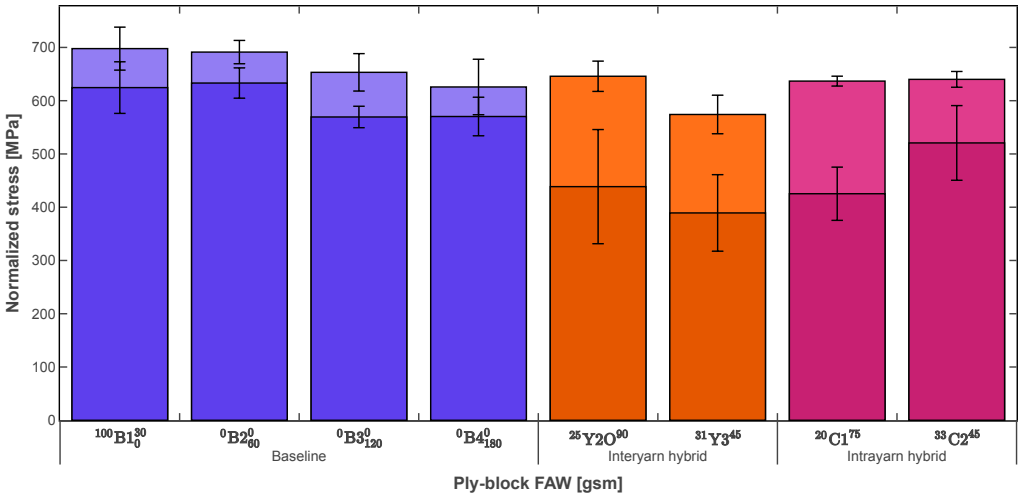

Figure 6.13: Baseline, interyarn, and intrayarn hybrid onset of damage (dark colors) and strength (light colors).

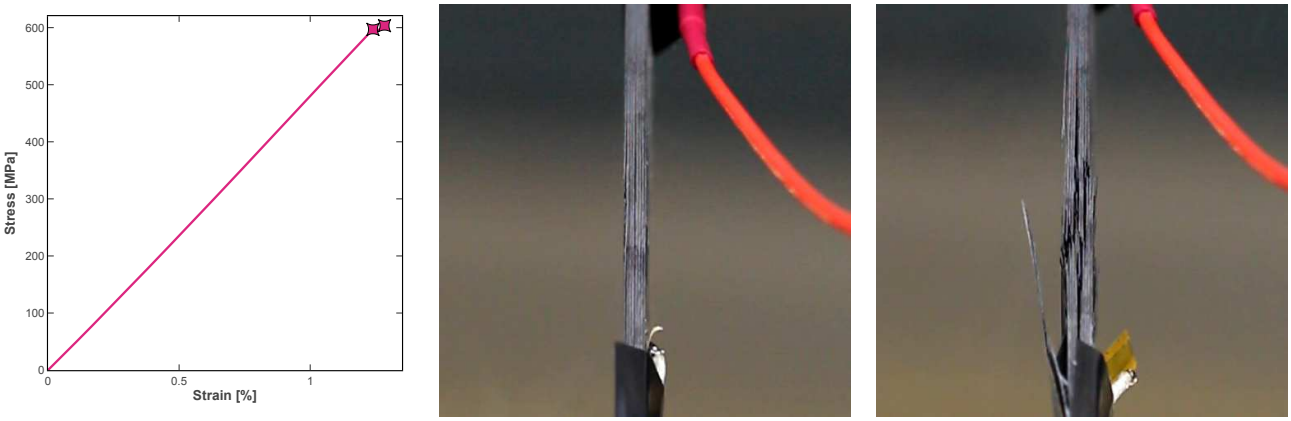

(a) **(b)** **(c)**

Figure 6.14: In-situ monitoring of free-edge delamination in an intrayarn $^{20}\mathrm{C1}^{75}$ specimen. The symbols on the load curves (a) highlight the load state of the sample when the pictures were acquired. In (b), the doubled central ply just delaminated. This led to a non-linearity and to the failure of the laminate in (c).

the onset of damage is triggered at an average value of 438 MPa for $^{25}\mathrm{Y2O}^{90}$ while the $a/\sqrt{t}$ scaling law for the 34-700 predicts 600 MPa for this ply-block FAW (27 % decrease). Interestingly, this value is comparable to the average stress at the onset of damage of 384 MPa reported for $^{33}\mathrm{L4S}^{60}_{120}$, an interlayer hybrid with a ply-block FAW of $180\,\mathrm{g}\cdot\mathrm{m}^{-2}$, thus similar to the FAW of the doubled 90° ply. However, the average strength of 646 MPa is close to the linear scaling prediction for the 34-700 (673 MPa), indicating that the hybridization is only slightly detrimental to the strength.

The reported hybrid effects are summarized in Figure 6.16, normalized with respect to the bilinear RoM scaled for the ply thickness (Equation 5.7). Overall, the positive hybrid effect magnitude is at least ±15 %. However, as noted for interlayer hybrids, there is no positive hybrid effect with respect to a linear scaled RoM. Note that these values are comparable to those reported for interlayer hybrid in Figure 5.18. This indicates that there is no significant contrasting effect on the strength of the different hybridization strategies, although the fiber dispersion is a priori better in interyarn and intrayarn hybrids.

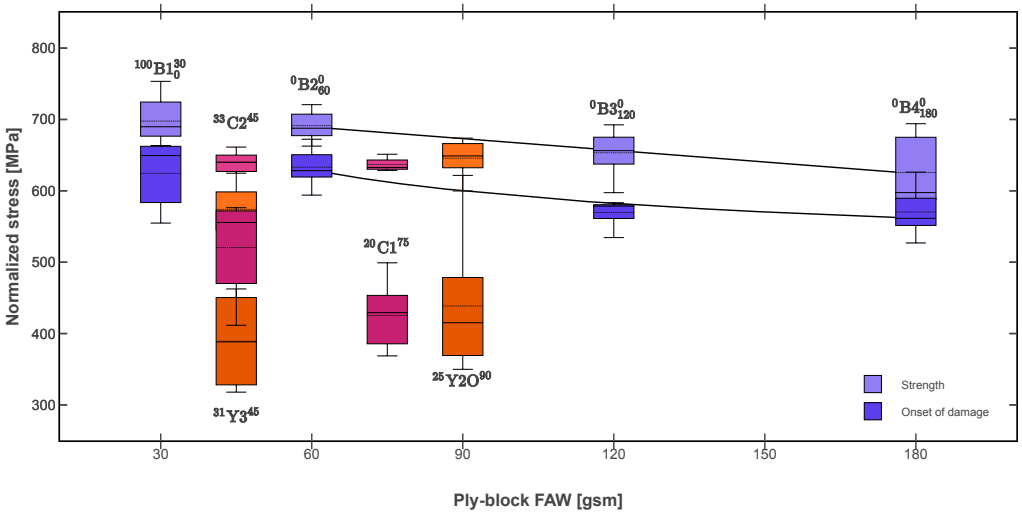

Figure 6.15: Baseline, interyarn, and intrayarn hybrid QI onset of damage (dark colors) and ultimate strength (light colors), as a function of ply-block FAW.

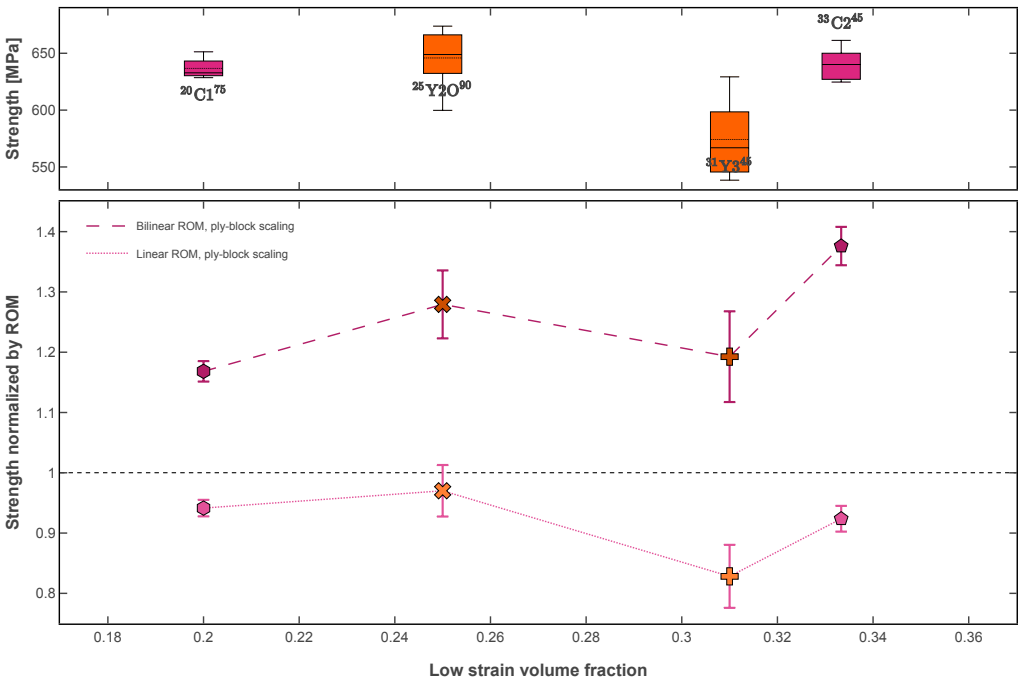

Figure 6.16: Strength normalized by RoM for interyarn and intrayarn hybrids.

As for the interlayer hybrids, all the interyarn and intrayarn hybrids reach an ultimate strain at least equal to the ultimate strain of the HR40 fiber (1.1 %, as depicted in Figure 6.17). It indicates that in most cases, the HR40 failure is not critical. Furthermore, the overall linearity of the loading curves shows that no substantial damage takes place before the laminate failure.

Finally, the strain at the onset of damage in hybrid specimen was normalized by the strain at the onset of damage of the HR40 material, scaled to the ply-block FAW. The results are shown in Figure 6.18. The intrayarn hybrid strain at the onset of damage is approximately 20 % higher than the strain

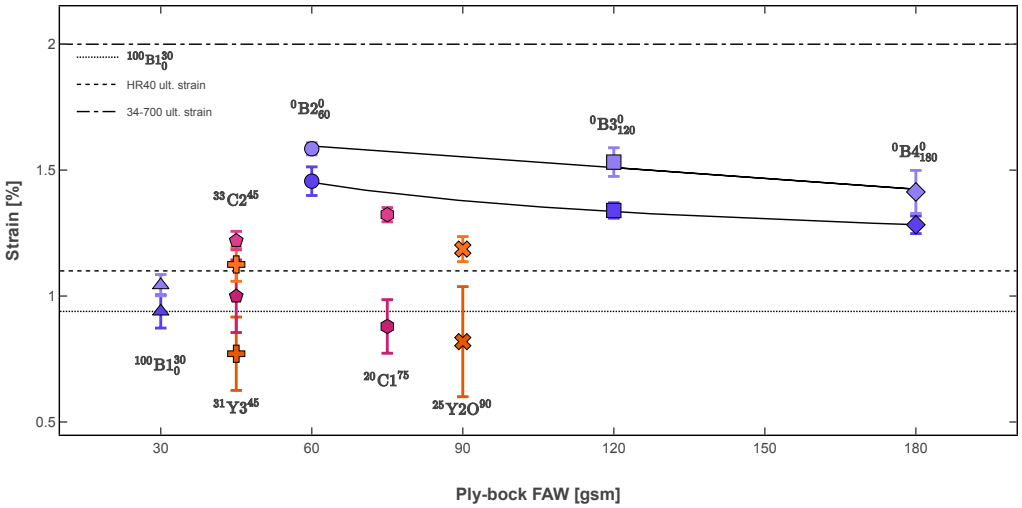

Figure 6.17: Baseline, interyarn and intrayarn hybrid strain at the onset of damage monitored by AE (dark colors) and failure (light colors), acquired with strain gauges, and compared to the HR40 ultimate strain (1.1 %) and 34-700 ultimate strain (2 %).

predicted for a ply block of the same thickness. As a result, the total ply-thickness of the intrayarn hybrid does not drive the strain at the onset of damage. On the other hand, the predictions are close to the strain at the onset of damage for $^{31}Y3^{45}$. This observation may be explained by the fact that in interyarn hybrids, the low-strain tow spans the whole ply-thickness. Furthermore, in $^{31}Y3^{45}$ the $45\,\mathrm{g}\cdot\mathrm{m}^{-2}$ FAW implies that the low-strain tows are spread over a larger width, thus the tow is more likely to behave as an individual ply of HR40 locally.

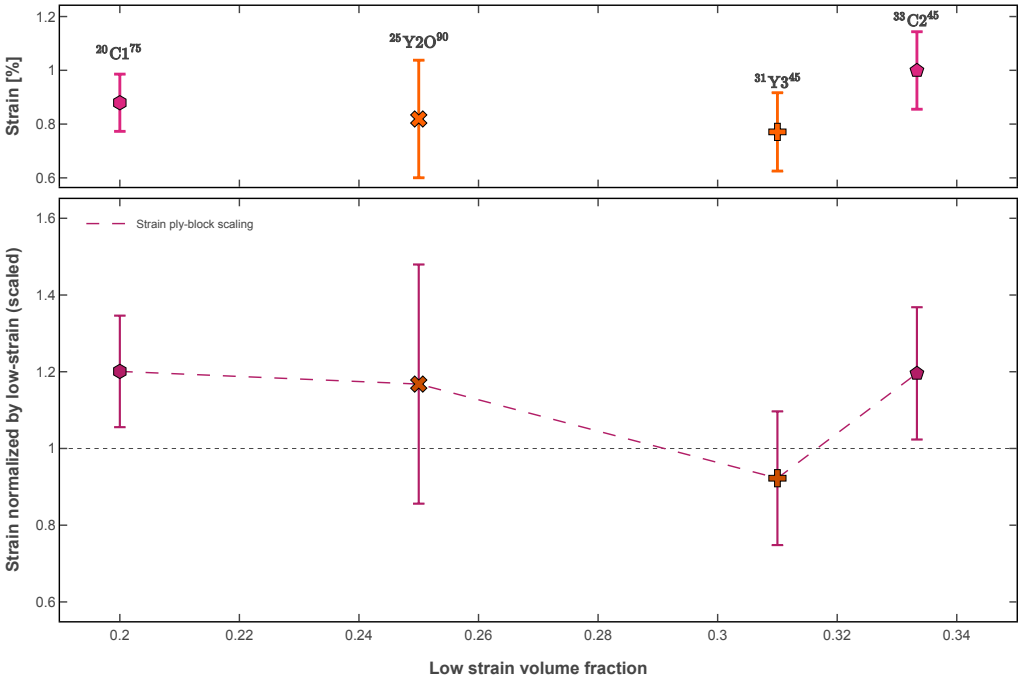

Figure 6.18: Baseline and interlayer hybrid strain at the onset of damage monitored by AE (dark colors) and failure (light colors), acquired with strain gauges. * jittered for readability

6.2.2 Modulus

Figure 6.19 shows that the QI interyarn and intrayarn hybrid laminates are also well aligned with a liner RoM for their moduli, as expected.

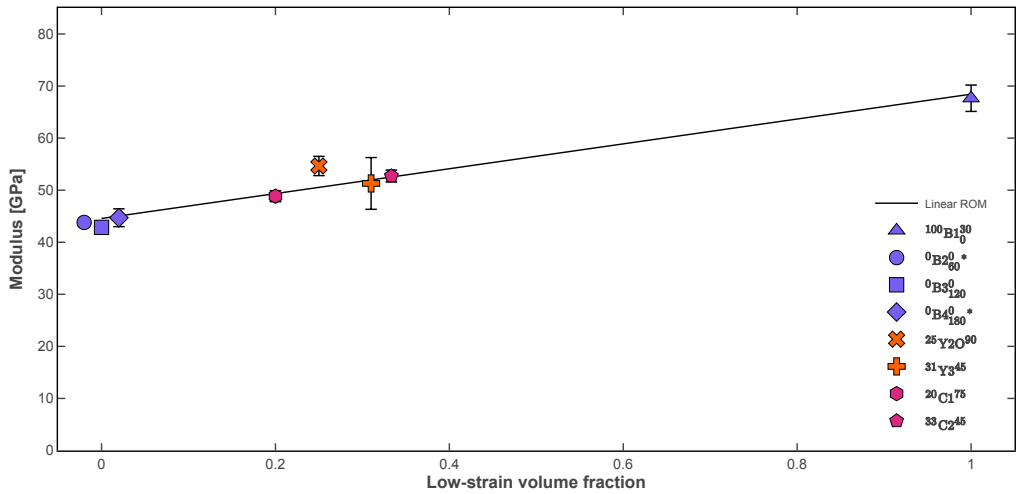

Figure 6.19: Baseline, interyarn and intrayarn tensile modulus as a function of the low-strain volume fraction γ. * jittered for readability

6.3 Open Hole Tensile (OHT) properties

OHT tests were performed on the intrayarn laminates at the University of Bristol. At the time of the testing campaign, the interyarn hybrids were not yet available and were consequently not characterized in OHT tension.

The typical loading curves for the OHT specimens are shown in Figure 6.20. As for the interlayer hybrids, the OHT far-field strength and notch sensitivity (defined as the ratio of OHT strength over the UNT strength) reported in Figure 6.21 shows that the notch strength is almost the same for both intrayarn configurations. Considering the discussion developed for interlayer hybrids, the intrayarn hybrids were expected to follow the same behavior.

The CT-scan reported in Figure 6.22 highlights that in contrast to the baselines, the intrayarn hybrids develop some damage at the stress concentration. This explains the positive hybrid effect noted for the initiation ERR, although the effect remains limited due to the size of the observed damage.
As for the interlayer hybrids, the fiber hybridization brings an apparent notch strength reduction improvement in the intrayarn hybrid compared to the baselines. Again, this is explained by the lower UNT strength of hybrids. Thus, for a constant OHT far-field stress, the notch strength reduction decreases.

To investigate the failure mechanisms at play, OHT specimens were loaded to 95 % of the ultimate

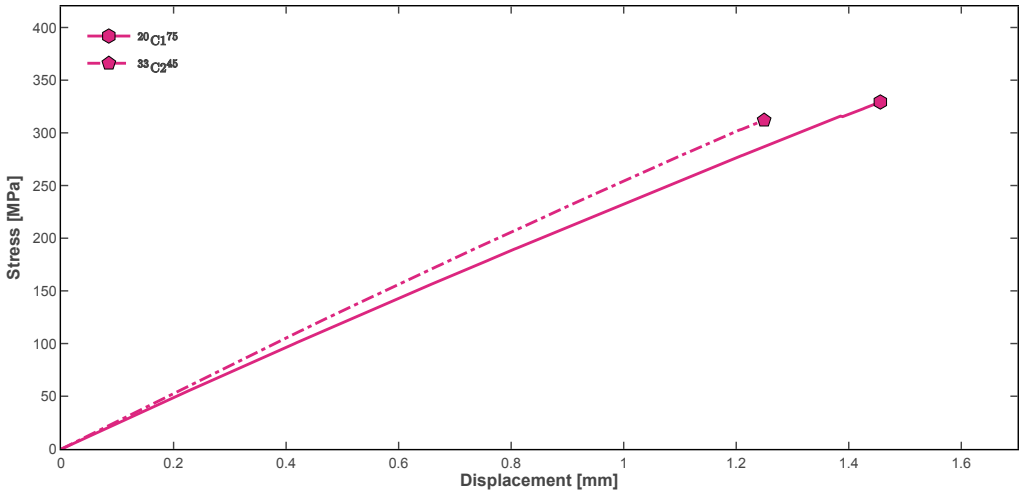

Figure 6.20: Typical load-displacement curves for QI OHT tests carried out on intrayarn specimens.

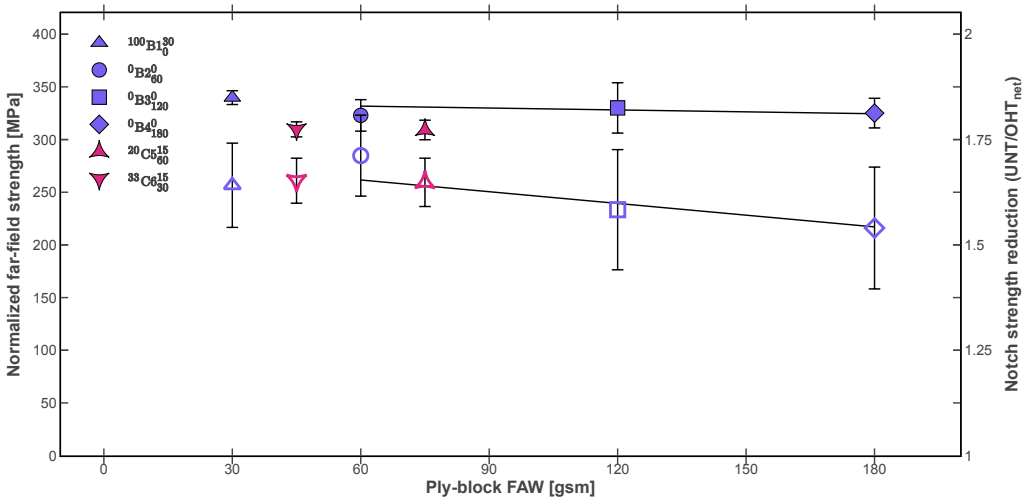

Figure 6.21: Baseline and intrayarn hybrid OHT far-field strength (filled symbols) and notch strength reduction (open symbols). Values normalized for 50 % V_f. * jittered for readability

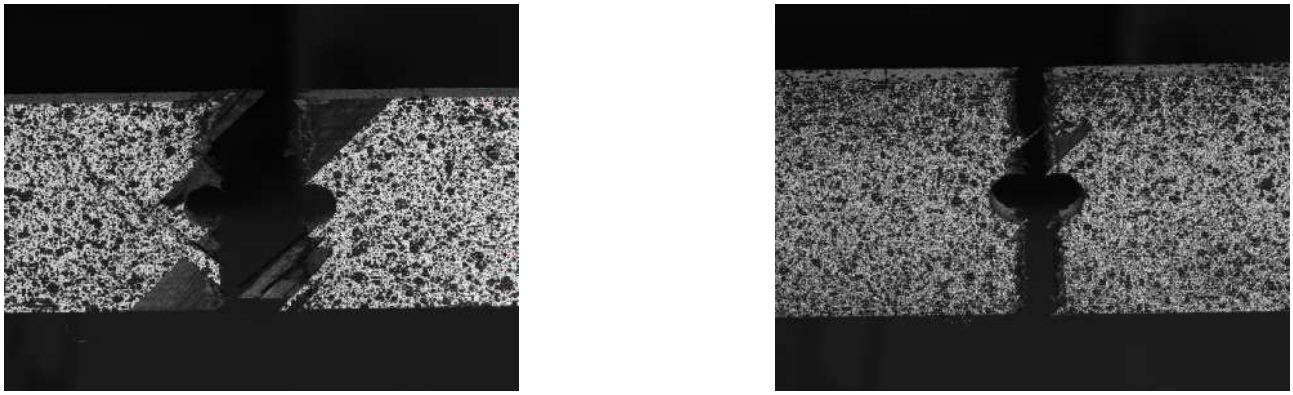

(a) $^{20}C1^{75}$ **(b)** $^{33}C2^{45}$

Figure 6.22: Post-mortem failure of intrayarn OHT specimens.

OHT load, then unloaded and analyzed with CT-scan. The results, reported in Figure 6.23, show that even the thinnest intrayarn hybrid develops more damage than the baselines of equivalent ply-block

thickness. These observations support the positive hybrid effect on the initiation ERR reported for intrayarn hybrids. Compared to the inerlayer hybrids, the intrayarn hybrids did not develop a longitudinal split at the apex oh the hole. Thus, it did not cancel the stress singularity and it may explain the reduced OHT strength.

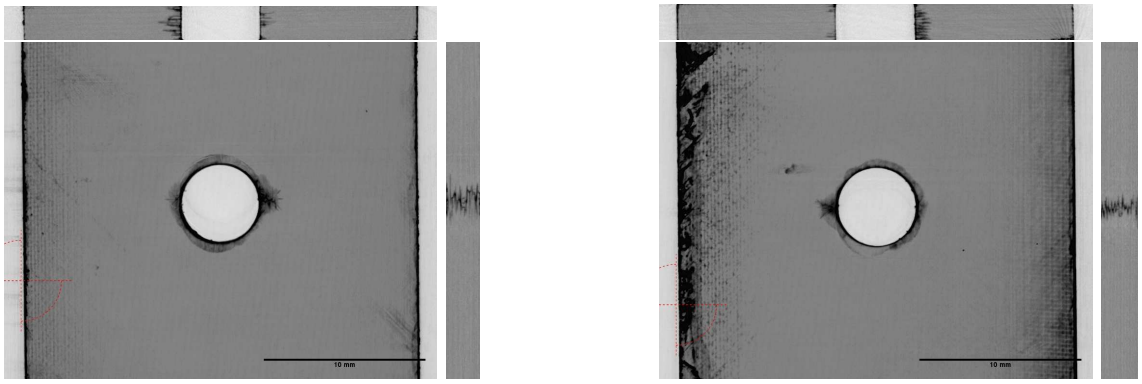

(a) $^{20}C1^{75}$ **(b)** $^{33}C2^{45}$

Figure 6.23: CT-scan of OHT samples after loading to 95 % of the OHT strength.

6.4 Conclusion

Interyarn and intrayarn fiber-hybridization have been shown to bring effective toughening mechanisms for thin-ply composites. Notably, these approaches do not require to stack plies of different materials but are achieved during prepreg production. Thus, their processing is closer to the usual process, and, more importantly, very thin-ply hybrids can be produced at an industrial scale.

The interyarn overlayed architecture has been demonstrated to substantially improve the translaminar toughness of the thin-ply composites, both with respect to a scaled RoM and to the ply-thickness effect. This observation was attributed to a substantial bridging effect of the low-strain overlayed tows during the crack propagation. The absence of extensive pull-out bundles after the crack propagation in these specimens indicates that the low-strain fibers may not have reached their ultimate strain during the bridging process. Further investigations, for instance with CT-scan, are required to clarify this mechanism.

Conversely, the overlayed interyarn specimens did not exhibit significant damage before their ultimate failure. Thus, they achieved higher strength than for instance the interlayer hybrids and are therefore more suitable for simultaneous optimization of the strength and the translaminar toughness.

Nevertheless, the slight loss of ultimate strength for the interyarn hybrids still places them behind or at the same level as the 34-700-TP415 system in terms of strength-to-translaminar-toughness ratio, as depicted in Figure 6.24. However, it is worth noting that the QI $^{25}Y1^{90}$ laminate exhibited a

modulus of 54.7 GPa, a value approximately 23 % higher than that obtained for a pure QI 34-700 laminate ${}^{0}\mathrm{B3}^{0}_{120}$. At the same time, ${}^{25}\mathrm{Y1}^{90}$ fails at a similar strength (assuming ${}^{25}\mathrm{Y2O}^{90}$ strength as an approximation) and with a similar translaminar toughness. Therefore, this work highlights a clear interest in further investigating the interyarn and intrayarn hybrids.

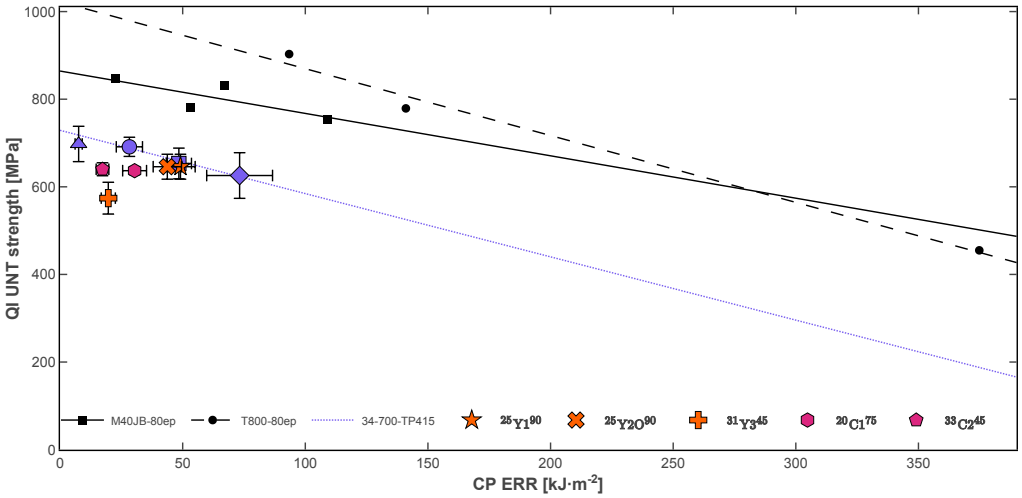

Figure 6.24: Ashby plot of the QI UNT strength with respect to the CP translaminar toughness of the interyarn and intrayarn hybrids. Assumes the same strength for ${}^{25}\mathrm{Y1}^{90}$ and ${}^{25}\mathrm{Y2O}^{90}$. M40JB-80ep reference values: ERR from [39], strength from [38]. T800-80ep reference values: ERR from DENT tests [56] and [175] assuming a similar behavior for the IM21 system, strength scaled from [24].

Chapter 7

Phenomenological study

How to explain the observed results?

The list of available data, codes, and publications generated for this work is available on Zenodo [204].

The previous chapters have experimentally demonstrated the positive impact of fiber-hybridization on the translaminar toughness of thin-ply composites independently of the ply-thickness effect. With this in mind, two questions arise: (i) how to account for the change in translaminar toughness by phenomenological mechanisms and (ii) is it possible to predict these phenomenological mechanisms to engineer microstructural features that will promote them?

Two different mechanisms have been identified in this work. First, the overlayed interyarn hybrids have been shown to improve substantially the translaminar toughness through a substantial crack bridging applied by the low-strain tows. However, this bridging does not result in a substantial pull-out length at the fracture surface, indicating that energy may not be dissipated by pull-out.

Second, the intrayarn and interlayer hybrids are susceptible to promote the pull-out length. For instance, the use of asymmetric ply-blocks in interlayer hybrids promoted the nucleation of secondary damage. These diffuse damage locations may be correlated with an increased pull-out length that would account for the increased dissipated energy. In this chapter, the latter is addressed by analyzing the fracture surfaces of CP specimens.

First, a methodology is developed based on optical microscopy to systematically characterize the pull-out distributions. Then, a dual-scale model is proposed to formulate a macroscopic cohesive law representative of the fracture process, and validated against experimental data.

7.1 Optical microscopy observations

Figure 7.1 shows the post-mortem observations of two $^{14}\text{L5A}^{30}_{180}$ specimens, acquired with a VHX-5000 Keyence optical microscope, using the stitching feature along with the depth-of-field reconstruction. The depth-of-field algorithm detects the focus point of any pixel in a picture while translating the microscope stage in the height direction. When a pixel is in focus (or more specifically, a small subset around it), it is possible to deduce its height value by knowing the position of the stage. Additional fracture surfaces are reported in Appendix C.

The stitching technique combines successive observations at different locations to perform continuous data acquisition over a surface larger than the field of view of the microscope. Typically, the VHX-5000 Keyence software is able to stitch a surface up to 20 mm in each direction. Consequently, the observations performed in this work represent approximately half the crack length, including the initial crack.

Figure 7.1a is the post-mortem fracture surface of a short initial crack specimen while Figure 7.1b exhibits a large initial crack. The specimen in Figure 7.1a was affected by crack splitting as shown in Figure 5.10d. Qualitatively, a contrast is observed in Figure 7.1: the pull-out bundles are more numerous and longer in the short initial crack specimen compared to the long one. The following section exposes the procedure employed to extract quantitative information from these observations.

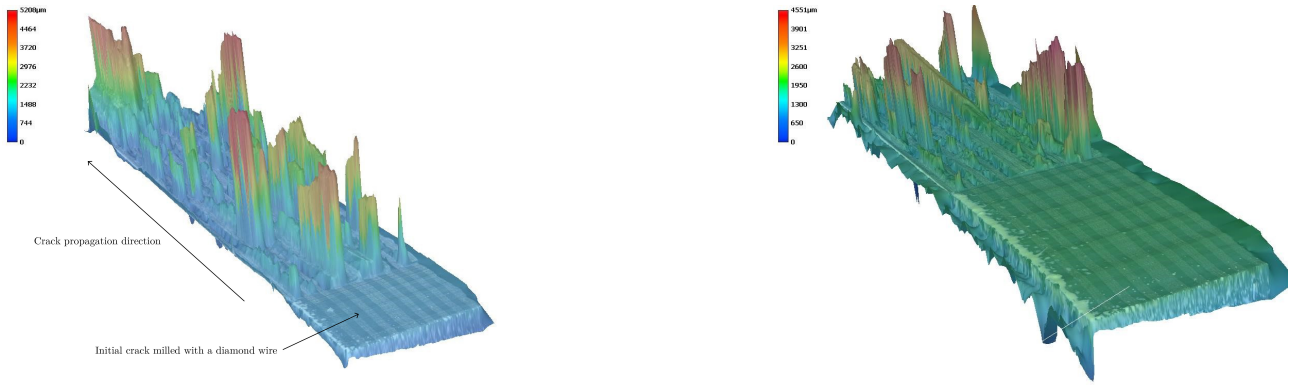

(a) **(b)**

Figure 7.1: Post-mortem failure of interlayer CT fracture surfaces: (a) $^{14}\text{L5A}^{30}_{180}$ with a short initial crack and (b) $^{14}\text{L5A}^{30}_{180}$ with a large initial crack.

7.2 Profile analysis

First, the 3D data were simplified by extracting one-pixel-thick 2D fracture surface profiles in the transverse direction, i.e. along the direction perpendicular to the crack propagation. This profile extraction was carried out every 10 px along the crack profile direction. As the VHX-5000 Keyence resolution in the focus plane is $1.055\,\mu\text{m}\cdot\text{px}^{-1}$, it corresponds to a resolution of approximately 10 µm in the crack propagation direction. Initial crack and bridging areas were manually discarded by defining

areas of exclusion in the processing algorithm, which was implemented as a Python script. A typical resulting profile is shown in Figure 7.2.

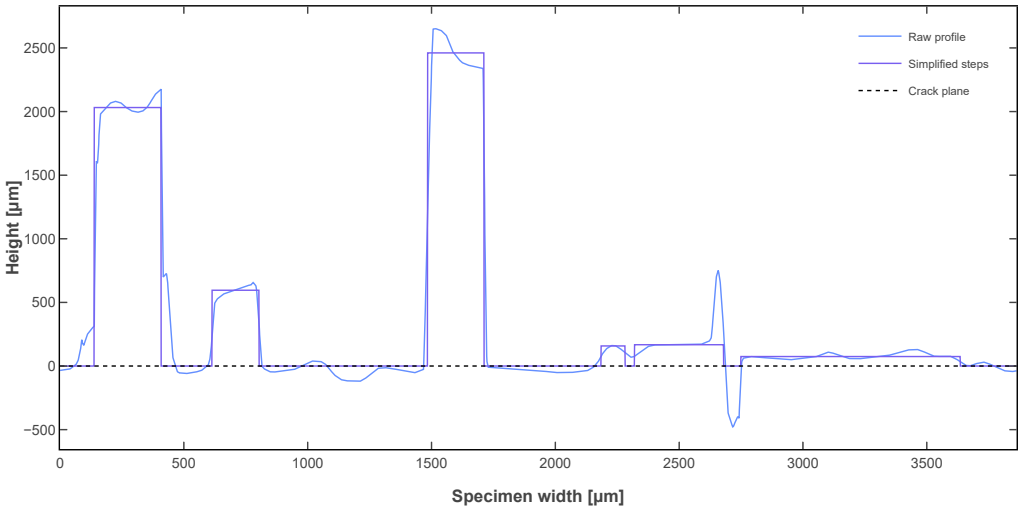

Figure 7.2: Typical post-mortem pull-out profile.

The post-mortem profile appears asymmetric with respect to the crack plane. This is due to the failure of the optical microscope to resolve deep and narrow openings. To mitigate this issue, both lower and upper crack surfaces were observed to obtain a complete profile. In practice, a crack plane was manually defined using the same 90° plies for both surfaces. Positive pull-out bundles were then measured with respect to this crack plane. Due to misalignment and optical artifacts, the profile matching from one surface to another is challenging.

Each profile was thus treated as an independent observation. The resulting statistical descriptor is in fact only accounting for 50 % of the information, in terms of density. Thus, it was scaled accordingly by a factor two. With this approach, matching the profiles is not required and the whole procedure can be automated but data are lost about the small pull-out bundles close to the crack plane, due to the incertitude regarding the crack position, and the unknown distance between two consecutive positive and negative bundles.

A Python step detection algorithm was implemented to simplify the profiles by idealizing the pull-out bundle edges as rectilinear. Small features whose dimensions were below 50 µm were considered noise and discarded, i.e., they were merged with larger features as deleting them would bias the results. The height, width, and probability of step occurrence, including the 90° plies, were used as statistical descriptors to characterize the pullout distribution for each material configuration. The developed lengths of the profiles were similarly aggregated to characterize the overall crack dimension. For instance, Figure 7.3 shows that the mean pull-out length is larger in the short initial crack length specimen than in the large one and may therefore explain why it dissipates more energy in translaminar fracture.

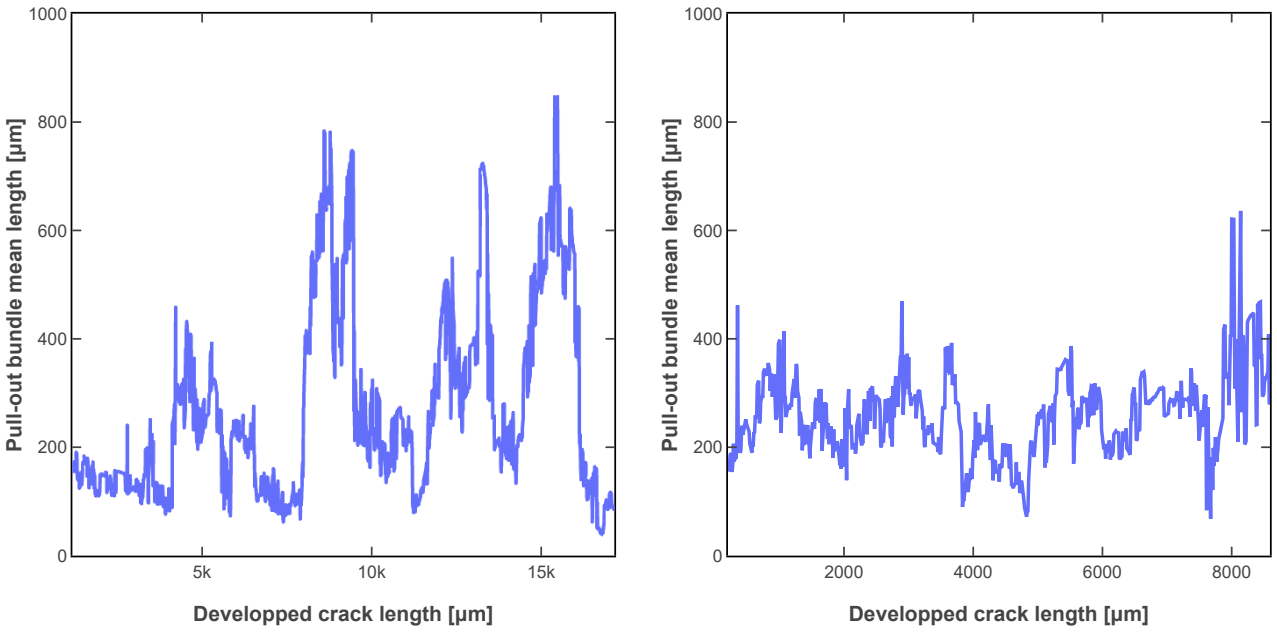

Figure 7.3: Mean pull-out length along the crack direction for CT fracture surfaces: (a) $^{14}\text{L5A}^{30}_{180}$ with a short initial crack and (b) $^{14}\text{L5A}^{30}_{180}$ with a large initial crack.

The pull-out length distribution reported in Figure 7.4 further highlights the contrast between the two specimens. For instance, the specimen without secondary damage exhibits pull-out bundles no greater than approximately 2500 µm while the specimen with a crack splitting exhibits pull-out length up to more than 3500 µm. This difference demonstrates a significant change in fracture behavior that interactions between the main crack path and secondary damage could cause. More importantly, it provides input data to model the translaminar toughness associated with each pull-out bundle and to build a phenomenological cohesive law capturing the crack propagation energy according to the pull-out bundle distribution.

This procedure was applied to all the baseline and interlayer samples, for the short initial cracks if available. Note that only large initial crack data were available for $^{0}\text{B2}^{0}_{60}$ and $^{33}\text{L1A}^{30}_{60}$. As interyarn and intrayarn specimens did not exhibit significant pull-out, they were not included in the analysis. The resulting distributions are shown in Figure 7.5 and summarized in Table 7.1.

The distribution can be analyzed in a twofold way. On the one hand, the pull-out bundles as usually defined, i.e., for the 0° ply, are long and their width is limited to the ply-block width. This is for instance clearly visible for $^{0}\text{B4}^{0}_{180}$. On the other hand, the samples exhibit very large but short bundles. This corresponds to the variation of the crack plane with respect to the 90° ply. These bundles are predominant in non-hybrid thin-ply materials, while the long pull-out bundles become more predominant with ply-block thickness increase and hybridization. For $^{14}\text{L5A}^{30}_{180}$ and $^{20}\text{L6S}^{60}_{240}$, bundles between these two categories are observed. These bundles are typically pull-out of several adjacent

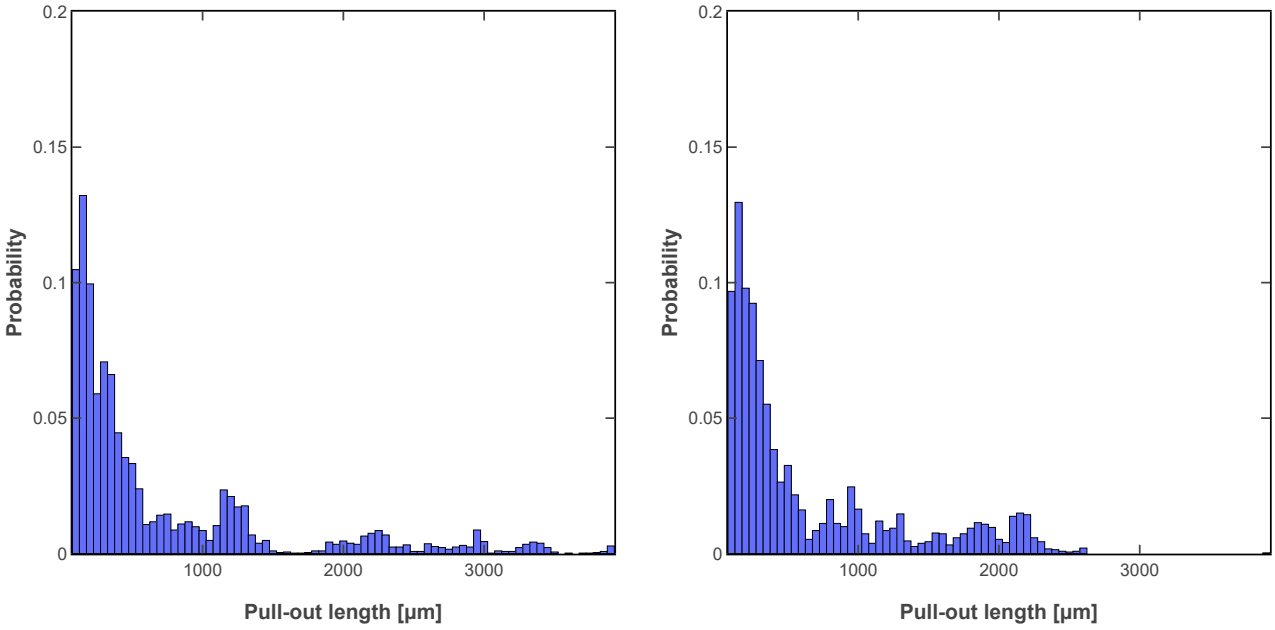

Figure 7.4: Pull-out length distribution for CT fracture surfaces: (a) $^{14}\text{L5A}^{30}_{180}$ with a short initial crack and (b) $^{14}\text{L5A}^{30}_{180}$ with a large initial crack.

0° plies at the same time, sometimes with 90° bridging in between, as observable in Figure 7.1a. It highlights a change in the failure mode and may be correlated to the observed delamination in these specimens.

The maximal pull-out length was found to be well correlated with the ply-block FAW, as shown in Figure 7.6. Remarkably, the 34-700 baselines are perfectly aligned. However, there is a clear hybrid effect which is most of the time negative. The interlayer hybrids, whose maximal pull-out length is reduced, are also those for which a negative hybrid effect has been reported on ERR. A similar conclusion is reached with the mean values reported in Figure 7.7. The mean pull-out width seems to decrease as the mean length increases. However, this should not be interpreted as an absence of crack plane variation in the 90° plies. It only indicates that the step-fitting algorithm treats the variations at these scales additively. If the low-frequency component was of interest, it could be obtained by wavelet decomposition.

Another metric of importance is the number of pull-out bundles by unit of crack surface. These values are also found to increase with the ply-block FAW and fiber hybridization, as shown in Figure 7.9. Thus, it is noticed that the maximal pull-out length, the mean pull-out length, and the density of pull-out bundles increase with the ply-thickness, and eventually with the ply hybridization, as shown by the divergences from the scaling defined by the 34-700 baselines. In this regard, Figure 7.8 reports that the maximal pull-out length appears to be a function of the low-strain volume fraction γ. However, the lowest γ is achieved for the highest ply-block FAW, thus a great part of the apparent effect is due to the ply-block effect. This observation is all the more valid as the pull-out length in low γ

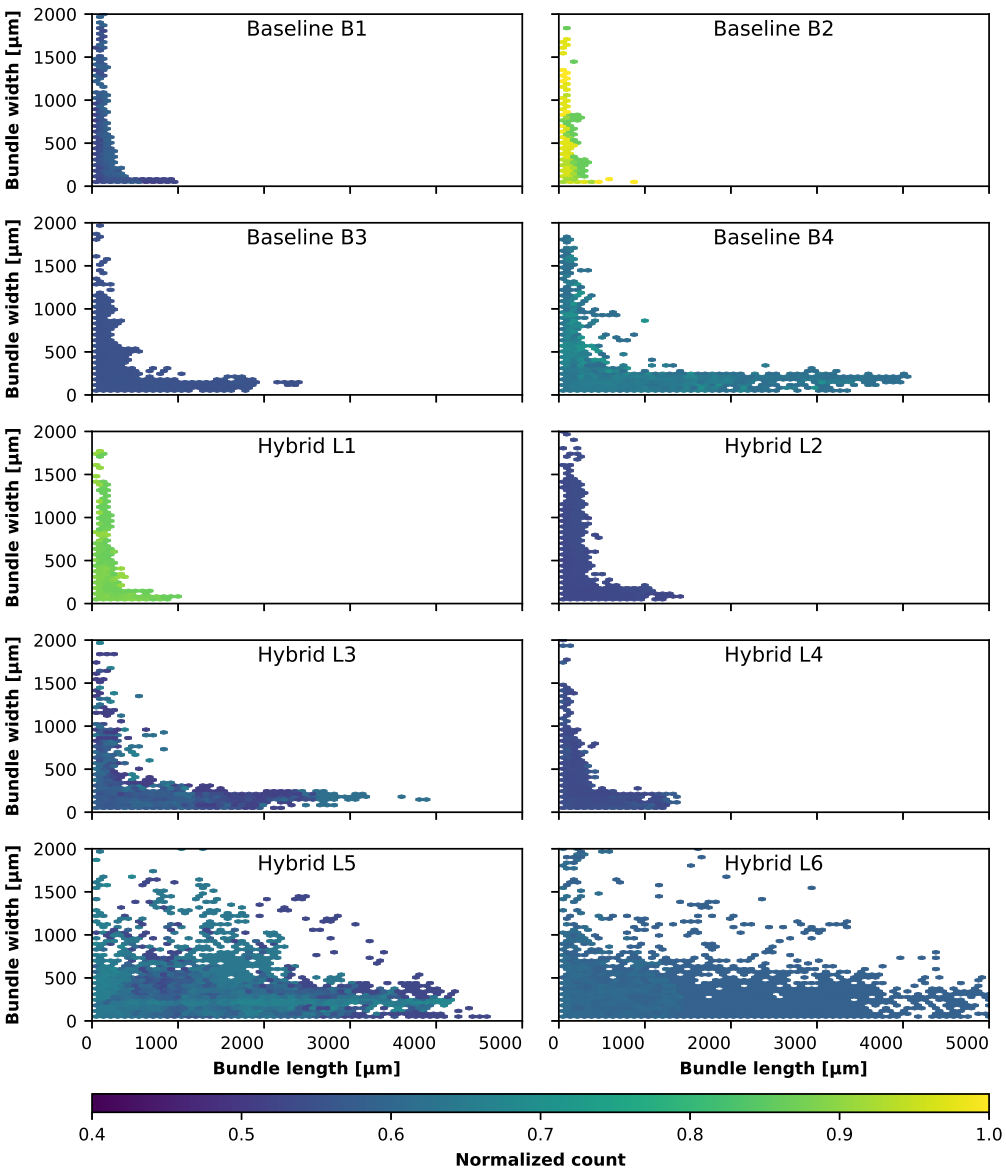

Figure 7.5: Pull-out distributions (width and length) for each interlayer and baseline configuration. The color scale is normalized with respect to the maximal bin over every distribution. Thus, a variation of color from one distribution to the other indicates a different count between the distributions and a variation of color inside a distribution indicates the relative distribution of the bins for this distribution. Note that the algorithm may be biased towards short distributions as in the presence of large bundles, the small ones tend to be aggregated with it. The nomenclature is used in this figure, for instance B4 is ${}^{0}\mathrm{B4}^{0}_{180}$.

intrayarn with a FAW of $75\,\mathrm{g}\cdot\mathrm{m}^{-2}$ was observed to remain limited (Figure 7.10).

Nevertheless, there is a clear hybridization effect on the pull-out length. For instance, ${}^{33}\mathrm{L3A}^{60}_{120}$ and ${}^{33}\mathrm{L4S}^{60}_{120}$ show the same contrast in maximal pull-out length and propagation ERR. Furthermore, for the symmetric ply-blocks exhibiting a FAW below $240\,\mathrm{g}\cdot\mathrm{m}^{-2}$, the maximal pull-out length is in relatively good agreement with the predictions obtained with the shear-lag model (Equation 3.5 applied with values assumed from Table 3.3), as reported in Figure 7.11. This suggests that the pseudo-ductility framework is valid to predict the pull-out length in intermediate to thin-ply hybrid laminates

		Width [µm]				Length [µm]			
Configuration	**Bundle count**	**Mean**	**Median**	**IQR***	**Max**	**Mean**	**Median**	**IQR***	**Max**
$^{100}B1^{30}_{0}$	$43e^3$	595	230	653	4255	64	0	114	954
$^{0}B2^{0}_{60}$	$26e^3$	571	250	491	3722	54	0	99	915
$^{0}B3^{0}_{120}$	$54e^3$	464	197	514	3804	112	0	151	2381
$^{0}B4^{0}_{180}$	$64e^3$	360	193	320	3831	210	0	212	4028
$^{33}L1A^{30}_{60}$	$33e^3$	477	210	592	3901	77	0	139	1030
$^{20}L2S^{30}_{120}$	$74e^3$	376	205	398	3940	89	0	150	1383
$^{33}L3A^{60}_{120}$	$75e^3$	326	181	271	3949	191	0	226	3920
$^{33}L4S^{60}_{120}$	$76e^3$	338	191	299	3910	105	0	165	1364
$^{14}L5A^{30}_{180}$	$66e^3$	356	210	305	3793	372	0	400	4551
$^{20}L6S^{60}_{240}$	$35e^3$	401	247	359	3570	403	0	431	5524

Table 7.1: Pull-out length analysis results. The bundle count metric stands for the number of analyzed pull-out bundles. Two samples were analyzed per configuration, resulting in four fracture surfaces, with the exception of $^{20}L6S^{60}_{240}$ for which only one sample was considered due to early out-of-plane failure in the others one. Only large initial crack data were available for $^{0}B2^{0}_{60}$ and $^{33}L1A^{30}_{60}$. Thus, the number of analyzed bundles is lower for these three configurations. The pull-out length median is close to 0 µm for all configurations. It indicates that most of the features, including the 90° plies, have a pull-out length close to 0 µm. * interquartile range

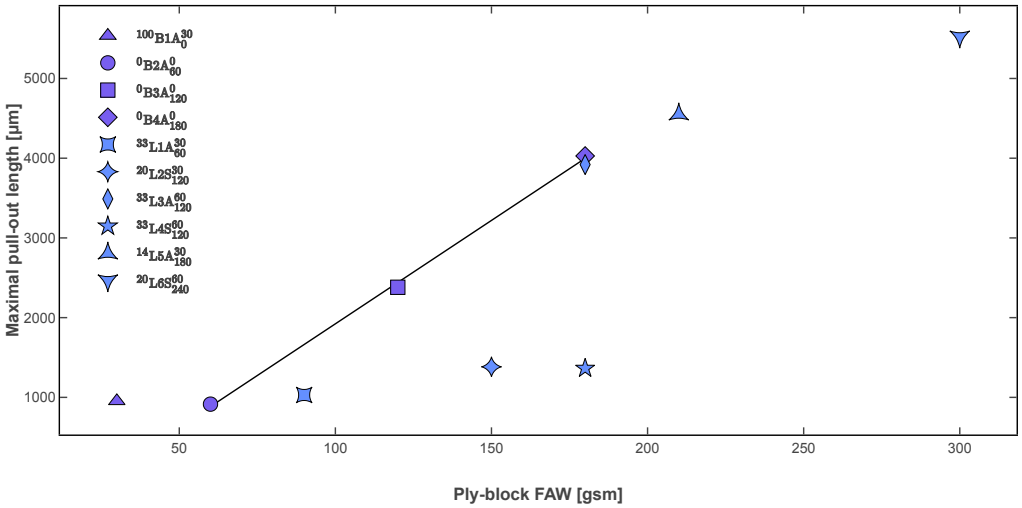

Figure 7.6: Maximal pull-out length as a function of ply-block FAW for interlayer hybrids.

designed for fragmentation. Moreover, this is an additional evidence that local pseudo-ductility was achieved, even if it was not observed at the macroscale. However, for thick laminates or asymmetric ply-blocks, the shear-lag model significantly underestimates the pull-out length. This confirms that the fragmentation is not the driving mechanism in these cases. Instead, the ply-thickness effect on the one hand, and the mismatch of moduli on the other, promote delimitation and then pull-out length.

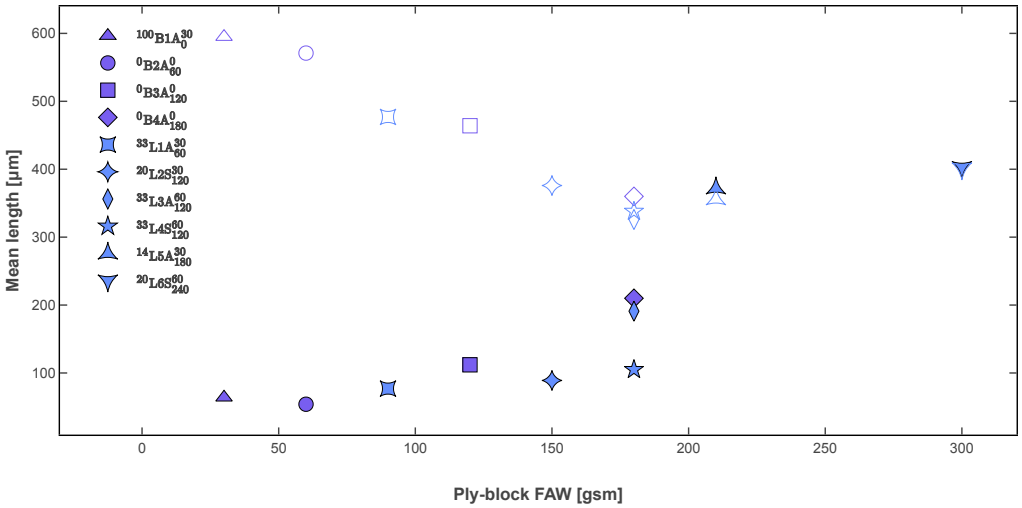

Figure 7.7: Mean pull-out length (filled symbol) and width (open symbol) as a function of ply-block FAW for interlayer hybrids.

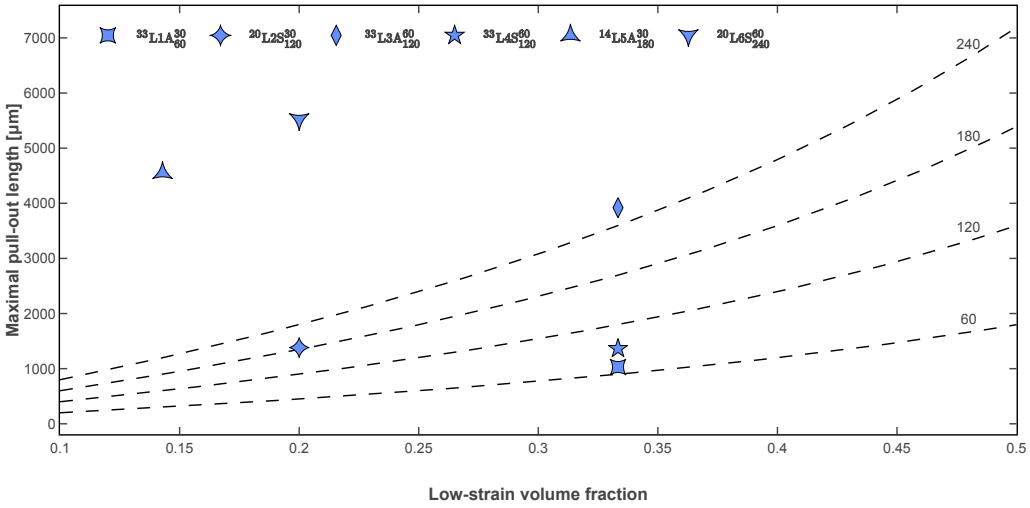

Figure 7.8: Maximal pull-out length as a function of low strain volume fraction γ for interlayer hybrids. The dashed lines correspond to the critical length predicted by Equation 3.5 for different values of high-strain FAW ($\mathrm{g \cdot m^{-2}}$).

In addition to the results obtained in this work, the pull-out lengths for the DENT specimens tested by Danzi et al. [56], and exhibiting stable fragmentation, were also analyzed. To do so, a rough estimate was obtained from CT-scan observations as detailed in Appendix C. As shown in Figure 7.11, these first-order measurements correlate well with the model predictions.

Both initiation and propagation ERR scale very well with the maximal pull-out length, as reported in Figure 7.12. It implies that the pull-out length is a valid descriptor for the translaminar toughness. It is therefore legitimate to develop strategies for promoting the pull-out length. Furthermore, it is remarkable that a simple linear regression with respect to the pull-out length provides a suitable first-order predictor for the translaminar toughness. Specifically, the three 34-700 baselines are almost

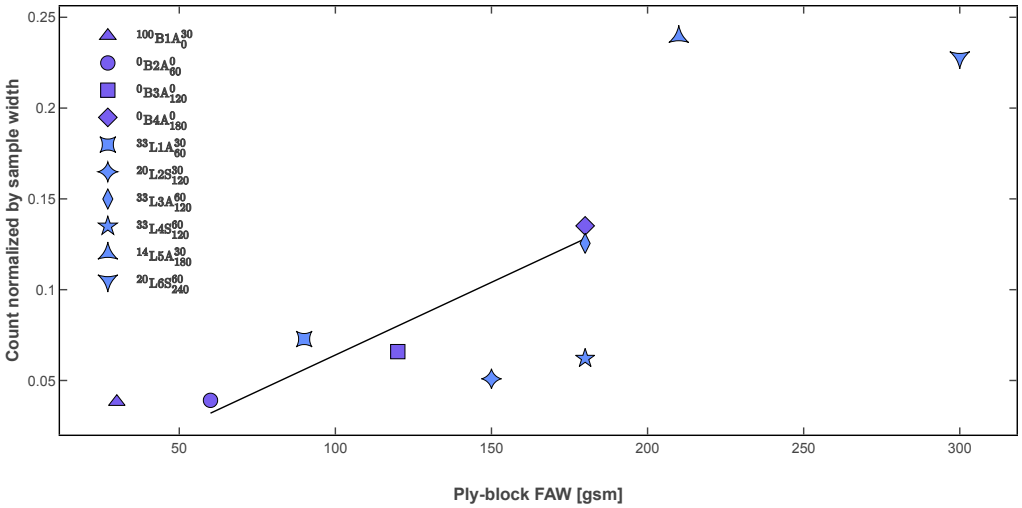

Figure 7.9: Count of pull-out bundles as a function of ply-block FAW for interlayer hybrids. Normalized by the sample width.

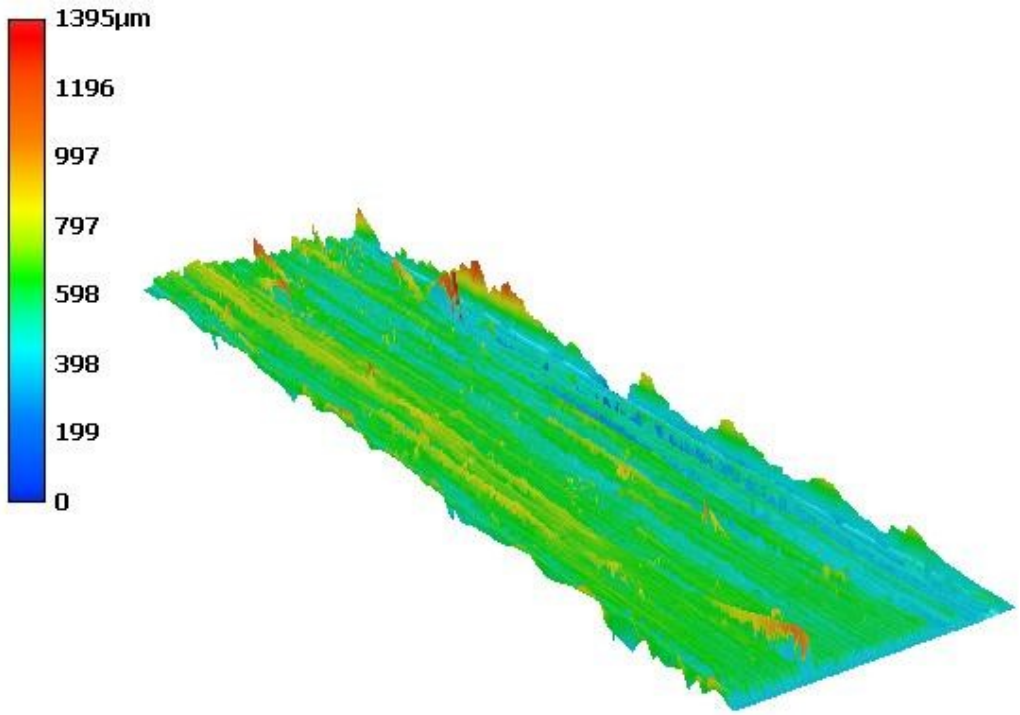

Figure 7.10: Post-mortem observation of $^{33}C2^{45}$ CT fracture surface.

perfectly aligned. Such a model assumes that the total ERR is driven by the total crack lateral surface, proportional to the pull-out length, through delamination, debonding and pull-out. The same result was obtained by Frossard [39] with M40JB-80ep specimens as shown in Figure 7.13a. It is worth noting that the linear fits do not pass through zero. The intercept value lies between $10\,\mathrm{kJ}\cdot\mathrm{m}^{-2}$ and $20\,\mathrm{kJ}\cdot\mathrm{m}^{-2}$. With more datapoints and a standardized measure of the pull-out length, it could be used to evaluate the toughness of the mode I translaminar toughness of the fibers and matrix. The results reported by Danzi et al. [56] also follow a similar linear trend shown in Figure 7.13b. However, its

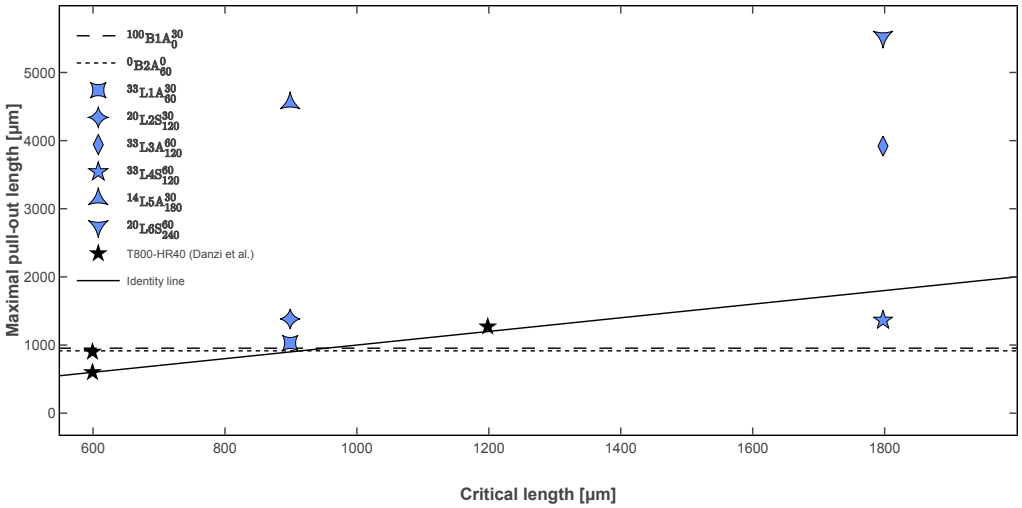

Figure 7.11: Correlation between maximal pull-out length and shear-lag model predictions. The pull-out lengths for the T800-HR40 were estimated from Danzi et al. [56] as detailed in Appendix C.

extrapolation lead to negative values for small pull-out lengths. This is likely to be due to the small number of points, the approximate method used to estimate the pull-out length (see Appendix C) and the test setup which was a DENT.

Material	t_H [g · m^{-2}]	t_L [g · m^{-2}]	**Pull-out length [µm]**	$J_{Ic,i}$ **[kJ · m^{-2}]**	$J_{Ic,ss}$ **[kJ · m^{-2}]**
T800-HR40/80ep	100	20	600	NA	118.8
T800-HR40/80ep	200	20	900	NA	168.7
T800-HR40/80ep	300	40	1270	NA	322.0
M40JB/80ep	30	NA	160	17.9	21.6
M40JB/80ep	75	NA	660	38.6	51.7
M40JB/80ep	100	NA	550	41.7	67.2
M40JB/80ep	150	NA	1100	60.3	109.1

Table 7.2: Pull-out lengths and translaminar toughness reported in the literature for CP laminates: Danzi et al. [56] for the T800-HR40 and Frossard [39] for the M40JB. Note that the T800-HR40 pull-out length is only an estimate obtained as detailed in Appendix C.

Finally, the deviations form the linear trend for the hybrid configurations demonstrate that the pull-out length cannot be the only metric considered to provide accurate predictions. In the following section, a more detailed approach based on the complete pull-out length distribution is proposed.

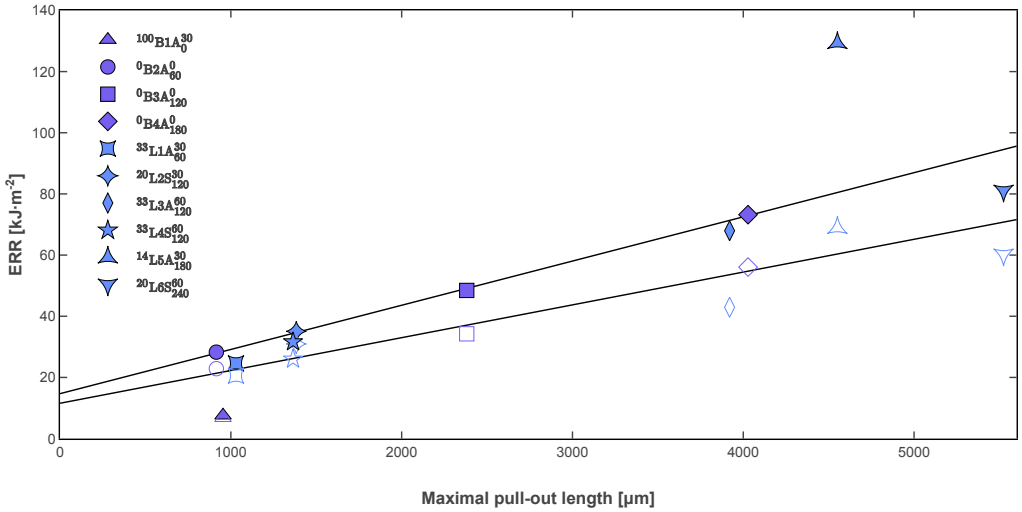

Figure 7.12: ERR as a function of maximal pull-out length for baselines and interlayer hybrids: initiation (open symbol) and propagation (filled symbol).

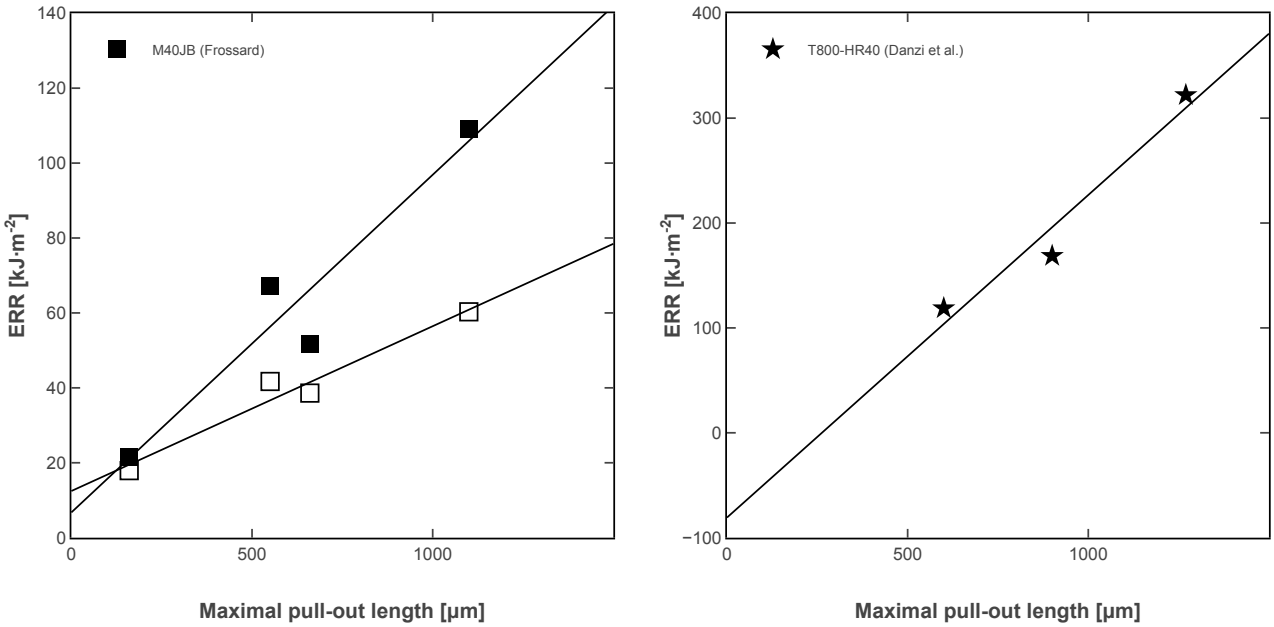

(a) **(b)**

Figure 7.13: ERR as a function of maximal pull-out length for specimens reported in the literature: (a) M40JB samples [39] (open symbols for initiation and filled symbols for ptopagation), and (b) T800-HR40 samples [56].

7.3 Translaminar toughness modeling

7.3.1 Mechanistic assumptions

The fracture process in a unidirectional ply of an interlayer laminate under longitudinal tensile loading is assumed to follow three sequential steps shown in Figure 7.14. First, the 0° pull-out bundle failure occurs. The low-strain fibers inside the process zone – around the crack tip – are the first to fail. When a low-strain fiber fails, it stops carrying the load around the breakpoint. This load is redistributed to neighboring fibers, increasing their stress and eventually leading to their own failure, creating a cluster of broken fibers. This process is well understood as reported in chapter 3.

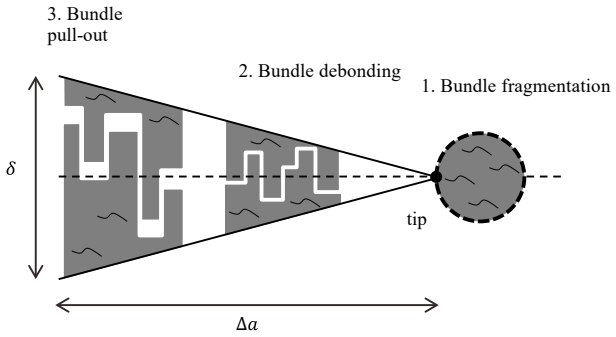

Figure 7.14: Modeled failure steps.

When a cluster of broken fibers reaches a critical size, a translaminar crack propagates inside the low-strain ply leading to its fragmentation. This transverse crack is confined to the low-strain ply by the thin-ply effect and high-strain plies keep carrying the load, preventing a catastrophic failure of the laminate. Pseudo-ductility may occur at this stage. However, as aforementioned, macro-scale pseudo ductility was not obtained with the chosen materials and laminates, as evidenced by the experimental results. Finally, as the laminate strain keeps increasing, the transverse crack is extended to the high-strain plies within a ply block – this is supported by observations of fracture surfaces.

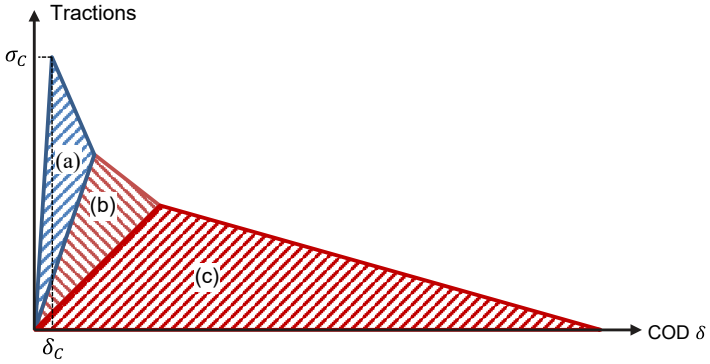

Figure 7.15: Schematic representation of the considered macroscopic cohesive law with (a) bundle fragmentation, (b) debonding, and (c) friction during pull-out.

Fragmentation (or more specifically bundle nucleation) happens at nearly zero COD (few micrometers) but at high stresses. This is the first part of the translaminar fracture process, thus the first part of the macroscopic cohesive law as depicted Figure 7.15. It corresponds to the initiation fracture toughness as measured in a CT test for example.

As the crack progresses, consecutive mode II delamination between ply-blocks and intralaminar cracks along 0° plies are followed by rough friction when the fragmented fiber bundles are pulled-out. These processes involve much lower stresses but are acting on a large COD (over several millimeters) and large developed surfaces. They are thus potentially very dissipative. They can be respectively represented

as a second and third part of the macroscopic cohesive law similar to bridging traction [142].

7.3.2 Modeling choices

Pull-out bundle failure

Investigating the full history of the pull-out bundle failure process would require a coupled micro-mesoscale approach as implemented by Mesquita et al. [165]. However, only the final state of failure is required by the present model, i.e., the pull-out length distribution and the associated toughness. Several methods may be implemented to estimate the pull-out length distribution: (i) a numerical model as implemented by Mesquita et al. [165], (ii) an analytical shear-lag model (see Equation 3.5), (iii) a stochastic approach as implemented by Bullegas et al. [149] and based on the analytical model proposed by Pimenta and Pinho [144], or (iv) an analysis based on a fracture surface assessment by optical microscopy as previously proposed.

To capture the fragmentation process as a cohesive law, the stress at the onset of damage can be estimated from the fragmentation equation reported in Table 3.1. The fracture energy associated with this first fracture process is determined from the experimental ERR at the initiation G_{Ic}. A linear decay of cohesive traction is assumed for this first part of the process so that the critical COD δ_1 at the end of the first process zone can be estimated from Equation 7.1.

$$G_{Ic} = \frac{1}{2}\sigma_{LF}\delta_1 \tag{7.1}$$

Bundle debonding and pull-out

The second and third process zones involve two possibly interacting and geometry-dependent mechanisms: mode II delamination and friction during debonding and pull-out, respectively. An analytical model such as the one proposed by Bullegas et al. [149] would not be able to capture these potential interactions. Therefore, in this work, a FEM was implemented at the ply-scale to represent those two interacting mechanisms for different pull-out bundle geometries (width and length) and interface properties (toughness and rough friction shear stress). This approach is more versatile as it could be further refined in the future. The FEM purpose is to predict the energy dissipated by debonding and bundle pull-out as a function of the COD δ. This was done for a thin representative layer, defined in the transverse plane, perpendicularly to the crack propagation, and for a given ply geometry and pull-out length distribution.

Traction-separation law identification

The energy dissipated by the previously described mechanisms can be considered to correspond to the work of traction forces σ applied over the COD δ. σ is then obtained by numerical derivation of the

energy ϵ with respect to δ, as noted in Equation 7.2.

$$\epsilon = \int \sigma d\delta \tag{7.2}$$

Evaluating the tractions for the successive value of COD δ_i, a discrete and macroscopic cohesive traction separation law was identified similarly to the approach proposed by Frossard et al. [142]. To achieve a dual-scale modeling framework and providing that the discretization of δ is fine enough, the identified macroscopic law can be implemented in a FEM software such as Abaqus using a tabular form for the cohesive damage parameter D defined in Equation 7.3.

$$D_i\left(\delta_i\right) = 1 - \frac{\sigma_i\left(\delta_i\right)/\delta_i}{\sigma_c/\delta_c} \tag{7.3}$$

7.3.3 Microscale model

Implementation

The FEM implementation consists of a Representative Volume Element (RVE) of a cross-ply laminate obtained with ply blocks in the 0-degree orientation and in the 90-degree orientation. The ply block is composed of low-strain HR-40 and high-strain 34-700 plies. They are modeled as homogenized solids according to the fiber datasheets (see Table 3.2). Typical homogenized elastic properties are reported in Table 7.3.

E_{11}	$E_{22} = E_{33}$	$\nu_{12} = \nu_{13}$	ν_{23}	$G_{12} = G_{13}$	G_{23}	γ
146 GPa	6 GPa	0.02	0.3	1.82 GPa	2.4 GPa	0.33

Table 7.3: Homogenized engineering constants for a 34-700-HR40 interlayer UD hybrids.

The initial configuration of the model is considered to be just after the ply block fragmentation. A median crack plane was defined in the laminate, as highlighted in Figure 7.16. The crack is assumed to remain, on average, in this plane while propagating in 90° ply blocks. Indeed, it is commonly observed that 90° transverse ply cracking occurs before fiber failure (see chapter 2). Thus those cracks are mostly aligned with the global crack propagation plane.

Translaminar crack planes in the 0-degree ply blocks were shifted from the median crack plane to a length corresponding to the local pull-out length l. The local pull-out length was randomly assigned, based on an experimentally measured or computer-generated pull-out length distribution. Finally, the direction of the shift (either positive or negative with respect to the median crack plane) was also randomly assigned. The RVE generation was implemented as a Python script for the CAE module of Abaqus 6.14 software.

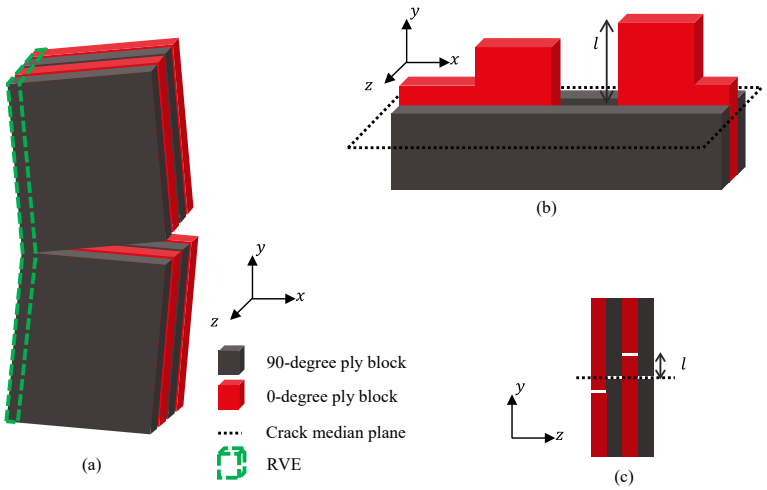

Figure 7.16: Schematic of (a) crack propagation in a cross-ply, (b) detailed view of the fracture surface, and (c) RVE.

C3D20R elements were used to model the ply blocks. The model is simplified to represent a single layer of 1 µm in-depth and includes N ply blocks of length L. A sensitivity study was carried out on the mesh size, the number of plies N, and the length L to ensure mesh independence and the representative volume size. Plane strain conditions are applied on its boundaries, and the crack opening displacement is imposed as a ramp loading via two reference points and kinematic couplings linked to the two extremities of the model, as shown in Figure 7.17a.

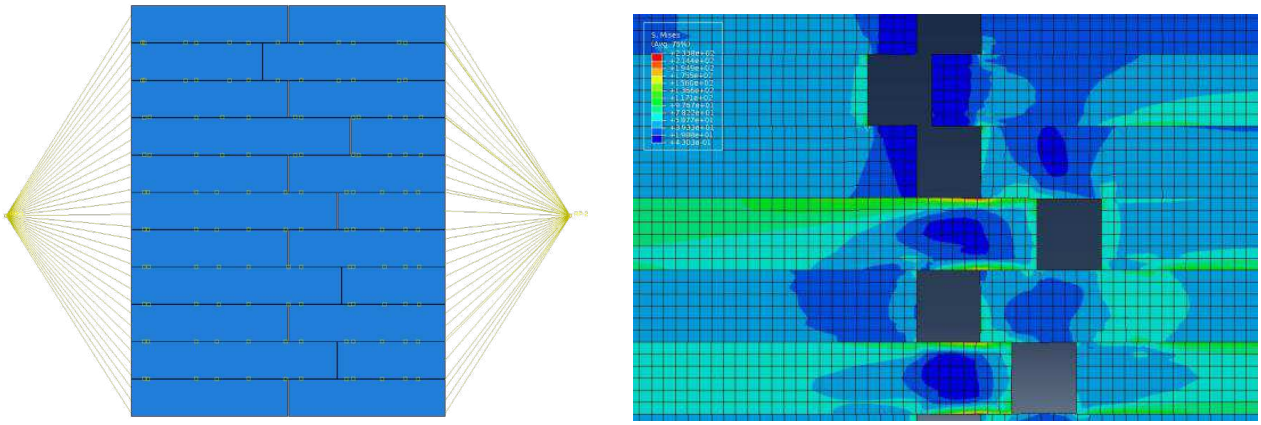

(a) **(b)**

Figure 7.17: Abaqus FEM illustrations: (a) FEM with $N = 5$ and (b) and loading state during the model resolution.

Cohesive surfaces were used to capture ply block debonding. They are formulated in such a way that they can only fail in shear–mode II. The interfacial stiffness was defined following Turon et al. [239]. The mode II interlaminar toughness with the cohesive law was adapted from experimental characterizations performed for the material selection with 4ENF samples (see Figure 3.2) and is close to values reported by Frossard [39] for the M40JB-80ep system. The interlaminar shear strength was assumed from the TP415 datasheet. The model properties are listed in Table 7.4.

$\boldsymbol{K_{nn} = K_{ss} = K_{tt}}$	$\boldsymbol{t_n^0}$	$\boldsymbol{t_s^0 = t_t^0}$	G_{IIc}	$\boldsymbol{\mu}$	τ_{max}
$3e^6\,\mathrm{N \cdot mm^{-3}}$	1000 MPa	30 MPa	$55\,\mathrm{N \cdot m^{-1}}$	1	5 to 40 MPa

Table 7.4: Cohesive and frictional properties. Note that the t_n^0 value is only used to avoid mode I failure and does not have a physical meaning.

The cohesive surface model is combined with a Coulomb frictional behavior, active after cohesive failure, to account for the friction caused by the bundle pull-out consecutive to the debonding. Due to the rough surfaces created during debonding (see section 7.4), it is assumed that the friction effects are mostly related to geometric interference of surface roughness.

The frictional shear stress is thus limited at a value τ_{max} corresponding to the failure of the interacting roughness, mostly matrix. To model such behavior, using the available "capped" Coulomb model in Abaqus, artificial overclosures are implemented to generate sufficient normal stresses and a friction coefficient μ of 1 is used. It ensures that the friction effect reaches the maximum shear stress defined in the model. Friction only becomes active after the failure of the cohesive interface and thus both mechanisms interact. For instance, friction can slow down crack growth.

Overclosures are resolved during the first implicit and static step to not interfere with the debonding and pull-out. Then, in a second implicit and dynamic step, the laminate is loaded under displacement control up to the COD δ. A small viscosity regularization coefficient of $1e^{-4}$ is used to achieve the convergence of cohesive elements. As a first step towards the model validation, this parametric model has been used to generate a database of damage and friction energies corresponding to several pull-out length, interlaminar toughness G_{IIc}, and frictional shear stress τ_{max} values, assuming no interactions between the plies (i.e., N=1). In this case, the database is valid for all hybrid configurations as the ply-block thickness has no influence.

Results and discussion

As shown by Figure 7.18, the total frictional energy and debonding energy dissipated by a pull-out bundle is a function of its length, as expected. More specifically, the debonding energy can be fitted and modeled by a linear function of the pull-out length while the frictional energy follows a second order power law. The apparent conciseness of this model is probably due to the absence of inter-plies interactions. The contribution of frictional energy is overall much more important than that of the debonding. For instance, with a pull-out length of 1000 µm, the debonding energy reported in Figure 7.18 represents approximately 5 % of the frictional energy. Furthermore, these results clearly indicate that promoting longer pull-out bundles is beneficial. Indeed, the frictional dissipation scales with both the pull-out length and the maximal COD, which is related to the pull-out length, hence

the quadratic effect of pull-out length.

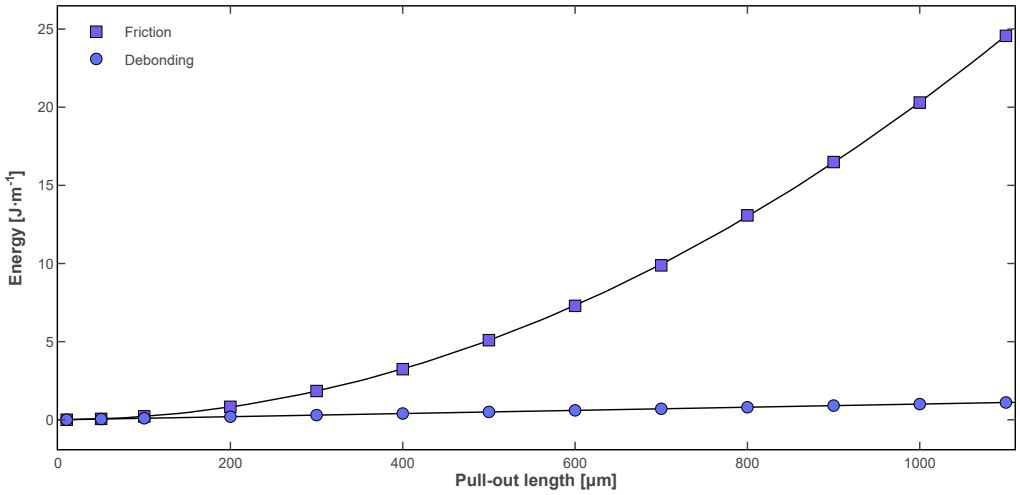

Figure 7.18: Total frictional and debonding energy for a pull-out bundle as a function of its length, for $G_{IIc} = 500\,\mathrm{kJ \cdot m^{-2}}$ and $\tau_{max} = 20\,\mathrm{MPa}$.

For a given pull-out length, the debonding energy and the frictional energy are respectively driven by the interlaminar toughness G_{IIc} and the frictional shear stress τ_{max}, through a linear relationship, as reported in Figure 7.19. As expected, the dissipated energy increases with the increase of these parameters.

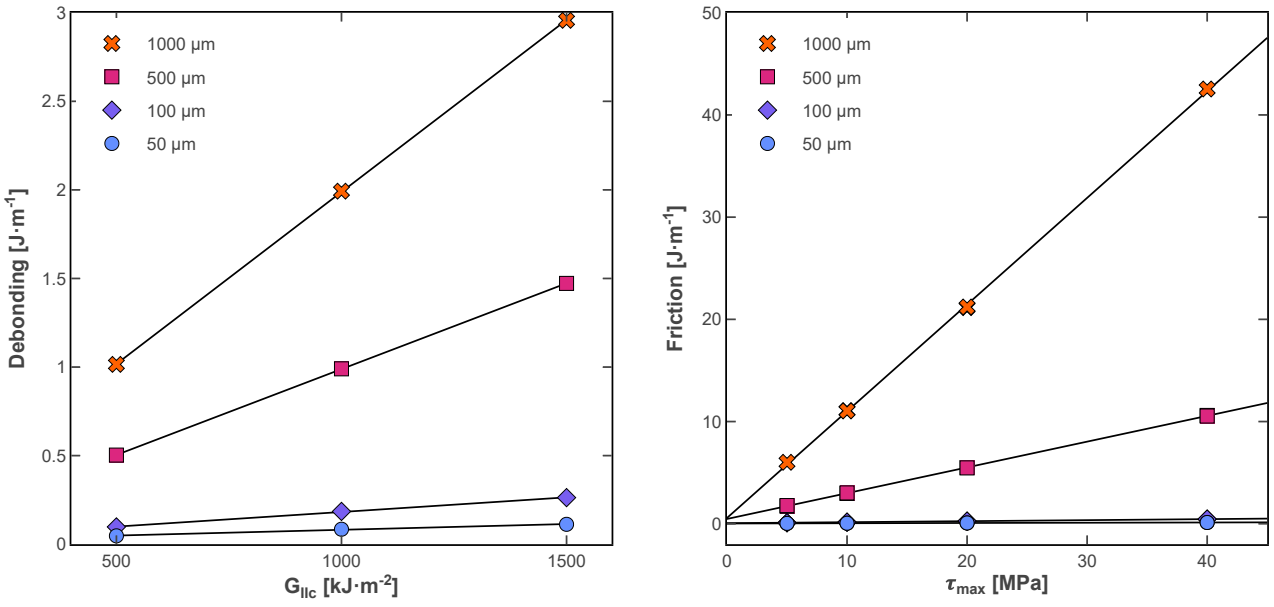

Figure 7.19: (a) Total debonding energy as a function of interlaminar toughness; (b) Total frictional energy as a function of frictional shear stress.

However, the total energy dissipated is necessary but not sufficient to identify a traction-separation

law. Instead, the energy history, i.e., the energy as a function of the COD δ, is required. Note that the total energy corresponds to the energy dissipated when the COD reached its maximal value, i.e. when the bundle is completely pulled-out. In this regard, the debonding energy is reported to saturate at small COD values in Figure 7.20. Indeed, the delamination occurs at small displacements, before the friction, and no more energy is dissipated once the bundle is debonded. If interplies interaction were considered, further delamitation may have happen due to local stress redistribution. Nevertheless, as the pull-out length increase, the debonding energy contribution quickly become limited compared to friction (for instance, above 200 µm with the parameters considered in Figure 7.18). Thus, considering additional delamination will not significantly alter the results. As highlighted in Figure 7.21, the rising part of the debonding energy and the frictional energy, as a function of the COD, may be fitted by power functions and second-order polynomial functions, respectively.

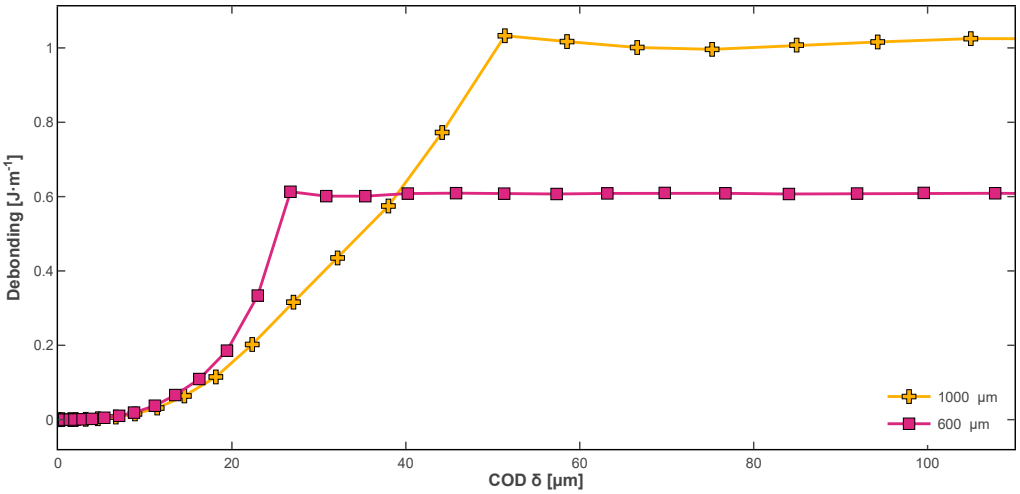

Figure 7.20: Debonding energy saturation.

Consequently, these analytical laws were used to predict the energy dissipated by a given pull-our bundles and speed-up the simulation pipeline. Indeed, a detailed and expansive database correlating the dissipated energy with the pull-out length and model parameters would have been required otherwise. Thus, the debonding energy is modeled as Equation 7.4, and the frictional energy as Equation 7.5, where δ is the COD. The parameters A, B, C, A', B', C', C'', and N are identified from the results previously presented and reported in Table 7.5.

$$\epsilon_d = \min\left(A\delta + C,\ B\delta^N + C'\right) \tag{7.4}$$

$$\epsilon_f = A'\delta + B'\delta^2 + C'' \tag{7.5}$$

Specifically, the interlaminar toughness is known from Figure 3.2 and fixed to this value. Then, one analytical relation is identified for the debonding energy. However, the frictional shear stress is assumed and there it must be possible to change its value in order to tune the model. Thus, a relation between parameters $A\prime$, $B\prime$, $C\prime\prime$ and the frictional shear stress τ_{max} is required. Plotting these coeffi-

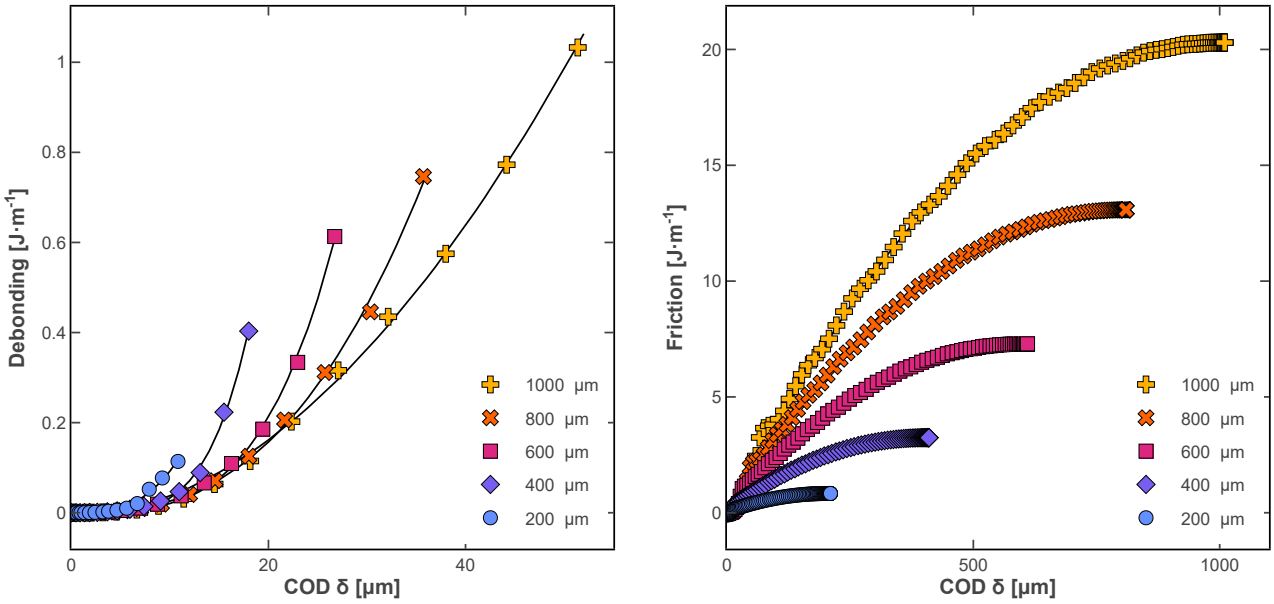

(a) **(b)**

Figure 7.21: (a) Debonding energy as a function of COD for several pull-out bundle lengths; (b) Frictional energy as a function of COD for several pull-out bundle lengths.

cients as a function of τ_{max} and the pull-out bundle length λ, as in Figure 7.22, one may notice that A' (Figure 7.22a) and B' (Figure 7.22b) may be approximated by direct functions of τ_{max}, while the intercepts are negligible.

$$A' = 2\tau_{max}\lambda \tag{7.6}$$

$$B' = -\tau_{max} \tag{7.7}$$

A	C	B	N	C'	A'	B'	C''
1010	2342	$2.86e^{-18}\lambda^{6.53} + 4.52$	$282.75\lambda^{-0.69}$	0	$2\tau_{max}\lambda$	$-\tau_{max}$	0

Table 7.5: Identified analytical parameters.

7.3.4 Macroscale model

Implementation

The CT test is modeled in 2D following the same approach as Frossard [39] with Abaqus 6.19. 8-nodes shell quadratic elements (CPS8R) and plane stress conditions are used. The translaminar fracture process is captured with two overlapping layers of cohesive elements (20 µm, COH2D4). The first one corresponds to the pull-our bundle failure and the second one to the debonding and pull-out, identified from the microscale model. The traction-separation laws are tabulated with at least 300 entries. The

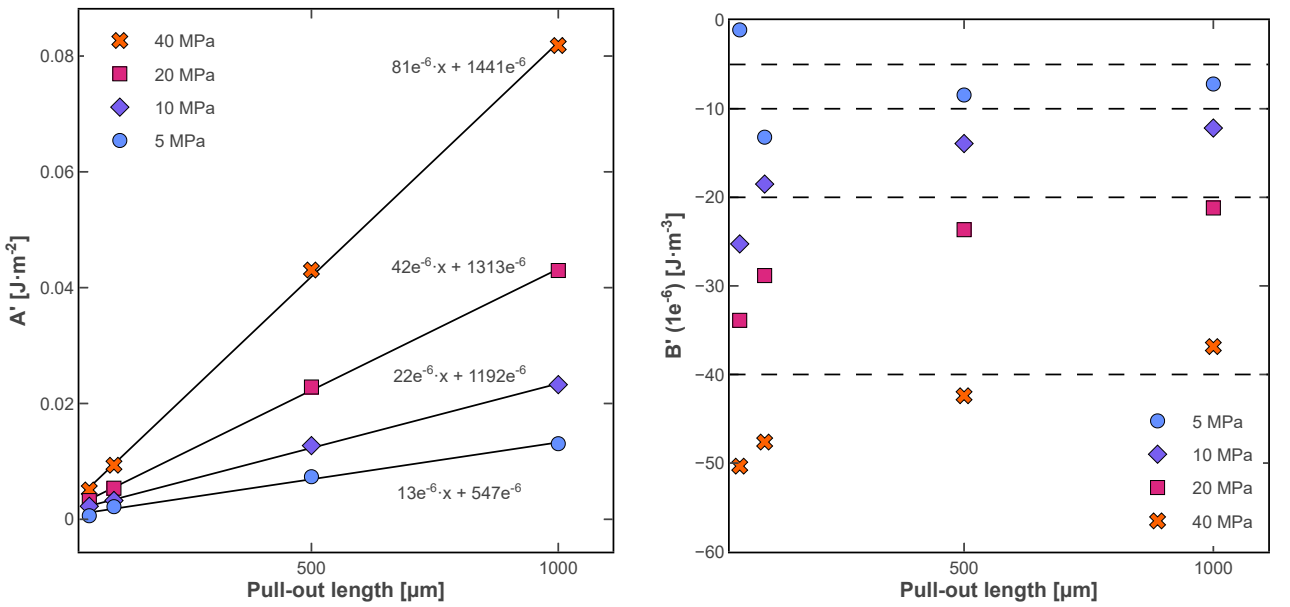

(a) **(b)**

Figure 7.22: Frictional energy parameters identification for several frictional shear stress τ_{max} values: (a) A' and (b) B'.

displacement is enforced through reference points and kinematic coupling to the loading holes. The viscosity regularization coefficient is tuned until convergence of the model.

To generate the traction-separation law corresponding to debonding and pull-out, During this procedure, a representative RVE is generated based on the experimental pull-out distributions. Then, the energy contribution for each pull-out bundle is calculated according to the analytical relations previously identified (Equation 7.4 and Equation 7.5). The total energy as a function of the COD is recorded and used to generate a damage law shown in Figure 7.23, applying Equation 7.3. The CT FEM experiment is then simulated and the numerical displacement curve is compared with the experimental one. The microscale model parameters are then updated until (here only τ_{max} varies) until the numerical predictions converge with the experimental results. Thus, an inverse identification of τ_{max} is performed, as described in Figure 7.24.

In this work, a 5 mm long and 4 mm wide RVE was considered. The width was chosen as the average width of the specimens. The length is a reasonable FPZ length considering the experimental observations previously reported. The number of pull-out bundles per unit of projected crack area is known from the profile analysis (section 7.2). Thus, a representative sample was drawn randomly from the pull-out bundle distributions, resulting in population size from 5000 to 15000 bundles. Arguably, the RVE is large enough to be representative of the mean response. As a consequence, the dissipated energy is averaged and only one traction-separation law is used for all the cohesive elements modeling the debonding and pull-out. A more detailed analysis should investigate the stochastic nature of the distributions with RVE corresponding, for instance, to the size of the cohesive elements. In this case,

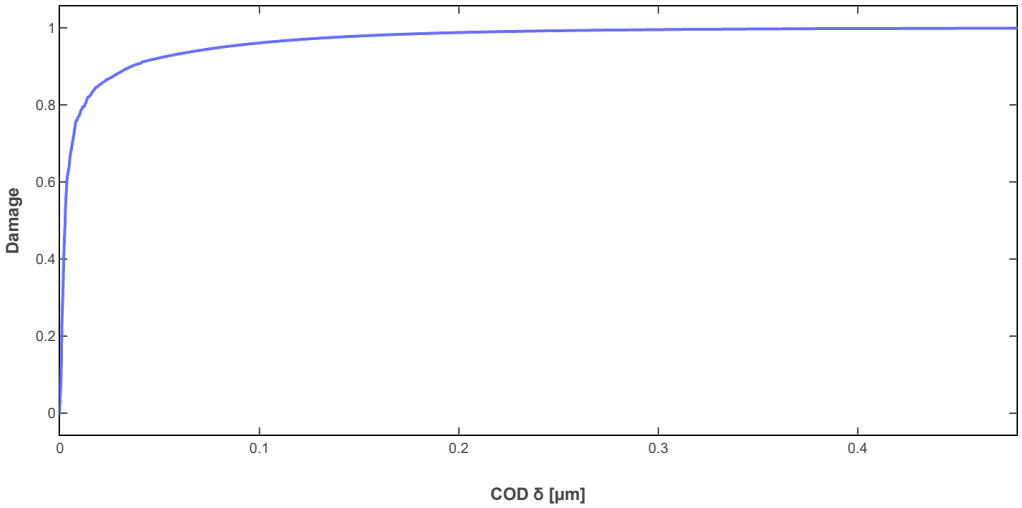

Figure 7.23: Illustration of a damage law for $^{20}\mathrm{L2S}^{30}_{120}$.

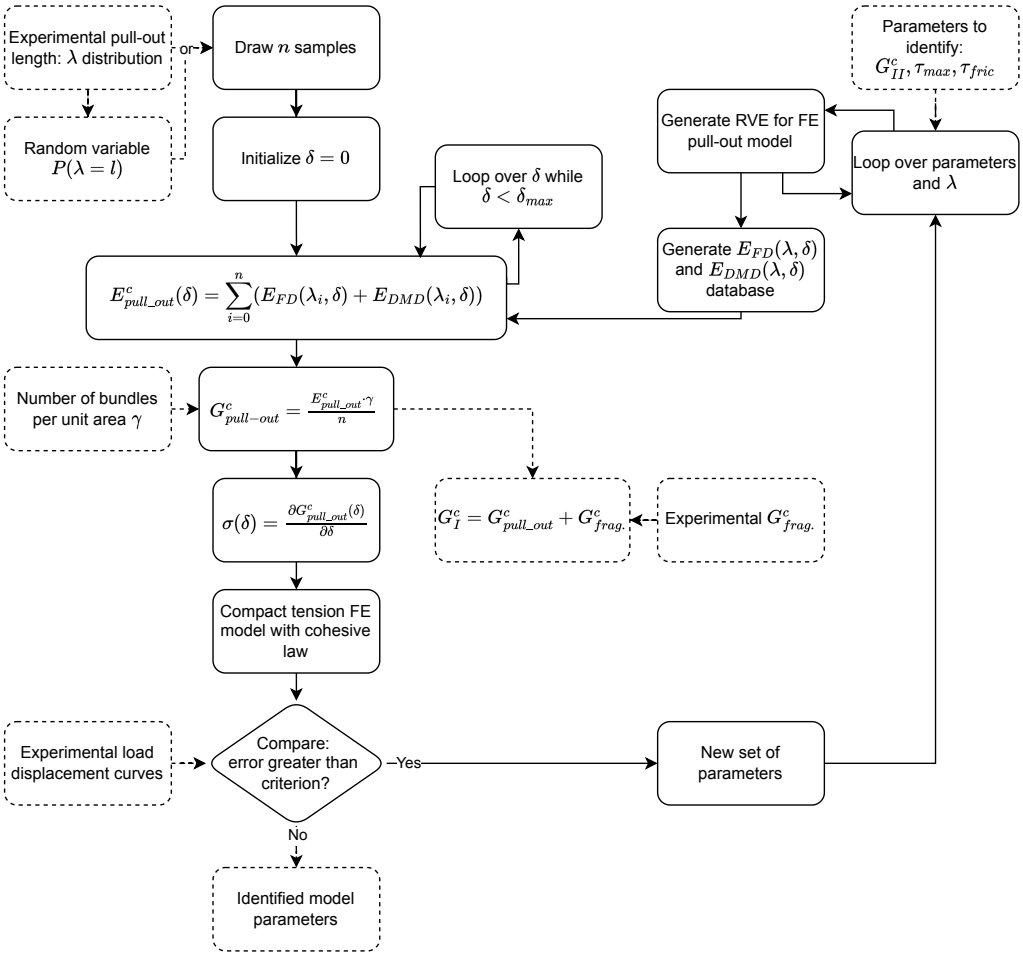

Figure 7.24: Model optimization loop.

each cohesive elements would be implemented with a different traction-separation law. This may capture the discrete nature of crack propagation observed in this work, but could lead to numerical issues.

Results and discussion

Instead, the proposed approach captures a continuous crack propagation, illustrated in Figure 7.25. Otherwise, it captures well the compliance of the sample as the crack propagates. Note that neither the interlaminar shear nor the non-linear in-plane shear deformation were implemented. Thus, the CT FEM did not capture the non-linearity of CP specimens correctly [39]. The laminate elastic constants were therefore tuned to achieve an elastic state close to the experimental one when the first crack propagation occurs. The optimization approach resulted in identifying the value of 20 MPa for τ_{max}.

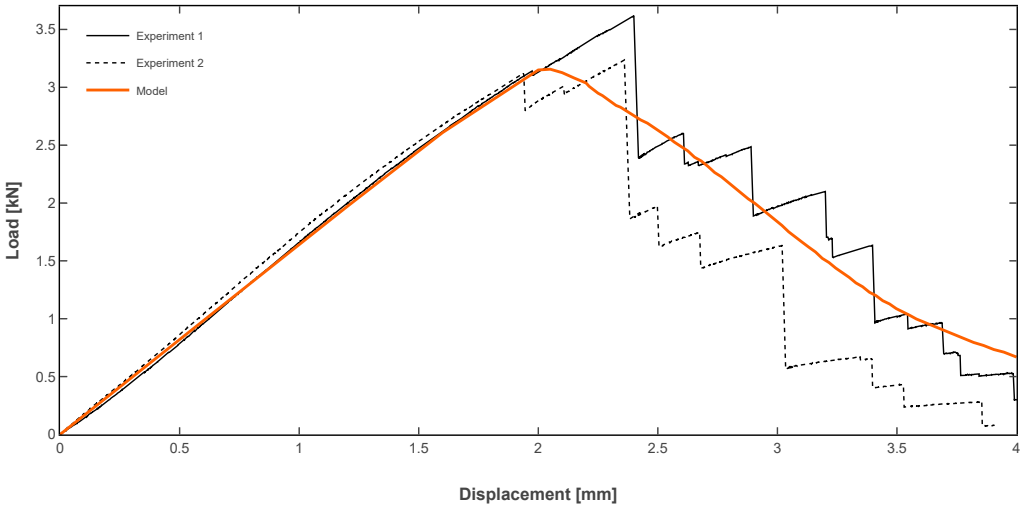

Figure 7.25: CT experimental and numerical load-displacement curves for ${}^{0}\mathrm{B}4^{0}_{180}$ interlayer hybrid specimens. $\tau_{max} = 20$ MPa was used.

This τ_{max} value was then used to predict the contribution of debonding and friction to translaminar toughness for the configurations tested in this work. These predictions are compared to the experimental results in Figure 7.26. More detailed results are provided in Appendix C. Overall, a very good correlation is found between the model and the experiment. It is worth noting that only ${}^{33}\mathrm{L}4\mathrm{S}^{60}_{120}$ was used to calibrate the model. Thus, these results demonstrate the model's predictive capability, with the exception of ${}^{20}\mathrm{L}6\mathrm{S}^{60}_{240}$. This deviation is explained by the early failure of ${}^{20}\mathrm{L}6\mathrm{S}^{60}_{240}$ specimens due to buckling and back end compression (see chapter 5). Consequently, the FPZ could not develop and the $J_{Ic,ss}$ value was never reached. However, the pull-out length distribution obtained for these specimens can be used to predict the $J_{Ic,ss}$ value.

Figure 7.27 highlights the effect of pull-out distribution for the interlayer hybrids ${}^{33}\mathrm{L}3\mathrm{A}^{60}_{120}$ and ${}^{33}\mathrm{L}4\mathrm{S}^{60}_{120}$, compared to their baseline ${}^{0}\mathrm{B}4^{0}_{180}$. According to the model, long pull-out bundles at the crack surface are key to improved translaminar toughness. As shown in Figure 7.27a and Figure 7.27b, few large bundles with a pull-out length greater than 500 µm account for the greater part of the dissipated energy. Thus, the difference in translaminar toughness between ${}^{33}\mathrm{L}4\mathrm{S}^{60}_{120}$ and ${}^{33}\mathrm{L}3\mathrm{A}^{60}_{120}$ is explained by the difference in bundle counts in the range 500 to 4000 µm. This observation supports the experimental finding that secondary damage that promote longer pull-out bundles are beneficial

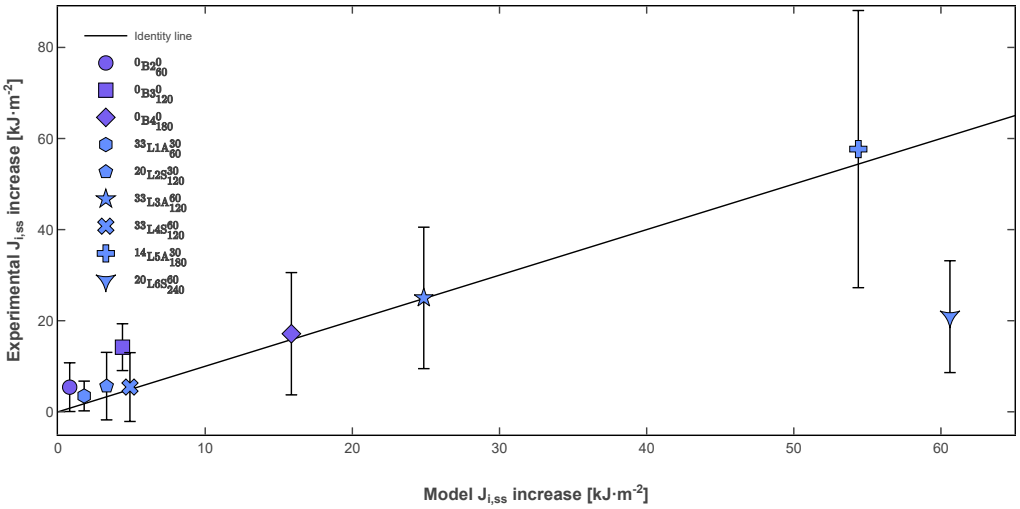

Figure 7.26: Correlation between experimental and simulation contribution of debonding and friction to the translaminar toughness.

for the translaminar toughness.

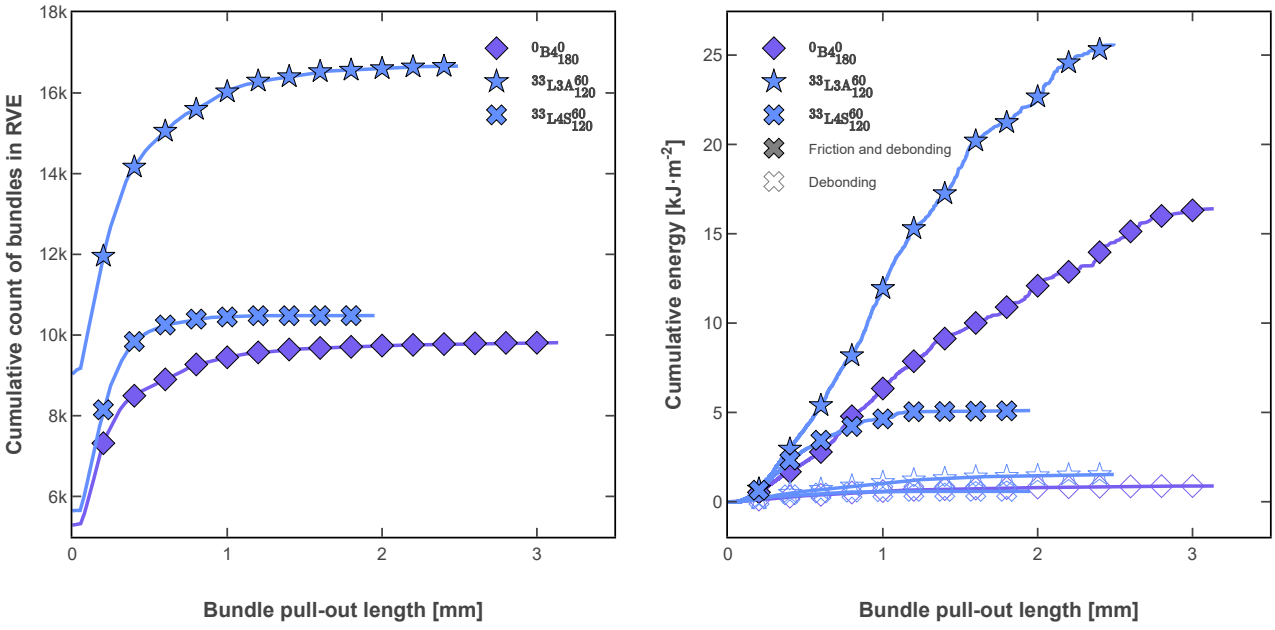

(a) **(b)**

Figure 7.27: (a) Cumulative count of pull-out bundles as a function of their length for three configurations; (b) Predicted cumulative energy dissipated by pull-out bundles as a function of their length for three configurations.

7.4 Scanning electron microscope phenomenological observations

This section reports phenomenological observations achieved with a SEM to support the results shown in this work. The specimens were coated with approximately 5 nm of gold, or gold and palladium, applied by sputtering. They were observed with a Zeiss GeminiSEM 300. Figure 7.28 highlights the different fractures surfaces exhibited by different configuration.

Specifically, Figure 7.28a illustrates the larger and longer bundles of $^{33}\text{L3A}^{60}_{120}$ compared to $^{33}\text{L4S}^{60}_{120}$ (note the difference of scale). It is worth noting that some bundles span across the complete ply-block thickness in Figure 7.28b, indicating that the ply-block behaved as an homogeneous material, although the majority of them contain a fracture surface at the low-to-high strain material interface. In $^{33}\text{L3A}^{60}_{120}$ (Figure 7.28a), the low-strain material, located on the side towards the central symmetry, have failed almost systematically at the average crack plane, while the high-strain material formed pull-out bundles. These observations correlate the finding that the translaminar toughness was in-between the ply-block scaling and the sub-ply scaling RoM (see chapter 5).

The interyarn specimens (Figure 7.28c and Figure 7.28d) exhibit a very specific fracture surface, without significant pull-out bundles, but with short individual pull-out fibers. Very interestingly, the majority of the fibers in the low-strain tow area (Figure 7.28c) seems to have failed in the same plane, which is not the average crack plane. Assuming that these fibers were bridging the crack as shown in chapter 6, it may indicate post crack propagation failure in a plane equidistant from the both crack surfaces.

Figure 7.29 highlights several details of the fracture surface that indicate a surface roughness compatible with the contribution of friction to the dissipated energy, as postulated in section 7.3.

Finally, Figure 7.30 shows the clustering of the toughening rubber particles in the matrix, or more exactly the micro-voids that result from cavitation under hydrostatic stress [240, 241]. Although the cavitation is intended as a beneficial effect, as it brings plasticity, and therefore toughness to the otherwise brittle epoxy matrix, the observed clustering of the rubber particles may lead to an early coalescence of the micro-voids. Such a coalescence could lead to matrix cracking and explain the moderate thin-ply effect observed in this work. Indeed, the tests conducted by NTPT on the TP415 epoxy system with T800S carbon fibers confirm that the thin-ply effect is much less significant in TP415 epoxy compared, for instance, to the TP190 (see Figure 7.31)[1]. Further research conducted with different matrix-toughener systems exhibiting a better thin-ply effect are required to investigate this point.

[1]Note that these tests were reported after the material selection for this study.

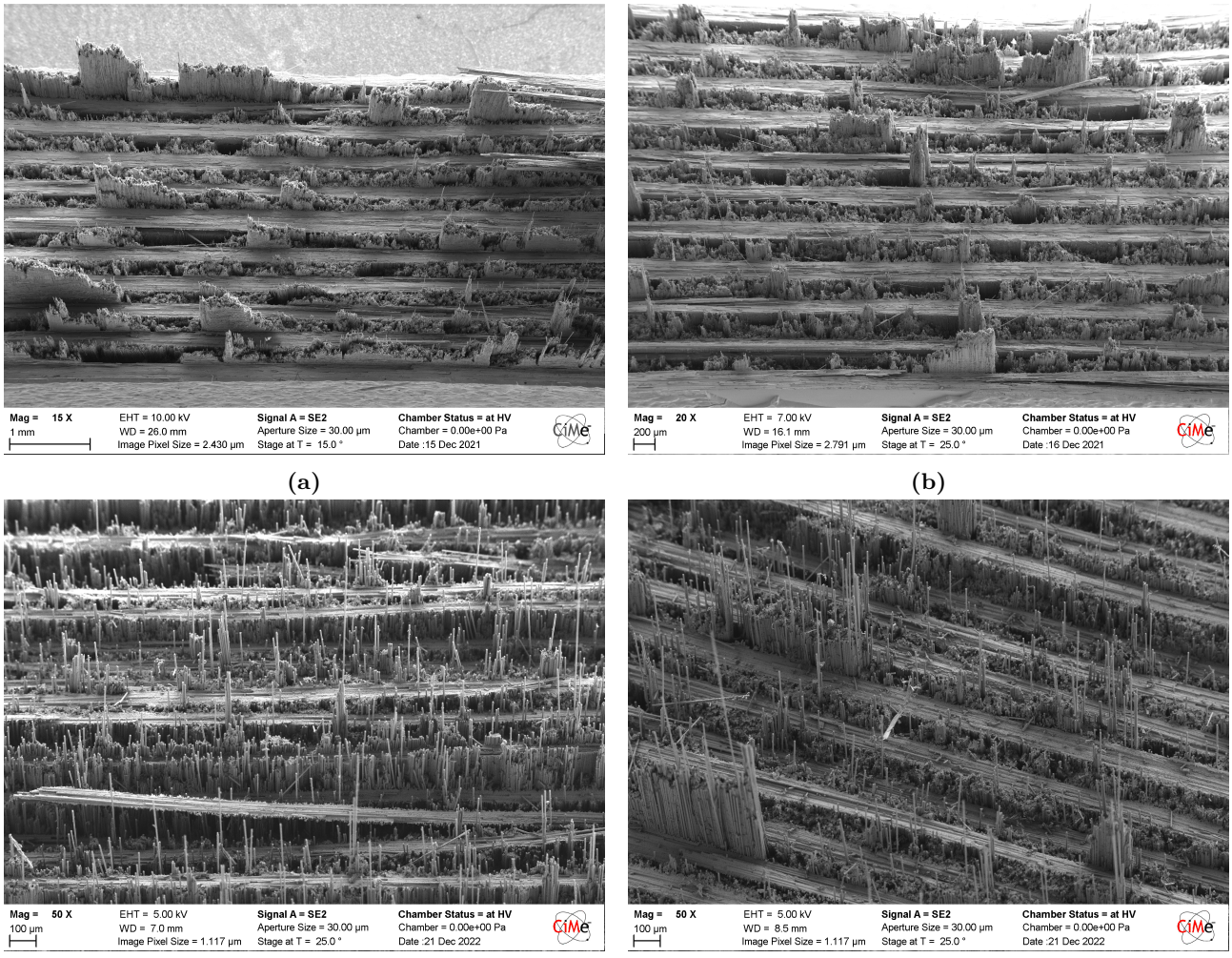

Figure 7.28: SEM fracture surface observations: (a) $^{33}\mathrm{L3A}^{60}_{120}$, (b) $^{33}\mathrm{L4S}^{60}_{120}$, (c) $^{31}\mathrm{Y3}^{45}$ in the low-strain tow, and (d) an interyarn hybrid with a FAW of $90\,\mathrm{g}\cdot\mathrm{m}^{-2}$ whose properties were not reported in this work.

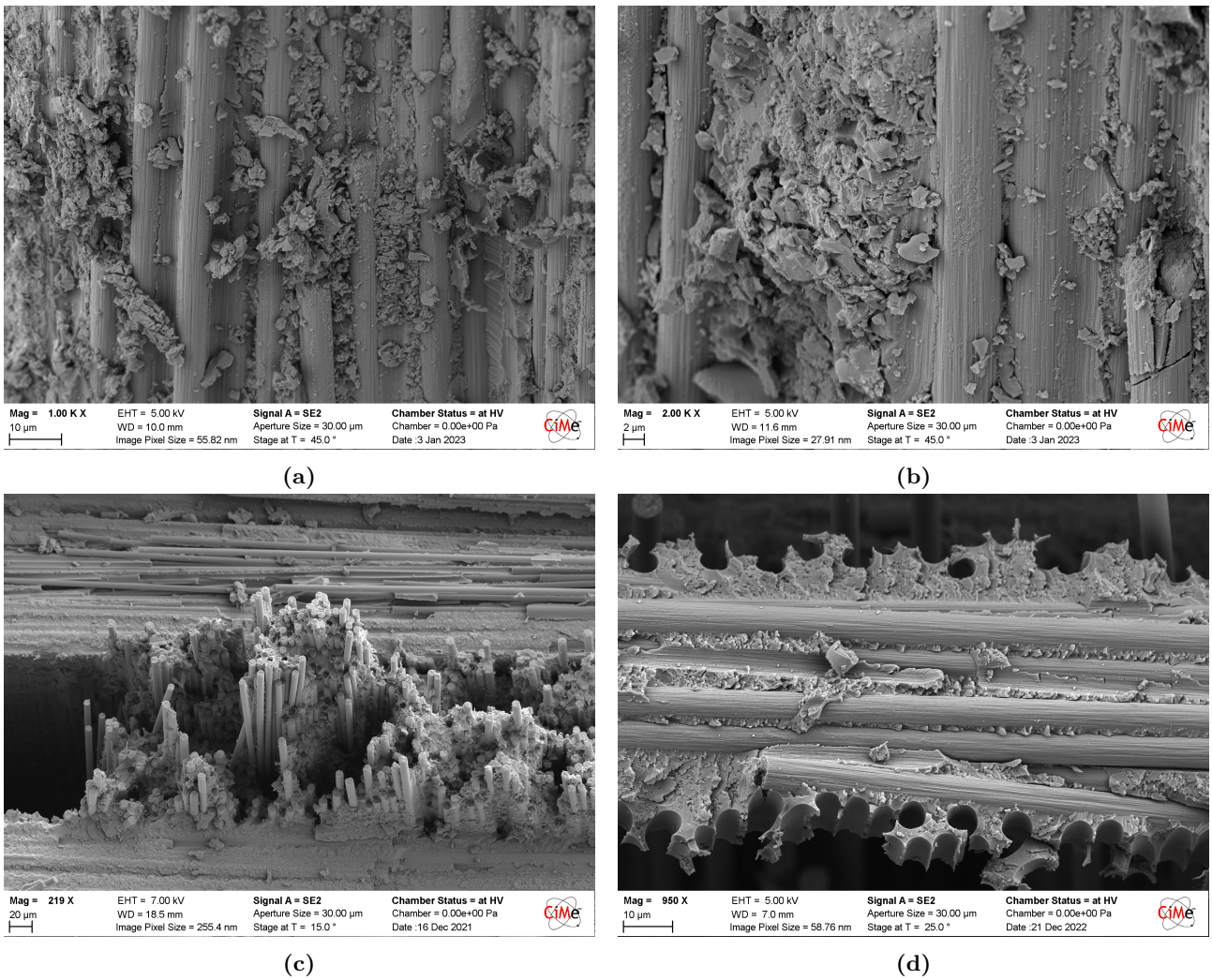

Figure 7.29: SEM fracture surface detailed observations: (a) and (b) roughness at the surface of pull-out bundles ($^{33}\text{L4S}^{60}_{120}$), (c) and (d) various details ($^{33}\text{L4S}^{60}_{120}$ and $^{31}\text{Y3}^{45}$, respectively).

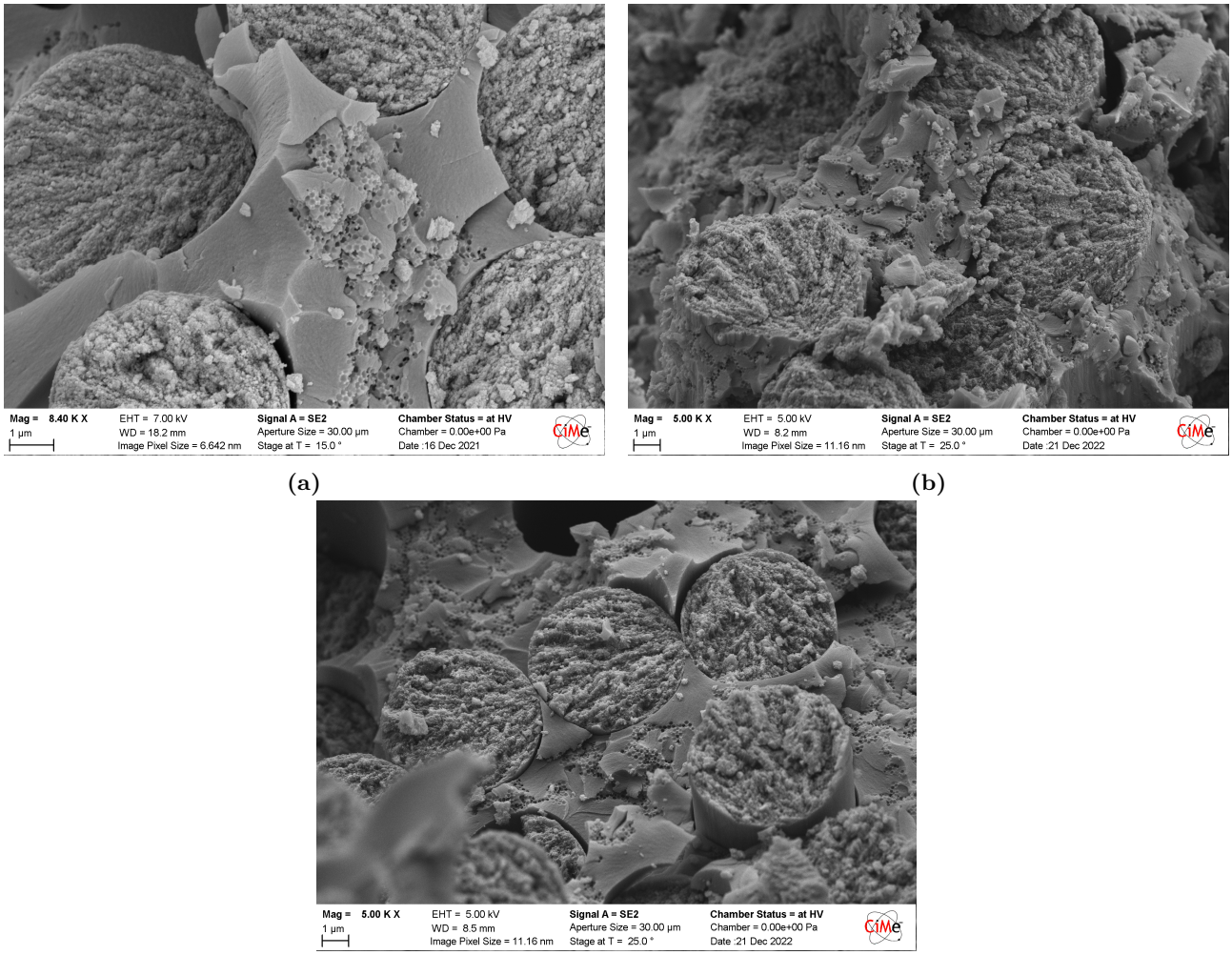

Figure 7.30: SEM observations of toughening particle clusters in different samples.

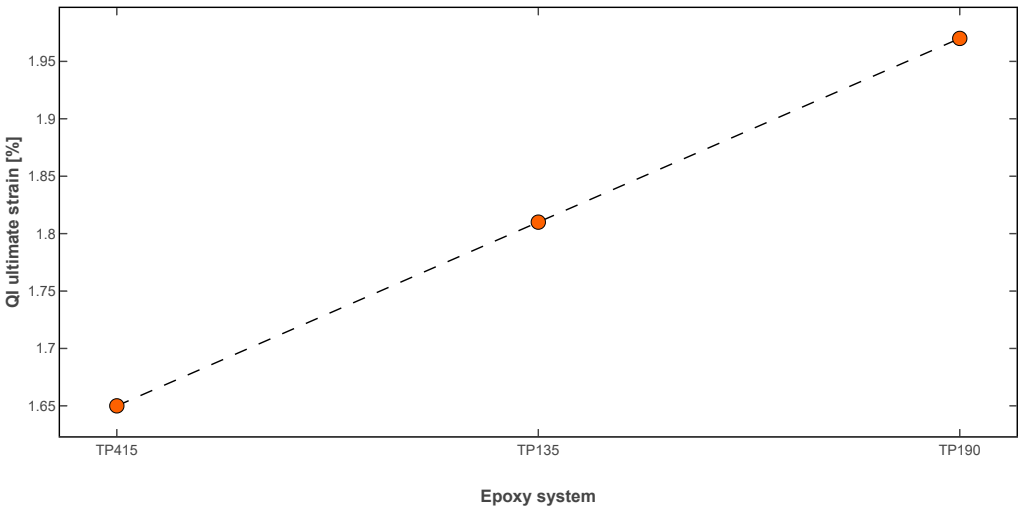

Figure 7.31: QI ultimate strain achieved with T800S carbon fibers and a plt FAW of $60\,\mathrm{g}\cdot\mathrm{m}^{-2}$ for NTPT epoxy systems TP415, TP315 and TP190, according to their datasheet. An higher ultimate strain indicates a better thin-ply effect. For reference, the T800S ultimate strain reported by its datasheet is 2 %.

7.5 In-situ phenomenological observations

Time-resolved SRCT was performed as part of the author's secondment at KULeuven. The author produced the samples following the mini-protruded CT specimen geometry proposed by Ahmadvashaghbash et al. [184], following the same processing route as for the regular CT specimen reported in this work. The laminate stacking was a symmetrical CP, with one layer in the 0° direction and two layers in the 90° direction to bring stability. The laminates typically exhibit a FAW of approximately $500\,\mathrm{g}\cdot\mathrm{m}^{-2}$. Therefore, the laminate was debulked at least 10 min for each ply during the stacking to ensure proper compaction of the plies and a flat surface. The initial crack was milled with a diamond wire of 125 µm diameter. However, the specimens were found sensitive to the resulting crack tip diameter, and the crack tip was further sharpened by Sina Ahmadvashaghbash using a thin steel foil.

Dr. Christian Breite and his colleagues performed the experiments at the TOMCAT beamline of the Swiss Light Source (Paul Scherrer Institut, Villigen, Switzerland) as access was restricted due to COVID-19-related regulations.

The volumes were reconstructed at KU Leuven and analyzed at EPFL by the author and Abdullah Aydemir in collaboration with Sina Ahmadvashaghbash. The author gratefully acknowledges Prof. Yentl Swolfs, Dr. Christian Breite, Dr. Mahoor Mehdikhani, Sina Ahmadvashaghbash, and Camilo Rojas for assisting with this experiment.

The SRCT results reveal the in-situ phenomenological mechanisms related to the pull-out of fiber bundles. Figure 7.32 depicted what is either a bridging or a pull-out bundle. Indeed, the field of view is too narrow to conclude regarding the presence of a translaminar crack. Nevertheless, a pull-out bundle of this size is fully compatible with the post-mortem analysis of fracture surfaces. For instance, pull-out lengths up to 4000 µm were reported in Figure 7.1 or in Figure C.4.

As shown in the side view, the bundle is fully bridging the COD. The top view highlights that the bundle is fully debonded. The minimum intensity projection of the ply is reported in Figure 7.33 and provides further shreds of evidence of the bundle debonding.

Two baselines and two hybrid configurations were investigated. While the damage sequence leading to the formation of the bundle still requires substantial further work and clarification, it is interesting that the bundle is bent quite significantly and thus appears loaded with a bending moment. A procedure is thus proposed to evaluate the forces at play. First, the curvature angle of the bundle was evaluated by implementing an image processing script to identify local fiber angles. Indeed, it is seen from the main view in Figure 7.32 that the fibers are locally aligned overall in the same direction, sufficiently in focus and contrasted to allow for edge extraction. Thus, the bundle was discretized with elements of approximately 400×400 µm and the OpenCV library was used to extract the image edges (mostly fibers here). A normal distribution was then fitted on the edge angles and the distribution

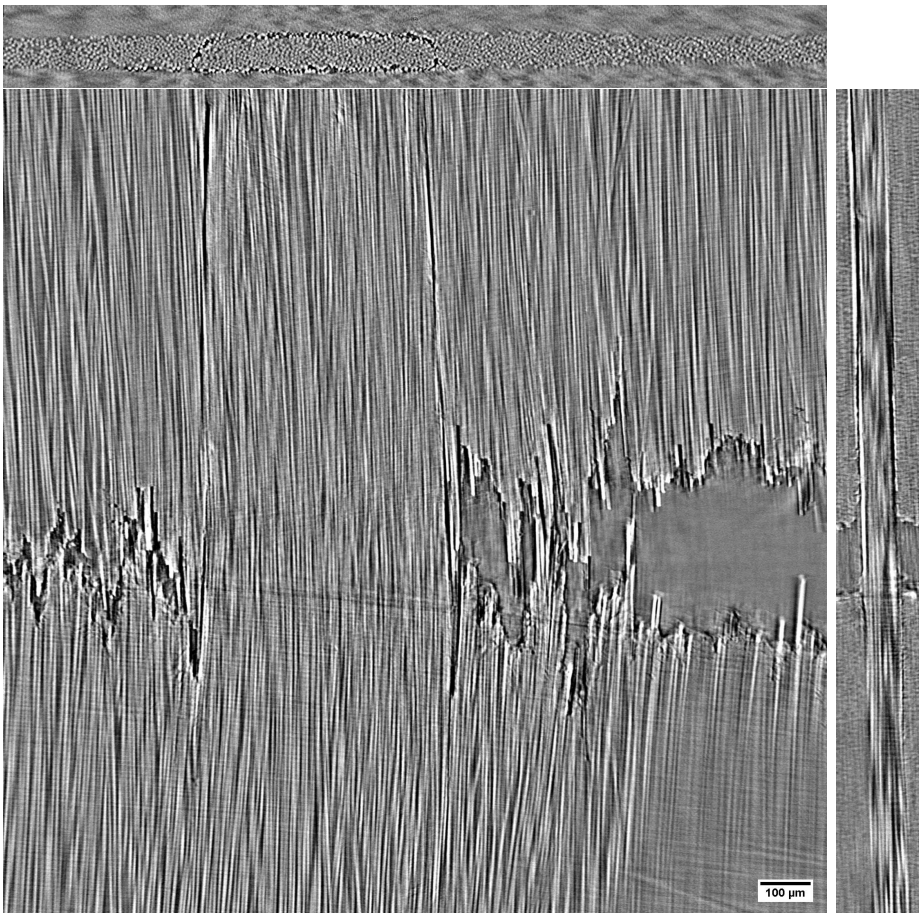

Figure 7.32: SRCT of a 34-700 $60\,\mathrm{g}\cdot\mathrm{m}^{-2}$ FAW specimen showing a pull-out bundle.

mean was considered a first-order approximation descriptor of the fiber's local orientation. Doing so, a curvature angle θ of approximately 3.6° was reported for the aforementioned bundle.

The parameterization of a beam (representing the bundle) undergoing bending is represented in Figure 7.34. The bending moment was evaluated as in Equation 7.8.

$$M_z = \frac{E_{11} I_{zz}}{\rho} \tag{7.8}$$

where:

M_z : the bending moment

I_{zz} : the inertia moment

ρ : the curvature

Introducing $I_{zz} = \frac{bh^3}{12}$ and $\rho = \frac{L_0}{\theta}$, and estimating from the scan 1.36 mm for L_0, 0.34 mm for h and 0.06 mm for b, M_z was evaluated to $0.12\,\mathrm{N}\cdot\mathrm{m}$. Further assuming that the beam (or bundle) is pinned at both ends and loaded with a uniform pressure P, then $P = \frac{12 M_z}{L_0^2}$ is roughly evaluated as 10 MPa. Such a pressure would be sufficient to cause for instance mechanical interlocking. Thus, it could contribute to the apparent frictional stress of 20 MPa identified with the FEM, even though the geometry (and thickness) of the samples were different in this particular case.

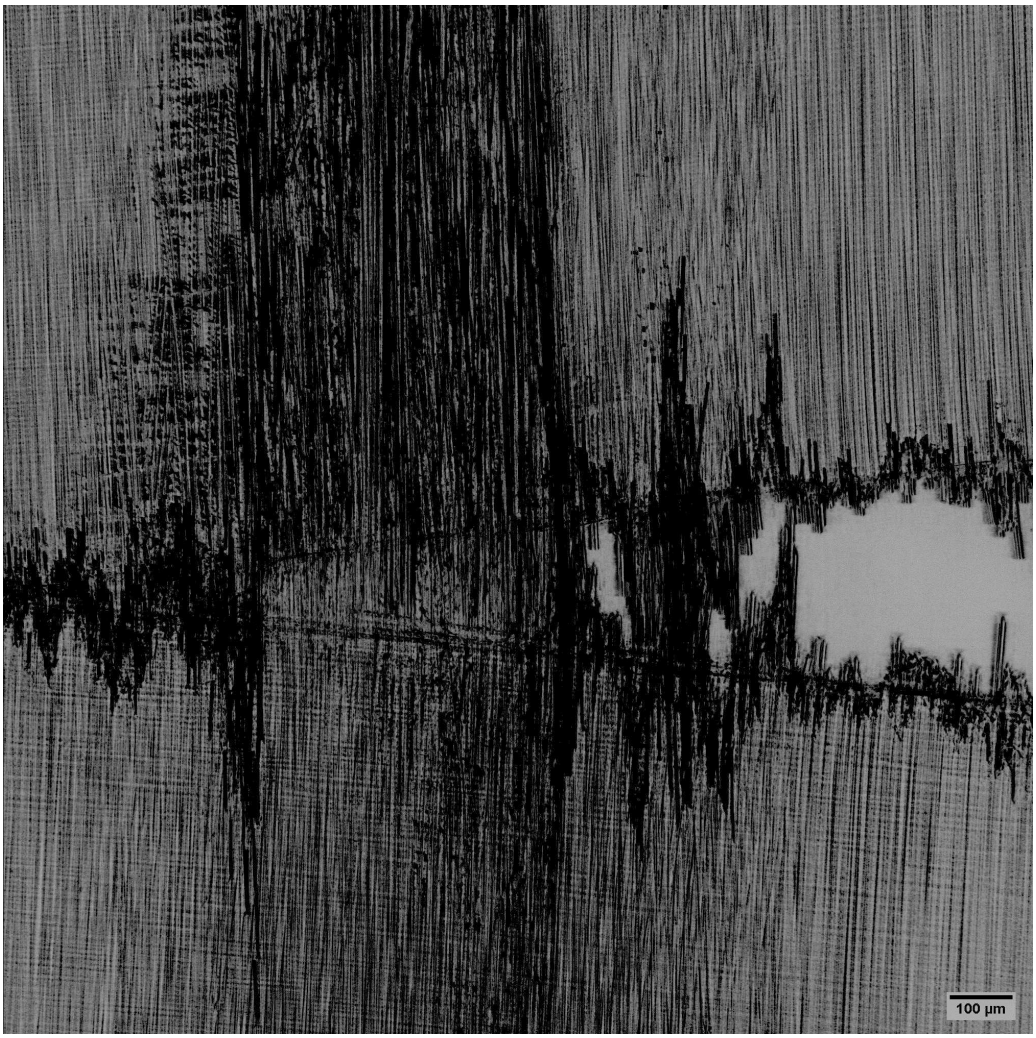

Figure 7.33: Minimum intensity projection for the SRCT of a 34-700 $60\,\mathrm{g}\cdot\mathrm{m}^{-2}$ FAW specimen showing a pull-out bundle.

This observation highlights that a more detailed bundle contact model considering bending and roughness interlocking is a promising research axis to further understand pull-out dissipation, especially when the crack surfaces are subjected to both a COD and a rotation.

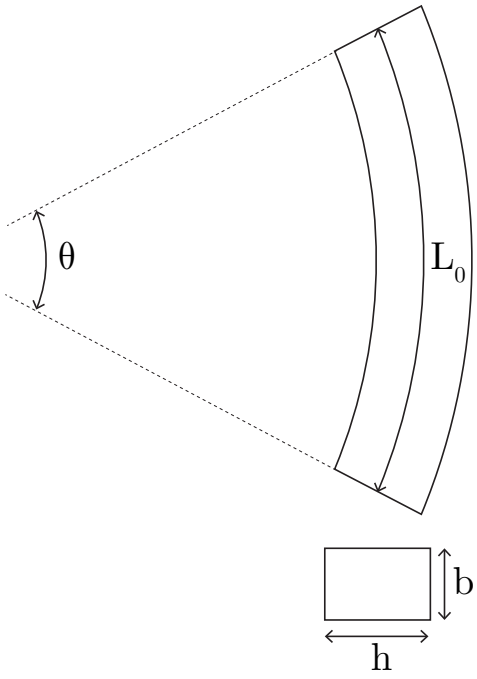

Figure 7.34: Bundle parametrization.

7.6 Conclusion

The pull-out length distributions of the samples tested in this work have been characterized. It has been shown that secondary damage in the samples is correlated with the presence of longer bundles. Furthermore, the longer pull-out bundles have been shown to be a satisfactory cause for the reported increased translaminar toughness, assuming a simple frictional model. Indeed, the energy dissipated by friction evolves geometrically with the pull-out length. These results are aligned with those obtained for instance by Pimenta and Pinho [144].

However, debonding and friction alone seem to not account for the total dissipated energy, as shown by the large apparent frictional strength required by the model. Similarly, the model of Pimenta and Pinho [144] could not account for the total energy dissipated in very long bundles as observed by Bullegas et al. [149]. The SRCT results shown in this chapter suggest an additional source of energy dissipation, through bundle bending and mechanical interlocking. Moreover, the bending effect is expected to increase with the length of the bundle, as a larger COD will be required to pull-out completely the larger bundles.

Chapter 8

Conclusion and outlook

8.1 Summary and Conclusion

In this work, carbon-carbon hybridization in thin-ply composites was investigated experimentally to analyze its effect on several key structural properties: the initiation and propagation mode I translaminar toughness, the unnotched tensile stress at the onset of damage, the unnotched tensile strength, and the notched strength through open-hole tension. From a practical point of view, the objective was to demonstrate the potential of fiber-hybridization as a toughening strategy for thin-ply composites. Indeed, state-of-the-art commercial thin-ply composites exhibit outstanding mechanical performance, especially in terms of stress at the onset of damage and strength in tensile applications, but critically lack translaminar toughness. Therefore, a large variety of fiber-hybrids were designed following three different hybridization architectures: interlayers, interyarns, and intrayarns.

Interlayer hybrids with a symmetric ply-block layup were chosen based on the shear-lag model developed for the pseudo-ductility framework by Jalalvand et al. [169]. Unlike previous studies, the focus was not towards a pseudo-ductility effect, but rather on triggering a low-strain fiber fragmentation before the laminate failure. This approach was considered suitable to increase the pull-out length and therefore improve the translaminar toughness. However, the thin-ply properties must not be too much impaired by the hybridization strategy. On the one hand, this implies that the fragmentation should occur as close as possible to the laminate failure. On the other hand, the material system should be selected so as to maximize the toughness improvement to tensile properties loss ratio. These considerations led to the choice of the 34-700-HR40 hybrid system. In parallel, the effect of an asymmetric interlayer hybrid layup was also considered. Here, the objective was to induce secondary damage through delamination at the hybrid interfaces.

Finally, interyarn and intrayarn hybrids were developed based on novel prepreg materials produced by NTPT. These hybrids were also designed according to the pseudo-ductile failure map. in these materials, the improved fiber dispersion offers an increased design space that was exploited to investigate different toughening mechanisms such as crack deflection or crack bridging.

The experimental characterization was performed based on Compact Tension tests, Un-Notched Tensile tests, and Open-Hole Tensile tests. The failure mechanisms were monitored through Digital Image Correlation, Accoustic Emission, optical microscopy of post-mortem fracture surfaces, CT-scan observations of interrupted Open-Hole Tensile tests, and in-situ Synchrotron Radiation Computed Tomography in mini-protruded Compact Tension specimens. Regarding the data reduction method for Compact Tension tests, a novel J-integral implementation was released as a Python code [235] and used to investigate three different formulations, reported in chapter 4. The parametric study demonstrated the suitability of the line J-integral algorithm to analyze results obtained with hybrid thin-ply laminates.

Overall, all hybrid specimens exhibited a change of damage behavior with respect to fiber-hybridization, either positive or negative. In interlayer hybrids, reported in chapter 5, the configurations intended to promote fragmentation were shown to have a negative hybrid effect on the translaminar toughness as compared to a scaled Rule-of-Mixtures. This was attributed to the impossibility of the 34-700 to reach more than 1.6 % of ultimate strain, instead of the 2 % indicated by the manufacturer's datasheet. This result was correlated to the observation of a mild ply-thickness effect for the 34-700-TP415 system whose causes remain unclear. In any case, the failure map updated for 1.6 % ultimate strain showed that the specimens were not able to achieve fragmentation, accounting for the reported results.

In contrast, the asymmetric interlayer structures were found as a suitable strategy to increase the translaminar toughness, with up to more than 100 % increase reported when secondary damage was achieved. The toughness improvement was correlated with an increase in pull-out length. These results were obtained in specific conditions, when the initial crack length was short, possibly due to a different initial loading state or to secondary damage too large with respect to the specimen size for a longer crack length. In any case, the plateau propagation of the Energy Release Rate was never reached in the presence of secondary damage, indicating that further improvements are possible. Under tension, the Quasi-Isotropic interlayer hybrids were found to exhibit an early onset of damage with extensive delamination. However, the reported delamination was not critical and a positive hybrid effect was reported on the strength.

To conclude, this work demonstrates that the 34-700-TP415 system is not suitable for interlayer hybridization with HR40 since its mild thin-ply effect does not sufficiently improve the admissible ultimate strain of 34-700 plies. The lack of ply-thickness effect may be attributed to fiber-matrix specific interaction, to fiber properties under the datasheet expectations or to damage induced by the tow-spreading. In any case, a stable fiber fragmentation was not achieved, in contrast with the results obtained by Frossard [39] or Danzi et al. [56] with T800-HR40 hybrids. Therefore, it was not possible to verify if fragmentation was actually beneficial to the pull-out length and translaminar toughness. In the case of asymmetric ply-block hybrids, the presence of secondary damage and its possible interaction with the crack has a positive influence on the pull-out length and compensates for the lack of

fragmentation.

Moreover, as shown in Figure 8.1, the asymmetric interlayer hybrids tested in this study and the T800-HR40 hybrids tested by Frossard [39] achieved a significant improvement with respect to their respective baselines. The T800-HR40 hybrids achieved stable fragmentation but also featured an asymmetric ply-block layup which may have been more beneficial. The experimental evidence acquired throughout this work tends to indicate that the effect of fragmentation is limited since the available carbon fibers do not allow to reach more than 2 to 3 mm of fragmentation length, while asymmetric interlayer hybrids tend to show a pull-out length larger than the one predicted by the shear-lag model. This assumption is further supported by the absence of a positive hybrid effect reported by Danzi et al. [56] for symmetric T800-HR40 interlayer hybrids. Thus, the two approaches should be tested for a system exhibiting fragmentation to conclude. Finally, when comparing the obtained translaminar toughness with a scaled Rule-of-Mixtures, the asymmetry was found more favorable in the sample configuration with the lowest volume fraction of low-strain material.

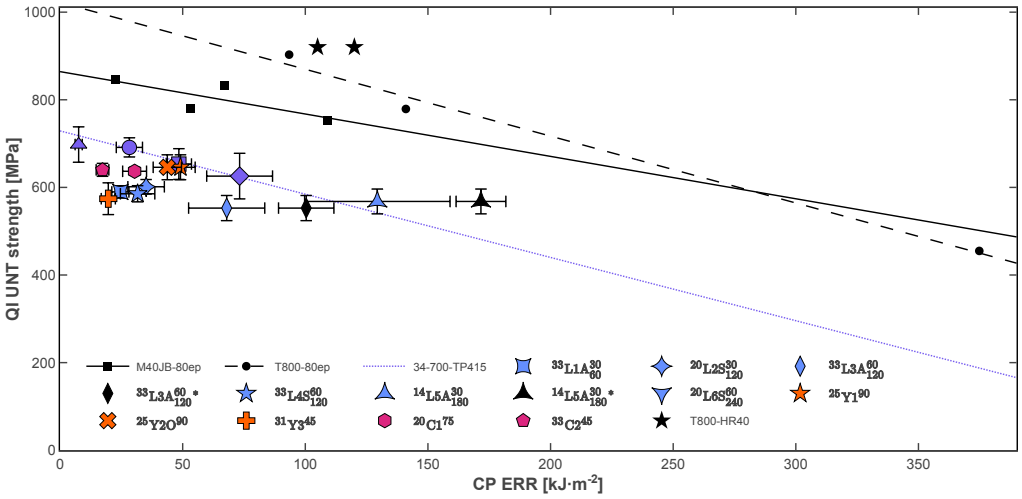

Figure 8.1: Ashby plot of the QI UNT strength with respect to the CP translaminar toughness of the interyarn and intrayarn hybrids. Assumes the same strength for $^{25}Y1^{90}$ and $^{25}Y2O^{90}$. M40JB-80ep reference values: ERR from [39], strength from [38]. T800-80ep reference values: ERR from DENT tests [56] and [175] assuming a similar behavior for the IM21 system, strength scaled from [24]. * maximal ERR reported for short initial crack length.

The main drawback associated with interlayer hybrids is the thickness of the resulting ply-block. Thus, even when there is a positive hybrid effect, the laminate strength remains consequently lower than the thin-ply ones, as highlighted in Figure 8.1. With this respect, interyarn and intrayarn widen considerably the design space as thin-ply hybrid can be obtained with a low-volume fraction of low-strain material as reported in chapter 6. However, the toughness improvement obtained in intrayarn hybrids was consequently inferior to the one obtained in asymmetric interlayer hybrids, possibly because of the absence of fragmentation.

Nevertheless, crack bridging by the low-strain tows in overlayed interlayer hybrids was observed.

This mechanism is different from those previously reported, and its toughness improvement was not associated with the presence of an increased pull-out length in the post-mortem fracture surface. A shown in Figure 8.1, this approach is also very promising to balance the translaminar toughness and strength in thin-ply composites.

8.2 Future outlook

Further experimental work ought to be carried out with a system exhibiting stable fragmentation to compare the effect of a symmetric and an asymmetric ply-block in interlayer hybrids.
However, the most promising hybridization strategy demonstrated in this work is, from a practical point of view, the overlayed interyarn one. Indeed, it enables crack bridging by the low-strain tows for a ply-block FAW remaining below $100\,\mathrm{g}\cdot\mathrm{m}^{-2}$. Thus, a complete characterization of its effect would be of great interest. Especially, developing a tow-by-tow approach with smaller and more regular tows may enable geometrical interactions to finely tune the translaminar crack bridging.

Regarding the fragmentation of fiber-hybrids, a key property is the strain ratio between the two fibers that should be sufficiently contrasted. In carbon-carbon hybrid, this reduces significantly the design space and restricts it to the use of high-modulus carbon fibers as low-strain material. Furthermore, the natural fragmentation of these fibers does not enable as long pull-out bundles as in laminates with engineered defects [53]. Consequently, an improvement of the fragmentation approach that would address these two points consists in achieving a hybridization with two similar carbon fibers. To achieve fragmentation, one of the two fibers should be made more brittle in order to artificially reduce its strength, for instance by ultra-short pulse laser treatment, or a slightly different processing route that treats the fibers more or less harshly depending on the position on the prepreg.

Bibliography

[1] 1883 eruption of Krakatoa. *Wikipedia*, November 2022.

[2] C. L. Pekeris. The propagation of a pulse in the atmosphere. *Proceedings of the Royal Society of London. Series A. Mathematical and Physical Sciences*, 171(947):434–449, July 1939. ISSN 0080-4630, 2053-9169. doi: 10.1098/rspa.1939.0076.

[3] Thomas B. Gabrielson. Krakatoa and the Royal Society: The Krakatoa Explosion of 1883. *Acoustics Today*, 6(2):14–19, April 2010. ISSN 1557-0215, 1557-0223. doi: 10.1121/1.3467643.

[4] Marc G. Millis and Eric W. Davis, editors. *Frontiers of Propulsion Science*. Number v. 227 in Progress in Astronautics and Aeronautics. American Institute of Aeronautics and Astronautics, Reston, Va, 2009. ISBN 978-1-56347-956-4.

[5] Statistics | Eurostat. https://ec.europa.eu/eurostat/databrowser/view/TPS00001/bookmark/table?lang=en&bookmarkId=6ef61f16-dadc-42b1-a6ce-3ddfda4727e8, .

[6] Quoc-Hy Dao, Pascal Peduzzi, Bruno Chatenoux, Andréa De Bono, Stefan Schwarzer, and Damien Friot. Environmental limits and Swiss footprints based on Planetary Boundaries. 2015.

[7] Série 010002077 Cours des matières premières importées - Pétrole brut Brent (Londres) – Prix en dollars US par baril | Insee. https://www.insee.fr/fr/statistiques/serie/010002077#Tableau.

[8] Statistics | Eurostat. https://ec.europa.eu/eurostat/databrowser/view/NRG_BAL_C/default/table?lang=en, .

[9] Office fédéral de la statistique. Energie: Panorama - 2020 | Publication. https://www.bfs.admin.ch/asset/fr/16704278, March 2021.

[10] S. C Burgess and J. M. J Choi. A parametric study of the energy demands of car transportation: A case study of two competing commuter routes in the UK. *Transportation Research Part D: Transport and Environment*, 8(1):21–36, January 2003. ISSN 1361-9209. doi: 10.1016/S1361-9209(02)00016-0.

[11] Reza Tolouei and Helena Titheridge. Vehicle mass as a determinant of fuel consumption and secondary safety performance. *Transportation Research Part D: Transport and Environment*, 14(6):385–399, August 2009. ISSN 1361-9209. doi: 10.1016/j.trd.2009.01.005.

[12] Martin Weiss, Kira Christina Cloos, and Eckard Helmers. Energy efficiency trade-offs in small to large electric vehicles. *Environmental Sciences Europe*, 32(1):46, March 2020. ISSN 2190-4715. doi: 10.1186/s12302-020-00307-8.

[13] Rolf Steinegger. Fuel economy for aircraft operation as a function of weight and distance. December 2017. doi: 10.21256/zhaw-3466.

[14] J. Fan and J. Njuguna. 1 - An introduction to lightweight composite materials and their use in transport structures. In J. Njuguna, editor, *Lightweight Composite Structures in Transport*, pages 3–34. Woodhead Publishing, January 2016. ISBN 978-1-78242-325-6. doi: 10.1016/B978-1-78242-325-6.00001-3.

[15] Hyung Chul Kim and Timothy J. Wallington. Life-Cycle Energy and Greenhouse Gas Emission Benefits of Lightweighting in Automobiles: Review and Harmonization. *Environmental Science & Technology*, 47(12):6089–6097, June 2013. ISSN 0013-936X, 1520-5851. doi: con.

[16] Georgios Fontaras, Nikiforos-Georgios Zacharof, and Biagio Ciuffo. Fuel consumption and CO2 emissions from passenger cars in Europe – Laboratory versus real-world emissions. *Progress in Energy and Combustion Science*, 60:97–131, May 2017. ISSN 0360-1285. doi: 10.1016/j.pecs.2016.12.004.

[17] Johannes Buberger, Anton Kersten, Manuel Kuder, Richard Eckerle, Thomas Weyh, and Torbjörn Thiringer. Total CO2-equivalent life-cycle emissions from commercially available passenger cars. *Renewable and Sustainable Energy Reviews*, 159: 112158, May 2022. ISSN 1364-0321. doi: 10.1016/j.rser.2022.112158.

[18] Fernando Enzo Kenta Sato and Toshihiko Nakata. Analysis of the impact of vehicle lightweighting on recycling benefits considering life cycle energy reductions. *Resources, Conservation and Recycling*, 164:105118, January 2021. ISSN 09213449. doi: 10.1016/j.resconrec.2020.105118.

[19] NASA - The Tyranny of the Rocket Equation. https://www.nasa.gov/mission_pages/station/expeditions/expedition30/tryanny.html.

[20] Ulf Paul Breuer. *Commercial Aircraft Composite Technology*. Springer International Publishing, Cham, 2016. ISBN 978-3-319-31917-9 978-3-319-31918-6. doi: 10.1007/978-3-319-31918-6.

[21] Bruno Castanie, Christophe Bouvet, and Malo Ginot. Review of composite sandwich structure in aeronautic applications. *Composites Part C: Open Access*, 1:100004, August 2020. ISSN 2666-6820. doi: 10.1016/j.jcomc.2020.100004.

[22] Daniel Gay. *Composite Materials: Design and Applications*. CRC Press, Boca Raton, fourth edition, August 2022. ISBN 978-1-00-319578-8. doi: 10.1201/9781003195788.

[23] Ti-6al-4v-datasheet-rev-01.pdf. https://www.maher.com/media/pdfs/ti-6al-4v-datasheet-rev-01.pdf.

[24] J. Cugnoni, R. Amacher, S. Kohler, J. Brunner, E. Kramer, C. Dransfeld, W. Smith, K. Scobbie, L. Sorensen, and J. Botsis. Towards aerospace grade thin-ply composites: Effect of ply thickness, fibre, matrix and interlayer toughening on strength and damage tolerance. *Composites Science and Technology*, September 2018. ISSN 02663538. doi: 10.1016/j.compscitech.2018.08.037.

[25] Camille Sohier. ArianeGroup to develop PHOEBUS for ESA, as a demonstrator for Ariane 6 future carbon upper stage, November 2022.

[26] Andrew J. Lee and Juan M. Fernandez. Inducing bistability in Collapsible Tubular Mast booms with thin-ply composite shells. *Composite Structures*, 225:111166, October 2019. ISSN 0263-8223. doi: 10.1016/j.compstruct.2019.111166.

[27] Tian-Wei Liu, Jiang-Bo Bai, and Nicholas Fantuzzi. Folding behavior of the thin-walled lenticular deployable composite boom: Analytical analysis and many-objective optimization. *Mechanics of Advanced Materials and Structures*, 0(0):1–19, March 2022. ISSN 1537-6494. doi: 10.1080/15376494.2022.2053766.

[28] Stephanie Wegmann, Christian Rytka, Mariona Diaz-Rodenas, Vincent Werlen, Christoph Schneeberger, Paolo Ermanni, Baris Caglar, Colin Gomez, and Véronique Michaud. A life cycle analysis of novel lightweight composite processes: Reducing the environmental footprint of automotive structures. *Journal of Cleaner Production*, 330:129808, January 2022. ISSN 0959-6526. doi: 10.1016/j.jclepro.2021.129808.

[29] Sujit Das. Life cycle assessment of carbon fiber-reinforced polymer composites. *The International Journal of Life Cycle Assessment*, 16(3):268–282, March 2011. ISSN 1614-7502. doi: 10.1007/s11367-011-0264-z.

[30] A. Keller, C. Dransfeld, and K. Masania. Flow and heat transfer during compression resin transfer moulding of highly reactive epoxies. *Composites Part B: Engineering*, 153:167–175, November 2018. ISSN 1359-8368. doi: 10.1016/j.compositesb.2018.07.041.

[31] Vincent Werlen, Christian Rytka, Stephanie Wegmann, Halime Philipp, Yara Khalaf, Véronique Michaud, Christian Brauner, and Clemens Dransfeld. Novel tooling for direct melt impregnation of textile with variotherm injection moulding: Methodology and proof of concept. *Journal of Composite Materials*, 56(28):4245–4257, December 2022. ISSN 0021-9983. doi: 10.1177/00219983221130720.

[32] S. R. Naqvi, H. Mysore Prabhakara, E. A. Bramer, W. Dierkes, R. Akkerman, and G. Brem. A critical review on recycling of end-of-life carbon fibre/glass fibre reinforced composites waste using pyrolysis towards a circular economy. *Resources, Conservation and Recycling*, 136:118–129, September 2018. ISSN 0921-3449. doi: 10.1016/j.resconrec.2018.04.013.

[33] Parthasarathi Aravindan, Federico Becagli, Marco L. Longana, Lourens G. Blok, Thomas R. Pozegic, Samantha J. Huntley, Thomas Rendall, and Ian Hamerton. Remanufacturing of Woven Carbon Fibre Fabric Production Waste into High Performance Aligned Discontinuous Fibre Composites. *Journal of Composites Science*, 4(2):68, June 2020. ISSN 2504-477X. doi: 10.3390/jcs4020068.

[34] Zhe Liu, Thomas A. Turner, Kok H. Wong, and Stephen J. Pickering. Development of high performance recycled carbon fibre composites with an advanced hydrodynamic fibre alignment process. *Journal of Cleaner Production*, 278:123785, January 2021. ISSN 0959-6526. doi: 10.1016/j.jclepro.2020.123785.

[35] Philip R. Barnett and Hicham K. Ghossein. A Review of Recent Developments in Composites Made of Recycled Carbon Fiber Textiles. *Textiles*, 1(3):433–465, December 2021. ISSN 2673-7248. doi: 10.3390/textiles1030023.

[36] E. A. Flores-Johnson, J. G. Carrillo, C. Zhai, R. A. Gamboa, Y. Gan, and L. Shen. Microstructure and mechanical properties of hard Acrocomia mexicana fruit shell. *Scientific Reports*, 8(1):9668, June 2018. ISSN 2045-2322. doi: 10.1038/s41598-018-27282-8.

[37] Bernd Gludovatz, Anton Hohenwarter, Keli V. S. Thurston, Hongbin Bei, Zhenggang Wu, Easo P. George, and Robert O. Ritchie. Exceptional damage-tolerance of a medium-entropy alloy CrCoNi at cryogenic temperatures. *Nature Communications*, 7(1):10602, April 2016. ISSN 2041-1723. doi: 10.1038/ncomms10602.

[38] R. Amacher, J. Cugnoni, J. Botsis, L. Sorensen, W. Smith, and C. Dransfeld. Thin ply composites: Experimental characterization and modeling of size-effects. *Composites Science and Technology*, 101:121–132, September 2014. ISSN 02663538. doi: 10.1016/j.compscitech.2014.06.027.

[39] Guillaume Frossard. Fracture of thin-ply composites: effects of ply thickness. page 189, 2017. doi: 10.5075/epfl-thesis-8032.

[40] Yousef Saadati, Gilbert Lebrun, Christophe Bouvet, Jean-François Chatelain, and Yves Beauchamp. Study of translaminar fracture toughness of unidirectional flax/epoxy composite. *Composites Part C: Open Access*, 1:100008, August 2020. ISSN 2666-6820. doi: 10.1016/j.jcomc.2020.100008.

[41] Libo Yan, Nawawi Chouw, and Krishnan Jayaraman. Flax fibre and its composites – A review. *Composites Part B: Engineering*, 56:296–317, January 2014. ISSN 1359-8368. doi: 10.1016/j.compositesb.2013.08.014.

[42] S Sihn, R Kim, K Kawabe, and S Tsai. Experimental studies of thin-ply laminated composites. *Composites Science and Technology*, 67(6):996–1008, May 2007. ISSN 02663538. doi: 10.1016/j.compscitech.2006.06.008.

[43] Hiroshi Saito, Mitsuhiro Morita, Kazumasa Kawabe, Manato Kanesaki, Hiroki Takeuchi, Mototsugu Tanaka, and Isao Kimpara. Effect of ply-thickness on impact damage morphology in CFRP laminates. *Journal of Reinforced Plastics and Composites*, 30(13):1097–1106, July 2011. ISSN 0731-6844. doi: 10.1177/0731684411416532.

[44] A. Arteiro, C. Furtado, G. Catalanotti, P. Linde, and P. P. Camanho. Thin-ply polymer composite materials: A review. *Composites Part A: Applied Science and Manufacturing*, 132:105777, May 2020. ISSN 1359-835X. doi: 10.1016/j.compositesa.2020.105777.

[45] Joel Galos. Thin-ply composite laminates: A review. *Composite Structures*, 236:111920, March 2020. ISSN 0263-8223. doi: 10.1016/j.compstruct.2020.111920.

[46] Alexander Kopp, Sven Stappert, David Mattsson, Kurt Olofsson, Erik Marklund, Guido Kurth, Erwin Mooij, and Evelyne Roorda. The Aurora space launcher concept. *CEAS Space Journal*, 10(2):167–187, June 2018. ISSN 1868-2510. doi: 10.1007/s12567-017-0184-2.

[47] Pedro P. Camanho, Carlos G. Dávila, Silvestre T. Pinho, Lorenzo Iannucci, and Paul Robinson. Prediction of in situ strengths and matrix cracking in composites under transverse tension and in-plane shear. *Composites Part A: Applied Science and Manufacturing*, 37(2):165–176, February 2006. ISSN 1359-835X. doi: 10.1016/j.compositesa.2005.04.023.

[48] S. Kohler, J. Cugnoni, R. Amacher, and J. Botsis. Transverse cracking in the bulk and at the free edge of thin-ply composites: Experiments and multiscale modelling. *Composites Part A: Applied Science and Manufacturing*, 124:105468, September 2019. ISSN 1359-835X. doi: 10.1016/j.compositesa.2019.05.036.

[49] M.R. Wisnom, S.R. Hallett, and C. Soutis. Scaling Effects in Notched Composites. *Journal of Composite Materials*, 44(2):195–210, January 2010. ISSN 0021-9983, 1530-793X. doi: 10.1177/0021998309339865.

[50] M. J. Laffan, S. T. Pinho, P. Robinson, and L. Iannucci. Measurement of the in situ ply fracture toughness associated with mode I fibre tensile failure in FRP. Part II: Size and lay-up effects. *Composites Science and Technology*, 70(4):614–621, April 2010. ISSN 0266-3538. doi: 10.1016/j.compscitech.2009.12.011.

[51] R.F. Teixeira, S.T. Pinho, and P. Robinson. Thickness-dependence of the translaminar fracture toughness: Experimental study using thin-ply composites. *Composites Part A: Applied Science and Manufacturing*, 90:33–44, November 2016. ISSN 1359835X. doi: 10.1016/j.compositesa.2016.05.031.

[52] J Cugnoni, G Frossard, R Amacher, and J Botsis. Translaminar fracture of regular and hybrid thin ply composites: Experimental characterization and modeling. page 9, 2018.

[53] Gianmaria Bullegas, Jacob Benoliel, Pier Luigi Fenelli, Silvestre T. Pinho, and Soraia Pimenta. Towards quasi isotropic laminates with engineered fracture behaviour for industrial applications. *Composites Science and Technology*, 165:290–306, September 2018. ISSN 0266-3538. doi: 10.1016/j.compscitech.2018.07.004.

[54] Gergely Czél, Tamas Rev, Meisam Jalalvand, Mohamad Fotouhi, Marco L. Longana, Oliver J. Nixon-Pearson, and Michael R. Wisnom. Pseudo-ductility and reduced notch sensitivity in multi-directional all-carbon/epoxy thin-ply hybrid composites. *Composites Part A: Applied Science and Manufacturing*, 104:151–164, January 2018. ISSN 1359-835X. doi: 10.1016/j.compositesa.2017.10.028.

[55] Lorenzo Mencattelli and Silvestre T. Pinho. Ultra-thin-ply CFRP Bouligand bio-inspired structures with enhanced load-bearing capacity, delayed catastrophic failure and high energy dissipation capability. *Composites Part A: Applied Science and Manufacturing*, 129:105655, February 2020. ISSN 1359-835X. doi: 10.1016/j.compositesa.2019.105655.

[56] F Danzi, RP Tavares, J Xavier, D Fanteria, and PP Camanho. Effects of hybridization and ply thickness on the strength and toughness of composite laminates. *Journal of Composite Materials*, 55(30):4601–4616, December 2021. ISSN 0021-9983. doi: 10.1177/00219983211041762.

[57] János Plocher, Lorenzo Mencattelli, Federico Narducci, and Silvestre Pinho. Learning from nature: Bio-inspiration for damage-tolerant high-performance fibre-reinforced composites. *Composites Science and Technology*, 208:108669, May 2021. ISSN 0266-3538. doi: 10.1016/j.compscitech.2021.108669.

[58] Rajnish Kumar, Lars P. Mikkelsen, Hans Lilholt, and Bo Madsen. Experimental Method for Tensile Testing of Unidirectional Carbon Fibre Composites Using Improved Specimen Type and Data Analysis. *Materials*, 14(14):3939, January 2021. ISSN 1996-1944. doi: 10.3390/ma14143939.

[59] Salvatore Giacomo Marino and Gergely Czél. Improving the performance of pseudo-ductile hybrid composites by film-interleaving. *Composites Part A: Applied Science and Manufacturing*, 142:106233, March 2021. ISSN 1359-835X. doi: 10.1016/j.compositesa.2020.106233.

[60] Sina AhmadvashAghbash, Christian Breite, Mahoor Mehdikhani, and Yentl Swolfs. Longitudinal debonding in unidirectional fibre-reinforced composites: Numerical analysis of the effect of interfacial properties. *Composites Science and Technology*, 218:109117, February 2022. ISSN 0266-3538. doi: 10.1016/j.compscitech.2021.109117.

[61] Olivier Hubert, Nikola Todorovic, and Alexander Bismarck. Towards separator-free structural composite supercapacitors. *Composites Science and Technology*, 217:109126, January 2022. ISSN 0266-3538. doi: 10.1016/j.compscitech.2021.109126.

[62] Z. Hashin. Analysis of Composite Materials—A Survey. *Journal of Applied Mechanics*, 50(3):481–505, September 1983. ISSN 0021-8936. doi: 10.1115/1.3167081.

[63] Denise Yin, Christopher Shumeyko, Julia Cline, Matt Dunstan, Philip Goins, and Dan Field. Snap, Crackle, and Pop: Breaking chocolate to understand composite design. *Journal of Materials Education*, 41:27–40, May 2019.

[64] Aliakbar Gholampour and Togay Ozbakkaloglu. A review of natural fiber composites: Properties, modification and processing techniques, characterization, applications. *Journal of Materials Science*, 55(3):829–892, January 2020. ISSN 1573-4803. doi: 10.1007/s10853-019-03990-y.

[65] Mahoor Mehdikhani, Larissa Gorbatikh, Ignaas Verpoest, and Stepan V Lomov. Voids in fiber-reinforced polymer composites: A review on their formation, characteristics, and effects on mechanical performance. *Journal of Composite Materials*, 53(12): 1579–1669, May 2019. ISSN 0021-9983. doi: 10.1177/0021998318772152.

[66] Tatyana Ageyeva, Ilya Sibikin, and József Gábor Kovács. A Review of Thermoplastic Resin Transfer Molding: Process Modeling and Simulation. *Polymers*, 11(10):1555, October 2019. ISSN 2073-4360. doi: 10.3390/polym11101555.

[67] Youkun Gong, Zengrui Song, Huiming Ning, Ning Hu, Xiongqi Peng, Xiaopeng Wu, Rui Zou, Feng Liu, Shayuan Weng, and Qiang Liu. A comprehensive review of characterization and simulation methods for thermo-stamping of 2D woven fabric reinforced thermoplastics. *Composites Part B: Engineering*, 203:108462, December 2020. ISSN 1359-8368. doi: 10.1016/j.compositesb.2020.108462.

[68] Victor Haguenauer, Eric Becker, Régis Bigot, Ludovic Freund, and Nicolas Bonnet. Forging C/Thermoplastic Printed Composite, Shaping Parameters Impact. *Procedia Manufacturing*, 47:169–173, January 2020. ISSN 2351-9789. doi: 10.1016/j.promfg.2020.04.165.

[69] Victor Haguenauer, Eric Becker, Régis Bigot, and Damien Félix. Effect of processing parameters on properties of printed and consolidated thermoplastic composites. *Journal of Reinforced Plastics and Composites*, page 073168442211408, November 2022. ISSN 0731-6844, 1530-7964. doi: 10.1177/07316844221140833.

[70] Arne Hindersmann. Confusion about infusion: An overview of infusion processes. *Composites Part A: Applied Science and Manufacturing*, 126:105583, November 2019. ISSN 1359-835X. doi: 10.1016/j.compositesa.2019.105583.

[71] Véronique Michaud. A Review of Non-saturated Resin Flow in Liquid Composite Moulding processes. *Transport in Porous Media*, 115(3):581–601, December 2016. ISSN 1573-1634. doi: 10.1007/s11242-016-0629-7.

[72] Pascal Hubert, Timotei Centea, Lessa Grunefelder, Steven Nutt, James Kratz, and Arthur Levy. 2.4 Out-of-Autoclave Prepreg Processing. In Peter W. R. Beaumont and Carl H. Zweben, editors, *Comprehensive Composite Materials II*, pages 63–94. Elsevier, Oxford, January 2018. ISBN 978-0-08-100534-7. doi: 10.1016/B978-0-12-803581-8.09900-8.

[73] P. Hubert, G. Fernlund, and A. Poursartip. 13 - Autoclave processing for composites. In Suresh G. Advani and Kuang-Ting Hsiao, editors, *Manufacturing Techniques for Polymer Matrix Composites (PMCs)*, Woodhead Publishing Series in Composites Science and Engineering, pages 414–434. Woodhead Publishing, January 2012. ISBN 978-0-85709-067-6. doi: 10.1533/9780857096258.3.414.

[74] Dirk H. J. A. Lukaszewicz, Carwyn Ward, and Kevin D. Potter. The engineering aspects of automated prepreg layup: History, present and future. *Composites Part B: Engineering*, 43(3):997–1009, April 2012. ISSN 1359-8368. doi: 10.1016/j.compositesb.2011.12.003.

[75] Göran Fernlund, Christophe Mobuchon, and Navid Zobeiry. 2.3 Autoclave Processing. In Peter W. R. Beaumont and Carl H. Zweben, editors, *Comprehensive Composite Materials II*, pages 42–62. Elsevier, Oxford, January 2018. ISBN 978-0-08-100534-7. doi: 10.1016/B978-0-12-803581-8.09899-4.

[76] J. E. Bailey, P. T. Curtis, A. Parvizi, and Anthony Kelly. On the transverse cracking and longitudinal splitting behaviour of glass and carbon fibre reinforced epoxy cross ply laminates and the effect of Poisson and thermally generated strain. *Proceedings of the Royal Society of London. A. Mathematical and Physical Sciences*, 366(1727):599–623, July 1979. doi: 10.1098/rspa.1979.0071.

[77] Fw Crossman and Asd Wang. The Dependence of Transverse Cracking and Delamination on Ply Thickness in Graphite/Epoxy Laminates. In Kl Reifsnider, editor, *Damage in Composite Materials: Basic Mechanisms, Accumulation, Tolerance, and Characterization*, pages 118–118–22. ASTM International, 100 Barr Harbor Drive, PO Box C700, West Conshohocken, PA 19428-2959, January 1982. ISBN 978-0-8031-0696-3. doi: 10.1520/STP34324S.

[78] Multiscale experimental characterisation and modelling of transverse cracking in thin-ply composites. https://infoscience.epfl.ch/record/263781?ln=en.

[79] R Marissen, L Th. van der Drift, and J Sterk. Technology for rapid impregnation of fibre bundles with a molten thermoplastic polymer. *Composites Science and Technology*, 60(10):2029–2034, August 2000. ISSN 02663538. doi: 10.1016/S0266-3538(00)00122-6.

[80] Hassan M. EL-Dessouky and Carl A. Lawrence. Ultra-lightweight carbon fibre/thermoplastic composite material using spread tow technology. *Composites Part B: Engineering*, 50:91–97, July 2013. ISSN 1359-8368. doi: 10.1016/j.compositesb.2013.01.026.

[81] Sung Min Park, Myung Soon Kim, Yoon Sung Choi, Eun Soo Lee, Ho Wook Yoo, and Jin Sung Chon. Carbon Fiber Tow Spreading Technology and Mechanical Properties of Laminate Composites. *Composites Research*, 28(5):249–253, 2015. ISSN 2288-2103. doi: 10.7234/composres.2015.28.5.249.

[82] Gearóid Clancy, Daniël Peeters, Ronan M. O'Higgins, and Paul M. Weaver. In-line variable spreading of carbon fibre/thermoplastic pre-preg tapes for application in automatic tape placement. *Materials & Design*, 194:108967, September 2020. ISSN 0264-1275. doi: 10.1016/j.matdes.2020.108967.

[83] Arthur Schlothauer, Georgios A. Pappas, and Paolo Ermanni. Thin-ply thermoplastic composites: From weak to robust transverse performance through microstructural and morphological tuning, April 2022.

[84] NTPT. NTPT TP415.

[85] MS Irfan, VR Machavaram, RC Murray, FN Bogonez, CF Wait, SD Pandita, MA Paget, M Hudson, and GF Fernando. The design and optimisation of a rig to enable the lateral spreading of fibre bundles. *Journal of Composite Materials*, 48(15): 1813–1831, June 2014. ISSN 0021-9983. doi: 10.1177/0021998313490770.

[86] Daniel Gizik, Christian Metzner, and Peter Middendorf. Spreading of Heavy Tow Carbon Fibers for the use in aircraft structures. In *P17th European Conference on Composite Materials (ECCM17)*, June 2016.

[87] Narihito Nakagawa and Yasumasa Ohsora. Fiber separator for producing fiber reinforced metallic or resin body, April 1992.

[88] Josef Temburg. Vorrichtung an einer faserverarbeitenden Textilmaschine zur Führung eines Faserverbandes, June 1999.

[89] Joseph Lee Lifke, Lincoln Drake Busselle, Dana Jesse Finley, and Brent William Gordon. Method and apparatus for spreading fiber bundles, April 2000.

[90] Ronald G. Krueger. Apparatus and method for spreading fibrous tows into linear arrays of generally uniform density and products made thereby, November 2001.

[91] Peter A. Kiss, Jeffrey M. Deaton, Michael S. Parsons, and Donald Coffey. Apparatus and method for splitting a tow of fibers, May 2002.

[92] Jean-michel Guirman, Bernard Lecerf, and Alain Memphis. Method and device for producing a textile web by spreading tows, January 2005.

[93] Jürgen Nestler, Frank Vettermann, and Dietmar Reuchsel. Vorrichtung und Verfahren zum Ausbreiten eines Karbonfaserstrangs, April 2007.

[94] Hiroji Oishibashi. Fiber spreading apparatus, February 2008.

[95] Ryutaro Izumi and Mark Takahama. Process and apparatus for expanding multiple filament tow, April 2018.

[96] M. S. Irfan, V. R. Machavaram, R. S. Mahendran, N. Shotton-Gale, C. F. Wait, M. A. Paget, M. Hudson, and G. F. Fernando. Lateral spreading of a fiber bundle via mechanical means. *Journal of Composite Materials*, 46(3):311–330, February 2012. ISSN 0021-9983, 1530-793X. doi: 10.1177/0021998311424624.

[97] Todd Ames, Ricky Lee Kenley, Edward J. Powers, William West, William T. Wygand, Jean-claude Abed, and Bobby R. Lomax. Apparatus, method and system for air opening of textile tow and opened textile tow web produced thereby, April 2003.

[98] Todd Ames, Ricky Kenley, and Bobby Lomax. Method and Apparatus for Making an Absorbent Composite, April 2005.

[99] Kazumasa Kawabe and Shigeru Tomoda. Method of producing a spread multi-filament bundle and an apparatus used in the same, August 2009.

[100] Yuji Yamashita and Yasuhiro Koyama. Method of producing opened fiber bundle, method of producing cleaning member, apparatus which opens fiber bundle, and system which produces cleaning member, July 2014.

[101] Gerard Fernando and Venkata Machavaram. Fibre spreading, July 2021.

[102] Kazumasa Kawabe, Tatsuki Matsuo, and Zen-ichiro Maekawa. New Technology for Opening Various Reinforcing Fiber Tows. *Journal of the Society of Materials Science, Japan*, 47(7):727–734, 1998. ISSN 1880-7488, 0514-5163. doi: 10.2472/jsms.47.727.

[103] James A Newell and Allan A Puzianowski. Development of a Pneumatic Spreading System for Kevlar-Based Sic-Precursor Carbon Fibre Tows. *High Performance Polymers*, 11(2):197–203, June 1999. ISSN 0954-0083, 1361-6412. doi: 10.1088/0954-0083/11/2/004.

[104] J. C. Chen and C. G. Chao. Numerical and experimental study of internal flow field for a carbon fiber tow pneumatic spreader. *Metallurgical and Materials Transactions B*, 32(2):329–339, April 2001. ISSN 1073-5615, 1543-1916. doi: 10.1007/s11663-001-0056-0.

[105] Hai-hong Wu, Shi-chao Li, Jin-na Zhang, and Liyong Tong. Electrical resistivity response of unidirectional thin-ply carbon fiber reinforced polymers. *Composite Structures*, 228:111342, November 2019. ISSN 0263-8223. doi: 10.1016/j.compstruct.2019.111342.

[106] Ernest M. Sternberg. Method and apparatus for charging a bundle of filaments, June 1976.

[107] Jonathan M. Peritt, Richard Everett, and Alan Edelstein. Electrostatic fiber spreader including a corona discharge device, April 1993.

[108] Juergen NESTLER, Frank Vettermann, and Dietmar Reuchsel. Device and method for spreading a carbon fiber hank, May 2009.

[109] Shridhar Iyer and Lawrence T. Drzal. Method and system for spreading a tow of fibers, August 1991.

[110] Daisaku Akase, Hidetaka Matsumae, Tohru Hanano, and Toshihide Sekido. Method and Apparatus for Opening Reinforced Fiber Bundle and Method of Manufacturing Prepreg, October 1998.

[111] How is tow spread? https://www.compositesworld.com/articles/how-is-tow-spread.

[112] Christophe Baley, Marine Lan, Peter Davies, and Denis Cartié. Porosity in Ocean Racing Yacht Composites: A Review. *Applied Composite Materials*, 22(1):13–28, February 2015. ISSN 1573-4897. doi: 10.1007/s10443-014-9393-4.

[113] J. A. Bailie, R. P. Ley, and A. Pasricha. A summary and Review of Composite Laminate Design Guidelines. Technical Report NASA Contract NAS1-19347, Northrop Grumman CorporationNorthrop Grumman Corporation, October 1997.

[114] Johann Körbelin, Philip Goralski, Benedikt Kötter, Florian Bittner, Hans-Josef Endres, and Bodo Fiedler. Damage tolerance and notch sensitivity of bio-inspired thin-ply Bouligand structures. *Composites Part C: Open Access*, 5:100146, July 2021. ISSN 2666-6820. doi: 10.1016/j.jcomc.2021.100146.

[115] J. D. Fuller and M. R. Wisnom. Pseudo-ductility and damage suppression in thin ply CFRP angle-ply laminates. *Composites Part A: Applied Science and Manufacturing*, 69:64–71, February 2015. ISSN 1359-835X. doi: 10.1016/j.compositesa.2014.11.004.

[116] J. D. Fuller and M. R. Wisnom. Ductility and pseudo-ductility of thin ply angle-ply CFRP laminates under quasi-static cyclic loading. *Composites Part A: Applied Science and Manufacturing*, 107:31–38, April 2018. ISSN 1359-835X. doi: 10.1016/j.compositesa.2017.12.020.

[117] M. Herráez, N. Pichler, G. A. Pappas, C. Blondeau, and J. Botsis. Experiments and numerical modelling on angle-ply laminates under remote mode II loading. *Composites Part A: Applied Science and Manufacturing*, 134:105886, July 2020. ISSN 1359-835X. doi: 10.1016/j.compositesa.2020.105886.

[118] A. Wagih, P. Maimí, E. V. González, N. Blanco, J. R. Sainz de Aja, F. M. de la Escalera, R. Olsson, and E. Alvarez. Damage sequence in thin-ply composite laminates under out-of-plane loading. *Composites Part A: Applied Science and Manufacturing*, 87:66–77, August 2016. ISSN 1359-835X. doi: 10.1016/j.compositesa.2016.04.010.

[119] M. R. Wisnom, B. Khan, and S. R. Hallett. Size effects in unnotched tensile strength of unidirectional and quasi-isotropic carbon/epoxy composites. *Composite Structures*, 84(1):21–28, June 2008. ISSN 0263-8223. doi: 10.1016/j.compstruct.2007.06.002.

[120] Tomohiro Yokozeki, Yuichiro Aoki, and Toshio Ogasawara. Experimental characterization of strength and damage resistance properties of thin-ply carbon fiber/toughened epoxy laminates. *Composite Structures*, 82(3):382–389, February 2008. ISSN 0263-8223. doi: 10.1016/j.compstruct.2007.01.015.

[121] Tomohiro Yokozeki, Akiko Kuroda, Akinori Yoshimura, Toshio Ogasawara, and Takahira Aoki. Damage characterization in thin-ply composite laminates under out-of-plane transverse loadings. *Composite Structures*, 93(1):49–57, December 2010. ISSN 0263-8223. doi: 10.1016/j.compstruct.2010.06.016.

[122] A. Arteiro, G. Catalanotti, A. R. Melro, P. Linde, and P. P. Camanho. Micro-mechanical analysis of the in situ effect in polymer composite laminates. *Composite Structures*, 116:827–840, September 2014. ISSN 0263-8223. doi: 10.1016/j.compstruct.2014.06.014.

[123] G. Guillamet, A. Turon, J. Costa, J. Renart, P. Linde, and J. A. Mayugo. Damage occurrence at edges of non-crimp-fabric thin-ply laminates under off-axis uniaxial loading. *Composites Science and Technology*, 98:44–50, June 2014. ISSN 0266-3538. doi: 10.1016/j.compscitech.2014.04.014.

[124] Carbon fibre - determination of tensile properties of resin-impregnated yarn. Technical Report ISO 10618:2004, Geneva:ISO.

[125] M. R. Wisnom. Size effects in the testing of fibre-composite materials. *Composites Science and Technology*, 59(13):1937–1957, October 1999. ISSN 0266-3538. doi: 10.1016/S0266-3538(99)00053-6.

[126] Michael R. Wisnom. Size Effects in Composites. In Peter W. R. Beaumont and Carl H. Zweben, editors, *Comprehensive Composite Materials II*, pages 56–78. Elsevier, Oxford, January 2018. ISBN 978-0-08-100534-7. doi: 10.1016/B978-0-12-803581-8.03918-7.

[127] Francisco Mesquita, Steve Bucknell, Yann Leray, Stepan V. Lomov, and Yentl Swolfs. Single carbon and glass fibre properties characterised using large data sets obtained through automated single fibre tensile testing. *Composites Part A: Applied Science and Manufacturing*, 145:106389, June 2021. ISSN 1359-835X. doi: 10.1016/j.compositesa.2021.106389.

[128] Francisco Mesquita, Yentl Swolfs, Stepan V. Lomov, and Larissa Gorbatikh. In-situ synchrotron computed tomography tensile testing observations of the hybrid effect: A comparison with theory. *Composites Part B: Engineering*, 235:109765, April 2022. ISSN 1359-8368. doi: 10.1016/j.compositesb.2022.109765.

[129] Erik Adolfsson and Peter Gudmundson. Matrix crack initiation and progression in compositelaminatessubjected to bending and extension. *International Journal of Solids and Structures*, 36(21):3131–3169, July 1999. ISSN 0020-7683. doi: 10.1016/S0020-7683(98)00142-5.

[130] J. Andersons, R. Joffe, E. Spārniņš, and O. Rubenis. Progressive cracking mastercurves of the transverse ply in a laminate. *Polymer Composites*, 30(8):1175–1182, 2009. ISSN 1548-0569. doi: 10.1002/pc.20674.

[131] Hiroshi Saito, Hiroki Takeuchi, and Isao Kimpara. A study of crack suppression mechanism of thin-ply carbon-fiber-reinforced polymer laminate with mesoscopic numerical simulation. *Journal of Composite Materials*, 48(17):2085–2096, July 2014. ISSN 0021-9983, 1530-793X. doi: 10.1177/0021998313494430.

[132] G. Catalanotti. Prediction of in situ strengths in composites: Some considerations. *Composite Structures*, 207:889–893, January 2019. ISSN 0263-8223. doi: 10.1016/j.compstruct.2018.09.075.

[133] S. M. García-Rodríguez, J. Costa, P. Maimí, V. Singery, I. R. Cózar, A. Quintanas-Corominas, and A. Sasikumar. Experimental demonstration of the in-situ effect under transverse shear. *Composites Part A: Applied Science and Manufacturing*, 138:106047, November 2020. ISSN 1359-835X. doi: 10.1016/j.compositesa.2020.106047.

[134] Qingping Sun, Guowei Zhou, Haibin Tang, Zhaoxu Meng, Mukesh Jain, Xuming Su, and Weijian Han. In-situ effect in cross-ply laminates under various loading conditions analyzed with hybrid macro/micro-scale computational models. *Composite Structures*, 261:113592, April 2021. ISSN 0263-8223. doi: 10.1016/j.compstruct.2021.113592.

[135] Sébastien Kohler. Multiscale experimental characterisation and modelling of transverse cracking in thin-ply composites. 2019. doi: 10.5075/epfl-thesis-9132.

[136] George J. Dvorak and Norman Laws. Analysis of Progressive Matrix Cracking In Composite Laminates II. First Ply Failure. *Journal of Composite Materials*, 21(4):309–329, April 1987. ISSN 0021-9983. doi: 10.1177/002199838702100402.

[137] Hiroshi Saito, Hiroki Takeuchi, and Isao Kimpara. Experimental Evaluation of the Damage Growth Restraining in 90° Layer of Thin-ply CFRP Cross-ply Laminates. *Advanced Composite Materials*, 21(1):57–66, February 2012. ISSN 0924-3046. doi: 10.1163/156855112X629522.

[138] M. Herráez, C. González, and C.S. Lopes. A numerical framework to analyze fracture in composite materials: From R-curves to homogenized softening laws. *International Journal of Solids and Structures*, 134:216–228, March 2018. ISSN 00207683. doi: 10.1016/j.ijsolstr.2017.10.031.

[139] Hitoshi Hamori, Hisashi Kumazawa, Ryo Higuchi, and Tomohiro Yokozeki. Gas permeability of CFRP cross-ply laminates with thin-ply barrier layers under cryogenic and biaxial loading conditions. *Composite Structures*, 245:112326, August 2020. ISSN 0263-8223. doi: 10.1016/j.compstruct.2020.112326.

[140] A. Arteiro, G. Catalanotti, J. Xavier, and P. P. Camanho. Notched response of non-crimp fabric thin-ply laminates. *Composites Science and Technology*, 79:97–114, April 2013. ISSN 0266-3538. doi: 10.1016/j.compscitech.2013.02.001.

[141] G. Frossard, J. Cugnoni, T. Gmür, and J. Botsis. Mode I interlaminar fracture of carbon epoxy laminates: Effects of ply thickness. *Composites Part A: Applied Science and Manufacturing*, 91:1–8, December 2016. ISSN 1359-835X. doi: 10.1016/j.compositesa.2016.09.009.

[142] G. Frossard, J. Cugnoni, T. Gmür, and J. Botsis. An efficient method for fiber bridging traction identification based on the R-curve: Formulation and experimental validation. *Composite Structures*, 175:135–144, September 2017. ISSN 0263-8223. doi: 10.1016/j.compstruct.2017.04.032.

[143] Kelly Anthony, Cottrell Alan Howard, and Kelly Anthony. Interface effects and the work of fracture of a fibrous composite. *Proceedings of the Royal Society of London. A. Mathematical and Physical Sciences*, 319(1536):95–116, October 1970. doi: 10.1098/rspa.1970.0168.

[144] Soraia Pimenta and Silvestre T. Pinho. An analytical model for the translaminar fracture toughness of fibre composites with stochastic quasi-fractal fracture surfaces. *Journal of the Mechanics and Physics of Solids*, 66:78–102, May 2014. ISSN 0022-5096. doi: 10.1016/j.jmps.2014.02.001.

[145] M. Herráez, N. Pichler, and J. Botsis. Improving delamination resistance through tailored defects. *Composite Structures*, 247:112422, September 2020. ISSN 0263-8223. doi: 10.1016/j.compstruct.2020.112422.

[146] A. P. Mouritz. Review of z-pinned laminates and sandwich composites. *Composites Part A: Applied Science and Manufacturing*, 139:106128, December 2020. ISSN 1359-835X. doi: 10.1016/j.compositesa.2020.106128.

[147] Verónica Rodríguez-García, M. Herráez, Vanesa Martínez, and Roberto Guzman de Villoria. Interlaminar and translaminar fracture toughness of Automated Manufactured Bio-inspired CFRP laminates. *Composites Science and Technology*, 219: 109236, March 2022. ISSN 0266-3538. doi: 10.1016/j.compscitech.2021.109236.

[148] Seyed Mohammad Mirkhalaf Valashani and Francois Barthelat. A laser-engraved glass duplicating the structure, mechanics and performance of natural nacre. *Bioinspiration & Biomimetics*, 10(2):026005, March 2015. ISSN 1748-3190. doi: 10.1088/1748-3190/10/2/026005.

[149] Gianmaria Bullegas, Silvestre T. Pinho, and Soraia Pimenta. Engineering the translaminar fracture behaviour of thin-ply composites. *Composites Science and Technology*, 131:110–122, August 2016. ISSN 0266-3538. doi: 10.1016/j.compscitech.2016.06.002.

[150] Yentl Swolfs, Ignaas Verpoest, and Larissa Gorbatikh. Recent advances in fibre-hybrid composites: Materials selection, opportunities and applications. *International Materials Reviews*, 64(4):181–215, May 2019. ISSN 0950-6608. doi: 10.1080/09506608.2018.1467365.

[151] J. M. Finley, H. Yu, M. L. Longana, S. Pimenta, M. S. P. Shaffer, and K. D. Potter. Exploring the pseudo-ductility of aligned hybrid discontinuous composites using controlled fibre-type arrangements. *Composites Part A: Applied Science and Manufacturing*, 107:592–606, April 2018. ISSN 1359-835X. doi: 10.1016/j.compositesa.2017.11.028.

[152] L.N. Phillips. The hybrid effect — does it exist? *Composites*, 7(1):7–8, January 1976. ISSN 00104361. doi: 10.1016/0010-4361(76)90273-1.

[153] A. R. Bunsell and B. Harris. Hybrid carbon and glass fibre composites. *Composites*, 5(4):157–164, July 1974. ISSN 0010-4361. doi: 10.1016/0010-4361(74)90107-4.

[154] J. Summerscales and D. Short. Carbon fibre and glass fibre hybrid reinforced plastics. *Composites*, 9(3):157–166, July 1978. ISSN 0010-4361. doi: 10.1016/0010-4361(78)90341-5.

[155] Yentl Swolfs, Robert M. McMeeking, Ignaas Verpoest, and Larissa Gorbatikh. The effect of fibre dispersion on initial failure strain and cluster development in unidirectional carbon/glass hybrid composites. *Composites Part A: Applied Science and Manufacturing*, 69:279–287, February 2015. ISSN 1359-835X. doi: 10.1016/j.compositesa.2014.12.001.

[156] M. R. Wisnom, G. Czél, Y. Swolfs, M. Jalalvand, L. Gorbatikh, and I. Verpoest. Hybrid effects in thin ply carbon/glass unidirectional laminates: Accurate experimental determination and prediction. *Composites Part A: Applied Science and Manufacturing*, 88:131–139, September 2016. ISSN 1359-835X. doi: 10.1016/j.compositesa.2016.04.014.

[157] Mohamad Fotouhi, Meisam Jalalvand, and Michael R. Wisnom. Notch insensitive orientation-dispersed pseudo-ductile thin-ply carbon/glass hybrid laminates. *Composites Part A: Applied Science and Manufacturing*, 110:29–44, July 2018. ISSN 1359-835X. doi: 10.1016/j.compositesa.2018.04.012.

[158] Xun Wu, Jonathan D. Fuller, Marco L. Longana, and Michael R. Wisnom. Reduced notch sensitivity in pseudo-ductile CFRP thin ply angle-ply laminates with central 0° plies. *Composites Part A: Applied Science and Manufacturing*, 111: 62–72, August 2018. ISSN 1359-835X. doi: 10.1016/j.compositesa.2018.05.011.

[159] Y. Shan and K. Liao. Environmental fatigue of unidirectional glass–carbon fiber reinforced hybrid composite. *Composites Part B: Engineering*, 32(4):355–363, January 2001. ISSN 1359-8368. doi: 10.1016/S1359-8368(01)00014-2.

[160] Zhishen Wu, Xin Wang, Kentaro Iwashita, Takeshi Sasaki, and Yasumasa Hamaguchi. Tensile fatigue behaviour of FRP and hybrid FRP sheets. *Composites Part B: Engineering*, 41(5):396–402, July 2010. ISSN 1359-8368. doi: 10.1016/j.compositesb.2010.02.001.

[161] Chensong Dong, Sudarisman, and Ian J. Davies. Flexural Properties of E Glass and TR50S Carbon Fiber Reinforced Epoxy Hybrid Composites. *Journal of Materials Engineering and Performance*, 22(1):41–49, January 2013. ISSN 1544-1024. doi: 10.1007/s11665-012-0247-7.

[162] Yentl Swolfs, Yoran Geboes, Larissa Gorbatikh, and Silvestre T. Pinho. The importance of translaminar fracture toughness for the penetration impact behaviour of woven carbon/glass hybrid composites. *Composites Part A: Applied Science and Manufacturing*, 103:1–8, December 2017. ISSN 1359-835X. doi: 10.1016/j.compositesa.2017.09.009.

[163] A. Ortega, P. Maimí, E. V. González, J. R. Sainz de Aja, F. M. de la Escalera, and P. Cruz. Translaminar fracture toughness of interply hybrid laminates under tensile and compressive loads. *Composites Science and Technology*, 143:1–12, May 2017. ISSN 0266-3538. doi: 10.1016/j.compscitech.2017.02.029.

[164] Yentl Swolfs, Larissa Gorbatikh, and Ignaas Verpoest. Stress concentrations in hybrid unidirectional fibre-reinforced composites with random fibre packings. *Composites Science and Technology*, 85:10–16, August 2013. ISSN 0266-3538. doi: 10.1016/j.compscitech.2013.05.013.

[165] Francisco Mesquita, Yentl Swolfs, Stepan V. Lomov, and Larissa Gorbatikh. Ply fragmentation in unidirectional hybrid composites linked to stochastic fibre behaviour: A dual-scale model. *Composites Science and Technology*, 181:107702, September 2019. ISSN 0266-3538. doi: 10.1016/j.compscitech.2019.107702.

[166] Meisam Jalalvand, Gergely Czél, and Michael R. Wisnom. Parametric study of failure mechanisms and optimal configurations of pseudo-ductile thin-ply UD hybrid composites. *Composites Part A: Applied Science and Manufacturing*, 74:123–131, July 2015. ISSN 1359-835X. doi: 10.1016/j.compositesa.2015.04.001.

[167] Gergely Czél and M.R. Wisnom. Demonstration of pseudo-ductility in high performance glass/epoxy composites by hybridisation with thin-ply carbon prepreg. *Composites Part A: Applied Science and Manufacturing*, 52:23–30, September 2013. ISSN 1359835X. doi: 10.1016/j.compositesa.2013.04.006.

[168] Meisam Jalalvand, Gergely Czél, and Michael R. Wisnom. Numerical modelling of the damage modes in UD thin carbon/glass hybrid laminates. *Composites Science and Technology*, 94:39–47, April 2014. ISSN 0266-3538. doi: 10.1016/j.compscitech.2014.01.013.

[169] Meisam Jalalvand, Gergely Czél, and Michael R. Wisnom. Damage analysis of pseudo-ductile thin-ply UD hybrid composites – A new analytical method. *Composites Part A: Applied Science and Manufacturing*, 69:83–93, February 2015. ISSN 1359835X. doi: 10.1016/j.compositesa.2014.11.006.

[170] Gergely Czél, Meisam Jalalvand, and Michael R. Wisnom. Design and characterisation of advanced pseudo-ductile unidirectional thin-ply carbon/epoxy–glass/epoxy hybrid composites. *Composite Structures*, 143:362–370, May 2016. ISSN 0263-8223. doi: 10.1016/j.compstruct.2016.02.010.

[171] Gergely Czél, Meisam Jalalvand, Michael R. Wisnom, and Tibor Czigány. Design and characterisation of high performance, pseudo-ductile all-carbon/epoxy unidirectional hybrid composites. *Composites Part B: Engineering*, 111:348–356, February 2017. ISSN 13598368. doi: 10.1016/j.compositesb.2016.11.049.

[172] Mohamad Fotouhi, Meisam Jalalvand, and Michael R. Wisnom. High performance quasi-isotropic thin-ply carbon/glass hybrid composites with pseudo-ductile behaviour in all fibre orientations. *Composites Science and Technology*, 152:101–110, November 2017. ISSN 0266-3538. doi: 10.1016/j.compscitech.2017.08.024.

[173] C. Furtado, A. Arteiro, G. Catalanotti, J. Xavier, and P. P. Camanho. Selective ply-level hybridisation for improved notched response of composite laminates. *Composite Structures*, 145:1–14, June 2016. ISSN 0263-8223. doi: 10.1016/j.compstruct.2016.02.050.

[174] G A O Davies and Shen Zhen. Notch sensitivity of angle-ply carbon fibre composites. *The Journal of Strain Analysis for Engineering Design*, 19(3):161–165, July 1984. ISSN 0309-3247, 2041-3130. doi: 10.1243/03093247V193161.

[175] G. Catalanotti, A. Arteiro, M. Hayati, and P. P. Camanho. Determination of the mode I crack resistance curve of polymer composites using the size-effect law. *Engineering Fracture Mechanics*, 118:49–65, March 2014. ISSN 0013-7944. doi: 10.1016/j.engfracmech.2013.10.021.

[176] Robert O. Ritchie. The conflicts between strength and toughness. *Nature Materials*, 10(11):817–822, November 2011. ISSN 1476-1122, 1476-4660. doi: 10.1038/nmat3115.

[177] T. L. Anderson. *Fracture Mechanics: Fundamentals and Applications*. CRC Press/Taylor & Francis, Boca Raton, fourth edition edition, 2017. ISBN 978-1-4987-2813-3.

[178] M. J. Laffan, S. T. Pinho, P. Robinson, and A. J. McMillan. Translaminar fracture toughness testing of composites: A review. *Polymer Testing*, 31(3):481–489, May 2012. ISSN 0142-9418. doi: 10.1016/j.polymertesting.2012.01.002.

[179] M. J. Laffan, S. T. Pinho, P. Robinson, and L. Iannucci. Measurement of the in situ ply fracture toughness associated with mode I fibre tensile failure in FRP. Part I: Data reduction. *Composites Science and Technology*, 70(4):606–613, April 2010. ISSN 0266-3538. doi: 10.1016/j.compscitech.2009.12.016.

[180] S. T. Pinho, P. Robinson, and L. Iannucci. Fracture toughness of the tensile and compressive fibre failure modes in laminated composites. *Composites Science and Technology*, 66(13):2069–2079, October 2006. ISSN 0266-3538. doi: 10.1016/j.compscitech.2005.12.023.

[181] A. Ortega, P. Maimí, E. V. González, and Ll. Ripoll. Compact tension specimen for orthotropic materials. *Composites Part A: Applied Science and Manufacturing*, 63:85–93, August 2014. ISSN 1359-835X. doi: 10.1016/j.compositesa.2014.04.012.

[182] Carlos G. Dávila, Cheryl A. Rose, and Pedro P. Camanho. A procedure for superposing linear cohesive laws to represent multiple damage mechanisms in the fracture of composites. *International Journal of Fracture*, 158(2):211–223, August 2009. ISSN 0376-9429, 1573-2673. doi: 10.1007/s10704-009-9366-z.

[183] C.T. Sun and K.M. Prewo. The Fracture Toughness of Boron Aluminum Composites. *Journal of Composite Materials*, 11 (2):164–175, April 1977. ISSN 0021-9983, 1530-793X. doi: 10.1177/002199837701100204.

[184] Sina Ahmadvashaghbash, Mahoor Mehdikhani, and Yentl Swolfs. Translaminar Fracture of Thin-Ply Composites: A Novel Design for 4D Synchrotron Computed Tomography. In *20th European Conference on Composite Materials (ECCM20)*, Lausanne, Switzerland, June 2022. doi: 10.5075/epfl-298799_978-2-9701614-0-0.

[185] Xiaoyang Sun, Shin-ichi Takeda, Michael R. Wisnom, and Xiaodong Xu. In situ characterization of trans-laminar fracture toughness using X-ray Computed Tomography. *Composites Communications*, 21:100408, October 2020. ISSN 2452-2139. doi: 10.1016/j.coco.2020.100408.

[186] Andrew Bergan, Carlos Dávila, Frank Leone, Jonathan Awerbuch, and Tein-Min Tan. A Mode I cohesive law characterization procedure for through-the-thickness crack propagation in composite laminates. *Composites Part B: Engineering*, 94:338–349, June 2016. ISSN 1359-8368. doi: 10.1016/j.compositesb.2016.03.071.

[187] Adrián Ortega, Pere Maimí, Emilio V. González, and Daniel Trias. Specimen geometry and specimen size dependence of the R-curve and the size effect law from a cohesive model point of view. *International Journal of Fracture*, 205(2):239–254, June 2017. ISSN 1573-2673. doi: 10.1007/s10704-017-0195-1.

[188] P. Maimí, A. Ortega, E. V. González, and J. Costa. Should the translaminar fracture toughness of laminated composites be represented by the R or the J curve? A comparison of their consistency and predictive capability. *Composites Part A: Applied Science and Manufacturing*, 156:106867, May 2022. ISSN 1359-835X. doi: 10.1016/j.compositesa.2022.106867.

[189] Ingrid Kongshavn and Anoush Poursartip. Experimental investigation of a strain-softening approach to predicting failure in notched fibre-reinforced composite laminates. *Composites Science and Technology*, 59(1):29–40, January 1999. ISSN 0266-3538. doi: 10.1016/S0266-3538(98)00034-7.

[190] Xiangqian Li, Stephen R. Hallett, Michael R. Wisnom, Navid Zobeiry, Reza Vaziri, and Anoush Poursartip. Experimental study of damage propagation in Over-height Compact Tension tests. *Composites Part A: Applied Science and Manufacturing*, 40(12):1891–1899, December 2009. ISSN 1359-835X. doi: 10.1016/j.compositesa.2009.08.017.

[191] Xiaodong Xu, Michael R. Wisnom, Yusuf Mahadik, and Stephen R. Hallett. Scaling of fracture response in Over-height Compact Tension tests. *Composites Part A: Applied Science and Manufacturing*, 69:40–48, February 2015. ISSN 1359-835X. doi: 10.1016/j.compositesa.2014.11.002.

[192] Xiaodong Xu, Xiaoyang Sun, and Michael R. Wisnom. Initial R-curves for trans-laminar fracture of quasi-isotropic carbon/epoxy laminates from specimens with increasing size. *Composites Science and Technology*, 216:109077, November 2021. ISSN 0266-3538. doi: 10.1016/j.compscitech.2021.109077.

[193] G. Catalanotti, P. P. Camanho, J. Xavier, C. G. Dávila, and A. T. Marques. Measurement of resistance curves in the longitudinal failure of composites using digital image correlation. *Composites Science and Technology*, 70(13):1986–1993, November 2010. ISSN 0266-3538. doi: 10.1016/j.compscitech.2010.07.022.

[194] Pere Maimí, Ahmed Wagih, Adrián Ortega, José Xavier, Norbert Blanco, and Pedro Ponces Camanho. On the experimental determination of the J-curve of quasi-brittle composite materials. *International Journal of Fracture*, 224(2):199–215, August 2020. ISSN 1573-2673. doi: 10.1007/s10704-020-00456-0.

[195] A. Ortega, P. Maimí, E. V. González, and D. Trias. Characterization of the translaminar fracture Cohesive Law. *Composites Part A: Applied Science and Manufacturing*, 91:501–509, December 2016. ISSN 1359-835X. doi: 10.1016/j.compositesa.2016.01.019.

[196] G. P. Cherepanov. Crack propagation in continuous media: PMM vol. 31, no. 3, 1967, pp. 476–488. *Journal of Applied Mathematics and Mechanics*, 31(3):503–512, January 1967. ISSN 0021-8928. doi: 10.1016/0021-8928(67)90034-2.

[197] J. R. Rice. A Path Independent Integral and the Approximate Analysis of Strain Concentration by Notches and Cracks. *Journal of Applied Mechanics*, 35(2):379–386, June 1968. ISSN 0021-8936. doi: 10.1115/1.3601206.

[198] M. Herráez, N. Pichler, G.A. Pappas, C. Blondeau, and J. Botsis. Experiments and numerical modelling on angle-ply laminates under remote mode II loading. *Composites Part A: Applied Science and Manufacturing*, 134:105886, July 2020. ISSN 1359835X. doi: 10.1016/j.compositesa.2020.105886.

[199] Rostand Moutou Pitti, Claudiu Badulescu, and Michel Grédiac. Characterization of a cracked specimen with full-field measurements: Direct determination of the crack tip and energy release rate calculation. *International Journal of Fracture*, 187(1):109–121, May 2014. ISSN 1573-2673. doi: 10.1007/s10704-013-9921-5.

[200] D. M. Montenegro, L. P. Canal, J. Botsis, M. Zogg, A. R. Studart, and K. Wegener. On the validity of the J-integral as a measure of the transverse intralaminar fracture energy of glass fiber-reinforced polyurethanes with nonlinear material behavior. *International Journal of Solids and Structures*, 139–140:15–28, May 2018. ISSN 0020-7683. doi: 10.1016/j.ijsolstr.2018.01.019.

[201] T. H. Becker, M. Mostafavi, R. B. Tait, and T. J. Marrow. An approach to calculate the J-integral by digital image correlation displacement field measurement. *Fatigue & Fracture of Engineering Materials & Structures*, 35(10):971–984, 2012. ISSN 1460-2695. doi: 10.1111/j.1460-2695.2012.01685.x.

[202] S.M. Barhli, M. Mostafavi, A.F. Cinar, D. Hollis, and T.J. Marrow. J-Integral Calculation by Finite Element Processing of Measured Full-Field Surface Displacements. *Experimental Mechanics*, 57(6):997–1009, July 2017. ISSN 1741-2765. doi: 10.1007/s11340-017-0275-1.

[203] Tobias Strohmann, David Melching, Paysan Florian, Alina Klein, Dietrich Eric, Guillermo Requena, and Eric Breitbarth. Crack Analysis Tool in Python - CrackPy. Zenodo, November 2022.

[204] Guillaume Broggi. Multi-scale characterisation and modelling of notched strength and translaminar fracture in hybrid thin-ply composites based on different carbon fibre grades: Data, codes and publications. February 2023. doi: 10.5281/zenodo.7656585.

[205] Gonzalo Pincheira, Cristian Canales, Carlos Medina, Eduardo Fernández, and Paulo Flores. Influence of aramid fibers on the mechanical behavior of a hybrid carbon–aramid–reinforced epoxy composite. *Proceedings of the Institution of Mechanical Engineers, Part L: Journal of Materials: Design and Applications*, 232(1):58–66, January 2018. ISSN 1464-4207, 2041-3076. doi: 10.1177/1464420715612827.

[206] Yoran Geboes, Amalia Katalagarianakis, Jeroen Soete, Jan Ivens, and Yentl Swolfs. The translaminar fracture toughness of high-performance polymer fibre composites and their carbon fibre hybrids. *Composites Science and Technology*, 221:109307, April 2022. ISSN 0266-3538. doi: 10.1016/j.compscitech.2022.109307.

[207] B. Harris and A. R. Bunsell. Impact properties of glass fibre/carbon fibre hybrid composites. *Composites*, 6(5):197–201, September 1975. ISSN 0010-4361. doi: 10.1016/0010-4361(75)90413-9.

[208] G. Marom, S. Fischer, F. R. Tuler, and H. D. Wagner. Hybrid effects in composites: Conditions for positive or negative effects versus rule-of-mixtures behaviour. *Journal of Materials Science*, 13(7):1419–1426, July 1978. ISSN 1573-4803. doi: 10.1007/BF00553194.

[209] G. Kretsis. A review of the tensile, compressive, flexural and shear properties of hybrid fibre-reinforced plastics. *Composites*, 18(1):13–23, January 1987. ISSN 0010-4361. doi: 10.1016/0010-4361(87)90003-6.

[210] Yongli Zhang, Yan Li, Hao Ma, and Tao Yu. Tensile and interfacial properties of unidirectional flax/glass fiber reinforced hybrid composites. *Composites Science and Technology*, 88:172–177, November 2013. ISSN 0266-3538. doi: 10.1016/j.compscitech.2013.08.037.

[211] Durai Prabhakaran Raghavalu Thirumalai, Tom Løgstrup Andersen, Christen Malte Markussen, Bo Madsen, and Hans Lilholt. Tensile and compression properties of hybrid composites – A comparative study: 19th International Conference on Composite Materials. *Proceedings of the 19th International Conference on Composite Materials (ICCM19)*, pages 1029–1035, 2013.

[212] Yentl Swolfs, Larissa Gorbatikh, and Ignaas Verpoest. Fibre hybridisation in polymer composites: A review. *Composites Part A: Applied Science and Manufacturing*, 67:181–200, December 2014. ISSN 1359835X. doi: 10.1016/j.compositesa.2014.08.027.

[213] Anthony Bunsell, Larissa Gorbatikh, Hannah Morton, Soraia Pimenta, Ian Sinclair, Mark Spearing, Yentl Swolfs, and Alain Thionnet. Benchmarking of strength models for unidirectional composites under longitudinal tension. *Composites Part A: Applied Science and Manufacturing*, 111:138–150, August 2018. ISSN 1359-835X. doi: 10.1016/j.compositesa.2018.03.016.

[214] Rodrigo P. Tavares, Jose M. Guerrero, Fermin Otero, Albert Turon, Joan A. Mayugo, Josep Costa, and Pedro P. Camanho. Effects of local stress fields around broken fibres on the longitudinal failure of composite materials. *International Journal of Solids and Structures*, 156–157:294–305, January 2019. ISSN 0020-7683. doi: 10.1016/j.ijsolstr.2018.08.027.

[215] C. Breite, A. Melnikov, A. Turon, A. B. de Morais, C. Le Bourlot, E. Maire, E. Schöberl, F. Otero, F. Mesquita, I. Sinclair, J. Costa, J. A. Mayugo, J. M. Guerrero, L. Gorbatikh, L. N. McCartney, M. Hajikazemi, M. Mehdikhani, M. N. Mavrogordato, P. P. Camanho, R. Tavares, S. M. Spearing, S. V. Lomov, S. Pimenta, W. Van Paepegem, and Y. Swolfs. Detailed experimental validation and benchmarking of six models for longitudinal tensile failure of unidirectional composites. *Composite Structures*, 279:114828, January 2022. ISSN 0263-8223. doi: 10.1016/j.compstruct.2021.114828.

[216] Yentl Swolfs, Robert M. McMeeking, Ignaas Verpoest, and Larissa Gorbatikh. Matrix cracks around fibre breaks and their effect on stress redistribution and failure development in unidirectional composites. *Composites Science and Technology*, 108: 16–22, February 2015. ISSN 0266-3538. doi: 10.1016/j.compscitech.2015.01.002.

[217] Yentl Swolfs, Ignaas Verpoest, and Larissa Gorbatikh. Maximising the hybrid effect in unidirectional hybrid composites. *Materials & Design*, 93:39–45, March 2016. ISSN 0264-1275. doi: 10.1016/j.matdes.2015.12.137.

[218] Jin Zhang, Khunlavit Chaisombat, Shuai He, and Chun H. Wang. Hybrid composite laminates reinforced with glass/carbon woven fabrics for lightweight load bearing structures. *Materials & Design (1980-2015)*, 36:75–80, April 2012. ISSN 0261-3069. doi: 10.1016/j.matdes.2011.11.006.

[219] Ying Shan and Kin Liao. Environmental fatigue behavior and life prediction of unidirectional glass–carbon/epoxy hybrid composites. *International Journal of Fatigue*, 24(8):847–859, August 2002. ISSN 0142-1123. doi: 10.1016/S0142-1123(01)00210-9.

[220] Gergely Czél, Meisam Jalalvand, and Michael R. Wisnom. Hybrid specimens eliminating stress concentrations in tensile and compressive testing of unidirectional composites. *Composites Part A: Applied Science and Manufacturing*, 91:436–447, December 2016. ISSN 1359-835X. doi: 10.1016/j.compositesa.2016.07.021.

[221] Babak Fazlali, Sagar Ashokbhai Ashodia, Valter Carvelli, Stepan V. Lomov, and Yentl Swolfs. Proper Tensile Testing of Unidirectional Composites. In *American Society for Composites 2022*. Destech Publications, Inc., September 2022. ISBN 978-1-60595-690-9. doi: 10.12783/asc37/36410.

[222] Rajnish Kumar, Bo Madsen, Hans Lilholt, and Lars P. Mikkelsen. Influence of Test Specimen Geometry on Probability of Failure of Composites Based on Weibull Weakest Link Theory. *Materials*, 15(11):3911, January 2022. ISSN 1996-1944. doi: 10.3390/ma15113911.

[223] Yentl Swolfs, Yannick Meerten, Peter Hine, Ian Ward, Ignaas Verpoest, and Larissa Gorbatikh. Introducing ductility in hybrid carbon fibre/self-reinforced composites through control of the damage mechanisms. *Composite Structures*, 131:259–265, November 2015. ISSN 02638223. doi: 10.1016/j.compstruct.2015.04.069.

[224] S.B. Sapozhnikov, Y. Swolfs, and S.V. Lomov. Pseudo-ductile unidirectional high modulus/high strength carbon fibre hybrids using conventional ply thickness prepregs. *Composites Part B: Engineering*, 198:108213, October 2020. ISSN 13598368. doi: 10.1016/j.compositesb.2020.108213.

[225] S. B. Sapozhnikov, S. V. Lomov, Y. Swolfs, and V. Carvelli. Deformation and failure of pseudo-ductile quasi-isotropic all-carbon hybrid FRPS with an open hole under tension. *Composites Part B: Engineering*, 237:109870, May 2022. ISSN 1359-8368. doi: 10.1016/j.compositesb.2022.109870.

[226] N. Zobeiry and A. Poursartip. 3 - The origins of residual stress and its evaluation in composite materials. In P. W. R. Beaumont, C. Soutis, and A. Hodzic, editors, *Structural Integrity and Durability of Advanced Composites*, Woodhead Publishing Series in Composites Science and Engineering, pages 43–72. Woodhead Publishing, January 2015. ISBN 978-0-08-100137-0. doi: 10.1016/B978-0-08-100137-0.00003-1.

[227] Andreas Hauffe. eLamX^2 - expandable Laminate Explorer, July 2022.

[228] P. P. Camanho and G. Catalanotti. On the relation between the mode I fracture toughness of a composite laminate and that of a 0° ply: Analytical model and experimental validation. *Engineering Fracture Mechanics*, 78(13):2535–2546, August 2011. ISSN 0013-7944. doi: 10.1016/j.engfracmech.2011.06.013.

[229] David McGowan, Damodar Ambur, and Stephen McNeill. Full-Field Structural Response of Composite Structures: Analysis and Experiment. In *44th AIAA/ASME/ASCE/AHS/ASC Structures, Structural Dynamics, and Materials Conference*, Norfolk, Virginia, April 2003. American Institute of Aeronautics and Astronautics. ISBN 978-1-62410-100-7. doi: 10.2514/6.2003-1623.

[230] International Digital Image Correlation Society, Elizabeth Jones, Mark Iadicola, Rory Bigger, Benoît Blaysat, Christofer Boo, Manuel Grewer, Jun Hu, Amanda Jones, Markus Klein, Kavesary Raghavan, Phillip Reu, Timothy Schmidt, Thorsten Siebert, Micah Simenson, Daniel Turner, Alessandro Vieira, and Thorsten Weikert. A Good Practices Guide for Digital Image Correlation. Technical report, International Digital Image Correlation Society, October 2018.

[231] F. Z. Li, C. F. Shih, and A. Needleman. A comparison of methods for calculating energy release rates. *Engineering Fracture Mechanics*, 21(2):405–421, January 1985. ISSN 0013-7944. doi: 10.1016/0013-7944(85)90029-3.

[232] Carl De Boor. *A Practical Guide to Splines: With 32 Figures*. Number v. 27 in Applied Mathematical Sciences. Springer, New York, rev. ed edition, 2001. ISBN 978-0-387-95366-3.

[233] Eugene Prilepin. Csaps: Cubic spline approximation (smoothing).

[234] Pauli Virtanen, Ralf Gommers, Travis E. Oliphant, Matt Haberland, Tyler Reddy, David Cournapeau, Evgeni Burovski, Pearu Peterson, Warren Weckesser, Jonathan Bright, Stéfan J. van der Walt, Matthew Brett, Joshua Wilson, K. Jarrod Millman, Nikolay Mayorov, Andrew R. J. Nelson, Eric Jones, Robert Kern, Eric Larson, C J Carey, İlhan Polat, Yu Feng, Eric W. Moore, Jake VanderPlas, Denis Laxalde, Josef Perktold, Robert Cimrman, Ian Henriksen, E. A. Quintero, Charles R. Harris, Anne M. Archibald, Antônio H. Ribeiro, Fabian Pedregosa, Paul van Mulbregt, SciPy 1.0 Contributors, Aditya Vijaykumar, Alessandro Pietro Bardelli, Alex Rothberg, Andreas Hilboll, Andreas Kloeckner, Anthony Scopatz, Antony Lee, Ariel Rokem, C. Nathan Woods, Chad Fulton, Charles Masson, Christian Häggström, Clark Fitzgerald, David A. Nicholson, David R. Hagen, Dmitrii V. Pasechnik, Emanuele Olivetti, Eric Martin, Eric Wieser, Fabrice Silva, Felix Lenders,

Florian Wilhelm, G. Young, Gavin A. Price, Gert-Ludwig Ingold, Gregory E. Allen, Gregory R. Lee, Hervé Audren, Irvin Probst, Jörg P. Dietrich, Jacob Silterra, James T Webber, Janko Slavič, Joel Nothman, Johannes Buchner, Johannes Kulick, Johannes L. Schönberger, José Vinícius de Miranda Cardoso, Joscha Reimer, Joseph Harrington, Juan Luis Cano Rodríguez, Juan Nunez-Iglesias, Justin Kuczynski, Kevin Tritz, Martin Thoma, Matthew Newville, Matthias Kümmerer, Maximilian Bolingbroke, Michael Tartre, Mikhail Pak, Nathaniel J. Smith, Nikolai Nowaczyk, Nikolay Shebanov, Oleksandr Pavlyk, Per A. Brodtkorb, Perry Lee, Robert T. McGibbon, Roman Feldbauer, Sam Lewis, Sam Tygier, Scott Sievert, Sebastiano Vigna, Stefan Peterson, Surhud More, Tadeusz Pudlik, Takuya Oshima, Thomas J. Pingel, Thomas P. Robitaille, Thomas Spura, Thouis R. Jones, Tim Cera, Tim Leslie, Tiziano Zito, Tom Krauss, Utkarsh Upadhyay, Yaroslav O. Halchenko, and Yoshiki Vázquez-Baeza. SciPy 1.0: Fundamental algorithms for scientific computing in Python. *Nature Methods*, 17(3): 261–272, March 2020. ISSN 1548-7091, 1548-7105. doi: 10.1038/s41592-019-0686-2.

[235] Guillaume Broggi, Joël Cugnoni, and Véronique Michaud. A Python implementation of J-integral data reduction methods for composite toughness. November 2022. doi: 10.5281/zenodo.7307418.

[236] Jerry L. Hintze and Ray D. Nelson. Violin Plots: A Box Plot-Density Trace Synergism. *The American Statistician*, 52(2): 181–184, 1998. ISSN 0003-1305. doi: 10.2307/2685478.

[237] N. Zobeiry, R. Vaziri, and A. Poursartip. Characterization of strain-softening behavior and failure mechanisms of composites under tension and compression. *Composites Part A: Applied Science and Manufacturing*, 68:29–41, January 2015. ISSN 1359-835X. doi: 10.1016/j.compositesa.2014.09.009.

[238] R F Teixeira, S T Pinho, and P Robinson. TRANSLAMINAR FRACTURE TOUGHNESS OF CFRP: FROM THE TOUGHNESS OF INDIVIDUAL PLIES TO THE TOUGHNESS OF THE LAMINATES. page 8, 2012.

[239] A. Turon, C. G. Dávila, P. P. Camanho, and J. Costa. An engineering solution for mesh size effects in the simulation of delamination using cohesive zone models. *Engineering Fracture Mechanics*, 74(10):1665–1682, July 2007. ISSN 0013-7944. doi: 10.1016/j.engfracmech.2006.08.025.

[240] D. Li, A. F. Yee, I. W. Chen, S. C. Chang, and K. Takahashi. Fracture behaviour of unmodified and rubber-modified epoxies under hydrostatic pressure. *Journal of Materials Science*, 29(8):2205–2215, April 1994. ISSN 1573-4803. doi: 10.1007/BF01154701.

[241] Viggo Tvergaard. Material Failure by Void Growth to Coalescence. In *Advances in Applied Mechanics*, volume 27, pages 83–151. Elsevier, 1989. ISBN 978-0-12-002027-0. doi: 10.1016/S0065-2156(08)70195-9.

Appendix A

Supporting information for chapter 4

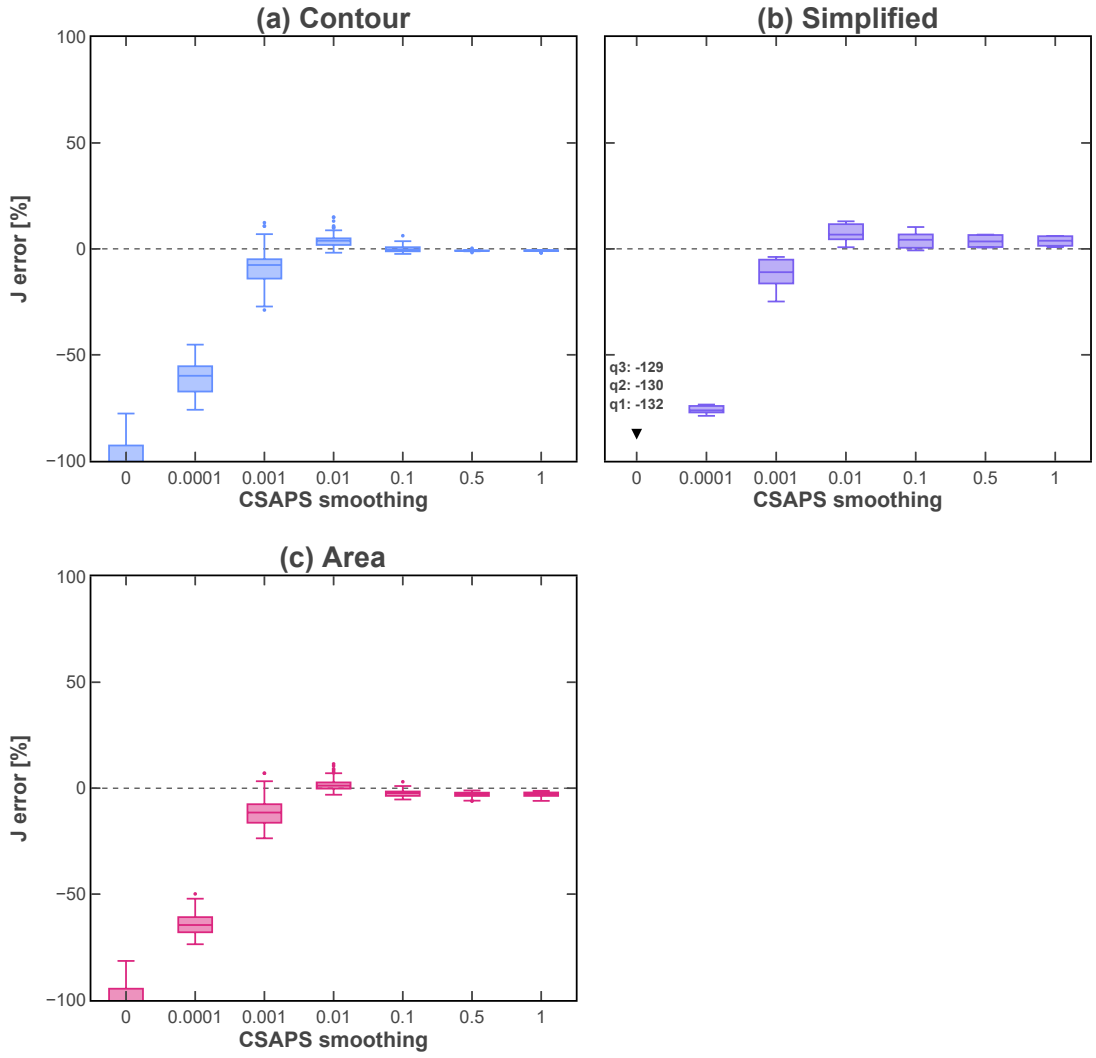

Figure A.1: Boxplots of the error committed on the J-integral results evaluated at a safe distance from the crack tip, as a function of the csaps smoothing value ranging from 0 to 1. No noise.

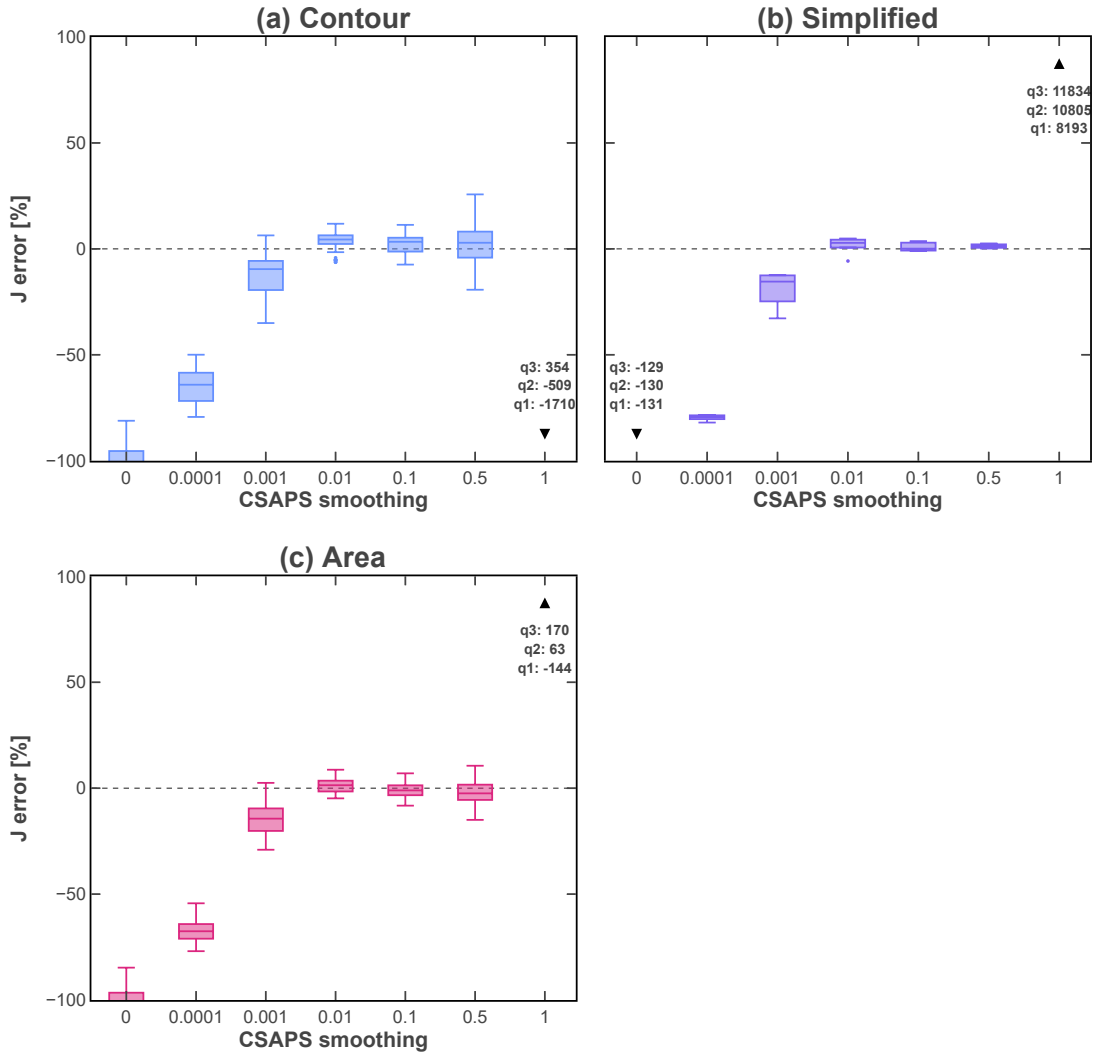

Figure A.2: Boxplots of the error committed on the J-integral results evaluated at a safe distance from the crack tip, as a function of the csaps smoothing value ranging from 0 to 1. Noise with $1e^{-2}$ mm standard deviation.

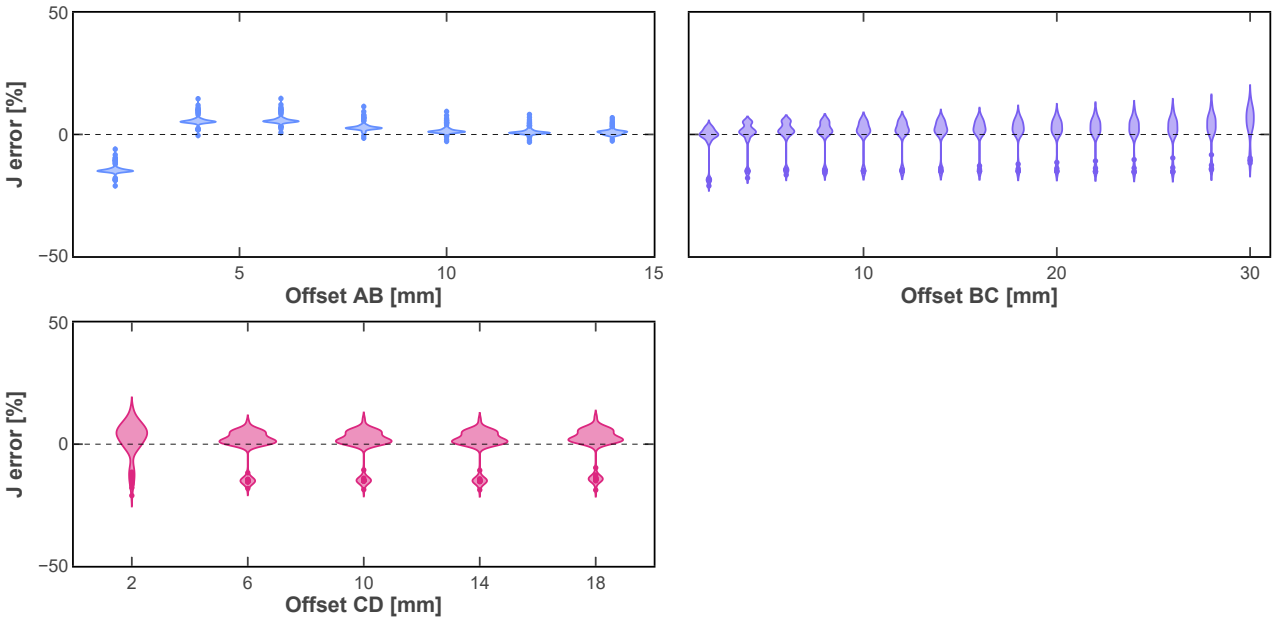

Figure A.3: Violin distributions of the J-integral results obtained with the line formulation as a function of offset values ranging from the crack tip (0 mm) to the sample edge (maximal value). No noise. Only a subset of the offsets is reported for readability. The values close to the crack tip are significantly off and not reported. The FEM J-integral value is reported as a dashed line.

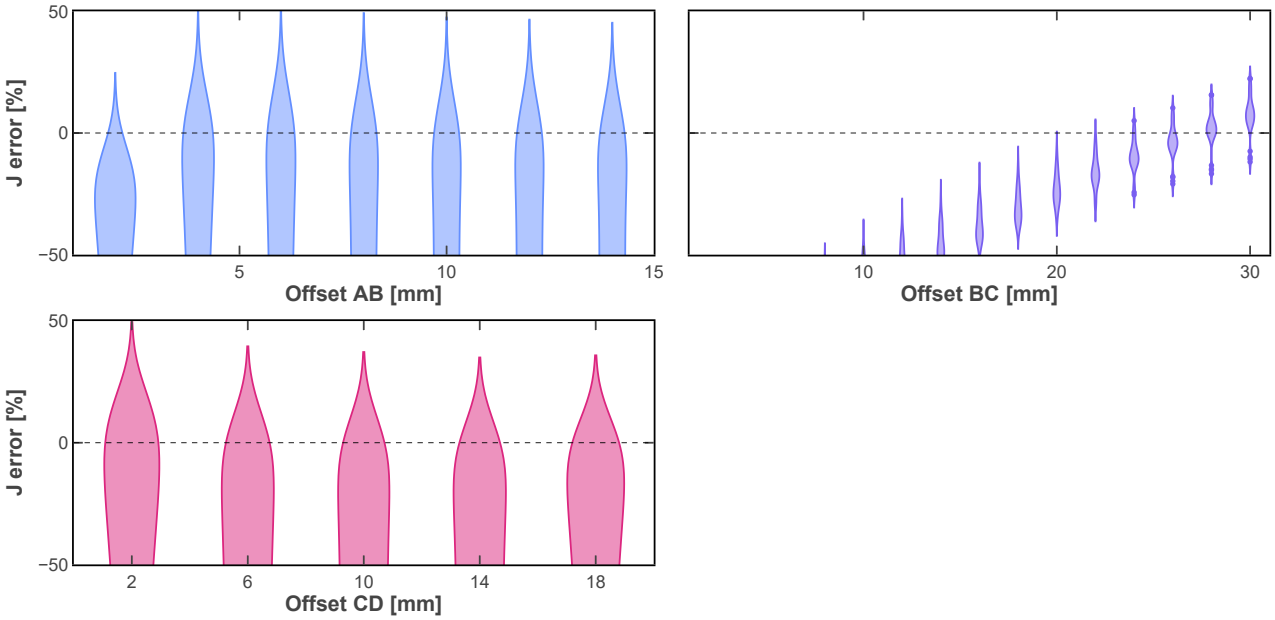

Figure A.4: Violin distributions of the J-integral results obtained with the simplified formulation as a function of offset values ranging from the crack tip (0 mm) to the sample edge (maximal value). No noise. Only a subset of the offsets is reported for readability. The values close to the crack tip are significantly off and not reported. The FEM J-integral value is reported as a dashed line.

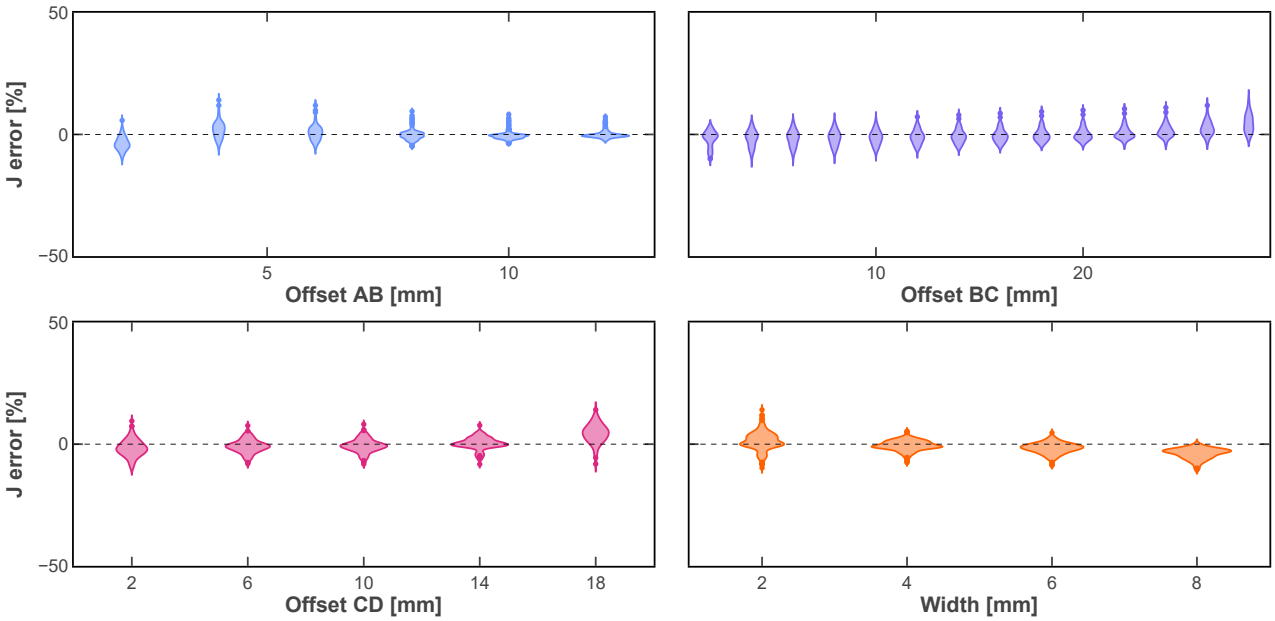

Figure A.5: Violin distributions of the J-integral results obtained with the surface formulation as a function of offset values ranging from the crack tip (0 mm) to the sample edge (maximal value). No noise. Only a subset of the offsets is reported for readability. he values close to the crack tip are significantly off and not reported. The FEM J-integral value is reported as a dashed line.

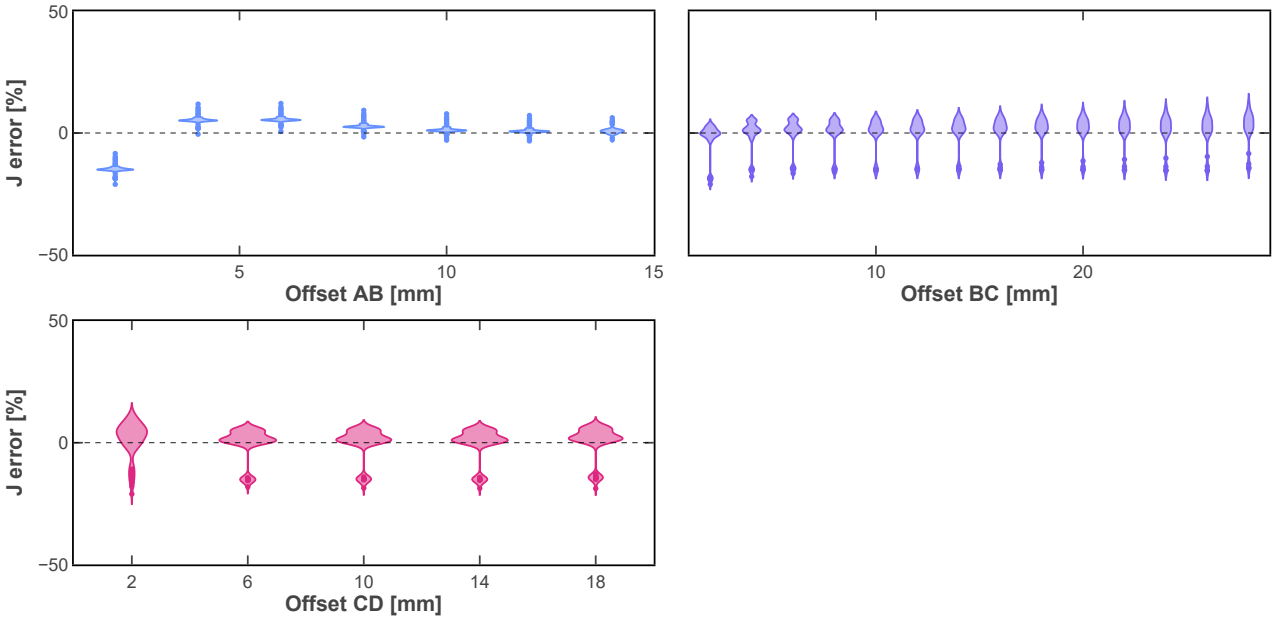

Figure A.6: Violin distributions of the J-integral results obtained with the line formulation as a function of offset values ranging from the crack tip (0 mm) to the sample edge (maximal value). Noise with 2.2e-4 mm standard deviation. Only a subset of the offsets is reported for readability. The values close to the crack tip are significantly off and not reported. The FEM J-integral value is reported as a dashed line.

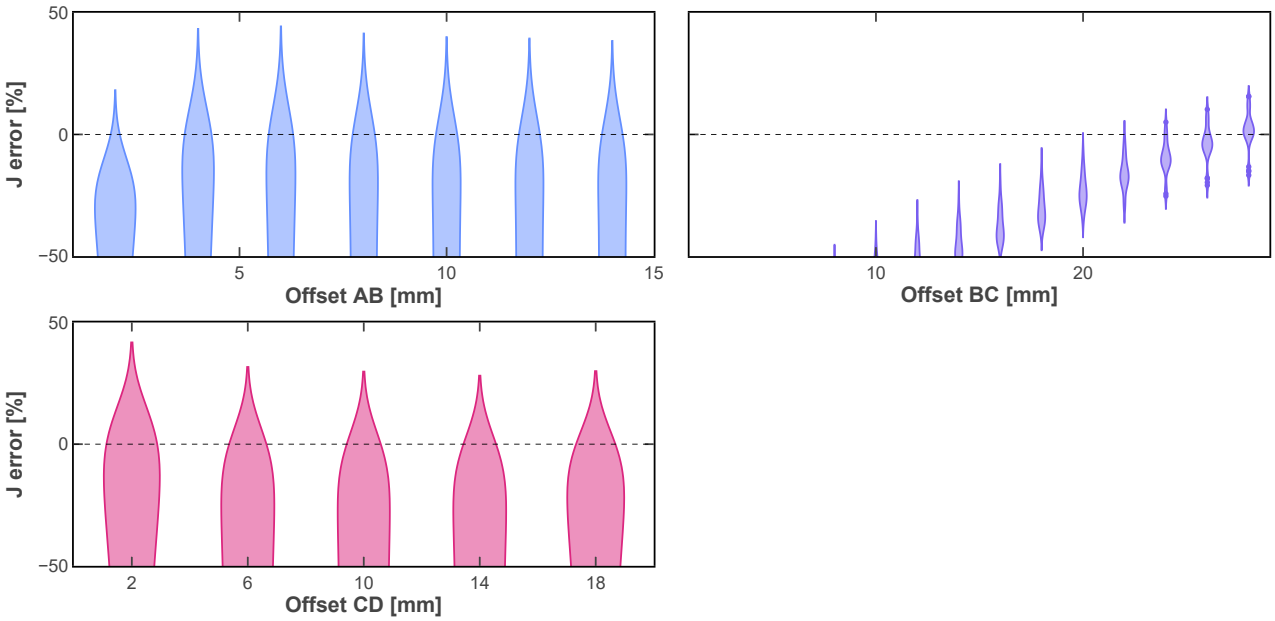

Figure A.7: Violin distributions of the J-integral results obtained with the simplified formulation as a function of offset values ranging from the crack tip (0 mm) to the sample edge (maximal value). Noise with 2.2e-4 mm standard deviation. Only a subset of the offsets is reported for readability. The values close to the crack tip are significantly off and not reported. The FEM J-integral value is reported as a dashed line.

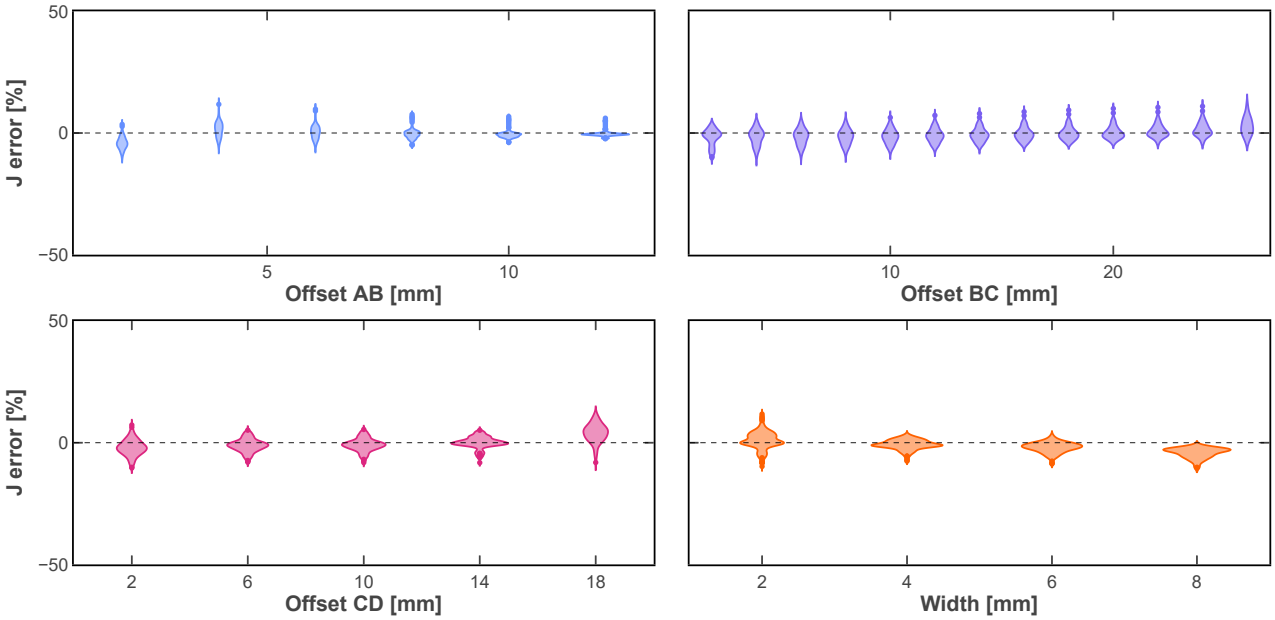

Figure A.8: Violin distributions of the J-integral results obtained with the surface formulation as a function of offset values ranging from the crack tip (0 mm) to the sample edge (maximal value). Noise with 2.2e-4 mm standard deviation. Only a subset of the offsets is reported for readability. The values close to the crack tip are significantly off and not reported. The FEM J-integral value is reported as a dashed line.

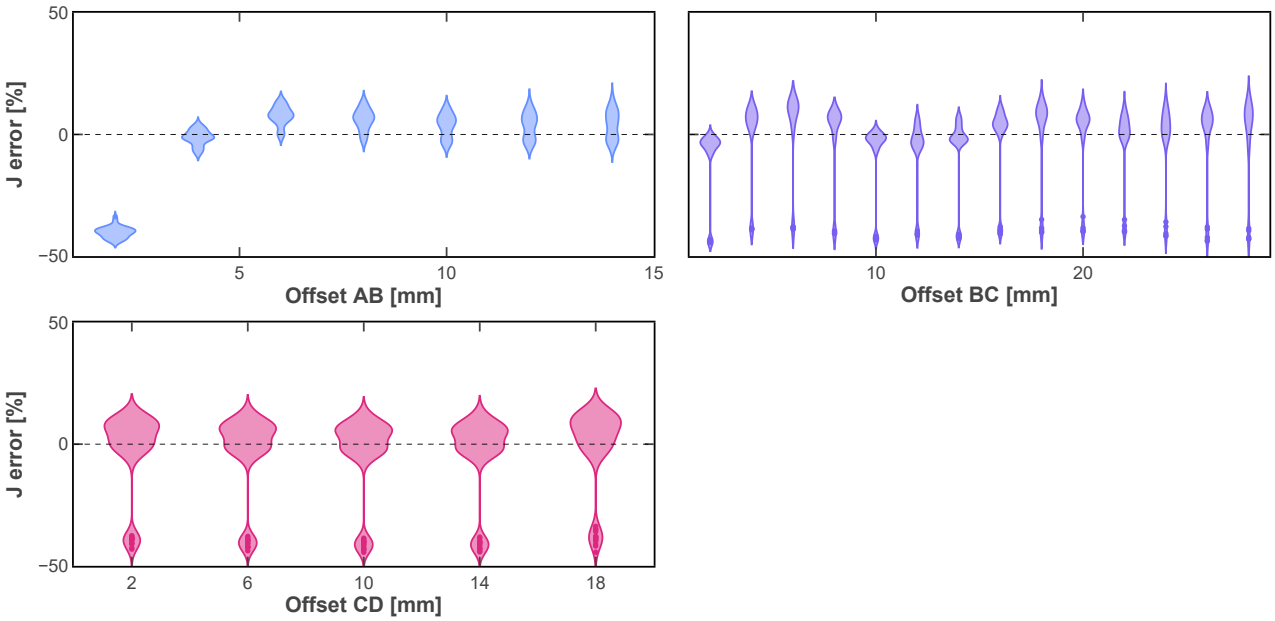

Figure A.9: Violin distributions of the J-integral results obtained with the line formulation as a function of offset values ranging from the crack tip (0 mm) to the sample edge (maximal value). Noise with 1e-2 mm standard deviation. Only a subset of the offsets is reported for readability. The values close to the crack tip are significantly off and not reported. The FEM J-integral value is reported as a dashed line.

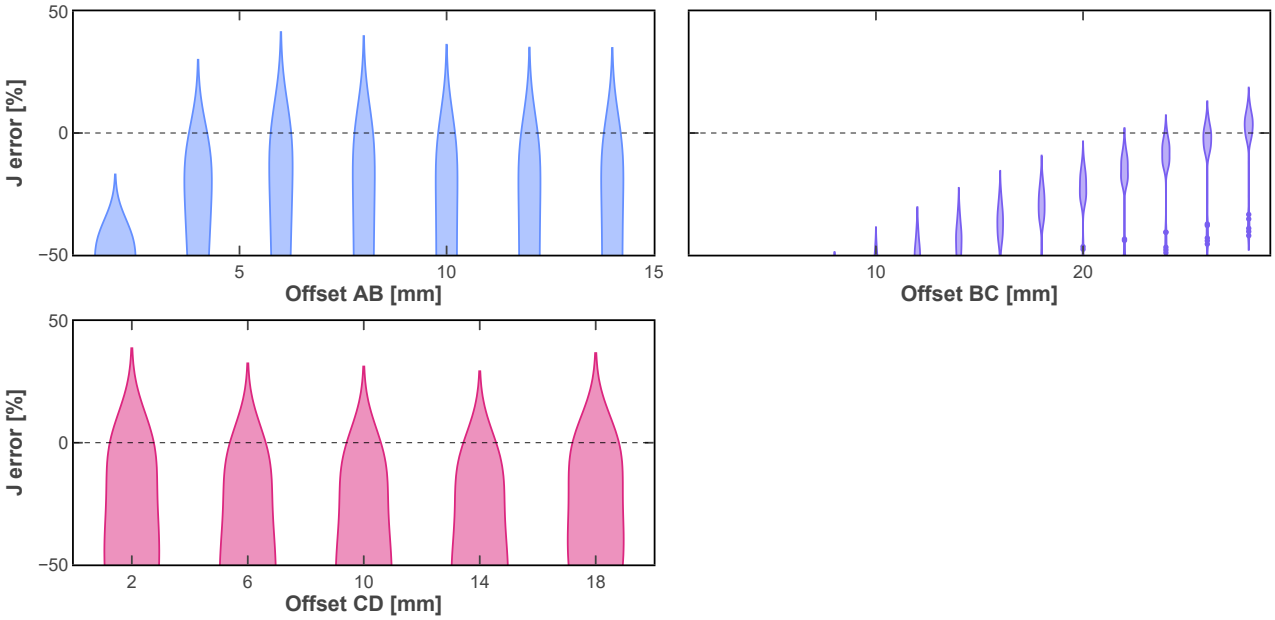

Figure A.10: Violin distributions of the J-integral results obtained with the simplified formulation as a function of offset values ranging from the crack tip (0 mm) to the sample edge (maximal value). Noise with 1e-2 mm standard deviation. Only a subset of the offsets is reported for readability. The values close to the crack tip are significantly off and not reported. The FEM J-integral value is reported as a dashed line.

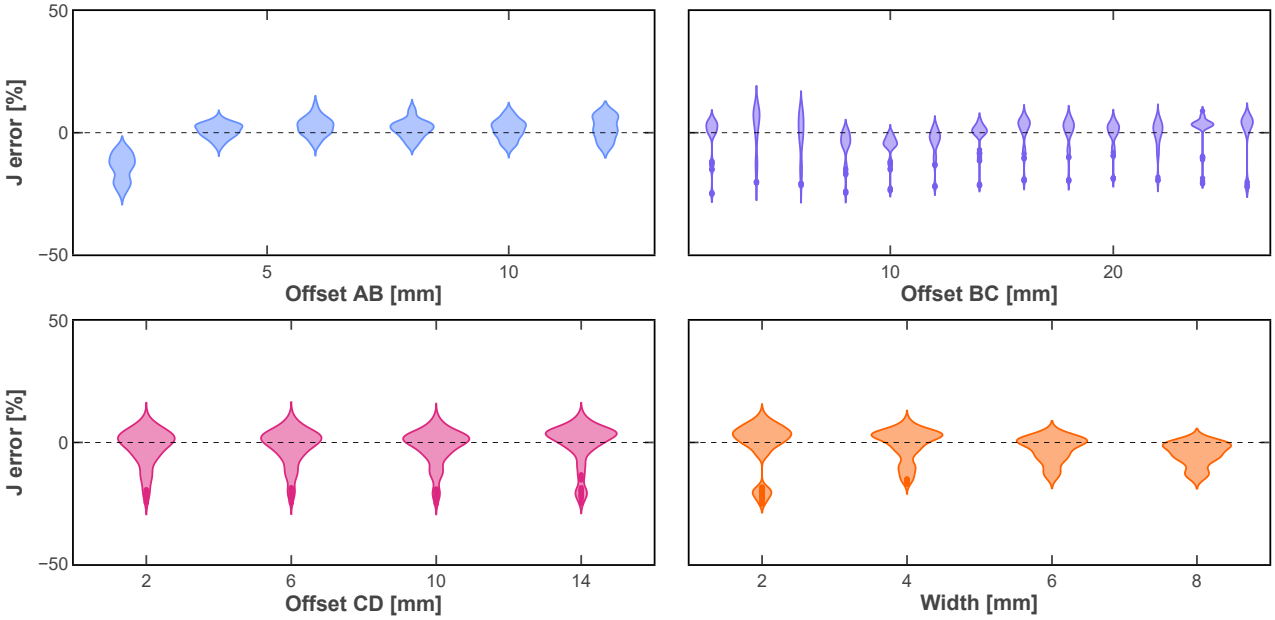

Figure A.11: Violin distributions of the J-integral results obtained with the surface formulation as a function of offset values ranging from the crack tip (0 mm) to the sample edge (maximal value). Noise with 1e-2 mm standard deviation. Only a subset of the offsets is reported for readability. The values close to the crack tip are significantly off and not reported. The FEM J-integral value is reported as a dashed line.

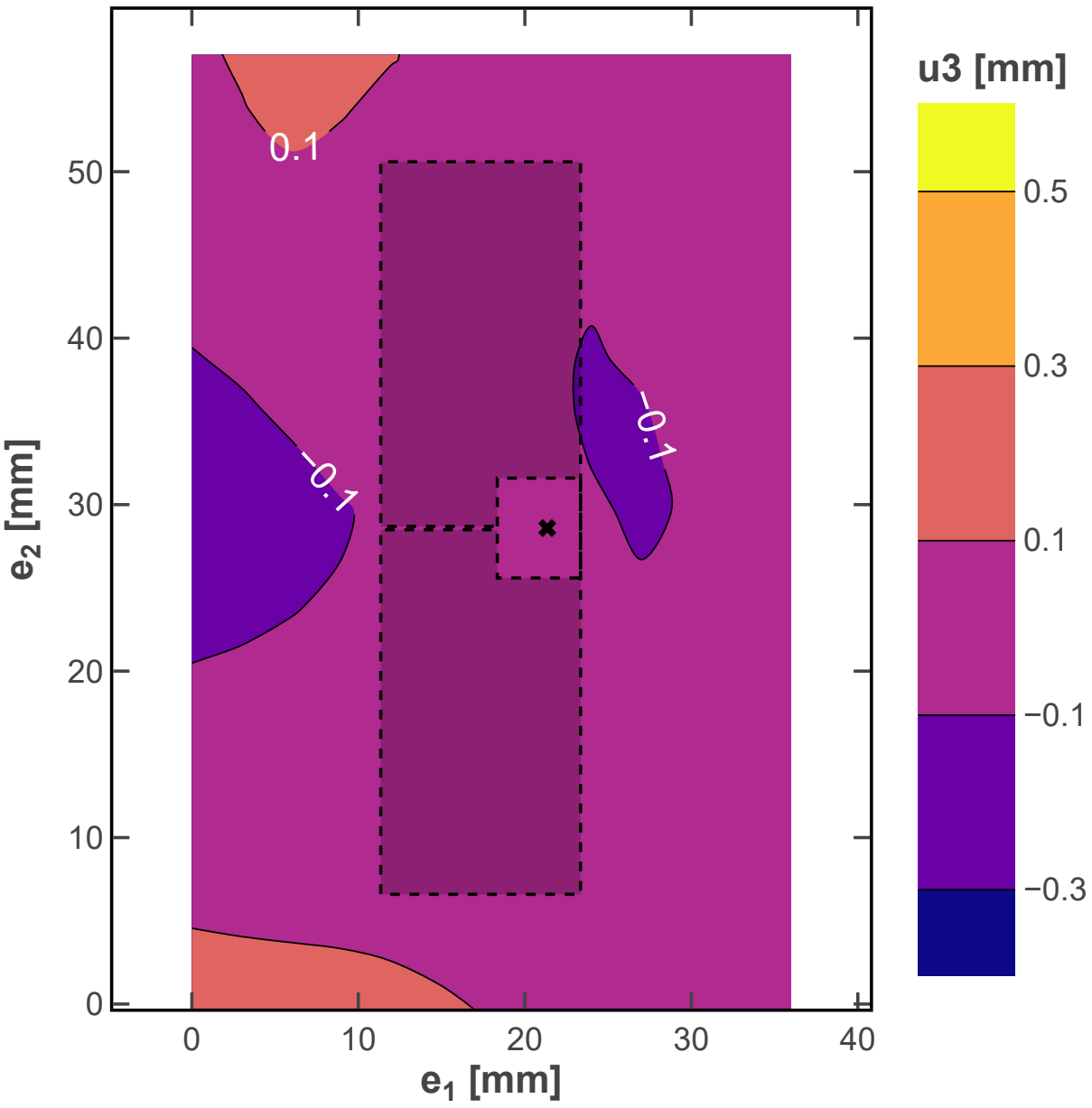

Figure A.12: Out of plane displacement monitored by DIC for frame 753 of sample C.

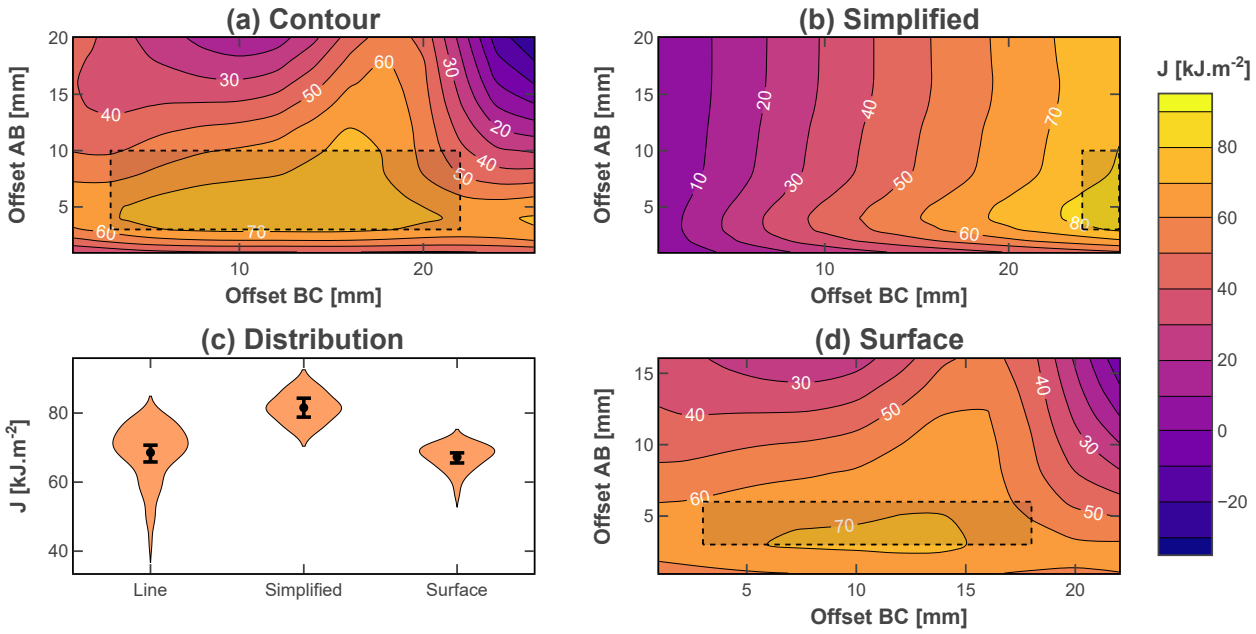

Figure A.13: Contours of the J-integral values for frame 753 of sample C as a function of offsets Δ_{AB} and Δ_{BC} using (a) line, (b) simplified and (b) surface methods. (c) Corresponding violin distributions obtained after constraining offsets Δ_{AB} and Δ_{BC} to the recommended range represented as a shaded black rectangle. The points stand for mean values and the error bars for the 99% confidence intervals obtained by bootstrapping over $1e^5$ iterations. The violin distributions are not normalized by the number of points for better readability.

Appendix B

Supporting information for chapter 5 and chapter 6

Acoustic Emission (AE) monitoring procedure for onset of damage characterization

The AE acquisition performed with an AMSY-5 dual-channel from Vallen Systeme equipped with two NANO-30 S/N749 probes. The probes were fixed at the two ends of the gauge length, as close as possible to the tabs, as depicted in Figure B.1. The contact between the probes and the samples was ensured with dielectric grease. The probes were secured with elastic insulating tape. Knowing the sound velocity v in the laminate composite, the event that generated an AE can be localized in the sample length by analyzing the difference between the acquisition times of both probes. This procedure, called Δt filtering, is used to reject the AE occurring outside of the gauge length.

To check the probe mounting and calibrate the Δt filtering, a graphite pencil lead is broken outside of the probes, for instance in the grips. Assuming that the acoustic frequencies thus obtained are close to the ones generated by composite damage, the velocity v can be calculated thanks to the acquisition times registered by the two probes. If the precise localization of the AE event is not required, the calibration can be relative, i.e., the distance between the probes can be set to an arbitrary value.

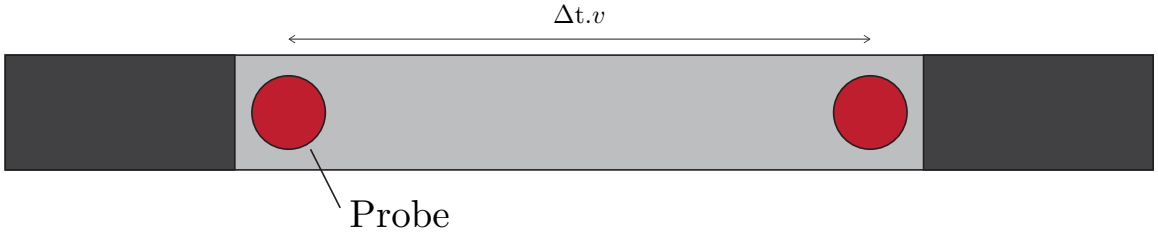

Figure B.1: AE setup.

The event energy and peak frequencies were recorder, but only the former was analyzed. A dual

channel acquisition can not localize the events outside of the probes, in contrast with a four-channel setup. As a consequence, the acquisition may be sensible to edge effects or reflections. Thus, the AE event were manually post-processed to reject outliers, namely high energy events localized immediately next to the probes. Furthermore, high energy events occurring for very small strains were considered as sample and fixture alignment events, and discarded. However, it should be highlighted that this procedure introduce several biases, from the choice of the outliers to the energy rate identification, especially considering that different samples from the same material may exhibit different cumulative energy curves, possibly due to probe wear or when damage occurred at the probe location. Nevertheless, a good repeatability of the AE analysis was achieved.

The cumulative energy was used to analyze AE. As shown in Figure B.2, it was assumed that AE events account for the cumulative energy at different rates depending on whether they correspond to background noise, delamination, or fiber breakage and other damage. Thus, an steep increase in this rate was considered as the onset of damage. Examples of analyses are provided in Figure B.3.

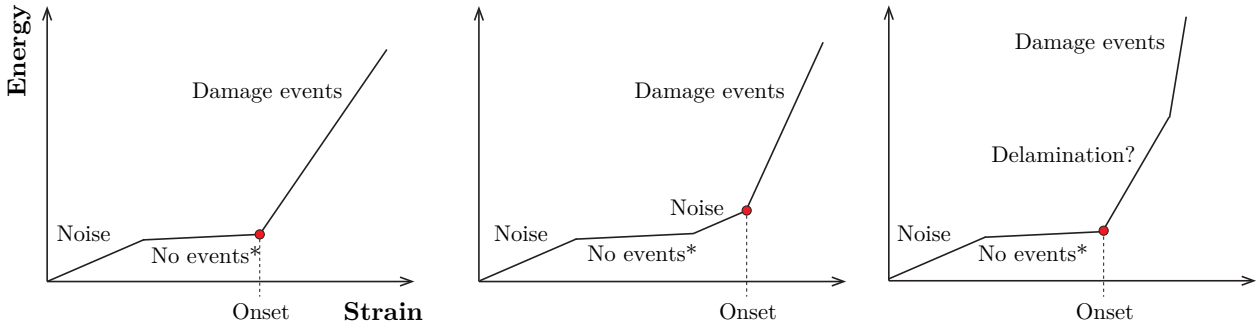

Figure B.2: Typical cumulative AE energy shapes. From left to right: in the first case, the knee point is clearly identifiable; in the second case, a first knee point is present but the rate of energy increase is similar to the initial background noise, thus it was not considered as the apparition of damage; in the third case the rate of energy increase after the first knee point is significantly more important than for the background noise and is possibly due to delamination. * scarse events with no significant energy contribution

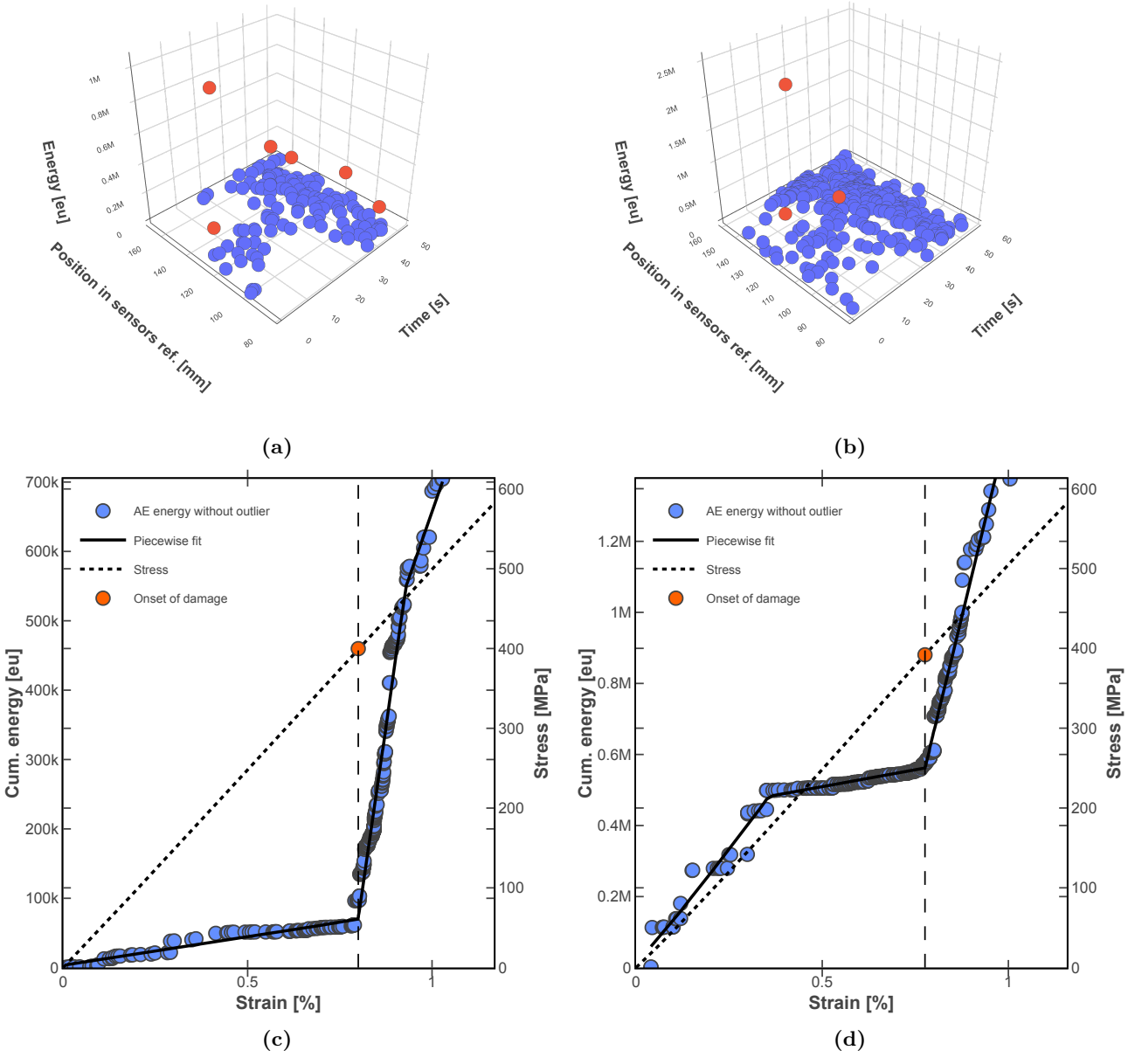

Figure B.3: AE events for (a) $^{33}\text{L3A}_{120}^{60}$ and (b) $^{33}\text{L4S}_{120}^{60}$ where red dots indicate outliers manually removed from the analysis; and corresponding AE analysis for (c) $^{33}\text{L3A}_{120}^{60}$ and (d) $^{33}\text{L4S}_{120}^{60}$.

UNT failure modes

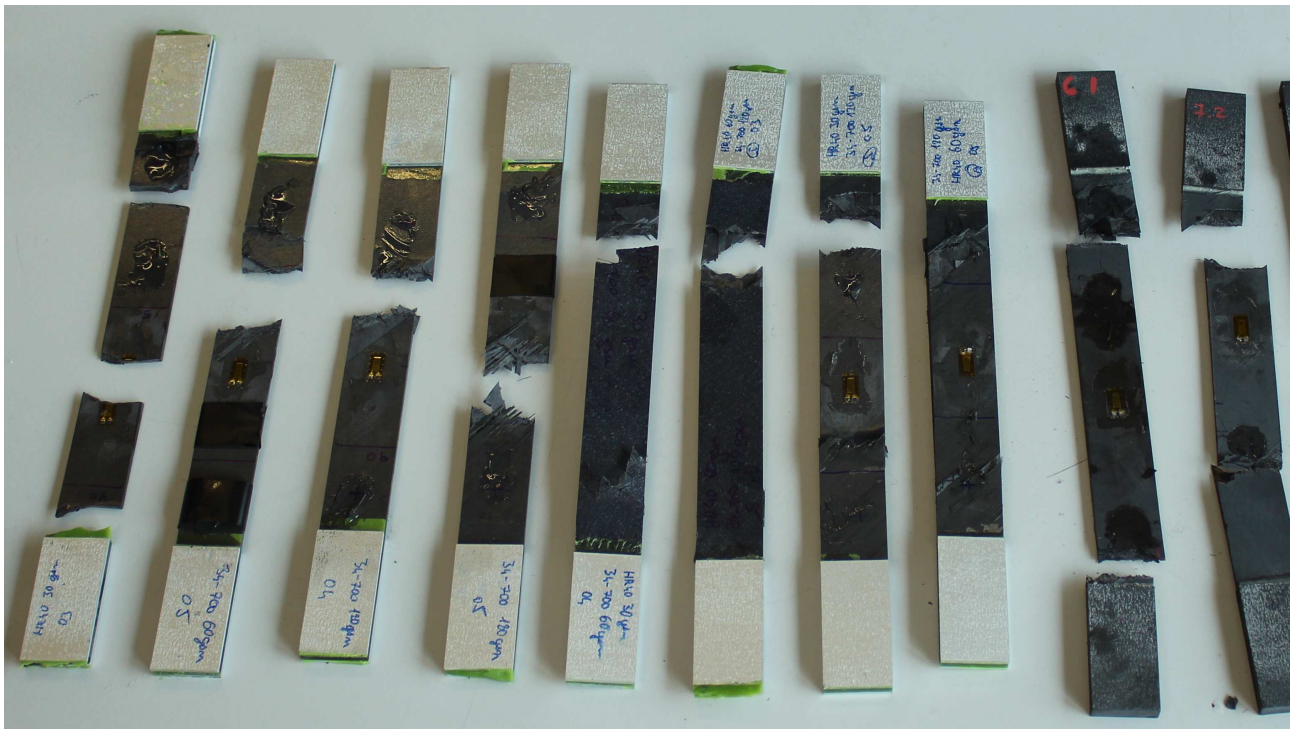

Figure B.4: Failure modes observed for, from left to right, $^{100}\mathrm{B1}_{0}^{30}$, $^{0}\mathrm{B2}_{60}^{0}$, $^{0}\mathrm{B3}_{120}^{0}$, $^{0}\mathrm{B4}_{180}^{0}$, $^{33}\mathrm{L1A}_{60}^{30}$, $^{33}\mathrm{L4S}_{120}^{60}$, $^{20}\mathrm{L2S}_{120}^{30}$, $^{33}\mathrm{L3A}_{120}^{60}$, $^{20}\mathrm{C1}^{75}$, and $^{33}\mathrm{C2}^{45}$.

Appendix C

Supporting information for chapter 7

Additional fracture surface observations

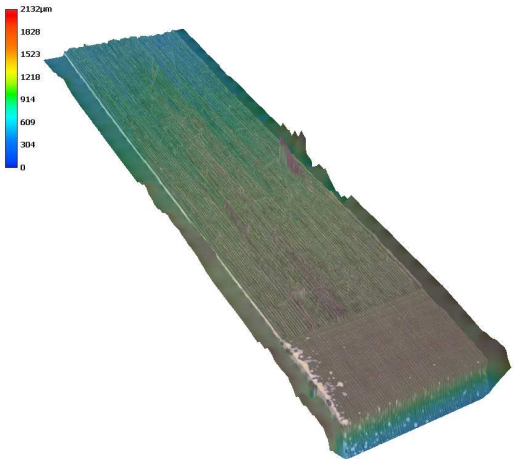

(a) $^{100}\mathrm{B1}_{0}^{30}$

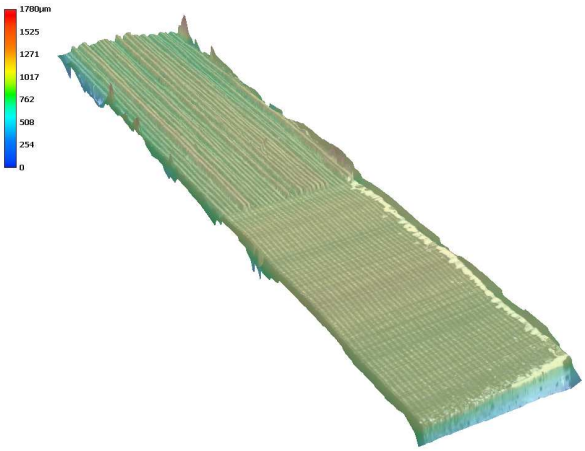

(b) $^{0}\mathrm{B2}_{60}^{0}$

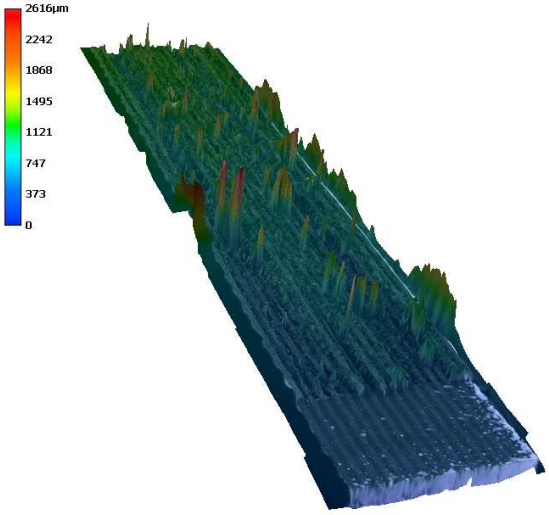

(c) $^{0}\mathrm{B3}_{120}^{0}$

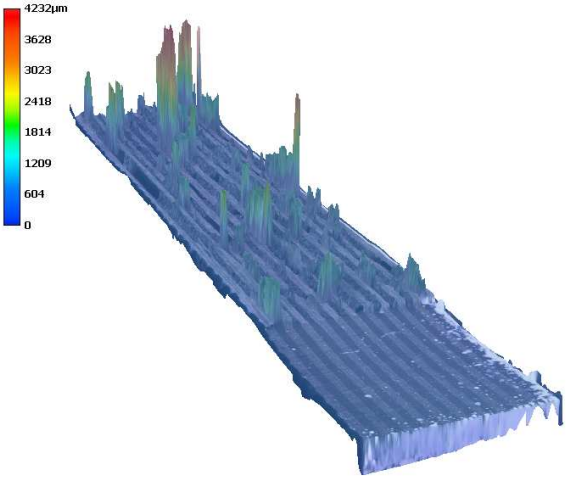

(d) $^{0}\mathrm{B4}_{180}^{0}$

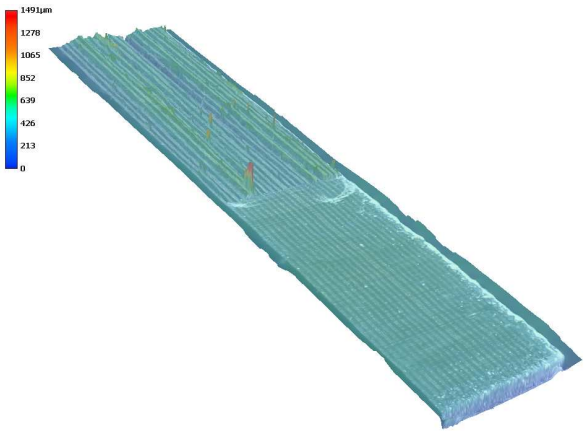

(e) $^{33}\mathrm{L1A}^{30}_{60}$

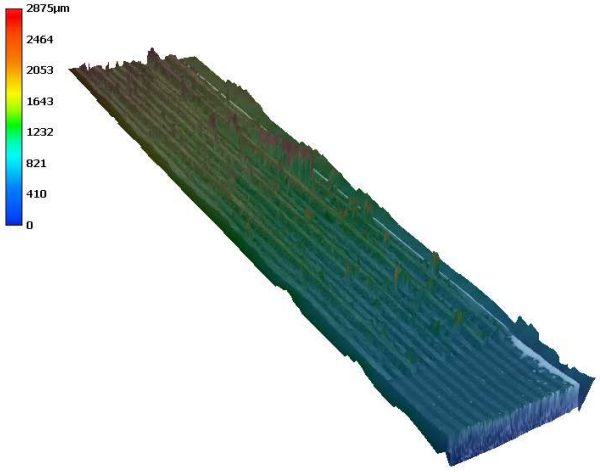

(f) $^{20}\mathrm{L2S}^{30}_{120}$

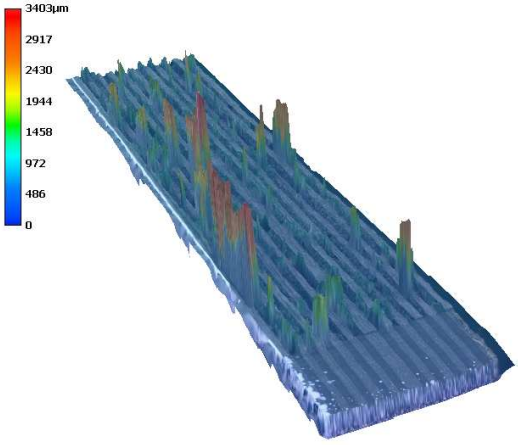

(g) $^{33}\mathrm{L3A}^{60}_{120}$

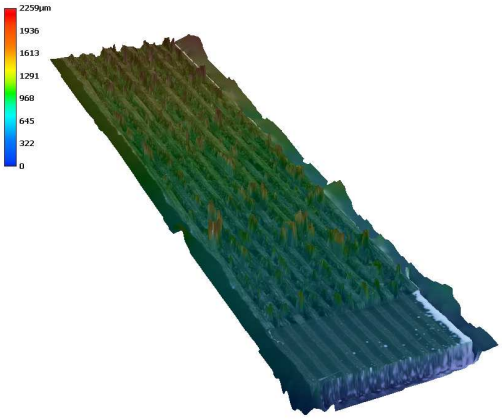

(h) $^{33}\mathrm{L4S}^{60}_{120}$

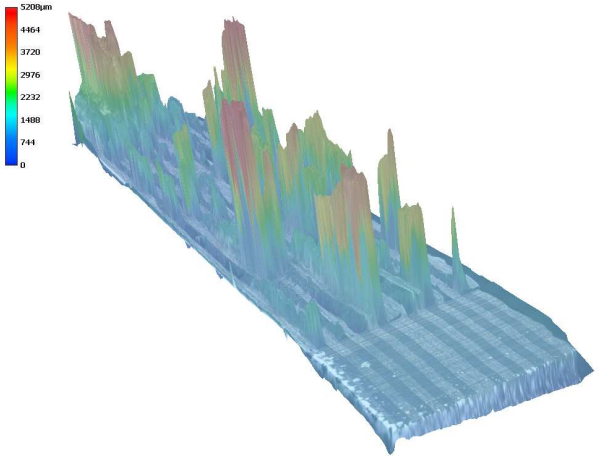

(i) $^{14}\mathrm{L5A}^{30}_{180}$

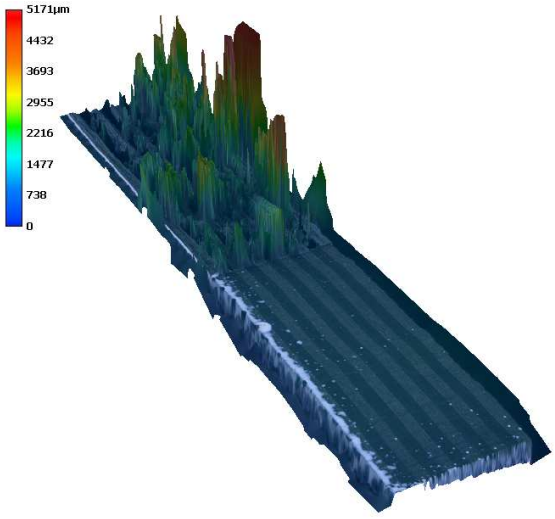

(j) $^{20}\mathrm{L6S}^{60}_{240}$

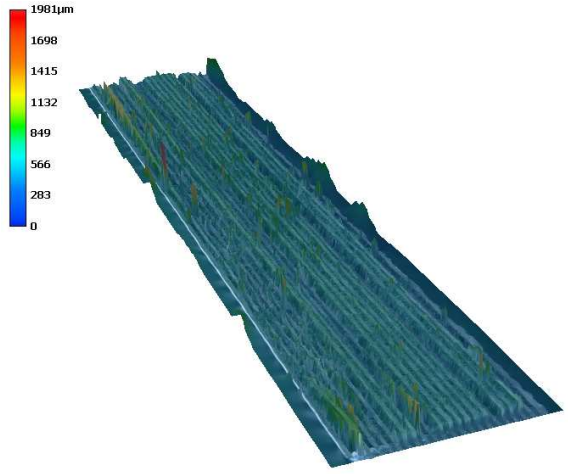

(k) $^{25}\mathrm{Y1}^{90}$

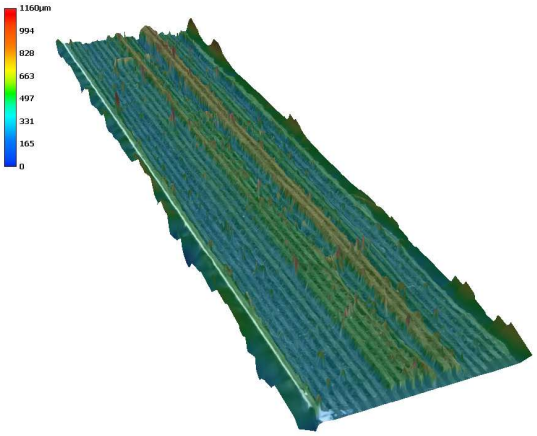

(l) $^{25}\mathrm{Y2O}^{90}$

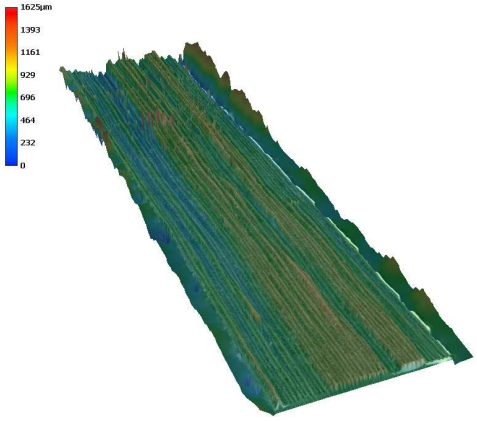

(m) $^{31}\mathrm{Y3}^{45}$

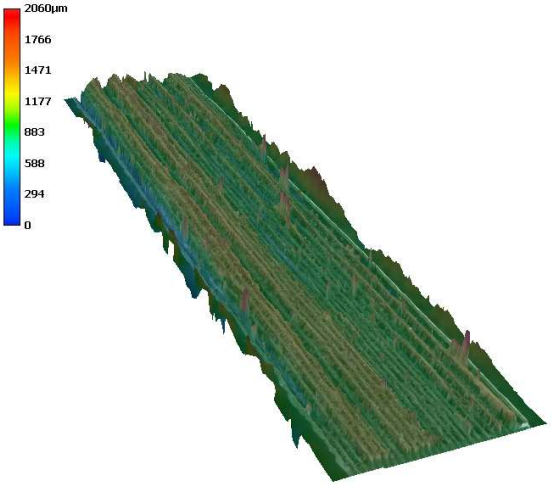

(n) $^{20}\mathrm{C1}^{75}$

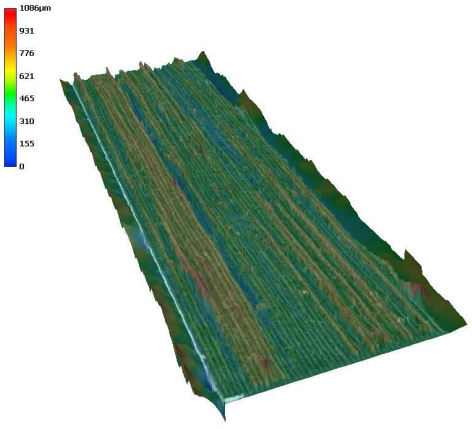

(o) $^{33}\mathrm{C2}^{45}$

Figure C.1: Fracture surface observations acquired with a VHX-5000 Keyence optical microscope.

Pull-out length estimations from Danzi et al. [56]

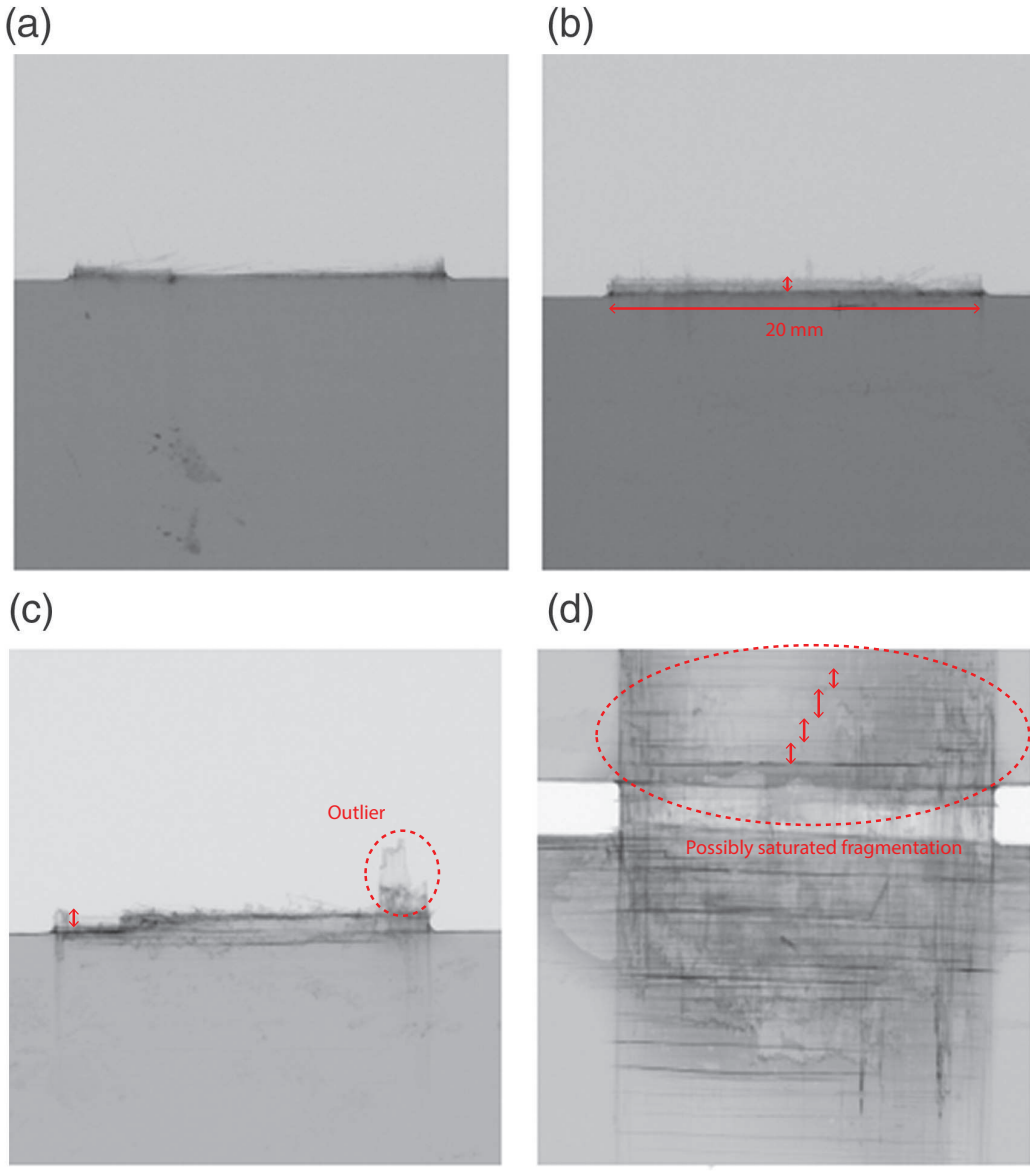

Figure C.2: T800-HR40 hybrids CT-scan observations. The pull-out lengths were approximately estimated as indicated by the red annotations for H1 (b), H2 (c), and H3 (d). For H3, the pull-out length was estimated from the top area that seems to exhibit a saturated fragmentation. Adapted from Danzi et al. [56].

Detailed model predictions

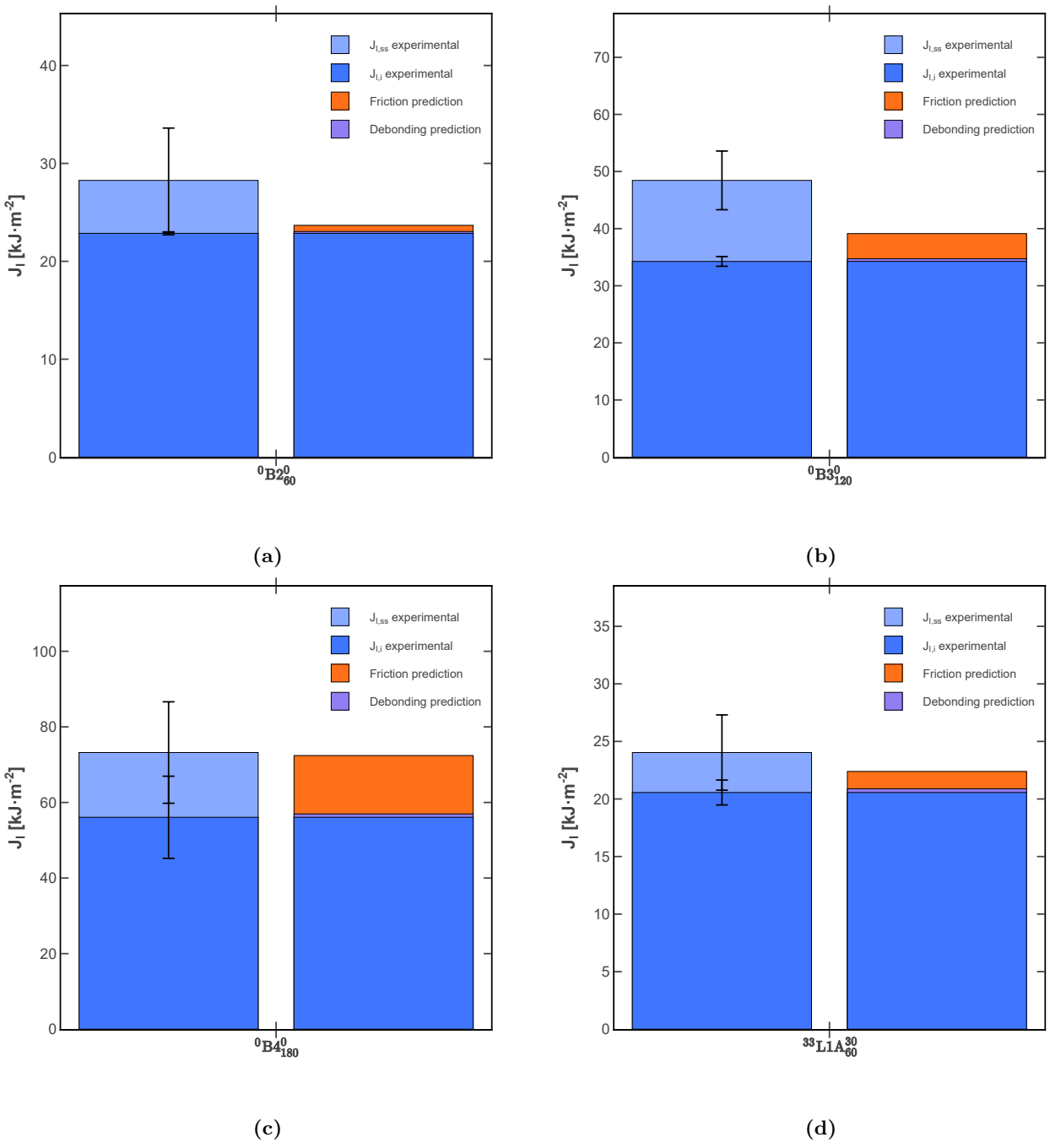

Figure C.3: Detailed model predictions. See section 7.3 for implementation details.

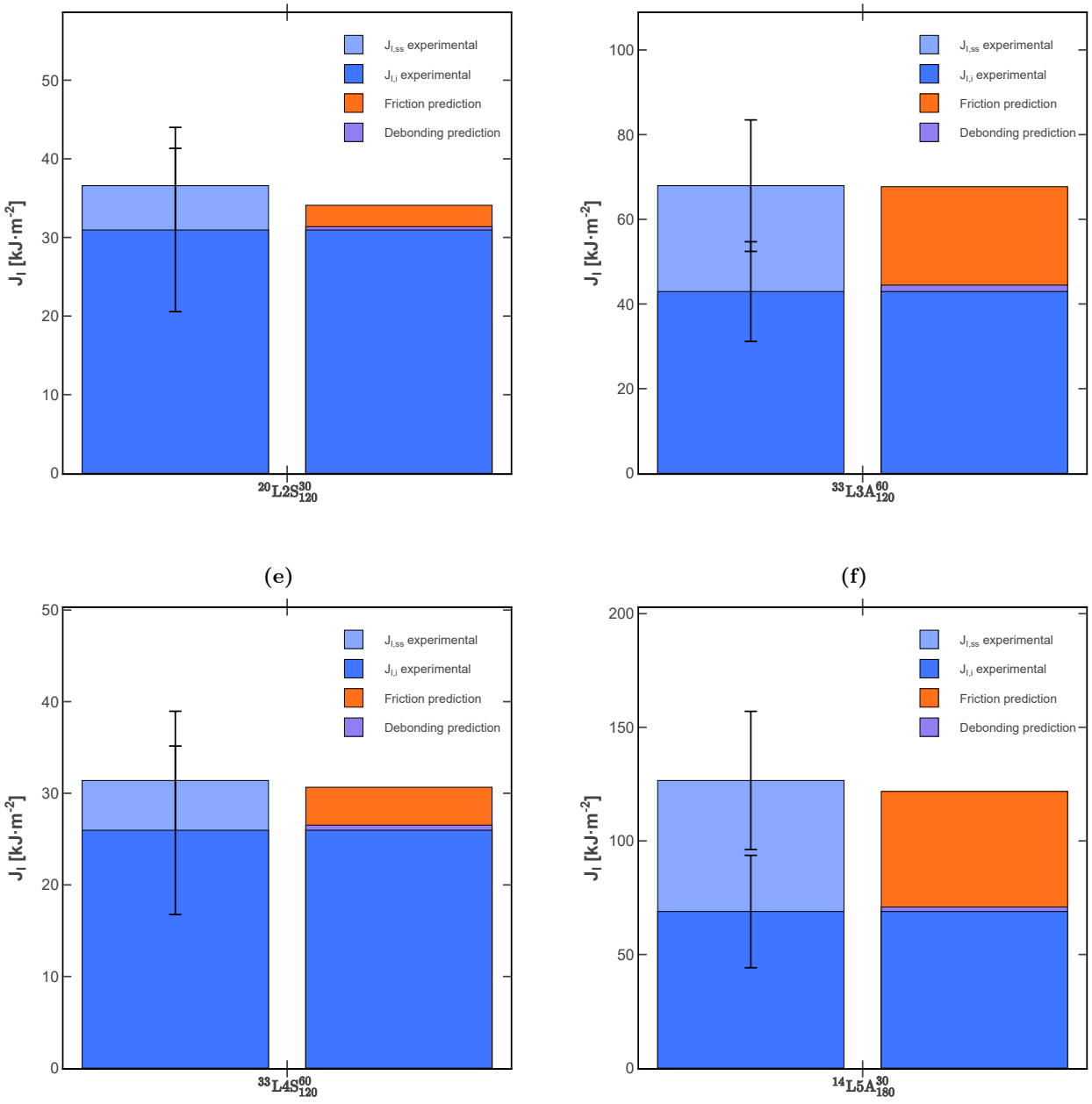

Figure C.3: Detailed model predictions. See section 7.3 for implementation details.

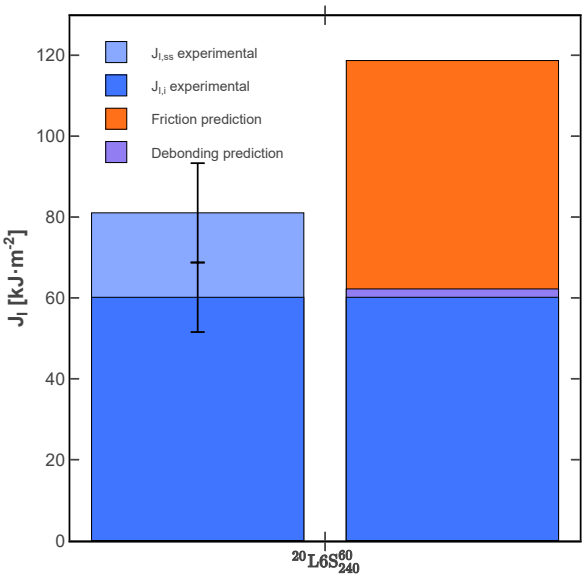

(i)

Figure C.3: Detailed model predictions. See section 7.3 for implementation details.

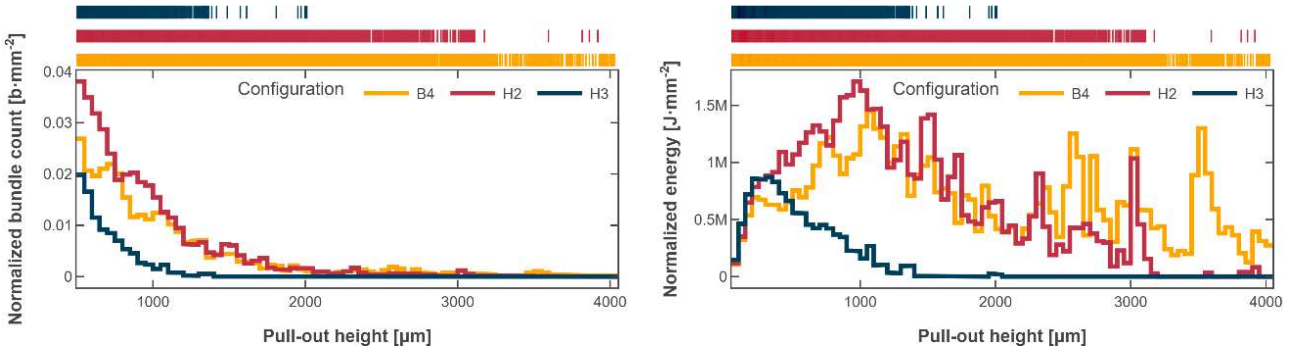

(a) **(b)**

Figure C.4: (a) Close-up on the bundle length distribution over the range 500 to 4000 µm for baseline $^{0}\mathrm{B4}^{0}_{180}$, interlayer hybrids $^{33}\mathrm{L3A}^{60}_{120}$ (H2) and $^{33}\mathrm{L4S}^{60}_{120}$ (H3), all with a FAW of 180 g · m^{-2}; (b) corresponding energy dissipated by the bundles in debonding and friction, predicted by the dual scale model. Counts and energies were normalized by the crack area projected onto the crack plane. Distributions are overlayed.

Guillaume BROGGI

guillaume@broggi.fr
+336.33.28.69.41
linkedin.com/in/GuillaumeBroggi

PhD candidate, MSCA Early Stage Researcher
ÉCOLE POLYTECHNIQUE FÉDÉRALE DE LAUSANNE

Education

2018 - Present — **École Polytechnique Fédérale de Lausanne** — *Lausanne, Switzerland*
MSCA Early Stage Researcher

- Multi-scale characterization and modelling of translaminar fracture and notched strength in thin-ply fiber-hybrid laminates
- Supervisors: Prof. Véronique Michaud and Prof. Joël Cugnoni
- Funded by the Marie Sklodowska-Curie grant agreement No 765881 (HyFiSyn H2020-MSCA-ITN-2017)
- Teaching activities

Curriculum: Deep Learning (EE-559); Fracture Mechanics (ME-432); SEM Techniques (MSE-636); Methods of Modelling and Simulation of Materials Science (MSE-641); Modelling of Advanced Composites: Processing and Mechanicals Properties (MSE-710); Design of Experiments (ENG-606)

2016 - 2017 — **Georgia Institute of Technology** — *Atlanta, USA*
Master of Science in Mechanical Engineering

- Double degree with Arts et Métiers Paristech
- GPA: 4.0 out of 4.0

Curriculum: Micromechanics of Materials; Elastic and Inelastic Deformation of Solids; Numerical Methods; Data and Visual Analytic; Mechatronics; Manufacturing Processes and Systems; Management for Engineers

2014 - 2017 — **Arts et Métiers ParisTech** — *Metz, France*
Diplôme d'Ingénieur, Mechanical and Industrial Engineering

Curriculum: Mechanical and Industrial Engineering; Mechanical Design; Process; Materials; Project Management; Industrial Automation; Mechanics of Solids; Numerical Methods; Fluid Mechanics; Thermodynamics

Research Projects

2018 (8 months) — **AMVALOR,** Arts et Métiers Technology Development and Transfer Institute — Metz, France
Research engineer

- Contribution to the EPITHER technology: development of an innovative large series process for industrial grade composite parts made of continuous carbon fibers and thermoplastic
- Numerical FEM and prototyping
- Industrial exhibition (JEC World)

Peer-reviewed publications

[1] B. Caglar, **G. Broggi**, M. A. Ali, L. Orgéas, V. Michaud. Deep learning accelerated prediction of the permeability of fibrous microstructures. *Composites Part A: Applied Science and Manufacturing*, 158: 106973, 2022
doi: 10.1016/j.compositesa.2022.106973

Presentations in Conferences

- 20th European Conference on Composite Materials, Lausanne, Switzerland, June 26-30th 2022
- HyFiSyn School and Conference, Leuven, Belgium, Sept 13-16th 2021
- CompTest 2021, virtual, May 18-20th 2021

Technical Projects

2016 **Mathematical forecast of consumption and supply optimization - Laboratory LCFC**
Two-people team, application to a practical case, implementation of the model through a web application (Python – Django)

2016 **Contribution to the Vulcain platform - Laboratory LCFC**
Project leader, five-people team, conception of a robotic mechanical gripper adapted to thixoforming

2015 **Investigation of fast and repeatable quenching in molten salt – Laboratory LEM3**
Project leader, five-people team, design and building of a quenching robotic arm

Associative and Outreach Activities

2019 - 2021 **PolyDoc, Committee member**
Developing the PhD community at EPFL by organizing regular events and by offering an interface between the EPFL governing bodies and the PhD students

2015 - 2016 **I-RESAM, Secretary**
Supply of an affordable and qualitative Internet access in the student's hall; technical, legal and administrative management

2015 - 2016 **AE-ENSAM, Responsible for public outreach**
Organization of information days and career guidance events for prospective students and young audience

Selected Technical Skills

- Composite manufacturing: prepreg lamination, curing in and out of autoclave, infusion, consolidation of thermoplastic laminates
- Composite characterization: tensile properties (UNT, OHT), toughness properties (DCB, 4ENF, CT), shear properties (ILSS), SEM, in-situ synchrotron X-ray tomography
- Finite Element Analysis: ABAQUS (e.g. mechanical behavior of composites, crack propagation), OpenFoam (CFD)
- Coding: Python, C/C++ for microcontrollers, Unix environment, Git, LaTeX
- Deep learning: PyTorch, limited experience with JAX
- Languages: English (C1/C2), Spanish (B2/C1), French (native)